A Position-Sensing System for the Top PMT Array in the LUX-ZEPLIN Dark Matter Experiment



Kathryn Boast

St. Peter's College

University of Oxford

A thesis submitted for the degree of

Doctor of Philosophy

Michaelmas 2017

Abstract

LUX-ZEPLIN (LZ) is a next-generation liquid xenon dark matter detection experiment, searching for direct interactions with WIMPs. As it is a low-background experiment using high-purity xenon, the sensors installed to monitor the experiment must be custom-made from a short list of acceptable materials. This includes the position sensors that will monitor the relative position of the top photomultiplier tube (PMT) array with respect to the cryostat vessel that surrounds it. LZ will operate at around $-100\,^{\circ}\mathrm{C}$, so must undergo a significant cooling period, during which the vessel that supports the PMT array is expected to shrink. It is crucial to monitor this.

The capacitive position sensors couple a change in relative position to a change in capacitance. However, the size of the LZ detector necessitates the use of cables around 12 m long to read out this signal. These cables will have a capacitance themselves of around 1 nanofarad, which can vary as the cable environment changes, while the sensor capacitances are around a thousand times smaller, so small variations in the cable capacitance could be misinterpreted as changes in position. To combat this, we created a novel feedback circuit for the sensor readout electronics, designed to suppress the effect of the cable capacitance.

To monitor precisely the position of the PMT array with respect to the cryostat vessel, we will use six position sensors mounted as a Gough-Stewart Platform Mechanism (GSPM) between the PMT truss and the cryostat vessel. The use of six sensors in this configuration will enable the reconstruction of all six degrees of freedom of the position of the PMT array. I have developed an algorithm that returns these six values given input from the position sensors. The six capacitive sensors connected as a GSPM, with the novel readout electronics, form the system of position sensors that will be used in the LUX-ZEPLIN experiment.

Acknowledgements

My first thanks must go to Professor Hans Kraus for giving me the opportunity to study for a DPhil in particle physics, and for the help and support he has given over the past four years.

I am very grateful to the Science and Technology Facilities Council for supporting not only my studies but also my secondment to the Parliamentary Office of Science and Technology, which was an incredible opportunity.

I have always found help and support in the Particle Physics sub-department, from a cheery smile with the admin staff to sincere friendship with the students in my cohort. I am also particularly grateful for the existence of the Oxford Women in Physics Society, through which I have made many good friends and met any number of inspiring women in physics. Thank you for providing a network I could rely on.

My special thanks must go to my mentor, Dr Aprajita Verma. Thank you for picking me up when I crashed into the final hurdles and seeing me over the finish line!

A large part of my work has involved the creation of mechanical devices that are well beyond my capabilities to fashion, for which the help of the Mechanical Workshop has been invaluable, and in particular that of Mike, Joe, Dan and Bob. Thank you for your persistent patience in the face of my often naive questions and sometimes demanding deadlines.

My time in the office and lab was always brightened by those around me, for which I was very grateful. I must particularly thank Junsong, for constant thoughtfulness, and FengTing: it has been a pleasure to share the ups and downs of the past four years of work with you.

To my parents, Peter and Jacqueline: thank you for your unwavering support. Your joy in my small successes has always spurred me on, and if I have learnt how to work hard, I have learnt it from you!

And finally, to my partner, Jake, for being there every step of the way. You are my rock.

Contents

1 The Dark Matter Problem **4**

1.1 Introduction 4

1.2 Early evidence for dark matter 4

1.2.1 The Coma Galaxy cluster 5

1.2.2 Galactic rotation curves 5

1.3 Gravitational lensing 7

1.3.1 Measuring gravitational lensing 7

1.3.2 The Bullet Cluster 7

1.3.3 The Coma Cluster Revisited 11

1.4 The Cosmic Microwave Background 12

1.4.1 Structure formation 12

1.4.2 Baryon acoustic oscillations 13

1.5 Avoiding dark matter 14

1.6 The WIMP hypothesis 15

1.6.1 Cold dark matter 16

1.6.2 MACHOs 16

1.6.3 Dark matter candidates 17

1.6.3.1 Neutrinos 17

1.6.3.2 Neutralinos 17

1.6.3.3 Sterile neutrinos 18

1.6.3.4 Axions 18

1.7 Beyond theory 19

2 Searching for Dark Matter **20**

2.1 Weak interactions & dark matter searches 20

2.1.1 Direct searches for WIMPs 22

2.2 From WIMP to detection 22

2.3 Results to date 23

2.3.1 Limits . . . 23
2.3.1.1 LUX . . . 24
2.3.1.2 PandaX-II . . . 24
2.3.1.3 XENON experiment . . . 24
2.3.1.4 Argon experiments . . . 26
2.3.1.5 Cryogenic experiments . . . 27
2.3.2 Discovery claims . . . 27
2.4 The LUX-ZEPLIN Experiment . . . 28
2.4.1 Xenon and WIMPs . . . 29
2.4.2 Signals . . . 30
2.4.2.1 Xenon contamination . . . 32
2.4.3 Instrumentation . . . 34
2.4.4 Sensitivity . . . 35
2.5 Backgrounds and cleanliness . . . 35
2.5.1 Decays and decay chains . . . 35
2.5.2 Radon-222 and Lead-210 . . . 39
2.5.2.1 Dust . . . 40
2.5.3 α emissions and α-n scattering . . . 40
2.5.4 Screening . . . 41
2.5.5 Cleaning . . . 42

3 Capacitive Sensor Readout in LZ 43
3.1 Sensors in LZ . . . 43
3.1.1 Position sensors . . . 44
3.1.2 Level sensors . . . 45
3.1.3 Acoustic sensors . . . 47
3.1.4 Loop antennae . . . 47
3.1.5 Thermometers . . . 47
3.2 Introducing the readout for capacitive sensors . . . 48
3.2.1 Cable capacitance variation with temperature . . . 51
3.2.2 Cable capacitance suppression . . . 52
3.3 A simple position sensor . . . 53
3.3.1 A spacing variation sensor . . . 53
3.3.2 Sensor design . . . 56
3.3.2.1 Fringe fields . . . 56
3.3.2.2 Plate configuration . . . 58

3.3.2.3 Calibration . . . 59
3.4 The readout electronics . . . 60
3.5 The feedback circuit . . . 60
3.5.1 Calculating the feedback . . . 62
3.5.2 Cable capacitance suppression . . . 65
3.5.3 Oscillation . . . 66
3.5.4 Phase shift . . . 68
3.6 The excitation . . . 69
3.6.1 Excitation shape . . . 70
3.6.2 Frequency . . . 71
3.7 The amplifiers . . . 73
3.7.1 The first stage . . . 73
3.7.2 The second stage . . . 76
3.7.3 The third stage . . . 77
3.7.4 Three stages of amplifiers . . . 78
3.8 Crosstalk . . . 79
3.8.1 Results . . . 81
3.9 Noise . . . 83
3.9.1 Filtering . . . 83
3.9.2 Noise from the electronics . . . 83
3.9.3 Noise from the cables . . . 86
3.10 Isolation of amplifiers . . . 88
3.11 Power supply . . . 88
3.12 Shielding and connectors . . . 90
3.13 Digital electronics . . . 92
3.13.1 Readout speed . . . 94
3.13.2 Digital output . . . 94
3.14 Conclusion . . . 95

4 Position Sensor Design **96**
4.1 Motivating position sensors . . . 96
4.1.1 The shrinking of the experiment . . . 97
4.1.1.1 Vertical Shrinking . . . 99
4.1.2 Other movements . . . 100
4.2 Choosing capacitive sensing . . . 102
4.2.1 Material considerations . . . 102

4.2.2 Sensing modalities . . . 103
4.2.2.1 Capacitive sensors . . . 103
4.2.2.2 Inductive sensors . . . 104
4.2.3 Merits and demerits of sensing methods . . . 104
4.2.4 Varying capacitance . . . 106
4.2.4.1 Spacing variation . . . 106
4.2.4.2 Area variation . . . 106
4.2.4.3 Dielectric variation . . . 106
4.2.4.4 Splitting capacitors . . . 108
4.2.4.5 Conclusion on capacitance variation . . . 110
4.3 Sensor design . . . 110
4.3.1 Design process . . . 110
4.3.2 Sensor geometry . . . 111
4.3.3 Design details . . . 113
4.3.4 Sensor output . . . 114
4.3.4.1 Optimising the dimensions . . . 118
4.3.5 Cooling and shrinking . . . 119
4.3.5.1 Dielectric variation . . . 124
4.3.5.2 Through-thickness shrinking . . . 124
4.3.5.3 In-plane shrinking . . . 125
4.3.5.4 Conclusion on shrinking . . . 128
4.3.6 Deviations . . . 128
4.3.7 Sensor integration . . . 129
4.4 Materials . . . 130
4.4.1 Capacitor plate substrate . . . 130
4.4.1.1 Photolithography . . . 133
4.4.2 Copper . . . 134
4.4.2.1 Copper screening . . . 134
4.4.2.2 Copper machining . . . 135
4.4.3 PEEK . . . 136
4.4.4 Wiring . . . 136
4.4.5 Connectors . . . 137
4.4.6 Total radioactivity . . . 137
4.5 System Test at SLAC . . . 138
4.5.1 The early runs . . . 138
4.5.1.1 Design . . . 138

4.5.1.2 Operation . . . 143
4.5.1.3 Calibration . . . 144
4.5.1.4 Results . . . 147
4.5.2 Run 7 . . . 150
4.5.2.1 Design . . . 150
4.5.2.2 Calibration . . . 151
4.6 Final sensor . . . 156
4.7 Conclusion . . . 156

5 A connected system of sensors 157
5.1 Using individual sensors . . . 157
5.1.1 Assembling the detector . . . 158
5.2 Gough-Stewart platform mechanisms . . . 160
5.2.1 Introduction . . . 160
5.2.2 Our application . . . 161
5.3 Tripods . . . 161
5.3.1 Motivation . . . 161
5.3.2 Design . . . 161
5.3.3 Analysis . . . 163
5.3.4 Data . . . 165
5.4 Hexapods . . . 168
5.4.1 The geometry . . . 168
5.4.2 An analytical solution . . . 171
5.4.3 A numerical solution . . . 172
5.4.4 Multiple solutions and singularities . . . 173
5.5 Hexapod design . . . 175
5.5.1 The design . . . 175
5.5.1.1 Mounting points . . . 176
5.5.1.2 Bars . . . 177
5.5.1.3 Platform corners . . . 178
5.5.1.4 Screwing down the hexapod . . . 178
5.5.1.5 Sensor connections . . . 180
5.5.2 Installation . . . 182
5.5.3 Electrical connection . . . 183
5.5.4 Sensitivity . . . 183
5.5.5 Temperature effects . . . 186

5.5.6 Error propagation 186
5.6 Testing the hexapod 188
5.6.1 CAD models 188
5.6.2 Hexapod test stand 189
5.7 Conclusion 192

Appendices **194**

A Analysing the analogue feedback circuit **195**

B Analysing the digital electronics **200**

C Materials List **204**

D On hexapods **205**

E Cylindrical sensor design **208**

F Engineering Drawings **211**

Bibliography **234**

List of Figures

1.1 The galactic rotation curve for NGC6503. The data points, lying across the top of the plot, indicate the orbital velocity of the gas in the galaxy. The dotted and dashed lines labelled 'gas' and 'disk' respectively indicate where the data points would be expected to lie if that contribution to the overall mass of the galaxy were the only contribution. The line labelled 'halo' is the predicted contribution from dark matter filling the galaxy. Figure from [1]. Permission to reproduce this figure has been granted by Oxford University Press. 6

1.2 Gravitational lensing by the Abell 2218 galaxy cluster. The distant galaxies viewed through this lens appear smeared out around the invisible central mass. Credit: NASA, ESA, and Johan Richard (Caltech, USA); Acknowledgement: Davide de Martin & James Long (ESA/Hubble) 8

1.3 Gravitational lensing. On the left is an image from the Hubble Space Telescope where the foreground galaxy cluster is lensing the images of the distant galaxies. On the right is a reconstructed map of the gravitational lensing power of the cluster, and hence also of the mass of the cluster. The sharp spikes correspond to the galaxies in the cluster, but there is additionally a smooth background that peaks in the centre of the cluster. This is the mass owing to the dark matter in the cluster. Image from [2], which is distributed under the terms of the Creative Commons Attribution 4.0 (CC-BY) License. 9

1.4 A composite image of the Bullet Cluster. The pink sections indicate the location of most of the baryonic matter, while the blue sections highlight the location of most of the mass. Credit: NASA / Chandra X-ray observatory. 10

1.5 X-ray image of the Coma Cluster from the ROSAT satellite. A gravitational potential provided by dark matter is needed to hold this gas in place. Image credit: ROSAT / MPE / S. L. Snowden, from https://heasarc.gsfc.nasa.gov/docs/rosat/gallery/clus_coma.html . . . 11
1.6 The power spectrum of the CMB from the Planck satellite. The red points with error bars mark the data. The green shape is the power spectrum given by a model containing 5% baryonic matter, 26% dark matter and 69% dark energy. Image from [2], which is distributed under the terms of the Creative Commons Attribution 4.0 (CC-BY) License. 13

2.1 The different ways to search for dark matter. Consider 'DM' to represent a dark matter particle and 'SM' to represent a standard model particle. This diagram demonstrates the connection between the different search methods. Direct searches look for the interaction of a dark matter particle with a standard model particle. Indirect searches look for standard model products that could result from dark matter annihilations. Collider searches aim to produce their own dark matter from a starting point of standard model particles, though further investigations would have to be undertaken to confiem whether the candidate particle found in the LHC is really the same as the particle that constitutes galactic dark matter. 21
2.2 The current spin-independent WIMP-nucleon interaction cross-section limits set by experiments discussed in this section. Xenon-1T result:[3]; DEAP-3600 result:[4]; CRESST-II result:[5]; LUX result:[6]; DarkSide-50 result:[7]; PandaX-II result:[8]. The most straightforward WIMP implementation is that that the WIMP is a heavy Dirac neutrino; this was originally suggested by Lee and Weinberg in 1977.[9] This simple model was ruled out in 1996 when experiments for the first time probed the relevant parameter space,[10] reaching down below 10^{-5} pb for the spin-independent WIMP-nucleon cross-section for a 50 GeV WIMP.[11] 25
2.3 Experimental residual rate of the single-hit scintillation events measured by DAMA/LIBRA-phase1 as a function of the time. Image reproduced from [12], which is distributed under the terms of the Creative Commons Attribution License 4.0. 28

2.4 The layered structure of the LZ inner and outer detectors, with their shielding. 29
2.5 The chain of events following an interaction with xenon resulting in a nuclear recoil or electron recoil. Adapted from [13]. 31
2.6 A demonstration of what a PMT 'hit map' might look like following an interaction at the centre of the detector. The largest signals in the top array (top picture) are from the S2 signal. The signals in the lower array (bottom picture), shown in subtle variations of blue, are from the S1 signal. 33
2.7 The predicted sensitivity of LZ, as given in [14]. The black line shows the predicted limit that LZ will reach. The orange shaded areas show regions where background NRs from cosmic neutrinos become a significant consideration. The predicted limit curve is shown alongside those achieved by other xenon dark matter search experiments, LUX, XENON1T and PandaX-II. As with all these experiments, LZ is less sensitive when there is a substantial discrepancy between the WIMP mass and the target mass (i.e. the mass of a xenon nucleus), as a result of the kinematic factor discussed in section 2.2. 36
2.8 The uranium-238 decay chain, showing the dominant decays. 38

3.1 Schematic illustrating some of the sensors in LZ. The position sensors, long level sensors and weir precision sensors are all capacitive sensors, for which the readout is the focus of this chapter. 44
3.2 A CAD model of the 'top corner' region, showing the anode and gate wire grids, and the weir that allows for liquid overspill. The liquid-gas interface should sit between the gate grid and anode grid. 46
3.3 A schematic of the workings of the weir and 'weir precision sensor'. As the liquid xenon is pumped into the bottom of the detector, liquid will overspill into the weir, flowing out of the detector through drains in the weir. The weir precision sensors sit within the weir to monitor the level of liquid within it. One capacitor plate sits above the top of the weir, while the other sits in the bottom, such that the liquid level (highlighted here in blue) will lie between the two. 46

3.4 The dimensions of the coaxial cable that is being produced by Axon for LZ. This will be used for the sensors. The dielectric and outer jacket are made of fluorinated ethylene propylene (FEP). Some of the cable can be seen in fig. 3.5. 48
3.5 A photograph of some of the coaxial cable that will be used in LZ. . . 49
3.6 The modelled output for one half (C_1) of the system test position sensor, discussed in detail in Chapter 4. The capacitance of this half varies by around 2.5 pF across the range of the sensor. The other half of the sensor takes the same values in reverse, and the readout is based on the difference between these two. 50
3.7 A diagram indicating a possible plate arrangement in a spacing variation sensor. An AC excitation voltage is applied to one plate ('Excitation') and picked up by the plate facing it ('Sensitive'). The voltage read out from this plate will depend on the capacitance of the plate arrangement. 54
3.8 A diagram to illustrate the voltages and distances as used in the calculation of the sensed voltage. 55
3.9 Illustration of the behaviour of three parallel plates as a potential divider and two capacitors 56
3.10 CAD model of prototype sensor: **a.** sense electrode, a central circular plate (false-coloured in model) with narrow extension to the edge of the surrounding electrode, **b.** guard electrode, **c.** excitation plates which carry the positive and negative excitations, coupled together, **d.** plunger fixed to the excitation plates, **e.** guard ground plates. 57
3.11 Photograph of prototype sensor in a basic test stand. **CS** Capacitive sensor, **L** Laser position sensor, **RE** Readout electronics, **P** Power cable for electronics, **C** Cables for sensor, consisting of: **G** a wire carrying ground to the outer plates, **E** a pair of wires carrying the excitations, and **S** the sense wire, housed in a thin copper tube for shielding. . . . 58
3.12 Illustration of fringe fields with and without guard electrode 58
3.13 A finite element analysis model of the electric field in the central region of the position sensor. The lines indicate equipotentials of the field between the excitation plates and the sense and ground plates. 59
3.14 A simplified schematic of the feedback loop that forms part of the readout electronics for the capacitive sensors. The sensor consists of capacitors C_1 and C_2. 61

3.15 A schematic of the feedback loop including the cable capacitance as a stray capacitance to ground and showing a feedback amplifier. A more detailed schematic including component values can be found in appendix A. 63
3.16 Results from an experiment to test the effect on the output of increasing the cable capacitance. A variable capacitor was connected in parallel with the cable capacitance so that the cable capacitance could effectively be altered. The output was recorded for a range of total capacitances. Top: A demonstration of the suppression of the cable capacitance. The output voltage is shown for a fixed pair of capacitors, which is a model for an unchanging capacitive sensor. For additional cable capacitances up to 1.35 nF, there is no systematic effect on the output. Bottom: If the cable capacitance is increased sufficiently, at levels well beyond those found in LZ, the signal begins to be suppressed by the enormous cable capacitances. This is the expected behaviour given the analysis of the feedback circuit. 67
3.17 A block diagram indicating the FPGA generating the positive and negative excitations for the summer amplifiers. 69
3.18 The addition of higher harmonics to an initial sine wave leads to an ever more accurate approximation of a square wave, demonstrating the high frequencies present in a square wave. 70
3.19 A block diagram of the amplifiers in the circuit. 72
3.20 The 'first stage' amplifier. This is an ADA4817 dual amplifier.[15] The input capacitor C_I is 1 µF. The feedback loop for the amplifier contains R_F, a 10 MΩ resistor and, in parallel, C_F, a 10 pF capacitor. These feed into the negative input terminal. The positive input terminal is connected to ground. The output will go on to the second stage amplifier. 73
3.21 The open-loop gain and phase vs. frequency for the ADA4817. In the regime of the first stage, where $C_I/C_F = 10^5$, this gives the gain and phase of the amplifier. From [15]; permission to reproduce this figure has been granted by Analog Devices. 74
3.22 The gain of the first stage plotted against $\frac{C_I}{C_F}$. For $\frac{C_I}{C_F} = 10^5$, the gain is clearly dominated by the open-loop gain of 1778. 76

3.23 The second stage amplifier, an LMH6626.[16] The input to the stage is the output from the first stage. The input to the amplifier features an input resistor, R_A, with a value of 1 kΩ. The feedback loop contains R_{F_2}, which is a 10 kΩ resistor, and C_{F_2}, which is a 10 pF capacitor. As this is configured as an inverting amplifier, the input is to the negative (inverting) input terminal of the amplifier, with the positive input terminal held at ground. 77

3.24 The third amplifier stage of the board, an LMH6626,[16] with the additional dual amplifier, an LM7322,[17] to separate off the large capacitive load (see section 3.10). The 'input' is the output from the second amplifier stage. This is fed via input capacitors and resistors to the negative input terminal of the op-amp. This signal is joined in the feedback loop via a capacitor and resistor by either the fixed positive excitation or the fixed negative excitation, dependent on which adder is under consideration. The positive input terminal is at ground. The output is thus the sum of the fixed excitation with the input. The component values are as follows: $C_E = 100$ nF, $R_E = 47$ kΩ, $C_I = 100$ nF, $R_I = 4.7$ kΩ, $C_F = 10$ pF, $R_F = 47$ kΩ. 78

3.25 The eight channel analogue electronic readout board. Dual amplifiers are used for the first and second stages, so only four are required to run eight channels. These are visible on the left hand side of this image. Each channel uses a single dual amplifier for its two adders that constitute the third stage. These are seen in two rows near the centre of the board. 80

3.26 The buffer (differential amplifier) that provides a ground without connecting a low impedance source to the ground plane. This helps to prevent crosstalk between channels. The amplifier is an AD8066, a high speed, high slew rate FET input amplifier, with excellent small-signal gain flatness up to frequencies of 10 MHz for a gain of 0 dB.[18] 81

3.27 A plot showing that there is no crosstalk between different channels on the electronics. The red triangles show the readout from one channel of the electronics, into which was input the signal from a pair of fixed capacitors. The blue circles show the readout from an adjacent channel on the electronics, into which was input a position sensor that moved over a range of 21 mm and accordingly changed its output. If there had been crosstalk between the channels, the varying position sensor signal (blue) would have affected the signal measured for the fixed capacitors (red). As this was not seen, there is no crosstalk between channels. The predicted value of the fixed capacitor channel was 200 ADC counts; the measurement is consistent with this within expected component value variations. 82
3.28 Diagram of noise sources at input to feedback loop, for calculation of noise dependence on cable capacitance 84
3.29 The interference from the switching power supply 89
3.30 The output from the switching power supply 89
3.31 The pinout for the DB25 connectors for the capacitive sensors. 91
3.32 The eight channel electronics board, with features to ensure the signals do not experience interference from the excitations or other external sources. 92
3.33 A block diagram of the digital electronics feedback loop. 93

4.1 The bottom of the detector, with the TPC supports on the ICV and the titanium PMT frame visible 97
4.2 A cross-section view through the TPC rings, as they feature in the CAD model of the detector. One set of segments of the PTFE rings is shown in pale green. The titanium rings are extended round to the right. 98
4.3 A CAD cross-section through the TPC and cryostat vessels around the top corner of the detector. Note particularly the limited space between the ICV (the OCV is not shown) and the structures at the top of the TPC. 101
4.4 A diagram of a linear variable differential transformer that can be used as a position sensor. 104

4.5 The movement of a dielectric slider (orange) between the plates of capacitors C_1 and C_2. The hole in the slider effectively changes the relative permittivity between the capacitor plates, thus changing the capacitance. When the slider is in the centre, the two capacitors have the same amount covered and uncovered, so they have equal capacitance. The two ends illustrate the two opposite extremes. 108
4.6 The insertion of a metal block into the original capacitor divides it into two capacitors, labelled here as C_A and C_B. They are connected via the metal block such that they effectively share a capacitor plate. Equally they can be considered as two capacitors in series. 109
4.7 The insertion of a metal block that partly shields the sense plates from the excitation plates results in the division of the original capacitor into three capacitors. The section without the metal block in (labelled here as C_E) takes the full width of the original capacitor. The remaining sections, labelled C_A and C_B, have much smaller plate spacings. As the block moves into the capacitor, the relative ratios of C_E, C_A and C_B change. To find the total capacitance, add C_A and C_B in series, and then add this series sum in parallel with C_E. 109
4.8 The essential parts of the sensor: the two excitation plates, with the connected sense plates opposite them, and the (mechanically but not electrically) connected metal blocks in between. 111
4.9 An exploded view of the sensor plates with sense and excitation electrodes, with the moving metal blocks between. 112
4.10 Abstractions from the sensor design seen in fig. 4.8, to show the capacitances that are present in the sensor. C_A, C_B and C_E together constitute C_1, with the other capacitors forming C_2. 112
4.11 A CAD model of the sensor, viewed from the outside 114
4.12 A cross-section through the sensor, with the parts artificially coloured for clarity. All of the blue parts move together when the rod at the top of the image is actuated. The yellow parts are the Cirlex boards. . . . 115
4.13 The dimensioned drawing of the design for the sensor plates. This is used to produce a photolithography mask that is in turn used to create the appropriate shapes of copper on the Cirlex. 116
4.14 The definitions of the sensor lengths and sections, and the sense of motion as used in the calculation of sensor output. 116

4.15 A diagram to illustrate the terminology used to calculate the sensor output. 117
4.16 A model of the sensor output, changing the thickness of the metal block between the plates between 0 mm and 4 mm. In this model, the metal block sits in a gap of 4 mm between the plates. 120
4.17 A model of the sensor output, changing the spacing between the capacitor plates between 3 mm and 10 mm. In this model, the metal block has a thickness of 3 mm. 121
4.18 A model of the sensor output with a fixed gap of 0.5 mm between the block face and plate face, but changing the total spacing between the capacitor plates. As shown, the larger the spacing, the greater the output of the sensor. This change is steepest for small spacings, and as the spacing increases further, the gain in output is less significant. 122
4.19 The output of the optimised sensor, according to the simple model. The sensor 'sense' plate is 25 mm long and the range of the sensor is 25 mm, i.e. 12.5 mm in each direction. The anticipated measurable vertical shrinking was calculated in section 4.1.1.1 to be 4.6 mm. If we suppose a worst-case scenario, we might anticipate an additional 10% shrinking. This would lead to an expected sensor length change of 4.0 mm, with the sensors in the system as described in chapter 5. In addition to this shrinking, the TPC could move outwards by up to 2 mm (see section 4.1.2). If this is also included, the sensor length change becomes 5.2 mm. Any twisting of the platform would result in further sensor extension. The sensor is expected only to operate in the central portion of its range. 123
4.20 A diagram to show the lengths of electrodes, blocks and gaps, as used in the calculation of the effect shrinking has on the sensor. The top pair of black lines represent the sense electrodes. The dashed grey block indicates the 'central' position of the block. 125
4.21 The dielectric permittivity of polymers in general as a function of temperature. These are difficult data to find, as although materials are regularly tested at high temperatures, there is less information about the behaviour of polymers, particularly their electric properties, at low temperatures. Adapted from [19]. 131
4.22 The image used to create the photolithography mask for producing the electrode design on the copper-clad Cirlex. 134

4.23 The dimensions of the cable used for the position sensors, as produced by Axon. 136
4.24 CAD model showing how position sensor is connected to cryostat vessel and TPC 139
4.25 A schematic of the electrodes and dielectric slider for the position sensor in the SLAC system test 140
4.26 Solid models showing the design of the position sensor and its stand for the system test. 141
4.27 The position sensor for the early runs of the system test. 142
4.28 Photographs of the position sensor in place in the system test 143
4.29 The fixing of the connector on the position sensor 144
4.30 Data taken with the position sensor before it was taken to SLAC. This is a demonstration of the linearity of the sensor. The residual is compared to a straight line fit, shown in red in the top plot. This suggests that the conversion factor between sensor reading in mV and position reading in mm is 0.034 mm/mV. 145
4.31 The calibration of the position sensor used in Runs 3 - 6 in the SLAC System Test. The height was added by inserting washers under the plunger, pushing the plunger into the sensor with each step. This was undertaken at ambient temperature while the system was open, and used the cables (2.3 m long) and electronics created for this run of the System Test. Uncertainties are not given here as this is not the final sensor configuration. 146
4.32 Data from first cooldown with position sensor. Nulled at room temperature (2.4 mm). As temperature drops, TPC cools and shrinks, dropping away from the position sensor. The small, brief rise at around 230 K was due to some interference on the electronics, and the same feature was seen on the other sensors that shared the position sensor's readout board. Once the system reaches around 180 K, the temperature fluctuates between 166K and 178K over 20 hours of operation. These fluctuations take time to propagate through materials and cause small amounts of shrinking and expansion. The calibration factor determined after the run is applied here. 148

4.33 Three weeks of data taken during Run 4 in which the temperature varied as measured by a thermometer attached to the TPC. The slight variations in position at each temperature are not unexpected, as the thermometer measures only one small point, and the heat will take time to diffuse throughout the material, causing different amounts of shrinking in different places resulting in different TPC sizes for the same measured temperature. The data here is given in uncalibrated ADC counts from the position sensor. The apparent 1 deg quantisation arises from the signal moving between distinct ADC bits. This suggests that we should perhaps have used a different gain; however the temperature changes and hence position changes here are tiny: the calibration factor is -0.0187 mm/count, so these movements are on the order of only 20 µm. Hence this level of quantisation is not a concern. 149

4.34 Inside the position sensor used in Run 7 of the System Test at SLAC. The copper blocks that change the capacitance can be seen between the pair of Cirlex plates. The central copper block holds these plates together while the central, rounded blocks outside the plates are used to fix the surrounding copper tube; the tapped holes for this can be seen. The stainless steel rods are fixed to the very top and bottom copper discs, and run through PEEK bushes in the interior copper discs. At the lower ends of the rods, the springs can be seen, holding apart the end and interior copper discs. The copper blocks move with the outer copper discs; a pair of flat rectangular rods (one can be seen at the back of the image, the other is removed) connect the blocks to the top and bottom discs. 152

4.35 Data from calibrating the system test Run 7 position sensor. The sensor was moved and its position measured on a Vernier scale while the output was recorded. An arbitrary x-offset has been removed from the data by hand. The data has been fitted with a fractional function with a linear numerator and quadratic denominator. The residual differences between this fit and the data are shown in the lower half of the plot. This curve is non-linear by comparison to fig. 4.30, but the data presented here are from a very different sensor design to that used for fig. 4.30, employing variation of capacitance by the movement of metal blocks to split the capacitance rather than by the movement of a slider that changes the dielectric in the capacitors. 153

4.36 Calibration data for three runs of the sensor. The negligible differences between the repeated points demonstrates the reliability of the sensor measurements. 153
4.37 Measurements by the position sensor as liquid nitrogen evaporates, reducing the liquid level in the sensor. This is plotted against the temperature as measured at the centre of the sensor. The sensor output drops after around three hours; at this point the sensor is partly filled with liquid nitrogen and partly filled with air. The mismatch in dielectric constants between the two halves of the centre cause this lower reading. Once the conditions revert to having the same dielectric in both halves of the sensor, the reading returns to its original level. . . 154
4.38 The detailed response of the sensor as liquid nitrogen boils off, reducing the liquid level in the sensor. The initial sensor reading (when stably filled with nitrogen) is around 675. The final reading when empty and warm is around 663, giving a change of around 12 ADC counts during warming. Between these level points, the sensor reading changes as the liquid level in the sensor changes. When one half of the sensor is filled with a different dielectric, the relative permittivities of the two halves will appear in the expression for the output, resulting in a deviation from the expected behaviour. 155
4.39 Data from calibrating one of the six 'final design' sensors built, fitted with a polynomial curve, against which the residuals in the lower plot are determined. 156

5.1 (A) The TPC is assembled, before (B) being lowered into the ICV, until the base of the TPC is at the bottom of the ICV (C). The cryostat dome is then lowered onto this (D) and secured in place. 158
5.2 The titanium structure that supports the array of PMTs. 159
5.3 A CAD model of the top corner of the detector, showing the PMT truss above the level of the flange at which the ICV main body and dome are connected. 159
5.4 A photograph of the demonstrator tripod. At the base of each sensor, a universal joint can be seen. This allows the sensor to move freely in any direction. At the top, the connection of the three sensors is extended to allow them to effectively meet at a single point, which is required for the geometric analysis. 162

5.5 A diagram showing the points and distances that constitute the base of the tripod. 164
5.6 A comparison of measured and reconstructed movements along the x- and y-axes. The displacement of the platform carrying the tripod was measured by comparing a marked point on the platform to a mm-scale ruler. This simple method of measuring the changing position gives rise to the horizontal error bars in these plots. 166
5.7 A comparison of measured and reconstructed movements along the z-axis. 167
5.8 A diagram showing the points on the base of the hexapod and the associated triangles 168
5.9 Left: A diagram showing the points on the base of the hexapod and the definition of the centre of the base. Right: with the addition of the vectors used to describe the position of point c, projected onto the base plane. Alternate views of these vectors are shown in fig. 5.10. . . 169
5.10 A diagram showing the definitions of the three vectors that constitute the vector from the origin to the top of a triangle. 170
5.11 A diagram showing the definitions of the angles χ and χ' in the base plane. 171
5.12 An illustration of some of the different hexapod configurations that constitute the sixteen possible solutions to the simultaneous equations. In every case, the leg lengths are the same, as are the lengths ab, bc and ca. (0) is the original, correct solution. (a), (b), (c) are the solutions where the corresponding vertex has been 'folded' through to the other side such that the triangle abc can still be constructed. (ab), (ac), (bc) have two sides 'folded' in this way. (abc) has all three sides 'folded' through. These eight configurations represent all the possible architectural solutions where the top platform is above the bottom platform. However, for each of these there is also an equivalent solution where the top platform is inverted below the bottom platform. The simplest of these is (i), and the remainder can be similarly constructed. 174

5.13 A CAD image showing the hexapod in place between the PMT truss and ICV dome. The hexapod will measure the position of the PMT truss with respect to the ICV, particularly during the cooling of the experiment, when the PMT truss is expected to move. This does not give the position of the PMTs with respect to the liquid xenon height, but gives valuable information about the movement and final position of the PMTs. 176
5.14 Parts of the hexapod and connections 177
5.15 A CAD image showing a section through the rod and sphere attached to the PMT truss (location shown by green square), with the corresponding cone-shaped cutaway in the corner connection piece of the hexapod. 179
5.16 A CAD image of the view directly down through the cable port at the top of the ICV. The attachment point for the hexapod can be seen straight through it. On the right, the cryostat vessel has been greyed out to make the interior clearer. The additional sleeve provides the small circular hole visible on the left hand side of the port. At the end of the green arm, a square guard can be seen, which will prevent the arm rubbing against the cables as it moves into place. 180
5.17 Left and Centre: CAD images of the stand for the captive screw. This is fixed into the extender bar runs from a corner of the hexapod along the PMT truss. The screw is what holds the hexapod in place on the truss. The screw is screwed through the stand before assembly of the hexapod. The long unthreaded core of the stand means that if the screw (which has a thread only on its lowest section) is unintentionally unscrewed rather than tightened, it will not unscrew from the stand. Right: The screw, stand and extender bar. 181
5.18 A CAD image showing the double ball and socket joint. These are the connection between the PMT truss and a pair of position sensors. . . 182

5.19 The outcome of the hexapod sensitivity optimisation. The blue line (upper) shows the heights and radii for which the hexapod is equally sensitive to vertical and horizontal movements. The red line (lower) shows the available heights and radii given the mechanical constraints of the ICV dome. The point of closest approach of these two lines is at a height of 215.1 mm, with a corresponding radius of 486.125 mm. This is where the hexapod will most closely approximate being equally sensitive to radial and vertical movements. 185
5.20 A CAD model of an arbitrary 6-3 GSPM structure. The CAD software was used to measure the lengths of the 'sensors', and this was an input to the algorithm. The algorithm produced the estimated positions of top platform, and this was compared to the positions in the CAD software. 188
5.21 The hexapod test stand constructed as a proof-of-principle model for the system of sensors and reconstruction algorithm. 190
5.22 Data from the hexapod test stand during a run of movement that moved the top platform vertically. Shown is the reconstructed position (left) and the differences between the reconstructed and measured positions (right). The actual motion was measured with a coordinate-measuring machine (CMM) that measured the position of a point on the top of the top platform. From this, the position of the centre of the ball and socket joint was inferred. Some error was introduced by this process, as the CMM had to be aligned with the point by eye, and this could not always be accurate. This introduces some errors into the 'measured position' value. In addition, the theoretical centre of the ball and socket joint, which is the point reconstructed by the algorithm, is unattainable, so the translation from the point on the top of the platform to the point at the centre of the joint can only be estimated. This introduces further errors into the 'measured' values. . 191

A.1 The analogue feedback circuit to be analysed. 196

B.1 The analogue feedback circuit to be analysed. 201

D.1 The tyre-testing platform created by Eric Gough in the 1950s. Image from [20]. Permission to reproduce this image has been granted by SAGE Publications. 206

D.2 The GSPM used for positioning the AMiBA telescope. This is, of course, much larger than the hexapod that will feature in LZ. Figure from [21], AAS. Reproduced with permission. 207

E.1 The CAD model of the cylindrical sensor designed for use in the tripod. 209

F.1 The full position sensor with a parts list detailing the components. . . 212
F.2 The tube that shields the internals of the sensor and provides it with structure. 213
F.3 The Cirlex plates that carry the sense and excitation electrodes. . . . 214
F.4 The cylindrical rods on which the internals of the position sensor slide. 215
F.5 The copper ends that hold the flat rods, which in turn support the moving metal blocks. 216
F.6 The flat rods that support the moving metal blocks and connect them to the rest of the sensor. 217
F.7 The copper spacer that separates the Cirlex boards. 218
F.8 The copper structures that support the ends of the Cirlex plates, and into which PEEK bushes are threaded. It is through these bushes that the cylindrical rods run. 219
F.9 The copper structures that connect the Cirlex plates to the tube. . . 220
F.10 The PEEK stopper that fits into the end of the copper tube. The rod to the ball-and-socket joint screws into this, connecting the ball-and-socket joint to the sensor body. 221
F.11 The PEEK stopper for the other end of the copper tube. The rod to the ball-and-socket joint runs freely through the centre of this stopper. 222
F.12 The metal block that moves within the capacitor plates, changing the capacitance. 223
F.13 The PEEK pieces that separate the moving metal blocks from the flat copper rods that support them. These ensure electrical isolation of the metal blocks. There are four per block. 224
F.14 The PEEK bushes that screw into the copper structure that holds the Cirlex plates. The cylindrical rods run smoothly through these. . . . 225
F.15 An overview of the hexapod inside LZ. 226
F.16 The positions of the mounting points of the hexapod inside the ICV dome. 227
F.17 The socket that will be welded to the inside of the cryostat dome, from which a connector to the ball and socket joint will hang. 228

F.18 The connector that screws onto the socket welded into the dome of the ICV. The ball-and-socket joint bolts onto the bottom of it. 229
F.19 The titanium corner piece that sits onto the PMT truss and connects two of the sides of the hexapod together. 230
F.20 The titanium piece that extends from a corner piece along the PMT truss and provides a point for the screw to screw into, connecting the PMT truss and hexapod. One end of the extender sits directly under the port in the cryostat dome. 231
F.21 The stand in which the captive screw sits, ready to connect the PMT truss and hexapod. 232
F.22 The design for the double ball-and-socket joint. 233

Introduction

LUX-ZEPLIN (LZ) is a terrestrial next-generation dark matter search experiment. LZ is the successor to the LUX and ZEPLIN experiments and, like its predecessors, it will use liquid xenon as a target material to search for the direct interactions of Weakly Interacting Massive Particles (WIMPs). Construction is currently underway on many components of the experiment, with underground installation to begin soon. Data collection is expected to begin from 2020.

Once the experiment is closed up, it will not be re-opened until its full run is over. Systems must therefore be in place to monitor the detector and ensure it is running as it should be, so that any corrective measures can be put in place in good time. Understanding the detector geometry is an important part of this. There is particular scope for this to change during the cooldown to LZ's running temperature of around $-100\,°\mathrm{C}$. During this cooling, parts of the experiment are expected to shrink by up to 5 mm. The volume of xenon in which interactions are searched for sits within the 'time projection chamber' (TPC), a cylindrical structure made up of rings of titanium and polytetrafluoroethylene (PTFE), otherwise known as Teflon. On top of this sits an array of photomultiplier tubes (PMTs) that detect the light from any interactions in the xenon. During cooling, the TPC is expected to shrink, resulting in the movement of the PMT array. It is important to monitor this shrinking, to ensure that the TPC and PMT array behave as expected, and that there is no distortion during cooling. However, the design of the experiment means it is not possible to instrument the sides of the TPC, so the behaviour of the TPC must be monitored from the position of the PMT array. Movement of the PMT array is considered with respect to the cryostat vessel that contains the xenon and surrounds the TPC and PMT array.

The work of this thesis concerns the design of a system of position sensors that will monitor the position of the top PMT array. This includes the design of a novel readout scheme and the creation of a system that interconnects six sensors as a single position measurement structure. As LZ is a low-background experiment using high-purity xenon, the sensors installed must be custom-made from a short list of

acceptable materials. This informs the design of the sensors. The final sensors are able to measure the relative position of two points to a precision of 80 µm over a range of 23 mm. The electronic readout system can measure picofarad capacitances to femtofarad precision behind a cable with capacitance of a nanofarad. The algorithm that connects the six sensors into a single system is able to precisely reconstruct the position (x, y and z) and inclination (pitch, roll and yaw) of one platform (the PMT array) with respect to another (the cryostat vessel). Together, these aspects provide a position-sensing system for the top PMT array in LZ.

Chapter 1 introduces the dark matter problem and sets out the compelling evidence for the existence of dark matter. It begins with some of the early historical hints, before discussing more recent results that leave little room for doubt. The final section introduces the 'WIMP' hypothesis of dark matter.

Chapter 2 takes this as its starting point and explores how to search for WIMPs. The evidence from recent and current experiments is set out, showing the latest set of null results from some experiments that use xenon, argon and cryogenic crystals as their target materials. The focus of this thesis is the LZ experiment, so the setup of this detector is examined in detail. As it is a rare event search experiment, it must have very low backgrounds. The origin of potential backgrounds is considered, alongside the steps taken to mitigate their effect.

Chapter 3 focuses more closely on the work undertaken for this thesis. The size and design of LZ necessitates the use of 12 m-long cables for reading out signals from monitoring sensors that sit near the TPC. Such a cable has a capacitance of around a nanofarad, while some of the monitoring sensors are capacitive sensors with a range on the order of a few picofarads. Reading out these sensors via this cable is a significant challenge, overcome via the design of a novel readout system that invokes a feedback circuit in the electronics to suppress the effect of the cable capacitance on the measurement. This third chapter is an exploration of this readout scheme.

Chapter 4 sets out in detail the design of the sensors used to monitor the position of the PMT array with respect to the cryostat vessel that surrounds it. The sensors use capacitance as their sensing modality, with capacitance changes being instigated by the movement of a metal block within a parallel plate capacitor. This meets the material and sensitivity requirements of LZ, as demonstrated in this chapter.

Chapter 5 explores the integration of the capacitive position sensors with the experiment. This is achieved through the employment of a Gough-Stewart Platform Mechanism (GSPM), in which six interconnected sensors are treated as a system to determine the position of one platform (the PMT array) with respect to another (the

cryostat vessel). The algorithm that reconstructs the platform position given the sensor lengths is discussed, alongside the design of the GSPM 'hexapod'. The sensor design, electronics readout and hexapod together provide a position sensing system for the top PMT array in the LZ dark matter experiment.



The LZ Collaboration at SLAC, March 2016. Photo by Steffen Luitz.

Chapter 1

The Dark Matter Problem

1.1 Introduction

The problem of the existence of 'dark matter', perhaps one of the greatest outstanding questions in physics, brings together particle physicists and astrophysicists from the domains of theory, phenomenology and experiment. Many astrophysical observations suggest the presence of unseen matter in the universe; this is the 'dark matter' in question.[22] When taken together, the data point to the existence of a particle beyond the Standard Model of particle physics that is neutral, stable, weakly interacting, massive and cold (non-relativistic).

In this chapter we will explore some of the astrophysical evidence for dark matter, including some of the earliest indications, to motivate our search for it. We will begin by considering Fritz Zwicky's and Vera Rubin's expectations of dark matter based on their results from galaxy clusters and galaxies respectively. We will then focus on more recent results, many of which involve the observation of gravitational lensing; the Bullet Cluster provides a useful illustration. Our final examination of evidence concerns the cosmic microwave background radiation and the role dark matter is required to play in the early universe. Subsequently we will consider what sort of dark matter the evidence points towards, and explore in some detail the 'WIMP hypothesis'.

1.2 Early evidence for dark matter

Perhaps the first suggestion of the existence of dark matter came from Lord Kelvin who, in 1904, attempted to estimate from dynamical considerations the amount of unseen matter in the universe.[23] Kelvin described the stars in the Milky Way as a gas of particles acting under gravitation. This permits the establishment of a relationship

between the size of the system and the velocity distribution of its constituents, i.e. the stars. The velocity dispersion observed was of the same order of magnitude as that predicted by Kelvin, leading to the suggestion by Henri Poincaré that 'there is no dark matter, or at least not so much as there is of shining matter'.[24]

A similar conclusion was drawn by Kapteyn in 1922 who attempted to use the observed motions of nearby stars at right angles to the plane of the galaxy to derive the total density of matter near the sun.[25] Kapteyn believed that 'it may be possible to determine the amount of dark matter from its gravitational effect', but concluded that the mass from dark matter 'cannot be excessive'.

Although both of these early studies were inconclusive as to the existence of dark matter, later evidence offers a compelling reason to spend significant time, effort and resources searching for a missing component of mass in the universe.

1.2.1 The Coma Galaxy cluster

The virial theorem concerns the average pressure (related to the internal kinetic energy) needed to support a self-gravitating system, balancing the gravitational potential energy with the kinetic energy.[26][27] In 1937, Swiss astronomer Fritz Zwicky applied the virial theorem to the Coma galaxy cluster to determine its mass.[28] Under the assumption that galaxy clusters represent stationary configurations, the virial theorem gives the total mass of a cluster in terms of the average square of the velocities of the individual galaxies that constitute this cluster. The line-of-sight velocity of a galaxy can be found by examining the redshift of its emission spectrum.

Zwicky found the galaxies in the Coma cluster to have average minimum mass values of $\overline{M} = 4.5 \times 10^{10} M_{\odot}$: the observed luminosity of a galaxy can provide an estimate for the mass of luminous matter. Given the galaxies' locations within the cluster, the expected velocity dispersion was around 80 km/s. However, the observed average velocity dispersion was approximately 1000 km/s.[29] This suggested the presence of dark matter in the Coma cluster in order to stop the galaxies flying apart. Moreover it pointed to its presence 'in much greater amount than luminous matter'.[30]

1.2.2 Galactic rotation curves

A galactic rotation curve describes the orbital speed of stars and gas in a galaxy about the galactic centre as a function of the distance from the centre. If the mass of a galaxy is concentrated in the stellar objects we see, we would expect most of the mass to lie near the centre of the galaxy. Keplerian dynamics hence suggest that the

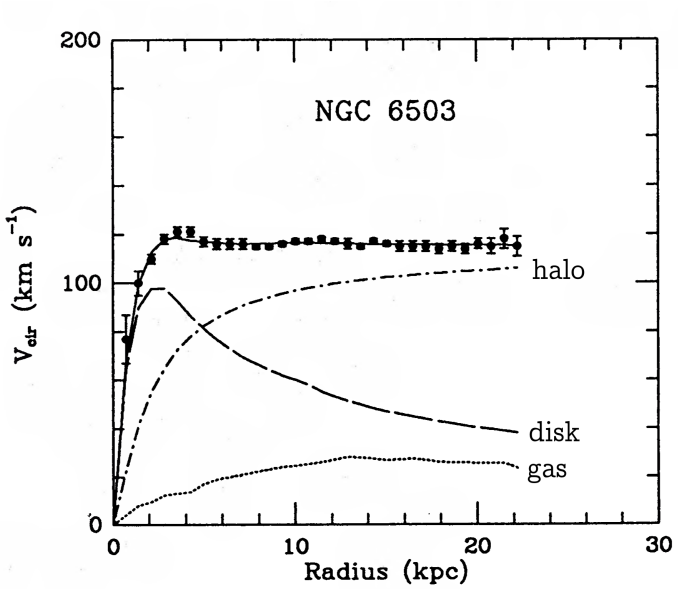


Figure 1.1: The galactic rotation curve for NGC6503. The data points, lying across the top of the plot, indicate the orbital velocity of the gas in the galaxy. The dotted and dashed lines labelled 'gas' and 'disk' respectively indicate where the data points would be expected to lie if that contribution to the overall mass of the galaxy were the only contribution. The line labelled 'halo' is the predicted contribution from dark matter filling the galaxy. Figure from [1]. Permission to reproduce this figure has been granted by Oxford University Press.

gas near the edge of the galaxy (beyond the distance to which most mass is interior) should be travelling more slowly than that nearer the centre.

In the 1970s, astronomer Vera Rubin began to study these rotation curves by measuring the Doppler shift of spectral lines to determine the speed and direction of motion of stars and gas in distant galaxies.[31] She discovered that, rather than the expected Keplerian drop-off of speeds, the stars at the edge of galaxies were moving at approximately the same speed as those near centre. A typical example of a galactic rotation curve found is shown in fig. 1.1.

The discrepancy between expectation and data could be attributed to a mistake either in our understanding of gravitation, leading to the suggestion that Newtonian dynamics is not valid on galactic scales, or in our understanding of the distribution of mass in galaxies, as these are the two ingredients in our prediction of rotation curves. If the galaxy's mass were not concentrated in the stellar core, but spread over a much wider volume, a model could be built that matched the apparent galactic rotation curve. This additional mass is posited to take the form of a 'halo' of dark matter that fills and extends beyond the galaxy.

On their own, galactic rotation curves are insufficient to prove either a theory of dark matter or a theory of modified gravitation, though they indicate that one of the two should be true. However, by the early 1980s, a consensus was emerging among astrophysicists that the gravitational force needed to hold together galaxies and galaxy clusters was due to invisible mass.[22] Yet more evidence for the existence of dark matter was still to come in the form of measurements of gravitational lensing.

1.3 Gravitational lensing

One consequence of Einstein's theory of General Relativity is that mass bends light: the geodesics along which light travels trace the curvature of spacetime, which is distorted by the presence of matter.[32] If we can measure the distortion, we can determine the quantity of matter causing this 'gravitational lensing'. In astrophysical data, gravitational lensing often manifests itself as the magnification, shearing or replication of the image of a distant galaxy by a large mass that lies between it and our telescopes.[22] A typical (and beautiful) example can be seen in fig. 1.2.[33]

1.3.1 Measuring gravitational lensing

Precise measurements of the distortions of images of galaxies can give estimates of the mass that intervenes.[22] When the masses for these galaxies and galaxy clusters is estimated in this way as significantly more than the combined mass of the baryonic matter (stars, dust and gas), some dark component can be invoked to make up the difference. Gravitational microlensing, where a relatively small mass slightly magnifies a more distant body, can also provide statistical studies of mass in our galaxy;[34] the results of just such a study will be explored further in section 1.6.2 below.

In studies of strong gravitational lensing, a map of the lensing strength and hence the matter distribution in a cluster can be drawn. One example of this is shown in fig. 1.3. Such maps make a clear case for the existence of dark matter in the cluster: in addition to the luminous galaxies, a smooth background of non-luminous matter exists throughout the cluster.

1.3.2 The Bullet Cluster

The 'Bullet Cluster', shown in fig. 1.4, is one of the most iconic images in the quest to understand dark matter. A composite image, it highlights a discrepancy between the location of most of the mass in this cluster and the location of regions of hot



Figure 1.2: Gravitational lensing by the Abell 2218 galaxy cluster. The distant galaxies viewed through this lens appear smeared out around the invisible central mass. Credit: NASA, ESA, and Johan Richard (Caltech, USA); Acknowledgement: Davide de Martin & James Long (ESA/Hubble)

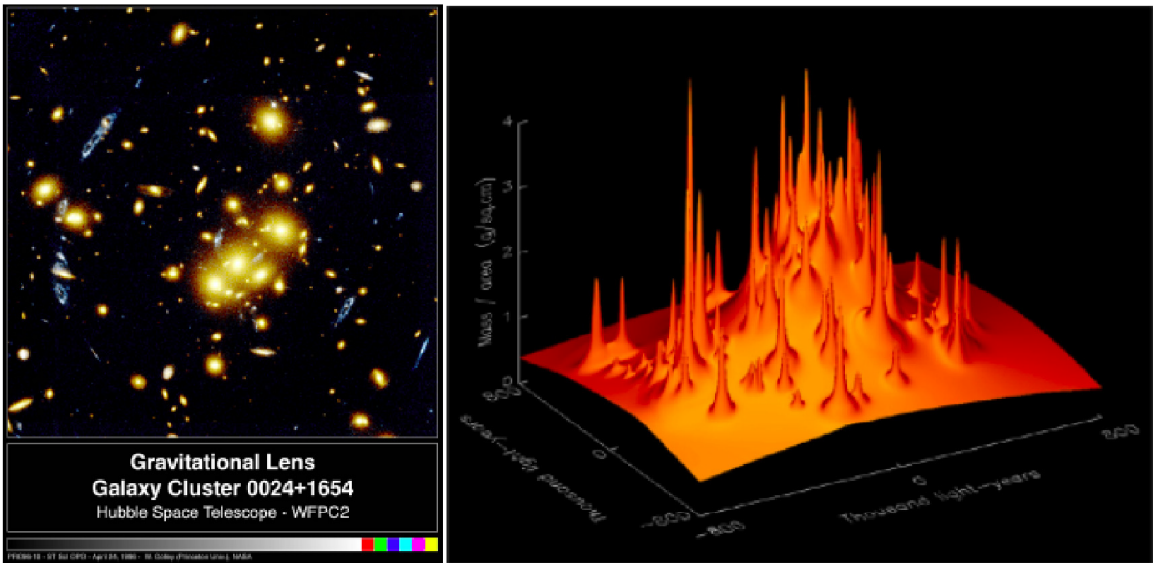


Figure 1.3: Gravitational lensing. On the left is an image from the Hubble Space Telescope where the foreground galaxy cluster is lensing the images of the distant galaxies. On the right is a reconstructed map of the gravitational lensing power of the cluster, and hence also of the mass of the cluster. The sharp spikes correspond to the galaxies in the cluster, but there is additionally a smooth background that peaks in the centre of the cluster. This is the mass owing to the dark matter in the cluster. Image from [2], which is distributed under the terms of the Creative Commons Attribution 4.0 (CC-BY) License.



Figure 1.4: A composite image of the Bullet Cluster. The pink sections indicate the location of most of the baryonic matter, while the blue sections highlight the location of most of the mass. Credit: NASA / Chandra X-ray observatory.

gas, which in turn constitutes the majority of the cluster's baryonic matter.[35] The former is indicated in blue while the latter is shown in pink.

The Bullet Cluster, so named for the bullet-shaped shock wave visible in the right half of the image, is the result of the collision of two smaller clusters of galaxies. Each of these had a baryonic component that included intergalactic gas (up to around 90% of the baryonic mass of the cluster) plus constituent galaxies, as well as a dark matter component.[35] When the two clusters collided, the gas in the two clusters interacted and became caught in the centre of the collision, emitting x-rays. It is these x-rays that indicate the location of the gas, detected with the Chandra x-ray telescope. The galaxies behave as collisionless particles, so in the course of the merging of the two galaxies, the galaxies spatially decouple from the gas.[35]

However, measurements of gravitational lensing indicate two distinct areas containing the majority of the cluster's mass that are not co-located with the gas (which contains the majority of the baryonic matter) but with the galaxies. This non-

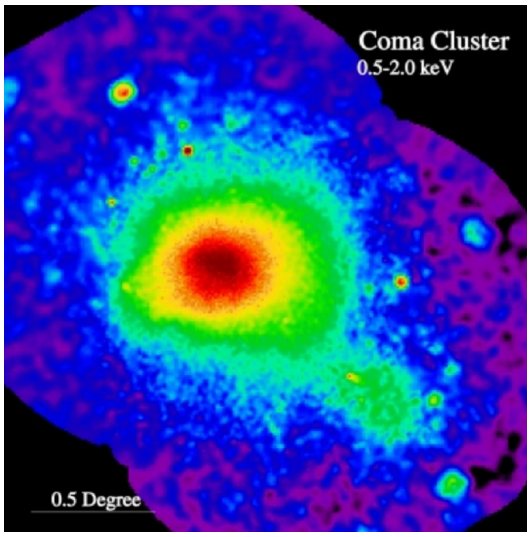


Figure 1.5: X-ray image of the Coma Cluster from the ROSAT satellite. A gravitational potential provided by dark matter is needed to hold this gas in place. Image credit: ROSAT / MPE / S. L. Snowden, from https://heasarc.gsfc.nasa.gov/docs/rosat/gallery/clus_coma.html

luminous mass is postulated to be dark matter and the result is explained as follows. The dark matter associated with each cluster prior to the collision did not significantly interact during the collision; the two clouds of dark matter passed through the centre of the collision. Thus two distinct foci of mass can be seen in the measurements of gravitational lensing strength.

That the mass appears distinct from the baryonic matter is strong evidence for dark matter being made up of something non-baryonic. Moreover, the separation of the masses and the gas in the Bullet Cluster is hard to reproduce with theories of modified gravity. Hence the Bullet Cluster is one of the key pieces of evidence for the existence of non-baryonic dark matter.

1.3.3 The Coma Cluster Revisited

The Coma Cluster gave one of the earliest indications of the existence of dark matter when studied by Fritz Zwicky. More recent x-ray measurements have indicated that the cluster contains large amounts of hot gas, shown in fig. 1.5.[36] The mass of gas thus observed together with the integrated galaxy mass is not large enough to account for all of the gravitational mass needed to bind the cluster.[36] Without an additional gravitational potential provided by dark matter, this gas would have evaporated.[2]

1.4 The Cosmic Microwave Background

The cosmic microwave background (CMB) radiation was famously (and accidentally) discovered by Penzias and Wilson in 1965,[37] and has made two distinct and significant contributions to the body of evidence for dark matter. The CMB is radiation that was released during the epoch of recombination, in which the early universe went from a plasma of interacting charged particles and photons to neutral atoms with which the photons did not interact.[38] The photons that were thus released filled the universe and still do, although the expansion of the universe has now stretched them to microwave wavelengths. The CMB has been studied most precisely by the Planck satellite,[39] indicating the role dark matter is required to have played in the early universe.

1.4.1 Structure formation

The CMB appears almost uniform across the entire sky; however, there are tiny anisotropies, on the order of one part in 100,000.[22] These indicate non-uniformities in the structure of the universe at the time of recombination when the photons were released. Aside from the anisotropies, the CMB is a black-body spectrum with a temperature of 2.725 K.[40]

Although the universe was broadly homogeneous, there were some regions that had a slightly higher density and others that had slightly lower densities. These show up respectively as slightly warmer and cooler areas of the CMB.[22] From these over-densities, when gravitation came to dominate after recombination, large-scale structure formation began, which led eventually to the state of the universe we see today.

However, the anisotropies seen in the CMB are not sufficient to alone have produced the structure we observe in the time we know to have elapsed. The universe would have had to have been more anisotropic than measurements of the CMB permit, in order to arrive at the observed degree of large-scale structure if only baryons existed.[41] However, as Peebles notes, 'the problem is relieved if the universe is dominated by massive, weakly interacting particles because density fluctuations on small scales can grow before decoupling'.[41] Without the addition of some matter that does not couple to photons, the large-scale structure of the universe cannot be explained in light of the observed CMB anisotropies.[38]

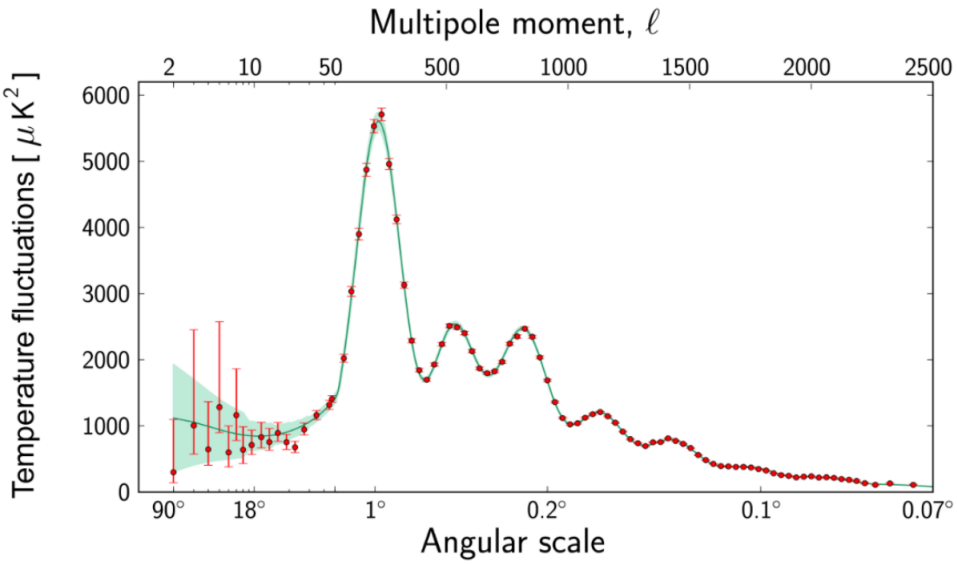


Figure 1.6: The power spectrum of the CMB from the Planck satellite. The red points with error bars mark the data. The green shape is the power spectrum given by a model containing 5% baryonic matter, 26% dark matter and 69% dark energy. Image from [2], which is distributed under the terms of the Creative Commons Attribution 4.0 (CC-BY) License.

1.4.2 Baryon acoustic oscillations

Although observations of the CMB in the 1980s were sufficient to provide evidence that large-scale structure formation required a dark component,[41] recent precise measurements of the nature of the anisotropies have added another angle to the evidence for dark matter.[39] The anisotropies are the result of baryon acoustic oscillations. These arise as follows: slight over-densities attract more baryons as a result of gravitation, but this results in increasing pressure acting against it. As the photons are coupled to the baryonic matter, they are affected by these oscillations, and at the moment of recombination, the oscillations are frozen into the radiation that becomes the CMB.[38]

The temperature anisotropies are usually expressed using a spherical harmonic expansion of the CMB sky.[42] A plot of the resulting power spectrum shows the amount of temperature fluctuation in the CMB spectrum at different angular scales on the sky; see fig. 1.6. The baryon acoustic oscillations determine the shape of parts of this power spectrum,[42] and the nature of the oscillations will depend on the constituents of the universe in which they are occurring.

Models can be built of the early universe in which baryonic acoustic oscillations are simulated (such as that described in [43]).[42] By finding the model that most closely

matches the data, it is possible to understand how much baryonic matter, dark matter and dark energy constituted the universe in the time just prior to recombination. This model is the 'Standard Model' of cosmology, in which dark matter accounts for approximately 85% of the mass.[38] Hence the universe must at that point have contained large amounts of dark matter in order to produce the measured power spectrum. Thus the CMB spectrum alone is very powerful evidence for the existence of dark matter.[2]

1.5 Avoiding dark matter

In the above sections is explored a significant weight of evidence in favour of particle dark matter. Nevertheless, some continue to question its existence, instead favouring theories based around an altered theory of gravity, or Modified Newtonian Dynamics (MOND). Originally proposed by Mordehai Milgrom in 1982,[44] MOND suggests that although gravitation behaves as we understand on small scales, the same theory does not hold in scenarios where the acceleration is extremely low, such as towards the edges of galaxies or in intergalactic space. Hence the usual Newtonian dynamics of $F = ma$ should be modified at these scales. These modifications are designed to explain the observed motion of stars and gas within galaxies (galactic rotation curves) without invoking a dark matter component to the galaxies.

Suppose that, at low accelerations, gravity scales as $F = m\frac{a^2}{a_0}$, where a_0 is a new fundamental constant. Then

$$\frac{GMm}{r^2} = \frac{m}{a_0}\frac{v^2}{r^2}. \tag{1.1}$$

Hence

$$v^2 = GMa_0 \tag{1.2}$$

which is to say, a star's orbital velocity is independent of its distance r from the centre of the galaxy. Hence, with the introduction of a new constant and the modification of Newtonian gravitation, MOND can explain the flat rotation curves seen by Rubin and others.

However, early versions of MOND run into some basic theoretical difficulties. The formulation described above does not conserve momentum or energy.[45] In addition, this formulation is not consistent with general relativity, so in order to be considered a viable alternative to dark matter, further theories had to be developed.[45]

Moreover, as the evidence for dark matter comes from many different quarters, theories that must account for astrophysical data without it become increasingly

contrived. The 2006 discovery of the Bullet Cluster was expected by some to bring an end to such theories of modified gravity, with the discovery touted as 'a direct empirical proof of the existence of dark matter'.[35] In addition, models of modified gravity fail to handle evidence from the CMB.[2] Without dark matter in the universe, the CMB power spectrum would have looked very different.

Finally, the recently discovered merger of two neutron stars by LIGO/VIRGO and electromagnetic telescopes may further sound the knell for 'dark matter emulator' theories such as MOND and its successors.[46] The gravitational waves from the merger of two neutron stars in a galaxy 40 Mpc away were detected by the LIGO interferometers on 17^{th} August 2017.[47] 1.7 seconds later, a corresponding gamma ray burst was detected by the Fermi Gamma Ray Burst Monitor.[47] Therefore there cannot be a large difference between the speed of travel of gravitational and electromagnetic waves. This was the first opportunity to test such a conjecture, as it is the first gravitational wave event detected for which an electromagnetic counterpart has been seen.

Light travelling through a gravitational potential undergoes a Shapiro delay: the relativistic time dilation results in a longer travel time than would be expected given the distance and vacuum speed of light. In dark matter emulator theories, dark matter does not exist, but the more advanced theories still account for the Shapiro time delay experienced by light travelling in a gravitational potential (or else such a theory could not be considered a successor to General Relativity). However, the Shapiro delay for gravitational waves depends only on the mass in the line of sight, and is not corrected, so under a dark matter emulator theory would depend only on baryonic matter. This leads to a difference in Shapiro time delays for electromagnetic and gravitational waves. Boran *et al.* calculate from astrophysical data that this difference in Shapiro time delays should be on the order of 1000 days. However, the signals on 17th August arrived a mere 1.7 seconds apart. Hence the gravitational and electromagnetic waves cannot have experienced the vastly different effective gravitational potentials that would have been predicted by a dark matter emulator theory. Boran suggests this data from the merger of the two neutron stars falsifies such dark matter emulator theories.

1.6 The WIMP hypothesis

The evidence above points towards the existence of dark matter, and many of its characteristics can be determined from the astrophysical observations discussed. The

early evidence for dark matter (rotation curves and galaxy clusters) did not demand anything more of this matter than that it be 'dark'—it was required only to be non-luminous and therefore in addition to the matter previously observed. However, as evidence mounted that astrophysical sources could not be found to contribute this additional mass, the idea that dark matter is a previously undiscovered species of subatomic particle came to the fore.[45] The observations suggested dark matter should be neutral, stable, weakly interacting, cold and massive. These characteristics taken together form the basis of the 'WIMP hypothesis', which posits the existence of a Weakly-Interacting Massive Particle to account for dark matter.[22]

1.6.1 Cold dark matter

In the mid-1980s, numerical simulations of the early universe were undertaken that explored the evolution of large numbers of dark matter particles under the force of gravity in an expanding universe.[45] These demonstrated that 'hot' dark matter (i.e. dark matter that was moving relativistically during the epoch of structure formation) would not lead to the observed structures being formed.[48] This places further constraints on the possible dark matter candidates: the particles must be 'cold' for structure formation to take place. No WIMP that would have relativistic energies in the early universe, such as the neutrino, can account for the majority of dark matter.[45]

1.6.2 MACHOs

If dark matter is required only to be cold and non-luminous, it could consist of baryonic matter that is simply generally unseen in astrophysical observations. It could take the form of black holes, planets, white dwarfs, neutron stars, red dwarfs or brown dwarfs, denoted collectively as massive compact halo objects, or MACHOs. However, a combination of studies have ruled out MACHOs as constituting the majority of dark matter, though they will be some small part. First, the cosmic baryon density as determined from measurements of the CMB precisely constrains the amount of baryonic matter in the early universe.[39] Even early measurements of the baryon density indicated that baryonic MACHOs could only make an insignificant contribution to the global baryon budget.[49] Thus they cannot be the dark matter required.

Second, MACHOs forming part of the 'dark halo' of the Milky Way were searched for with gravitational microlensing surveys: individual objects could gravitationally lens the images of distant stars by small amounts. By monitoring the brightness of

stars in the nearby Large Magellanic Cloud, astronomers could determine the number of microlensing events whereby the magnification of the star is increased as a result of the intervening MACHO.[34] The EROS collaboration searched for over six years and found only three microlensing candidates in their survey of the Large Magellanic Cloud.[50] As a result, the upper limit for the dark halo mass fraction from MACHOs is 8%: the majority of dark matter cannot be MACHOs.[51]

1.6.3 Dark matter candidates

The evidence for dark matter is powerful, and it has been demonstrated that baryonic contributions cannot make up a large fraction of the dark matter required. There is nevertheless a plethora of dark matter candidates, of which the most popular are Weakly Interacting Massive Particles (WIMPs) and axions (see below).[2] However, 'WIMP' refers to a class of particles defined by their characteristics; a WIMP is not a known particle in its own right. There are a number of different possible candidates that could constitute WIMP dark matter, and some of those given below have strong theoretical motivations, as will be discussed.

1.6.3.1 Neutrinos

A potential candidate is the neutrino, which is stable, neutral, has mass and interacts only weakly, apparently fulfilling the WIMP paradigm. However, in the epoch of structure formation in the early universe, neutrinos are predicted to have had highly relativistic velocities. This rules them out of being the cold dark matter required for structure formation, as discussed above.[45] Although they therefore cannot account for the majority of the dark matter in the universe, they will form some small fraction of it.

1.6.3.2 Neutralinos

Further WIMP candidates are not available in the Standard Model of particle physics, but theories of Beyond Standard Model physics such as supersymmetry can provide a particle that fulfils the requirements placed on dark matter. Supersymmetry posits a supermassive partner for every particle that exists in the Standard Model, as a result of an additional spacetime symmetry that relates fermions to bosons.[45]

The lightest supersymmetric particle (LSP) is by construction stable, which makes it a good dark matter candidate as it could be abundant in the present universe. Many versions of supersymmetry, including the popular Minimal Supersymmetric Model,

or MSSM, assign to all particles the property of 'R-parity'. This quantity must be conserved in any interactions, and is given as $+1$ for particles and -1 for their superpartners.[45] If an LSP were to decay to only standard model particles, R-parity would be violated, so such a decay is forbidden. Moreover, as the LSP is posited as the lightest SUSY particle, it cannot decay to any other SUSY particle. Hence it is predicted to be stable.

In addition, a stable LSP is expected to be electrically neutral and have only weak interactions.[52] If it were electrically charged, it would be expected to bind to conventional matter and be thus detectable; strongly interacting LSPs would be similarly detectable. Hence the stable LSP would be expected to interact only weakly. The favoured LSP dark matter candidate in the MSSM is the 'neutralino', an electrically neutral mixture of the superpartners of the photon and Z and Higgs bosons. As it is stable and only weakly interacting, it poses as an excellent WIMP candidate.

1.6.3.3 Sterile neutrinos

A sterile neutrino is so called because it is posited not to experience electroweak interactions but to otherwise behave as an additional neutrino species. Dodelson and Widrow proposed in 1993 that dark matter could consist of such particles.[53] Sterile neutrinos need not be as light as the three standard model species so are not automatically too hot to constitute dark matter.

1.6.3.4 Axions

The 'axion' is a theoretical particle first proposed by Peccei and Quinn to solve a dilemma known as the 'strong CP problem' of quantum chromodynamics.[54] The problem is essentially a challenge of fine-tuning. The QCD Lagrangian contains a term

$$\mathcal{L}_{\text{strong CP}} = \bar{\theta}\frac{\alpha_s}{8\pi}G_{\alpha\mu\nu}\tilde{G}^{\mu\nu}_{\alpha} \tag{1.3}$$

which would lead to an enormous neutron electric dipole moment, $d_n \sim e\bar{\theta}(m_q/M_N^2)$, unless the parameter $\bar{\theta}$ is tiny.[55] Measurements of the neutron electric dipole moment currently have set an upper limit of $d_n = -0.21 \pm 1.82 \times 10^{-26} e$ cm.[56] Hence, in order to be consistent with this, the phase $\bar{\theta}$ must be smaller than 10^{-10}.[45] It could be this small by coincidence - perhaps the universe is finely tuned in this way - but this is *prima facie* unlikely. A more favourable explanation is that some underlying new physics constrains the quantity to be very close to zero. Peccei and Quinn's solution was to introduce a new, spontaneously broken symmetry that drives the

quantity towards zero. The axion is the boson whose existence is implied by this broken symmetry.

In 1983, Preskill, Wise and Wilczek suggested the axion could be invoked to also solve the dark matter problem and account for the missing mass in the universe.[57] Axions are stable over cosmological timescales so would survive into the present if produced in the early universe.[45] Although axions must be relatively light, theories suggest they may be produced with non-relativistic velocities.[45] Hence axions, although not WIMPs, are nevertheless a well-motivated candidate for dark matter that broadly fulfil the required properties imposed by astrophysical evidence to date.

1.7 Beyond theory

The evidence discussed above for dark matter is wide-ranging. That so many different strands of astrophysical evidence point to very similar - if not the same - conclusions makes it particularly compelling. Although gravitational rotation curves are not incontrovertible evidence for dark matter, they provided an important early signpost to the existence of galactic dark matter. The advent of gravitational lensing measurements provided some of the most visual demonstrations of the existence of non-luminous matter, and the Bullet Cluster image is rightly lauded. However, the most compelling evidence is from cosmology: the universe's present state cannot be explained without non-baryonic dark matter.

The evidence for dark matter also places some constraints on what it could be, broadly indicating that it fulfils the WIMP or axion paradigms. Although there are many suggestions from theories as to what WIMP dark matter might precisely be, at present there is no conclusive front-runner. It is thus the turn of experimentalists to come to the fore and attempt to answer the question of what dark matter is by searching for it. It is to the question of how best to do this that we turn next.

Chapter 2

Searching for Dark Matter

The previous chapter summarised the astrophysical and cosmological evidence for dark matter, which together present a picture of the required nature of this unseen component of the universe. Some theoretical candidates that can fill this role were also explored; however no single prediction of what precisely dark matter is or how it arises could be declared the leader. This has motivated experimental physicists to search for many possible dark matter candidates in various ways. This chapter will examine some of these searches and their results to date. As the work of this thesis is dedicated to the LUX-ZEPLIN experiment,[58] this experiment will be explored in depth, in particular considering the detail of how this detector works and what a dark matter detection would look like. Finally, the importance of the ratio of signal to background will be noted and some of the possible sources of background signals will be detailed.

2.1 Weak interactions & dark matter searches

If we are to detect dark matter terrestrially, it must have some interaction with some standard model particle. As dark matter has thus far been seen only in terms of its gravitational effect, such an interaction is not a certainty; it is possible that dark matter interacts only gravitationally with baryonic matter.[45] WIMP dark matter is posited to not interact via the electromagnetic or strong forces.[2] As the name suggests, WIMP dark matter interactions with baryonic matter should be via either gravitation or the weak force.

There is a secondary motivation for suspecting a weak interaction strength. The dark matter that existed in the early universe could have been in thermal equilibrium with the baryonic matter. As the universe expanded and cooled, the rate of interactions between dark matter and standard model particles would eventually have fallen

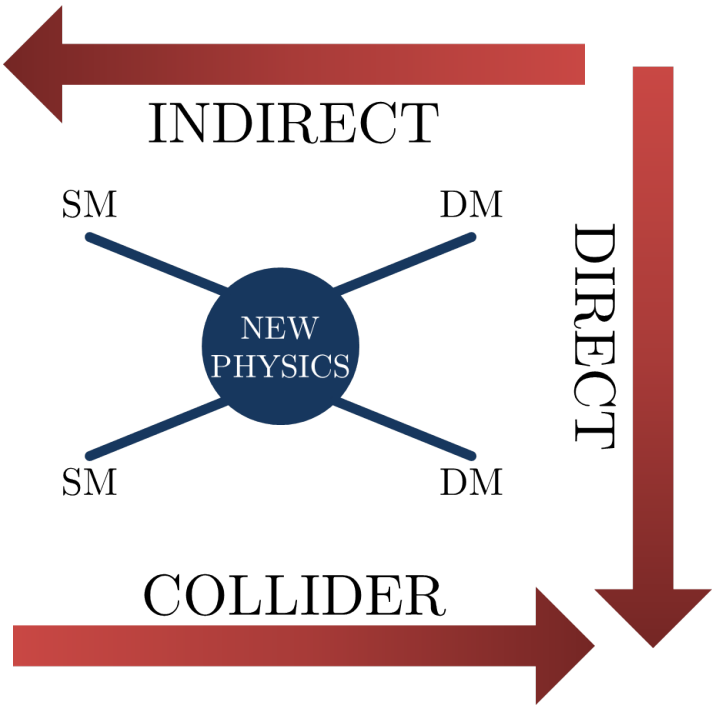


Figure 2.1: The different ways to search for dark matter. Consider 'DM' to represent a dark matter particle and 'SM' to represent a standard model particle. This diagram demonstrates the connection between the different search methods. Direct searches look for the interaction of a dark matter particle with a standard model particle. Indirect searches look for standard model products that could result from dark matter annihilations. Collider searches aim to produce their own dark matter from a starting point of standard model particles, though further investigations would have to be undertaken to confiem whether the candidate particle found in the LHC is really the same as the particle that constitutes galactic dark matter.

below the level required for thermal equilibrium, i.e. there came to be too few dark matter particles given the interaction cross-section for the interactions to happen frequently enough to maintain thermal equilibrium. In this way, the dark matter became decoupled from the baryonic matter, leading to a 'relic abundance' of dark matter. The lower this interaction cross-section is, the earlier this decoupling would have happened, so the higher the relic abundance would be. The relic abundance suggested by cosmological measurements is consistent with an annihilation cross-section characteristic of the weak interaction.[45] This line of reasoning, known as the 'Naturalness Argument', suggests that it is therefore not unreasonable to search for a WIMP by looking for its interactions with baryonic matter.

There are three categories of searches for dark matter, illustrated by the diagram in fig. 2.1. To date, no weakly-interacting massive particles have been found at colliders,

though with the LHC continuing to take data at ever higher energies, there is still scope for a discovery. Indirect searches have occasionally found hints that some take as evidence of dark matter, but this is widely seen as inconclusive.[1] It is on direct dark matter search experiments that we will focus from here on in.

2.1.1 Direct searches for WIMPs

The majority of WIMP direct search experiments fall into two categories: liquid noble detectors or cryogenic detectors. The former category includes the LUX-ZEPLIN experiment, as well as its predecessors: LUX and the ZEPLIN series of detectors. Liquid noble detectors use either liquid xenon or liquid argon as their target material. Two-phase experiments include some amount of noble gas, too.

When a WIMP interacts with a target nucleus, it can produce scintillation and ionisation, and deposit a certain amount of thermal energy (a phonon). Most detectors aim to detect two of these three channels, as this helps with particle identification and background discrimination. The liquid noble detectors all detect scintillation and the vast majority also detect ionisation signals.

Cryogenic detectors are geared to detecting the heat deposited in an interaction; by cooling a crystal down, any such phonons become obvious to the appropriate instrumentation. In addition, they can detect corresponding ionisation or scintillation, in order to undertake a two-channel measurement.

If a WIMP interacts with a target, it will do so via recoiling from the nucleus - a 'nuclear recoil' (NR). This could be from the nucleus as a whole (which is referred to as 'spin-independent' scattering) or from a single nucleon (which is 'spin-dependent' scattering). Both of these will result in signals. However, they are not the only possible interactions. If electrons or gamma rays are incident on the target material, they will interact with the electrons that surround the nuclei, resulting in an 'electron recoil' (ER).

2.2 From WIMP to detection

Once an experiment is running, a detection, or lack thereof, must be converted into a statement about the nature of WIMP dark matter. Following Lewin and Smith,[59] all direct dark matter search experiments, whether using ionisation, scintillation, low

[1] This naturalness argument can apply to a range of particle masses: it suggests the particle must be roughly heavier than $\sim 1 - 100\,\mathrm{keV}$, and could have masses on the order of TeV.[45] The LHC can continue to probe these possible higher masses.

temperature phonons or some combination as their detection signal, aim to detect or set limits on nuclear recoils arising from collisions between new heavy particles (WIMPs) and target nuclei. For the simplest case of a detector stationary with respect to the WIMP flux, the differential energy spectrum of these nuclear recoils is expected to be featureless and smoothly decreasing, with the form

$$\frac{dR}{dE_R} = \frac{R_0}{E_0 r} e^{\frac{-E_R}{E_0 r}} \tag{2.1}$$

where E_R is the recoil energy, E_0 is the most probable incident kinetic energy of a dark matter particle of mass M_D, r is a kinematic factor, R is the event rate per unit mass, and R_0 is the total event rate. The kinematic factor r is given by $\frac{4M_D M_T}{(M_D+M_T)^2}$, where M_D is the mass of the dark matter particle and M_T is the mass of the target nucleus. This will be maximised when M_D=M_T, that is, when the mass of the target nucleus matches the mass of the dark matter particle.

Experiments aim to reduce and reject background events by using radiopure materials, situating the detector in a low-background environment (generally underground) and finding ways to discriminate between NRs and ERs and between interactions from neutrons and potential WIMPs. Hence the experimental effort is devoted to the left hand side of eq. (2.1). When an experiment has set an upper limit to the differential rate at any particular value of E_R, the right hand side of eq. (2.1) allows a corresponding limit for R_0, the total event rate of dark matter interactions, to be calculated for each assumed value of particle mass M_D. This limit on R_0 can then be converted to a limit on the WIMP interaction strength or cross-section for interacting with the target. It is this limit on the interaction cross-section per dark matter particle mass that most experiments to date have presented.

2.3 Experimental results to date

2.3.1 Limits

Until a discovery is made, the best that experiments can do is to set limits on interaction cross-sections for WIMP masses on the basis of not having detected a WIMP signal after a certain length of run. This leads to a limit curve on a plot of WIMP-nucleon interaction cross-sections against WIMP masses, as seen in fig. 2.2.

There are three leading experiments that use broadly the same technology as will feature in LZ: LUX, PANDA-X, and the XENON experiments. Similar experiments using argon have some interesting developments and challenges so will also be noted.

The alternative technology, namely cryogenic crystal detectors, set experimental limits in different regions of the parameter space. Below will be considered some of the main experiments in each sphere, with their results presented in fig. 2.2.

2.3.1.1 LUX

LZ is, for the most part, an expansion and refinement of the Large Underground Xenon (LUX) experiment, drawing on the lessons learned and expertise gained. LUX used a two-phase xenon time projection chamber (TPC), surrounded by titanium cryostat vessels.[60] Situated in the Sanford Underground Research Facility (SURF), it contained an active volume of xenon of 250 kg. LUX ran from 2012 to 2016 and, from 2013 until the recent release of results from XENON1T (described in section 2.3.1.3 below),[3] LUX was the world's most sensitive direct detection experiment.[61] In the most recently released results, LUX achieved a limit on the WIMP-nucleon spin-independent cross-section of 1.1×10^{-46} cm^2 for a 50 GeV/c^2 WIMP mass, at a 90% confidence level.[6]

2.3.1.2 PandaX-II

PandaX is a two-phase xenon experiment located in the China Jinping Underground Laboratory (CJUL). The commissioning run began in November 2015 and since early 2016, the second phase of the project, PandaX-II, has been underway, using 580 kg of liquid xenon. The first results were presented in June 2016.[62]

2.3.1.3 XENON experiment

The XENON collaboration has produced a series of direct dark matter search experiments using liquid xenon as the target to search for WIMP-nucleon interactions. The current detector is XENON1T, which has a target mass of xenon of around 2000 kg (of which 1042 kg is used to search for WIMP interactions) and has been taking data since November 2016.[3] At present, XENON1T has produced a world-leading sensitivity to WIMPs in the range of 10 GeV/c^2 to 1 TeV/c^2; see fig. 2.2. The limit curve they derive for spin-independent WIMP-nucleon interaction cross sections has a minimum of 7.7×10^{-47}cm^2 for 35 GeV/c^2 WIMPs at 90% confidence level.[3]

The XENON1T experiment was preceded by XENON10 and XENON100, and will be followed by XENONnT. This latter experiment is likely to be LZ's main competitor. XENONnT will have a target mass of xenon of 5.7 tonnes and is expected to complete construction in 2018.[63] Many of the subsystems that are being used for the XENON1T experiment were designed to be re-employed in the upgraded

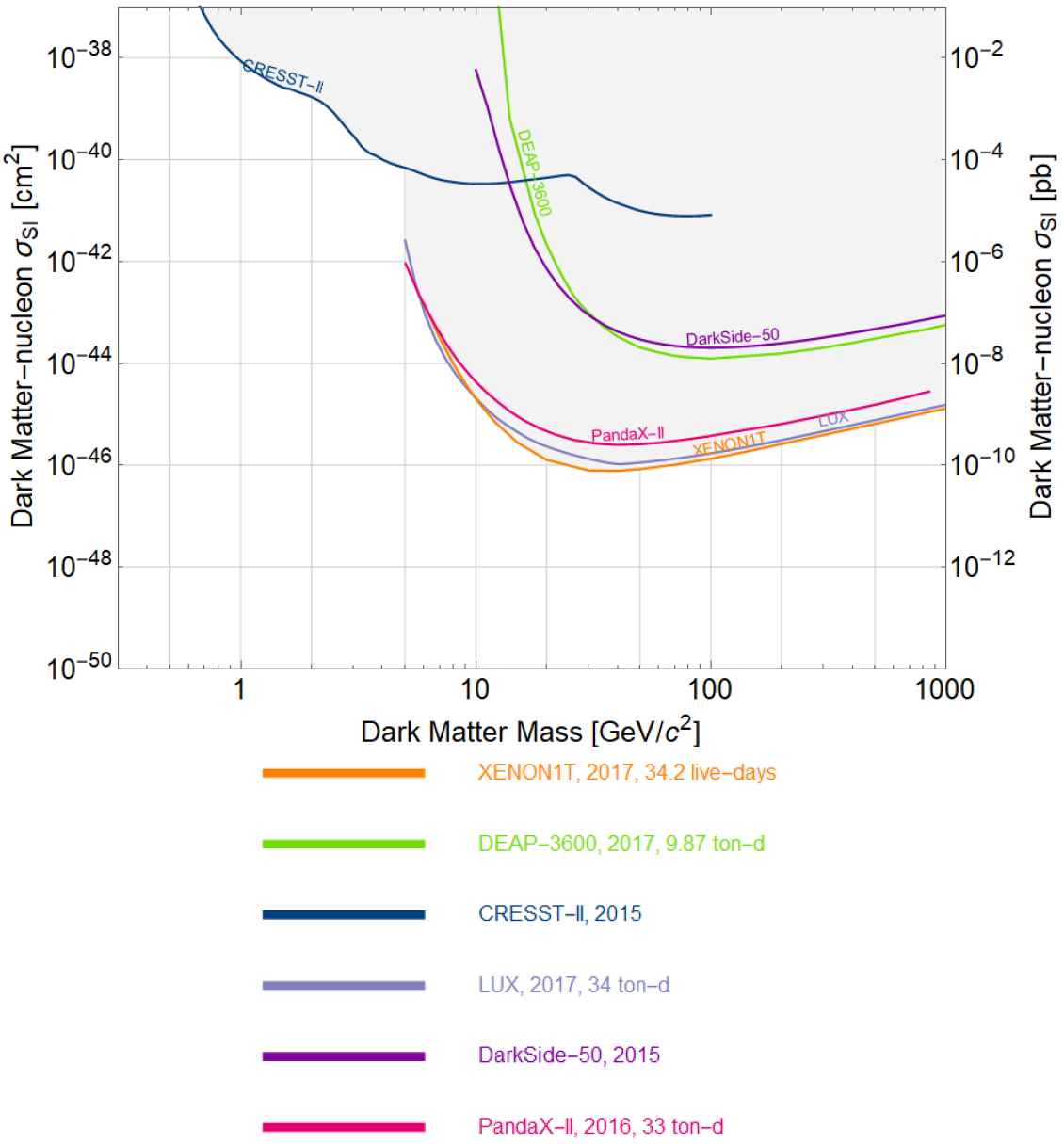


Figure 2.2: The current spin-independent WIMP-nucleon interaction cross-section limits set by experiments discussed in this section. Xenon-1T result:[3]; DEAP-3600 result:[4]; CRESST-II result:[5]; LUX result:[6]; DarkSide-50 result:[7]; PandaX-II result:[8]. The most straightforward WIMP implementation is that that the WIMP is a heavy Dirac neutrino; this was originally suggested by Lee and Weinberg in 1977.[9] This simple model was ruled out in 1996 when experiments for the first time probed the relevant parameter space,[10] reaching down below 10^{-5} pb for the spin-independent WIMP-nucleon cross-section for a 50 GeV WIMP.[11]

experiment.[64] For 20 tonne-years of exposure, XENONnT is expected to achieve a minimum spin-independent WIMP-nucleon cross-section of $1.6 \times 10^{-48}\text{cm}^2$ at a WIMP mass of $50\,\text{GeV/c}^2$, which is comparable to that predicted for LZ.

2.3.1.4 Argon experiments

An alternative to liquid xenon is the use of liquid argon as the interaction target. The two noble elements have their own merits and demerits as target materials, though the advantages of xenon have led to its predominance in the field.[65] The higher atomic number (A) of xenon (54, compared to argon's 18) leads to a higher WIMP-nucleus interaction cross-section, as the spin-independent cross-section contains a factor of A^2.[65] The high mass number Z of xenon also results in its better self-shielding capabilities. The scintillation properties of argon, on the other hand, lend themselves to better pulse-shape discrimination: two components of the scintillation are released at different times, and the proportion of the light that appears as these slow and fast components depends upon whether the interaction was an electron recoil or nuclear recoil event. In xenon, discrimination between the two components is much more difficult.[65] In addition, argon is much cheaper to procure than xenon, though challenges associated with natural backgrounds are discussed below.

The DarkSide-50 detector is an argon experiment with a two-phase TPC, the same technology used by the xenon experiments discussed above. This contains a 50 kg active mass of 'underground' liquid argon. Atmospheric argon contains the isotope Ar-39, leading to an activity of around 1 Bq/kg.[7] By contrast, underground argon, sourced from underground CO_2 wells,[66] has been shown to contain Ar-39 at a level reduced by a factor of over 1000 relative to atmospheric argon, greatly reducing the contribution of this source of background events.[7]

An alternative design is employed by the DEAP-3600 experiment, which is a single-phase liquid argon detector. Currently running in SNOLAB, Canada, DEAP-3600 uses a spherical acrylic vessel filled entirely with 3600 kg of liquid argon and instrumented in every direction with PMTs.[4] The signal consists only of scintillation light from the interaction of an incoming particle with an argon atom. Background rejection in direct detection experiments often comes from the ability to compare two signals from a single interaction. This is not possible if only scintillation is detected. Instead, DEAP-3600 uses pulse-shape discrimination to single out candidate events from background. DEAP-3600 have also developed some interesting novel technologies, including a robotic 'resurfacer' to *in situ* remove contaminants from the interior surface of the acrylic vessel after construction.[67]

The necessity of using underground, low-background argon in order to avoid large backgrounds makes the use of argon as a target material more complicated. An additional challenge faced by argon experiments is that the scintillation light produced in argon has a wavelength of around 128 nm, which is absorbed by most materials. Hence a thin layer of wavelength shifter must cover all exposed surfaces.[66] For a future detector, four liquid argon dark matter search experiments (ArDM, DarkSide-50, DEAP-3600 and MiniCLEAN) have agreed to join forces to collaborate on the 'DarkSide-20k' project, which proposes to use a two-phase liquid argon time projection chamber experiment with an active mass of 23 tonnes of underground argon.[66]

2.3.1.5 Cryogenic experiments

As explained below, the mass of the target nucleus determines the WIMP mass to which a detector is tuned. Cryogenic dark matter search experiments use this to their advantage to probe low-mass parameter space. The CRESST-II detector, situated in the Laboratori Nazionali del Gran Sasso, Italy, uses calcium tungstate crystals at cryogenic temperatures as the target.[5] Although most of the energy of an interaction appears as a heat signal, a small fraction is emitted as scintillation light, yielding two-channel detection. As shown in fig. 2.2, CRESST-II has set a limit for lower WIMP masses than the xenon and argon experiments discussed.

The future SuperCDMS experiment will also search for low-mass WIMPs. Based in SNOLAB, the experiment will use cryogenic germanium and silicon crystals, and is designed to reach a sensitivity of 1×10^{-43} cm^2 for a WIMP mass of 1 GeV/c^2.[68] If attained, this would be an improvement of over five orders of magnitude on the current CRESST-II results.

2.3.2 Discovery claims

In spite of this range of null results, the DAMA/LIBRA experiment controversially maintain they have detected WIMP-nucleus interactions.[12, 69] DAMA/LIBRA uses 250 kg of highly radiopure sodium iodide crystals, which emit scintillation light when an interaction occurs. Their signal is an annual modulation of detections; see fig. 2.3. This modulating signal is claimed to correspond to a changing flux of WIMP interactions as the Earth's motion around the sun varies the detector's motion with respect to the galaxy and hence with respect to the galactic WIMP halo.[12]

That they have a modulating signal at the level of 9.2σ[12] is widely accepted, but the fact that their region of interest is excluded by other experiments leads to

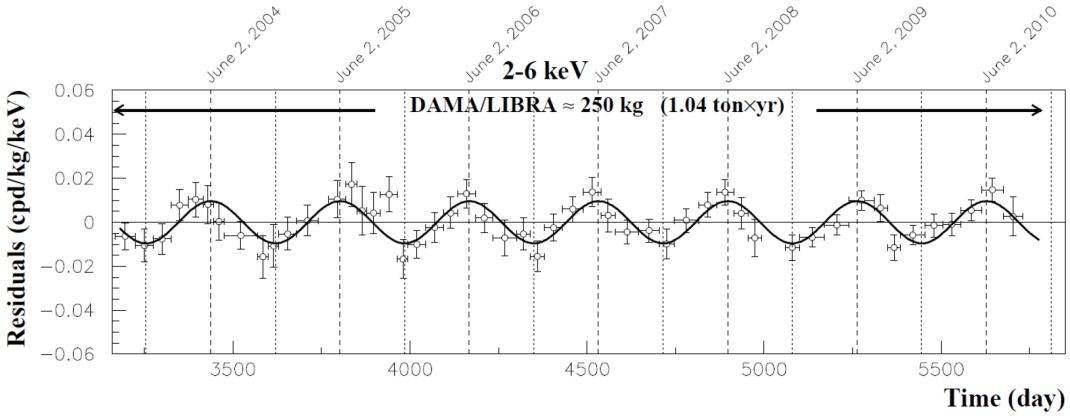


Figure 2.3: Experimental residual rate of the single-hit scintillation events measured by DAMA/LIBRA-phase1 as a function of the time. Image reproduced from [12], which is distributed under the terms of the Creative Commons Attribution License 4.0.

questions over whether they are truly seeing WIMP interactions. Their use of only scintillation (rather than using two channels as discussed in section 2.1.1) means they cannot easily discriminate between nuclear recoils (NR) and electron recoils (ER) and hence between a WIMP NR signal and an ER background. The clarify this, the KIMS-NaI experiment is repeating the DAMA/LIBRA experiment but using pulse shape discrimination to test whether the annual modulation signal observed is caused by nuclear recoil events.[70] To further allay the controversy and confirm or dismiss DAMA/LIBRA's result, the SABRE experiment will also search for the same annual modulation using the same target material as DAMA/LIBRA in both the northern and southern hemispheres.[71]

2.4 The LUX-ZEPLIN Experiment

LZ will be a two-phase direct detection experiment containing ten tonnes of liquid xenon.[58] The general structure of the experiment can be seen in fig. 2.4. The central volume of xenon is housed inside a time projection chamber (TPC) that consists of interlocking titanium and polytetrafluoroethylene (PTFE) rings. At the top and bottom of the TPC are two plates with arrays of photomultiplier tubes (PMTs). Outside the TPC (which is not xenon-tight) is a thin layer of xenon known as the 'skin' and also instrumented with PMTs (known as 'skin PMTs'), which are in addition to the top and bottom PMT arrays. All of these systems are housed within the 'inner cryostat vessel' (ICV), which is a titanium pressure vessel designed to contain

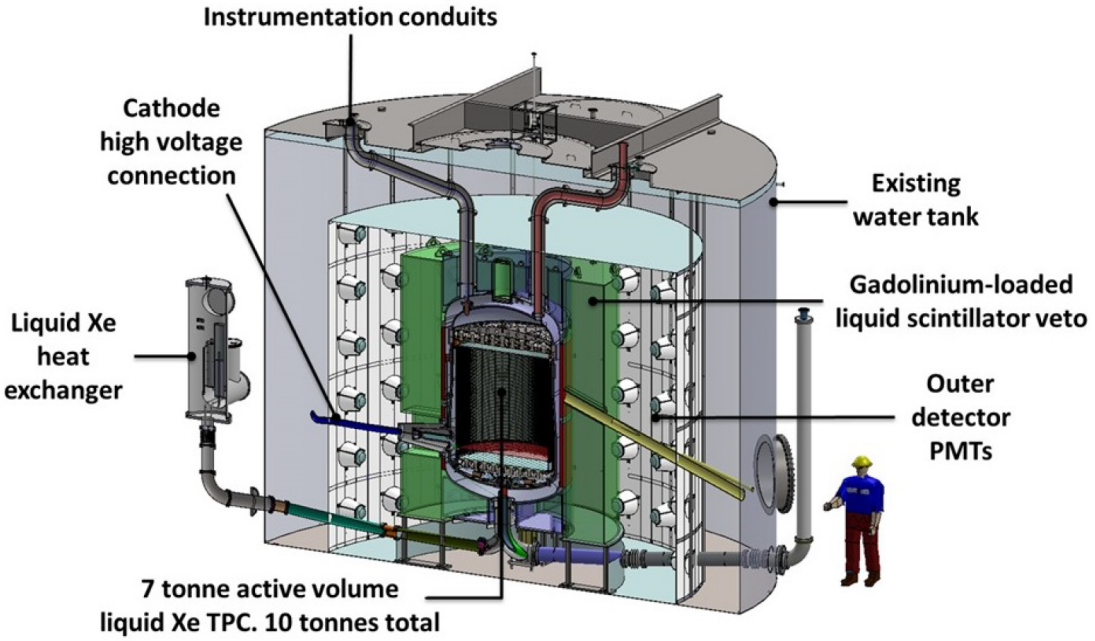


Figure 2.4: The layered structure of the LZ inner and outer detectors, with their shielding.

the xenon. A vacuum layer separates this from the 'outer cryostat vessel' (OCV), which forms the outer shell of the detector. Around this are further subsystems that provide additional detection opportunities. Clear acrylic tanks hold an organic liquid scintillator. This sits inside an outer water shield, which contains further PMTs directed towards the scintillator. The water shield provides additional protection from radiation that exists within the cavern, and the scintillator behaves as a detector for this and for any radioactivity from the detector materials themselves. This will be discussed further in section 2.5.

2.4.1 Xenon and WIMPs

As noted above, LZ is a two-phase xenon experiment; the TPC is filled with liquid, above which sits a small gas gap and the top array of PMTs. Using xenon as the target material maximises the signal that would be generated by a relatively heavy WIMP interacting with a target nucleus; the kinematic factor $r = \frac{4M_D M_T}{(M_D+M_T)^2}$ that features in eq. (2.1) above is maximised when the target nucleus mass and incident particle mass are equal. As the mass of a xenon nucleus is $120\,\mathrm{GeV/c^2}$, the LZ detector is tuned to search for WIMPs with masses in this region.

A further benefit of liquid xenon comes from its highly self-shielding nature: incident gamma rays and neutrons are powerfully attenuated as they pass through the liquid. This results from the dense, high-Z nature of liquid xenon. The outer few cm of xenon are therefore consigned to a shielding role, leaving a central 'fiducial volume' in which detections are considered as candidate interactions. The large size of the LZ detector also results in a low surface-to-volume ratio, enabling the maximum benefit from xenon's self-shielding capacity.

2.4.2 Signals

The larger the detector, the greater the likelihood of an incident WIMP interacting with the target material. By increasing the mass of xenon with which the WIMP could interact, the exposure is increased. However, increasing the signal is insufficient if the ratio of signal to background is poor. Having a very low background detection rate is crucial in rare event search experiments, as without such minimisation, small signals are indistinguishable from fluctuations in the background event rate. Thus the background must be kept as low as possible. This necessitates the selection of materials with low radioactivities wherever possible; see section 2.5. It also drives such a sensitive experiment underground and away from cosmic rays, which would flood the detector if run at the surface. LUX-ZEPLIN will be in the Davis Cavern of the Sanford Underground Research Facility,[58] in Lead, South Dakota, USA, placing the detector 4.850 feet (=1.48 km) underground. The main source of detector contamination is from dust entering the experiment on components. This, and other sources of background, will be further discussed in section 2.4.2.1 and section 2.5.

LZ is designed to detect signals from the ionisation and scintillation produced by a WIMP-nucleus interaction. The 'S1' signal is produced by the scintillation that accompanies the interaction, as shown in the left half of fig. 2.5. The xenon atom excited as a result of the interaction combines with a non-excited atom to form a strongly-bound exciton (Xe_2^*), which relaxes and emits two photons at 178 nm. These photons are mostly collected in the bottom PMT array, as a result of total internal reflection at the liquid surface from the mismatch of refractive indices between the liquid and gas.[72] These photons constitute the S1 signal.

In addition, the displacement of the nucleus from the recoil ionises the atom, releasing some electrons; see the right half of fig. 2.5. Although some of these will recombine with the xenon ion, most are drifted away from the interaction site by the high electric field that is generated along the length of the TPC. This accelerates the released electrons upwards to and through the liquid-gas interface near the top of the

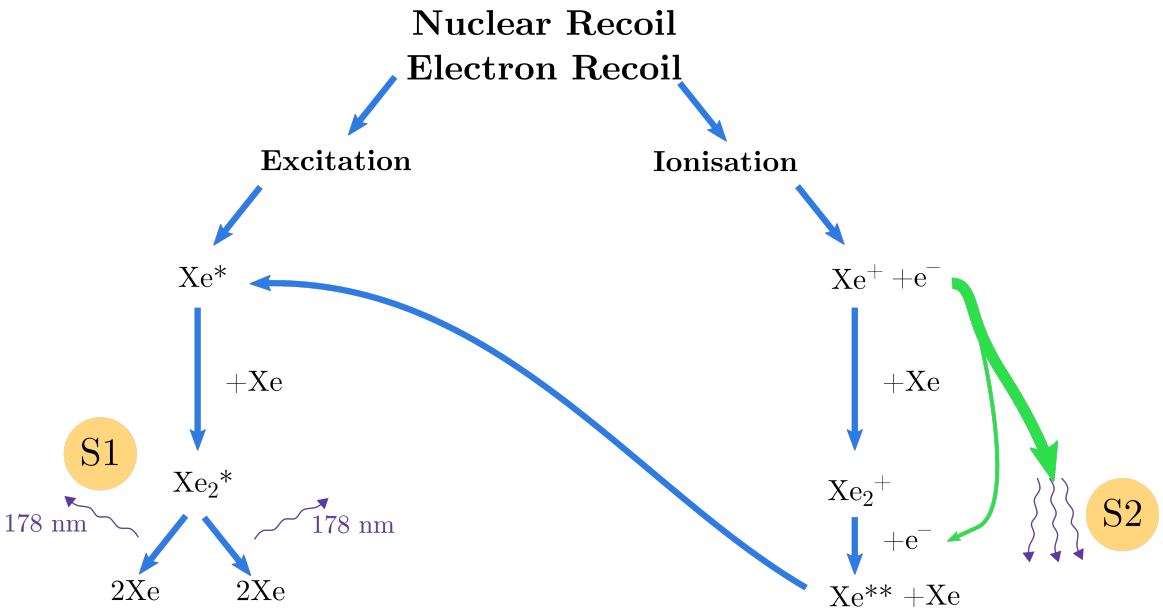


Figure 2.5: The chain of events following an interaction with xenon resulting in a nuclear recoil or electron recoil. Adapted from [13].

detector. Once in the gas, which is at a nominal pressure of 1.8 bar,[72] the electrons are accelerated by the applied electric field to sufficient energies to excite the xenon gas atoms and thus produce secondary scintillation known as 'electroluminescence'.[65] The number of photons emitted as a result of one electron travelling a set distance is dependent upon the gas pressure and electric field strength.[65] The total number of photons is then proportional to the drift path length.[65] In LZ, the electrons that reach the gas gap are predicted to produce 910 photons each.[72] These photons, mostly detected in the top PMT array, form the second, 'S2' signal.

The time delay between the S1 and S2 photons can be interpreted as the depth at which the interaction occurred: the deeper the interaction, the longer the electrons will have taken to be drifted to the gas phase, so the later the S2 signal will appear. Additionally, the electrons will diffuse in both x-y and z while they drift, leading to a broader S2 peak the deeper the interaction occurs. Hence the depth of the interaction can be determined from the S1 and S2 signals.

In section 2.4.1, the fiducialisation of the xenon volume was explained. In order for this to be practicable, the location of an interaction must be determined from the signals received. The depth is calculable as just described. The x-y position is also determinable via position reconstruction algorithms. From any interaction, a 'hit map' can be produced, indicating which PMTs on the array received more or fewer photons. An example can be seen in fig. 2.6. From this distribution of photons, the

original interaction position can be reconstructed. This is used to decide whether the interaction is a candidate WIMP interaction (i.e. if it is within the fiducial volume), or whether it is a background event.

WIMP-nucleus interactions will appear as 'nuclear recoil' (NR) events. However, 'electron recoil' (ER) events, whereby it is not the nucleus but the surrounding electrons that recoil, are also possible and will produce S1 and S2 signals. Electron recoils will result from interactions with gamma rays, but could not be from a WIMP interaction. Therefore, the discrimination of NR and ER signals is an important part of selecting candidate events. Although NR and ER interactions both produce S1 and S2 signals (see fig. 2.5), they do so in different ratios, as charge recombination behaves differently in the two cases.[65] In particular, for a given electric field strength, the fraction of electrons escaping recombination (and hence being drifted to the liquid surface) is higher for electron recoils than for nuclear recoils.[65] Hence the S2 for an electron recoil is larger than that for a nuclear recoil. The quantity of S2/S1 is therefore used to discriminate between the electron recoils and nuclear recoils.

2.4.2.1 Xenon contamination

The purity of the xenon is critical if the S2 signal is to be preserved; with a detector as large as LZ, this is particularly important, as the electrons must drift up to 1.5 m through the liquid xenon from an interaction to the liquid-gas interface. Any electronegative species, such as O_2 and H_2, will capture drifting electrons, leading to the degradation of the S2 signal. If severe enough, this could hamper differentiation between ER and NR events. In addition, oxygen and hydrogen are particularly prone to absorbing S1 light at 178 nm, so such impurities could also impede the S1 signal.

In order to prevent this problem, materials are not permitted if they could leak electronegatives into the xenon at a substantial rate, a process known as 'outgassing'. Many polymers and epoxies are thus ruled out as potential materials to be included in detector components. There is also a significant effort to purify the xenon while the detector is running, via an online xenon purification system.[73] Liquid xenon is removed from the detector at a rate of around 1.0 l/min. It is then evaporated, compressed to a higher pressure, purified and recondensed before being returned to the detector.[73] By choosing low-outgassing materials and constantly purifying the xenon, the S1 and S2 signals will be preserved.

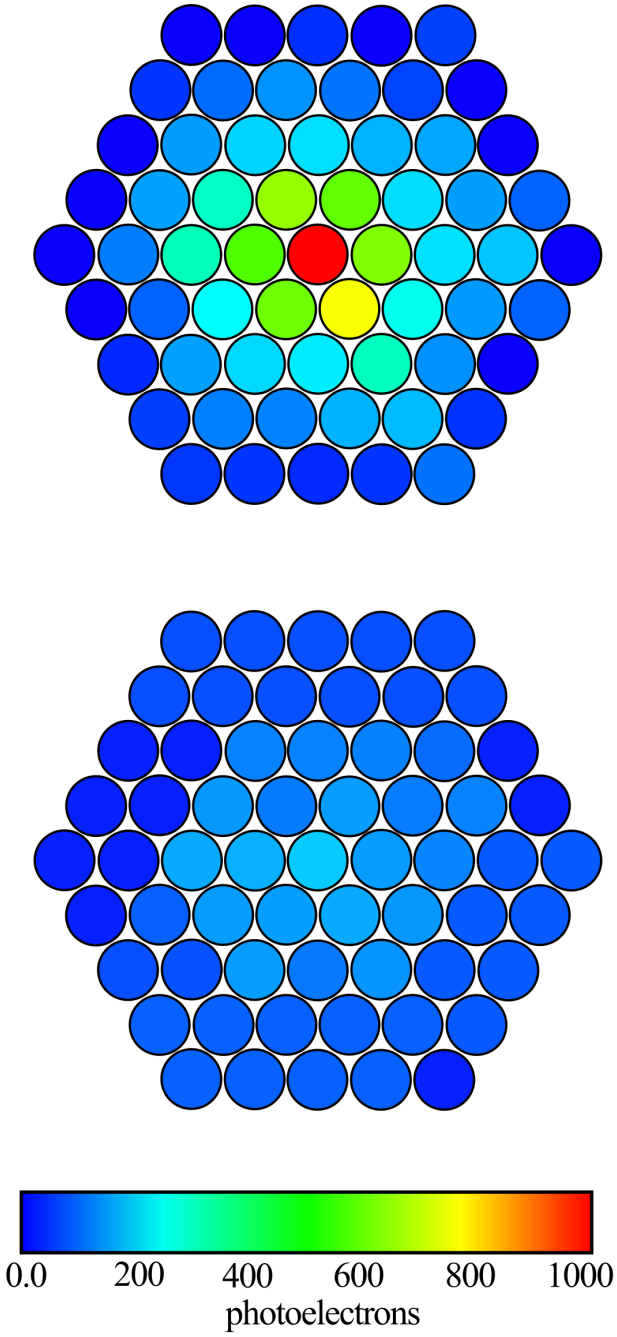


Figure 2.6: A demonstration of what a PMT 'hit map' might look like following an interaction at the centre of the detector. The largest signals in the top array (top picture) are from the S2 signal. The signals in the lower array (bottom picture), shown in subtle variations of blue, are from the S1 signal.

2.4.3 Instrumentation

The photons emitted as a result of an interaction are detected by photomultiplier tubes (PMTs) situated in two arrays, one at the bottom of the TPC, in liquid, and one at the top, in gas. The S1 scintillation signals can be seen in both arrays, but the S2 ionisation signals will be most prominent in the top array, as the electrons are drifted to the top of the TPC and the photons arise from electroluminescence in the gas gap. Importantly, no wavelength shifter is required for the signals to be detectable by the PMTs: quartz-windowed photomultipliers will register the photons that constitute the S1 and S2 signals without any additional interface.

All of the surfaces interior to the ICV will be covered in sheets of PTFE, acting as a reflective coating to ensure maximal light from every event reaches the PMTs. The reflectance of PTFE in liquid xenon is $> 95\%$ for the the S1 light at 178 nm.[74] The PTFE covering is moreover carefully designed to ensure that light from within the TPC reaches only the top and bottom PMT arrays, while light emitted in the xenon skin region outside the TPC reaches only the skin PMTs (see section 2.4), and not the PMTs that form the top and bottom arrays. This isolation ensures the signals cannot be misconstrued. In addition to the PMTs, LZ has many sensors that monitor the detector to ensure it is running as it should. These will be discussed in more depth in section 3.1.

The electric field that drifts the electrons to the liquid-gas interface is fed its required high voltage via a dedicated conduit. The field is generated via a high voltage cathode at the base of the TPC and a high voltage anode just above the liquid-gas interface. The cathode and anode are both grids of fine, evenly-spaced wires that carry the high voltage. A grid is used rather than a plate so as to be transparent to the majority of the S1 and S2 light, which must pass through the grid to reach the PMTs. The field in the bulk of the detector, although determined by the anode and cathode, is further manipulated by the titanium 'field shaping rings' that form part of the structure of the TPC. The rings are designed to ensure the field is as uniform as possible throughout the detector. Any non-uniformities would disturb the path of the electrons to the surface and could potentially lead to a false position being reconstructed for the original event, unless there is a significantly higher analysis effort in which non-uniformities are accounted for. A false event position reconstruction could lead to the incorrect inclusion or rejection of the event. Hence the uniformity of the electric field is very important.

At the goal drift field of 0.65 kV/cm, the electron drift velocity will be 2.2 mm/µs and a maximum drift time of 665 µs.[58] The drift velocity of the xenon ions is given

by

$$v = \mu\mathcal{E} \tag{2.2}$$

where $\mu = 3.5 \times 10^{-3}\text{cm}^2/(\text{Vs})$ and $\mathcal{E}$ is the electric field.[65] Hence for the goal drift field of $0.65\,\text{kV/cm}$, the ion drift velocity will be $v = 2.08\,\text{cm/s}$.

2.4.4 Sensitivity

LZ is expected to achieve a median sensitivity at a mass of approximately $40\,\text{GeV/c}^2$ of $2.3 \times 10^{-48}\text{cm}^2$. The details of the predicted sensitivity of LZ are shown in fig. 2.7. This shows the baseline sensitivity, which is that expected if every aspect and component in LZ just meets the requirements placed on it. If the 'Goal' values for performance are attained, the sensitivity stands to be significantly improved, particularly at lower WIMP masses.

2.5 Backgrounds and cleanliness

The sensitivity goal of LZ informs the acceptable level of background rates in the detector. This has a significant impact on our selection of materials, as any material chosen must satisfy these requirements. Indeed, this motivates the in-house design of many parts of the experiment, as will be explored in later chapters. This section will discuss the procedures in place in LZ for understanding the background signals arising from the materials that the detector is made from. In particular, the decay chain of uranium-238 is significant, and radon-222 is a critical element that must be controlled in LZ. Controlling the dust that enters the detector on components or during construction plays a particularly large role in limiting the background signals. Finally, we will examine how we can measure and model the radioactivity of our detector materials, how this informs our design and procedure choices, and the expected outcome of the programme.

2.5.1 Decays and decay chains

A supernova explosion creates conditions of incredibly high temperature and pressure, which produce a wealth of heavy elements not created during the main stage of a star's life. From the cloud of debris, stars and planets can eventually form; the Earth arose in this way from the remnants of a supernova. As such, all materials have contained traces of the heavy elements produced by the supernova, including uranium, thorium and potassium. Uranium-238, with a half-life of around 4.5 billion

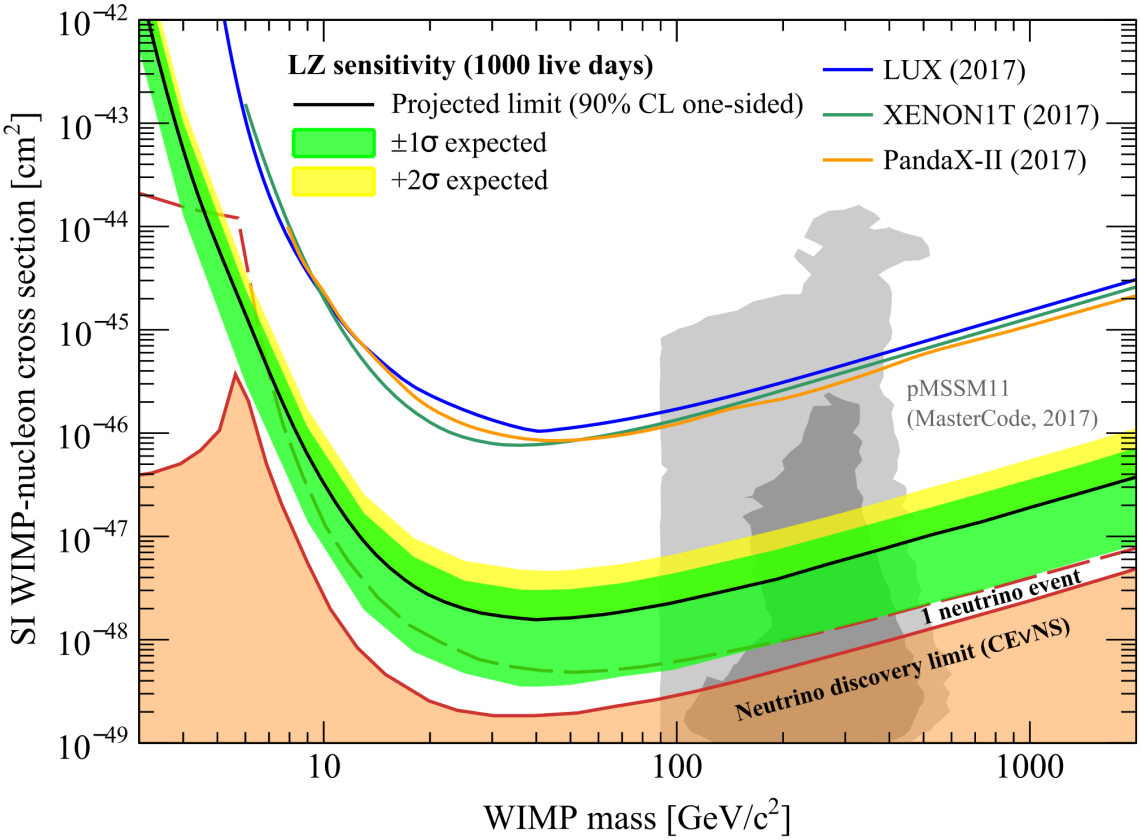


Figure 2.7: The predicted sensitivity of LZ, as given in [14]. The black line shows the predicted limit that LZ will reach. The orange shaded areas show regions where background NRs from cosmic neutrinos become a significant consideration. The predicted limit curve is shown alongside those achieved by other xenon dark matter search experiments, LUX, XENON1T and PandaX-II. As with all these experiments, LZ is less sensitive when there is a substantial discrepancy between the WIMP mass and the target mass (i.e. the mass of a xenon nucleus), as a result of the kinematic factor discussed in section 2.2.

years, is still present and decaying in the materials around us. If any decay happens in the detector, the photon, electron or alpha particle produced will generate a signal. These signals from material activity constitute a significant part of the background signal. Minimising this is an important part of making the detector as sensitive as possible. The higher the background, the less likely we are to spot a true signal. As an illustration, we below consider how isotopes of potassium and cobalt might impact on LZ, before examining the decay chain of uranium-238 and the challenges its progeny cause.

Potassium-40 One of the less concerning radioactive elements is potassium-40. 0.001% of potassium-40 decays are beta decays to an excited state of argon-40, which subsequently decays to the ground state via the emission of a photon of energy 1.02 MeV. This de-excitation photon, coming after the beta electron, could be directed into the xenon volume. If so, it will excite the electrons, resulting in an ER signal. However, owing to the self-shielding properties of liquid xenon, this track is unlikely to reach the fiducial volume. Therefore this decay of potassium does not have much impact on the dark matter search potential of LZ.

Cobalt-60 Almost all (99.88%) decays of cobalt-60 are to the ground state of nickel-60, resulting in two de-excitation photons as it decays. Pertinently, cobalt-60 has a half-life of 5.3 years, so the background contribution from cobalt-60 and its daughters will vary over the lifetime of the detector. Hence if there is any significant cobalt-60 background, this must be modelled in detail to be accounted for. Nevertheless, cobalt-60 decay photons are of around the same energy as those from potassium-40 and, as penetration is a function of photon energy, they too will be stopped by the self-shielding effect of the xenon. On the other hand if there are significantly many cobalt-60 decays, the higher number of photons results in higher statistics and so the probability of a photon reaching the fiducial volume must increase. It is therefore important to keep the contribution from this isotope low.

Uranium-238 The decay chain of uranium-238 can be seen in fig. 2.8. This is usually considered in two halves: the 'early chain' concerns all the decays as far as radium-226, while the 'late chain' is the term given to all the decays after radium. The chain is split in this way because there can easily be a disequilibrium between the two halves. Radium is a very reactive element with a fairly long half-life. Because

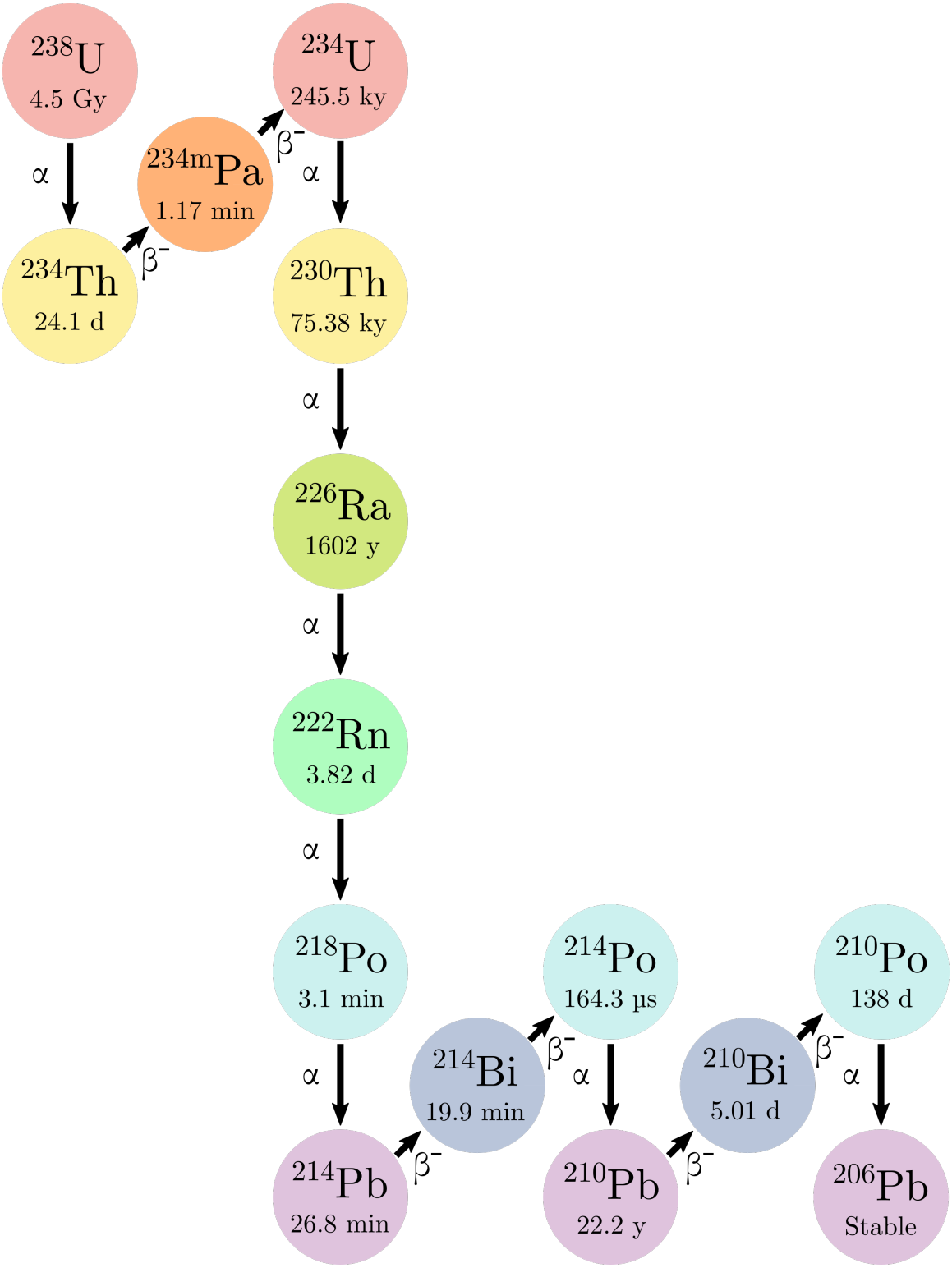


Figure 2.8: The uranium-238 decay chain, showing the dominant decays.

of its reactivity, it can easily be removed from a material, or likewise added, (either intentionally or unintentionally), resulting in an 'equilibrium break' in the chain.

Radium will eventually decay into radon-222, which is expected to be the single largest background in the LZ detector.[75] The radon decays via isotopes of bismuth, polonium and lead until it finally reaches the stable state of lead-206. The challenges associated with radon and lead-210 are discussed in section 2.5.2. The problems caused by the α decays in this part of the chain are considered in section 2.5.3.

2.5.2 Radon-222 and Lead-210

Radon exhibits long diffusion lengths in solids as a result of its chemical inertness. Therefore, when the radium in a material decays to radon, that radon is capable of moving within or out of the material. This is known as 'radon emanation'. If the radon enters the xenon, it is then free to move anywhere within the xenon, including into the fiducial volume. Furthermore the 3.82 day half-life allows enough time for this, yet the half-life is short enough that the radon will almost certainly decay during the running of the experiment.

Once the radon decays, it fairly rapidly works through a succession of daughters: polonium-218, lead-214, bismuth-214, polonium-214 and then lead-210. The half-life of lead-210 is 22.2 years, so this is a relatively stable point in the chain. The αs, βs and photons emitted during decay or de-excitation could appear anywhere throughout the xenon if the radon has emanated from its initial material. They are thus liable to produce a significant level of ER signals and these could be in the fiducial volume of the liquid xenon. In particular, lead-214 produces a β particle that may be mistaken for a nuclear recoil 0.5% of the time, and a further 9.2% of these occur without any associated photon emission, resulting in a background event indistinguishable from signal.[75] Nevertheless, this chain has a particular signature that can make it possible to identify its occurrence. The α decay of the polonium-214 generally follows very closely after the β decay of its parent bismuth-214.[76] This results in the two decays being recorded in the same event, as the time window for an event in LZ is twice the maximum drift time,[77] i.e. $\sim 1.3\,\text{ms}$. The bismuth and polonium decays coinciding in one event, resulting in multiple S1 and S2 signals being present in one event, is known as the 'BiPo' coincidence and is a signature of this chain.[76]

Although radon is itself a noble element, so unreactive, its progeny will readily stick to surfaces.[78] This leads to a build-up of lead-210 on material surfaces ('plate-out') as it has a relatively long half-life of 22 years. Radon-222 is present in air at levels of around ten to hundreds of Bq/m^3.[58] Hence materials and surfaces that are

exposed to air, for example during construction, are potentially subject to lead-210 plate-out, resulting in the introduction of radioactivity on the surfaces of the detector. The surface location of these radioactive isotopes mean that subsequent emissions are more likely to end up in the xenon volume, so have a greater chance of causing a background signal. In addition, the 22-year half-life of lead-210 is typically long compared to the lifetime of an experiment, so it is not feasible to wait for it to decay away. Thus radon can have two impacts on the detector background: atmospheric radon during construction can result in higher surface radioactivities, and radon that appears in materials can emanate into the xenon and further decay there.

2.5.2.1 Dust

One of the biggest concerns for radon emission is dust. Just like anything else, dust will contain background radioactive elements, some of which will be radium that can decay to radon. However because dust is particularly small, the radon is easily able to emanate. Hence dust on a surface has a two-fold impact: the emitter is already not in the bulk of a material, and any radon produced is especially susceptible to emanation. Dust is the major expected source of radon in LZ.[75] In spite of an extensive cleaning programme, as will be discussed in section 2.5.5, a total of 1 g of dust is expected on surfaces in LZ, and this is sufficient to introduce an estimated 10 mBq of radon into the experiment, contributing more than half of the total radon within the detector's xenon.[75] (A leak into the experiment would overshadow this, but should not occur.)

2.5.3 α emissions and α-n scattering

As discussed earlier, the photons from some nuclear decays are relatively harmless as they will generally appear as ER signals outside the fiducial volume of the detector. In general, the high-energy deposit of an α particle is also not a concern, as it is obviously beyond the region of interest for a WIMP search, in spite of the fact that it otherwise looks like a NR signal. Hence α particles alone are not a troubling background. Nevertheless, emitted α particles can cause significant problems. The α particles emitted from decays generally have quite high energies and can result in α-n reactions whereby an α particle is absorbed by a nucleus and a neutron is emitted as a result. These neutrons will produce NR signals in the detector so present a problematic background. Of particular concern are those neutrons thus produced that have similar energies to the WIMPs LZ is searching for, as an interaction of

such a neutron with the xenon could match the signature of a WIMP interaction. Of particular concern are the α particles produced by the decay of polonium-210, a granddaughter of plated-out lead-210 discussed above. These can generate neutrons via an α-n reaction with TPC materials with large α-n yields such as PTFE, which gives 10^{-5} n / α.[58] This is further reason to limit exposure to radon during detector construction.

2.5.4 Screening

Before being used in the detector, all materials must be screened. For many materials, the first step is for them to be placed on a high-purity germanium detector at a screening facility such as that at Boulby Underground Laboratory. The germanium detector is a crystal that detects the photons produced in the decay chain when elements transition to lower energy states following a decay. Germanium has a short path length for photons, so the full photon energy is deposited in the crystal and converted to a charge signal that is picked up and again converted in software to a recorded energy deposition.

The result of these measurements is an energy spectrum with peaks that correspond to the energy level transitions of daughter nuclei from radioactive decays in the material. This can be converted into a measurement of Bq/kg for each line, accounting for the geometric resolution of the detector, i.e. how many decays are likely to have occurred in the material and not have been captured by the germanium crystal because the resulting photons travelled away from the detector. This is then used to determine the quantities of each important radioactive element in the material; these are the data given in tables such as will be seen in section 4.4. From a set of these measurements, a neutron spectrum detailing the expected neutron emissions can be determined for the material, according to the amounts of these elements and their further decay chains. The effect of the component on LZ can then be found by simulating the component with the appropriate position and decay particle spectra, to see what interactions in the fiducial volume result from the component. This then is added to the 'backgrounds table' for the experiment, which keeps track of all of the contributions to background from the detector components. Once this has been done for all materials, the total experimental background is known, and it is to this that the final detector results are compared.

There are predicted to be a total of 722 electron recoils from radon-222 and no nuclear recoils.[58] Nevertheless, a ER/NR discrimination rate of 99.5% leaves 0.5% of ERs misidentified as NRs. Hence the radon-222 background produces 3.7 ERs that

are mistaken for NRs over a 1,000 day run.[75] Hence, even though the radon does not produce NRs, the signal from this background could still mimic a dark matter interaction.

2.5.5 Cleaning

A significant cleaning programme is being developed for LZ to eliminate background sources where possible. Materials produced externally and bought for use in LZ are not likely to have been produced in clean, radon-free facilities, as radon is present everywhere unless it is specifically removed. Many materials are therefore likely to have plated-out lead-210 on their surfaces. The longer the surface has been exposed to air, the higher the lead-210 contamination is likely to be. Therefore, where possible, the bulk material for producing components is to be bought larger than required so that the surface layers can be removed immediately prior to production and cleaning, to limit the exposure to air and hence limit the resulting lead-210.

Each component in LZ has an allocated 'cleaning protocol' to be followed after production and before packaging and shipping. This has a number of goals. Any grease or oil on the component that may have been acquired during the manufacturing process must be removed. Grease would provide electronegatives that would contaminate the xenon. The cleaning protocol is also instituted to remove any and all dust. Because dust on a component is such a significant source of radon, the total level of dust in LZ is required to be less than $500\,\mathrm{ng/cm^2}$ on all xenon-wetted surfaces. The cleaning protocol therefore includes wiping surfaces repeatedly to remove as much dust as possible.

Once components are clean, they are kept triple-bagged in special radon barrier bags. These prevent radon contamination of the air in which the component sits, limiting further plate-out of lead-210. The outer bag is for mechanical protection and is removed before the component is taken into the cleanroom construction facility. The second bag is for the transition to the cleanroom and the final bag is an additional barrier to dust and radon.

These measures are all to reduce the background in LZ as far as possible, as the smaller the background, the greater the ratio of signal to background will be and the more likely LZ will be achieve its goal of detecting the interactions of WIMPs with its target xenon, and thus discovering dark matter.

Chapter 3

Capacitive Sensor Readout in LZ

In the LUX-ZEPLIN dark matter search experiment, the primary event data come from photomultiplier tubes (PMTs), the signals from which result from the detection of photons from both the primary xenon scintillation (via the electronic transition to the ground state) and the subsequent electroluminescence (from the accelerated electrons released during ionisation).[65, 58] In addition to these detectors, a range of monitoring sensors are necessary to enable LZ to operate optimally as a dark matter detector. Furthermore, some of the sensors can contribute to decision-making as to whether a candidate event is more likely a dark matter event or caused by a departure from normal operating conditions of the detector.

This chapter introduces briefly the range of monitoring sensors employed in LZ before focusing on the development and demonstration of the capacitive sensor readout scheme necessary for position and liquid level sensors in LZ. The development of novel readout electronics was necessary to meet the requirements of sensor accuracy and precision that LZ needs to achieve its primary science goal. The main challenge is to prevent the capacitance of the cable between the sensor and the readout electronics from perturbing the sensor reading. This arises as a result of the size of the shielding in LZ and the hence unavoidable length of the cabling; the cable contributes a capacitance much greater than any sensor capacitance. Furthermore, cable capacitance is unlikely to be constant due to the temperature variations that the dielectric in it will be subjected to and is therefore best suppressed. This suppression is achieved with the novel readout electronics explored in detail below.

3.1 Sensors in LZ

The monitoring of certain aspects of the LUX-ZEPLIN experiment, such as the position of the xenon phase boundary, is crucial if the experiment is to perform well, be

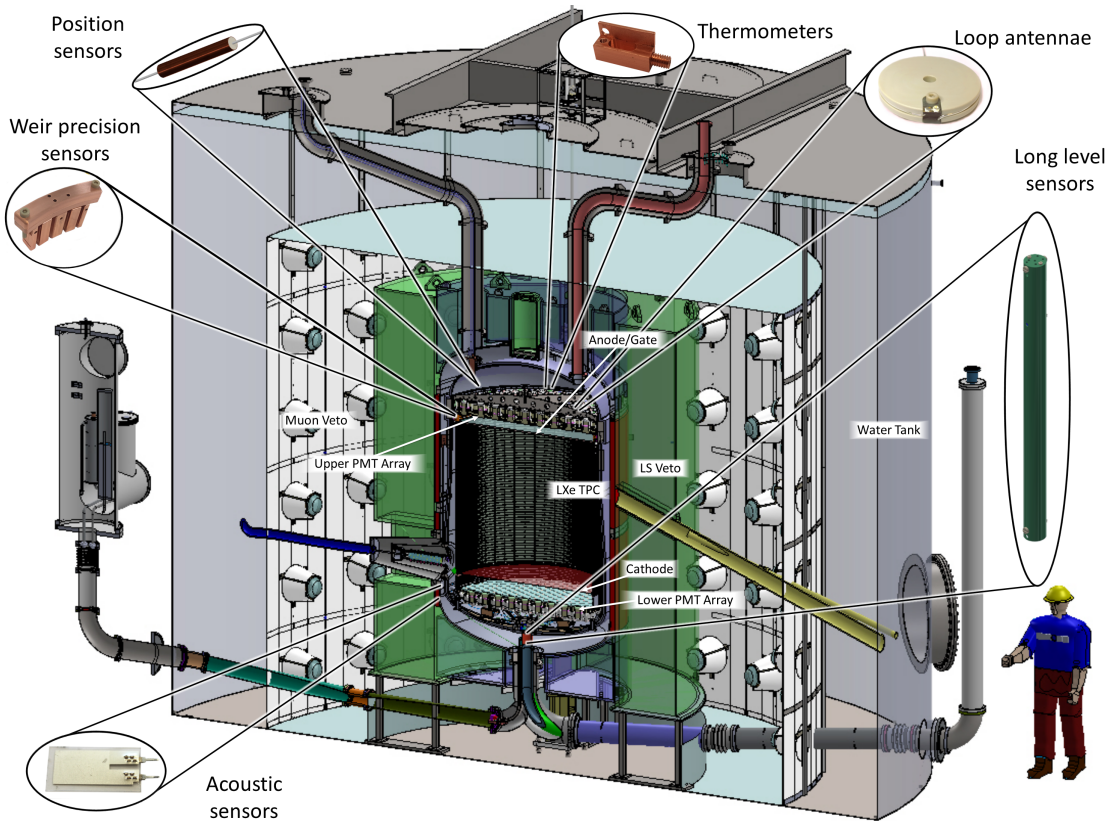


Figure 3.1: Schematic illustrating some of the sensors in LZ. The position sensors, long level sensors and weir precision sensors are all capacitive sensors, for which the readout is the focus of this chapter.

comprehensively understood, and run safely. The experiment will feature a range of sensors as seen in fig. 3.1, which together form the sensors work package in LZ. Each of these will be explained briefly below.

3.1.1 Position sensors

The position sensors are designed to measure the relative movement between the TPC and ICV. This is particularly important during the cooldown that will precede data-taking with LZ. Construction of the experiment will take place at an ambient temperature of up to around 30 °C. Prior to taking data, the experiment will then be cooled to around −100 °C, giving an expected temperature drop of around 130 K. The cooling enables the experiment to be filled with liquid xenon while maintaining a pressure that is only slightly higher than atmospheric pressure. The alternative to running at low temperature would be to run at high pressure. However the risks associated with running the experiment at high pressures are too great given the

location of the detector in a deep underground lab, and designing the vessels to fulfill appropriate safety requirements would have been very difficult.

The TPC consists of stacked PTFE and titanium rings, so during the cooling of the detector, it will shrink away from the ICV, as will be discussed in more detail in section 4.1.1. The position sensors will monitor the change in relative position of the PMT array, which sits on top of the TPC, allowing us to accurately characterise its position. Monitoring the position changes during cooling also enables the verification of the expected shrinking and movement of the TPC. The motivation for precisely measuring position will be discussed further in Chapter 4. A total of six interconnected position sensors will be used. The position sensor design will also be discussed in Chapter 4, and the system of connected sensors in Chapter 5.

The position sensors are capacitive sensors, so the position to be characterised can be monitored by measuring the output of the electronics, which will vary with the sensor capacitance. This readout is discussed in detail in this chapter. The simple position sensor used for testing the readout is described in more detail in section 3.3 below.

3.1.2 Level sensors

LZ uses a two-phase xenon TPC, with the liquid surface lying between the gate and anode wire grids near the top of the TPC; see fig. 3.2. The liquid level is maintained by filling the detector with liquid xenon at the bottom and having a weir at the top over which excess liquid spills. This is shown in fig. 3.2. The height of the liquid affects the size of the gas gap through which electrons are accelerated to produce electroluminescence. This in turn affects the size of the S2 signal. Hence knowing the liquid level precisely is important for being able to correct for this effect in the experimental data.

There are two designs of level sensor in LZ. The first is a 'long level sensor' that covers a range of around 20 cm, with the goal of monitoring the liquid level during the filling of the TPC. The second is a 'weir precision sensor' that precisely monitors the height of the liquid between the gate and anode grids during the running of the experiment. The sensor sits in the weir that controls the liquid level. A schematic of the weir function can be seen in fig. 3.3. The level sensors used in LZ are differential capacitive sensors and will use the novel readout described later in this chapter. The level sensors are partly filled with liquid and the varying liquid level changes the capacitance of the sensor. Therefore, by monitoring the sensor capacitance we can understand the position of the liquid-gas interface. The level sensors thus operate

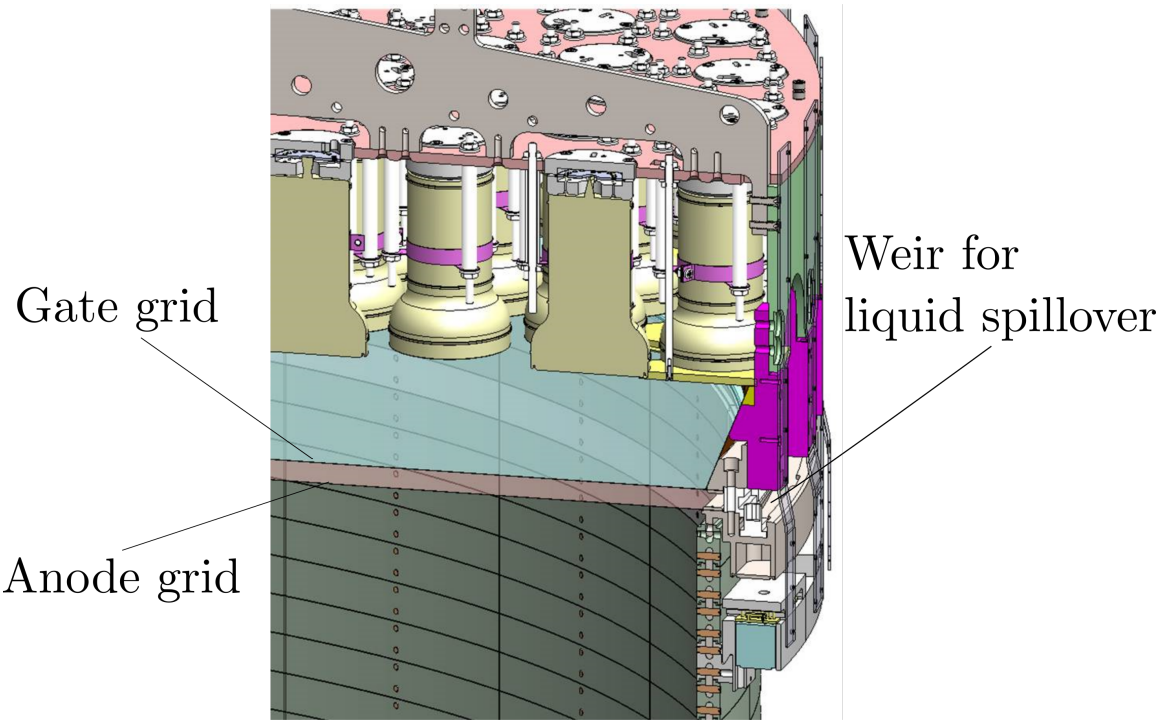


Figure 3.2: A CAD model of the 'top corner' region, showing the anode and gate wire grids, and the weir that allows for liquid overspill. The liquid-gas interface should sit between the gate grid and anode grid.

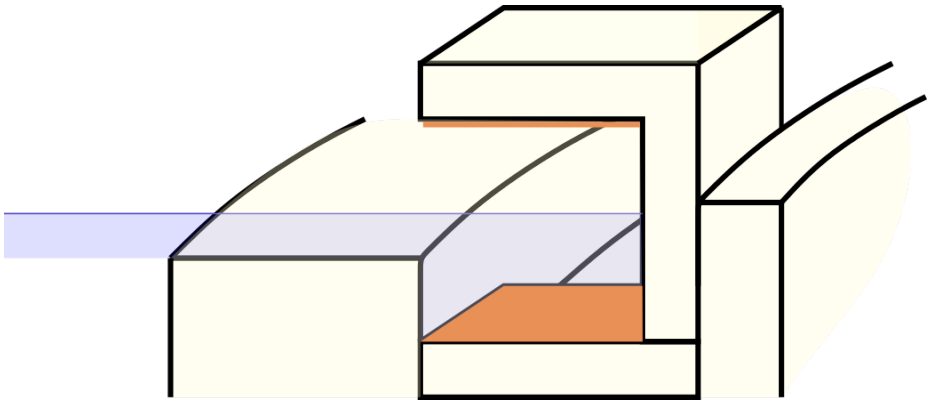


Figure 3.3: A schematic of the workings of the weir and 'weir precision sensor'. As the liquid xenon is pumped into the bottom of the detector, liquid will overspill into the weir, flowing out of the detector through drains in the weir. The weir precision sensors sit within the weir to monitor the level of liquid within it. One capacitor plate sits above the top of the weir, while the other sits in the bottom, such that the liquid level (highlighted here in blue) will lie between the two.

on the same principle as the position sensor, using the same electronics to read out the signal. Nevertheless, the design of the level sensors does not form a part of this thesis.

3.1.3 Acoustic sensors

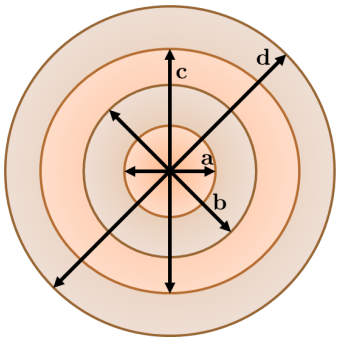
Commercial piezo-electric sensors will be used to monitor the acoustic environment of LZ. In particular they will be listening out for possible bubbling that could be caused by an overheating resistor on one of the bases of the PMTs, and possible dripping that could result from xenon liquid condensing in the gas region and then dripping back onto the liquid surface. Both of these phenomena will affect the stability of the liquid surface. Bubbles will also have optical effects within the liquid, scattering the S1 photons.

3.1.4 Loop antennae

The loop antenna sensors will pick up electromagnetic signals that result from high-voltage breakdowns inside the experiment. With a fast readout system connected to the high voltage controller, if the loop antennae detect a high voltage breakdown, the high voltages on the wire grids can be very quickly switched off to avoid damage to the PMTs or the rest of the experiment. The loop antennae will be situated in the gas region above the TPC. The readout for the loop antennae must be very fast, and much faster than is required for the other sensors, so they will not use the capacitive readout discussed here.

3.1.5 Thermometers

Understanding the temperature profile of the detector is crucial for success. The thermometers used are PT100 resistive thermometers read out with a four-wire measurement that ensures maximum accuracy. Thermometers will feature both inside and on the outer surface of the inner cryostat vessel, as well as within other systems in the experiment. These will be fed into LZ's slow control system. As will be discussed in Chapters 4 and 5, their output will play a role in the data from the system of position sensors.



a: 0.254 mm, bare copper core ($r = 0.127$ mm)
b: 0.83 mm, extruded FEP dielectric ($r = 0.415$ mm)
c: bare copper shield (woven)
d: 1.3 mm, outer jacket, extruded FEP

Figure 3.4: The dimensions of the coaxial cable that is being produced by Axon for LZ. This will be used for the sensors. The dielectric and outer jacket are made of fluorinated ethylene propylene (FEP). Some of the cable can be seen in fig. 3.5.

3.2 Introducing the readout for capacitive sensors

In both the position sensors and the level sensors, by measuring the changing capacitance, we monitor changes in the underlying variable. However, the large size of the detector in conjunction with radiopurity requirements necessitates the use of very long cables to connect the readout electronics to the sensors. The readout electronics cannot be within the detector as they would make a very large contribution to the radioactive background. Furthermore, designing electronics to work at $-100\,°\mathrm{C}$ would pose additional significant challenges in terms of component reliability at low temperature. Hence the cables carrying the sensor signals must run from the sensors close to the TPC, out of conduits that pass through the vacuum space between the cryostat vessels, through further conduits that cross the liquid scintillator veto and the water tank, and finally to a flange onto which the sensor readout electronics board is fixed. The total length required for the cables may vary by a small amount, subject to the final conduit routing. The current estimate from the experiment is that this totals 12 m, and the cables will be provided 13 m long. For what follows, we will use 13 m as an upper bound. As will be explained below, the capacitive sensor readout suppresses the cable capacitance to an extent that the precise length does not matter. The final cable length may be shorter than this, as once the cables have been 'pulled' through the appropriate vessels, they may be trimmed. The cable used for the sensors is Axon A21482C (with FEP jacket), for which the specifications can be seen in fig. 3.4.

The significant challenge for the capacitive sensors posed by these cables is that the capacitance of each one is around a thousand times the capacitance of the sensors that the cable is there to read out. The sensors have a varying capacitance of around

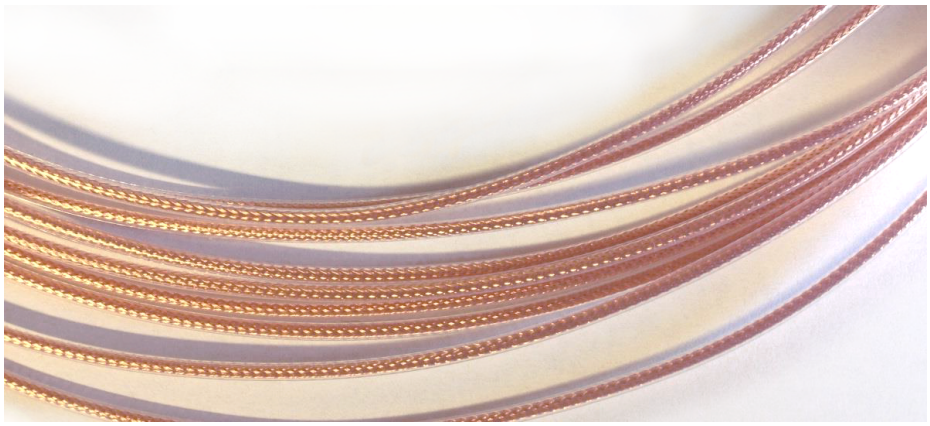


Figure 3.5: A photograph of some of the coaxial cable that will be used in LZ.

a few picofarads. The cable capacitance per unit length is calculated from the data sheet values as follows:

$$\begin{aligned} \frac{C}{\ell} &= \frac{2\pi\varepsilon_0\varepsilon_r}{\ln[\frac{b}{a}]} \\ &= \frac{2\pi\varepsilon_0 \times 2.1}{\ln[\frac{0.415}{0.127}]} \\ &= \frac{116.8}{1.184}\mathrm{pF/m} \\ &= 98.66\,\mathrm{pF/m} \end{aligned} \tag{3.1}$$

where ε_r is the relative permittivity of FEP. This agrees to within 1% with a measured value of 97.88 pF/m. Hence for a length of 13 m, the cables have a total capacitance of 1.28 nF.

If the cable capacitance were stable, the additional capacitance could be removed from the measurements as a fixed offset. This might be possible for the liquid level sensors, which operate only once the experiment is cool. However the position sensors must operate during cooldown, and in that period the capacitance of the cables is likely to change. For example, the dielectric in the coaxial cable will change its relative permittivity as it cools, and it will also shrink. These changes will alter the capacitance of the cable as described below in section 3.2.1. With such a long cable, these small changes add up to a significant effect. Even a change in the cable capacitance at the level of 0.1% would mean a change of the same order as that expected from the sensors across their full range; an example of the capacitive output of a sensor is seen for reference in fig. 3.6. Clearly the cable capacitance cannot be ignored.

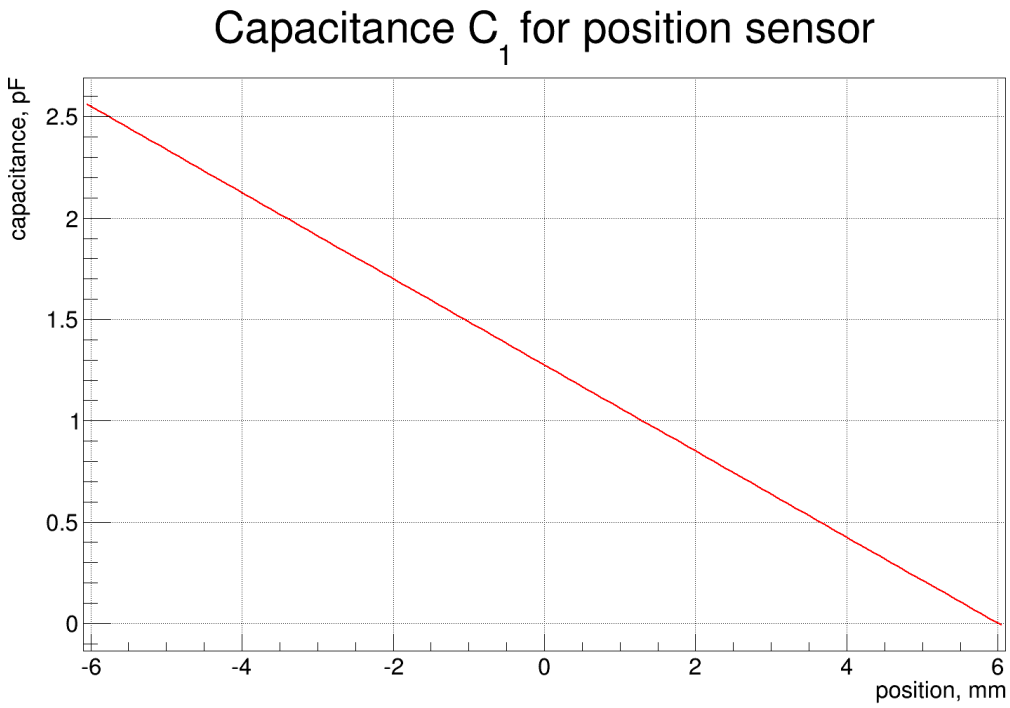


Figure 3.6: The modelled output for one half (C_1) of the system test position sensor, discussed in detail in Chapter 4. The capacitance of this half varies by around 2.5 pF across the range of the sensor. The other half of the sensor takes the same values in reverse, and the readout is based on the difference between these two.

3.2.1 Cable capacitance variation with temperature

As the detector cools, the cable capacitance will change owing to both the changing of the relative permittivity and the shrinking of the dielectric inside the cable that separates the cable core from the grounded sheath around it. In the cable used to carry signals in LZ, the dielectric is extruded FEP (fluorinated ethylene propylene). The cables will have a capacitance of 98.66 pF/m, as calculated above.

If the relative permittivity of the dielectric changes by 10%, i.e. from 2.1 to 1.9, the cable capacitance per unit length goes from being 98.7 pF/m to

$$\begin{aligned} \frac{C}{\ell_{cold}} &= \frac{2\pi\varepsilon_0\varepsilon_r}{\ln[\frac{a}{b}]} \\ &= \frac{2\pi\varepsilon_0 \times 1.9}{\ln[\frac{0.415}{0.127}]} \\ &= \frac{105.7}{1.184} \\ &= 89.3\,\mathrm{pF/m}\,. \end{aligned} \tag{3.2}$$

Hence we see a significant drop in the cable capacitance per unit length. However this calculation ignores the changing size of the dielectric.

The coefficient of linear thermal expansion (CLTE) of FEP is 135 µm/m/K. The CLTE of copper is around 16 µm/m/K. The diameter of the core will shrink by around $0.254\,\mathrm{mm}\times 16\times 10^{-6}\,/\mathrm{K}\times 130\,\mathrm{K} = 0.5\,\mu\mathrm{m}$. If the FEP were not surrounding a copper core, the inner diameter of the dielectric would shrink by 4.457 µm; as it is, it will shrink onto the copper, resulting in an inner boundary between the copper and FEP with a diameter of 0.2535 mm. The dielectric outer diameter changes by around $0.83\,\mathrm{mm}\times 135\times 10^{-6}\,/\mathrm{K}\times 130\,\mathrm{K} = 0.015\,\mathrm{mm}$, i.e. the cold dielectric outer diameter is 0.815 mm. The copper shield of the cable is surrounded by an outer jacket of extruded FEP. This will shrink as the cable cools and pull the woven sheath tight against the dielectric. Therefore the inner diameter of the sheath will be the same as the outer diameter of the dielectric.

Hence, using 1.9 as the value of the relative permittivity, the capacitance per unit length at −100 °C is:

$$\begin{aligned} \frac{C}{\ell} &= \frac{2\pi \times 1.9 \times 8.854\mathrm{pF/m}}{\ln[\frac{0.815}{0.2535}]} \\ &= 90.51\,\mathrm{pF/m}\,. \end{aligned}$$

The two effects oppose each other, but the change in dielectric constant dominates and overall a decrease in cable capacitance per unit length is expected of around

8.2 pF/m or $(98.66 - 90.51)/98.66 = 8\%$ due to the changing of the dielectric as the cable cools from 30 °C to −100 °C. This is a maximal estimate, as the dielectric constant is expected to change by no more than 10%. For 13 m of cable, this equates to a change in cable capacitance of around 103 pF under the extreme assumption that the entire cable reaches the lowest temperature. This change is significantly larger than the capacitance of the position sensors or level sensors, and far greater than the changes in capacitance that the sensors will undergo when running. There will likely be some temperature gradient along the cable that is difficult to quantify in advance, and that will vary with the rate of the cooling of the detector. A reasonable estimate might be to consider one quarter of the cable to be at −100 °C, one quarter to be halfway to this temperature, and the rest to be warm (30 °C). For the coldest part, the capacitance per unit length is 90.7 pF/m and for the warmest part, the capacitance per unit length is 98.66 pF/m. The intervening capacitance per unit length will be

$$\begin{aligned} \frac{C}{\ell_{cold}} &= \frac{2\pi\varepsilon_0\varepsilon_r}{\ln[\frac{a}{b}]} \\ &= \frac{2\pi\varepsilon_0 \times 2.0}{\ln[\frac{0.8227}{0.2537}]} \\ &= 94.58\,\text{pF/m}\,. \end{aligned} \tag{3.3}$$

This gives a total cable capacitance of

$$\begin{aligned} C_C = \frac{13}{4}\text{m} \times 90.7\,\text{pF/m} + \frac{13}{4} \times 94.58 + \frac{13}{2} \times 98.66 &= 1243.45\,\text{pF} \\ &= 1.243\,\text{nF}\,. \end{aligned} \tag{3.4}$$

Hence, if only one quarter of the cable reaches −100 °C, the change in capacitance will be 1.282 nF − 1.243 nF = 0.039 nF = 39 pF. This is large enough that it cannot be ignored. Moreover, because the temperature profile of the cable is unknown and will change, a robust way of handling the unknown and changing cable capacitance is required.

3.2.2 Cable capacitance suppression

The results from section 3.2.1 have demonstrated the scale of the necessary cable capacitance suppression. The readout electronics for the capacitive sensors quenches the effect that variations in the cable capacitance might have on the sensor measurement by actively suppressing the cable capacitance. This is achieved through a feedback circuit that adjusts the excitation applied to the sensor in such a way that the measured sensor signal is zero. The applied voltage is then the readout of the

system; this avoids the need to measure an absolute value of capacitance. The details of this scheme are explained in detail in section 3.5 below.

3.3 A simple position sensor

In order to characterise and validate the electronics used for the capacitive sensor readout, a simple position sensor was created. At its most basic, a capacitor is just two metal plates. For a pair of parallel capacitor plates with overlapping area A and spacing d, the capacitance C is given by

$$C = \frac{\varepsilon_0 \varepsilon_r A}{d} \tag{3.5}$$

where ε_0 is the permittivity of free space and ε_r is the relative permittivity of the material between the capacitive plates. From eq. (3.5), we see that we can alter the capacitance by changing either A, the area of overlap of the two plates, d, the distance between them, or ε_r, the dielectric that sits between the plates. By measuring the resulting change in capacitance, any of these methods could provide the basis for a capacitive measurement of displacement. In section 4.2.3 we will explore the merits and demerits of these options in more depth. To illustrate and test the electronics, a position sensor that varies the spacing between the capacitor plates was used. This simple sensor design avoids multiple dielectric materials in the sensor and is described below.

3.3.1 A spacing variation sensor

A spacing variation capacitive sensor measures changes in position along the axis perpendicular to the faces of the plates, to which the two components whose relative position is to be measured are connected. Sensitivity to motion in extraneous axes can be avoided by making one plate larger than the other so that the effective area of the capacitor, determined by the overlap of the plates, is constant even if the plates shift along these extraneous axes. If the sensor is designed such that the sensitive plate is the smaller one, then fringe fields created at the edges of the smaller plate will not be so important; see fig. 3.7.

So far the simple sensor considered has been one capacitor made up of two plates. If a third plate is introduced to this (such that all three plates share the axis perpendicular to their faces), the central plate behaves as a potential divider between the upper and lower plates, as the central plate will provide an equipotential surface; see fig. 3.9. Moving the central plate along an axis perpendicular to its face changes the

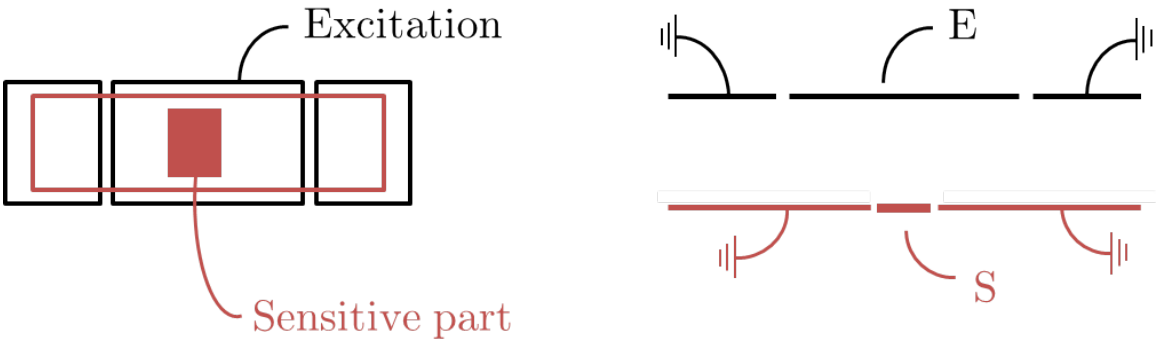


Figure 3.7: A diagram indicating a possible plate arrangement in a spacing variation sensor. An AC excitation voltage is applied to one plate ('Excitation') and picked up by the plate facing it ('Sensitive'). The voltage read out from this plate will depend on the capacitance of the plate arrangement.

ratio of the potential differences between the upper and central plates and the lower and central plates. It also changes the distances between the capacitor plates and hence the ratio of the capacitances. Consider the top plate to have a voltage V_1 and the bottom plate to have a voltage V_2, with the plates separated by a distance D, as shown in fig. 3.8. Hence

$$E = \frac{V_1 - V_2}{D} \tag{3.6}$$

where E is the electric field between the plates and $V_1 > V_2$. Consider a test charge q moving between the plate carrying V_1 and the sensitive plate V_s. The force on this charge is $F = qE$ and the work done in moving it is

$$W = qEd \tag{3.7}$$

$$= q\frac{V_1 - V_2}{D}d\,. \tag{3.8}$$

Hence the potential difference V_d between the top plate and the sensitive plate is given by

$$V_d = \frac{W}{q} \tag{3.9}$$

$$= (V_1 - V_2)\frac{d}{D}\,. \tag{3.10}$$

As such, the potential of the sensitive plate is

$$V_s = V_1 - V_d \tag{3.11}$$

$$= V_1\left(1 - \frac{d}{D}\right) + V_2\frac{d}{D}\,. \tag{3.12}$$

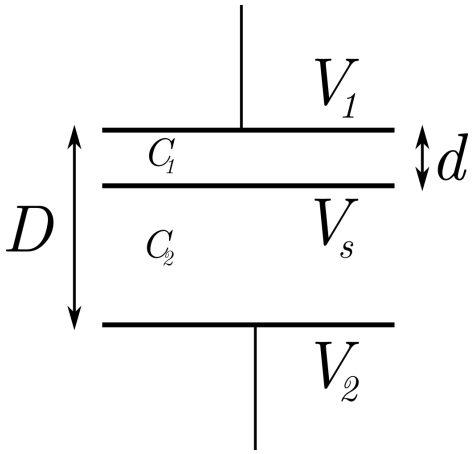


Figure 3.8: A diagram to illustrate the voltages and distances as used in the calculation of the sensed voltage.

We can use V_s as our measurement of capacitance. Consider the case where the central plate is between a potential and a ground plate, i.e. $V_2 = 0\,\mathrm{V}$. Hence

$$\frac{V_s}{V_1} = \left(1 - \frac{d}{D}\right). \tag{3.13}$$

For a general potential divider,

$$V_{out} = \frac{Z_2}{Z_1 + Z_2} V_{in}\,. \tag{3.14}$$

For the case of our two capacitors,

$$\left|\frac{V_{out}}{V_{in}}\right| = \frac{V_S}{V_1} \tag{3.15}$$

$$= \frac{C_1}{C_2 + C_1} \tag{3.16}$$

$$= \frac{\frac{\varepsilon_0 \varepsilon_r A}{d}}{\frac{\varepsilon_0 \varepsilon_r A}{D-d} + \frac{\varepsilon_0 \varepsilon_r A}{d}} \tag{3.17}$$

$$= \left(1 - \frac{d}{D}\right). \tag{3.18}$$

Hence measuring the potential of the central plate measures a ratio of capacitances. By considering such a ratio of capacitances, the output will to first order be insensitive to unwanted variations of dielectric constant, area and most other circuit and system variables. Moreover, using a pair of capacitors eliminates the effect of common-mode interference. This interference would affect both potential differences so would to first order cancel out. This also motivates having both capacitors in (approximately) the

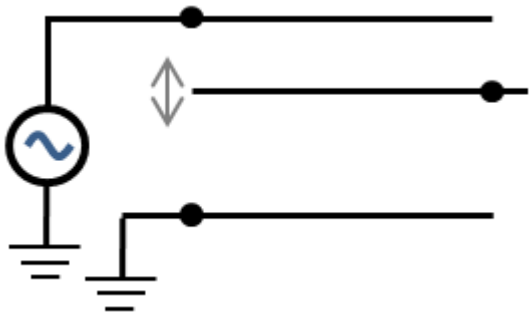


Figure 3.9: Illustration of the behaviour of three parallel plates as a potential divider and two capacitors

same place: if there was one capacitor measuring the position and a second reference capacitor elsewhere, such as on the electronics board, this cancellation would not happen. This is a strong motivation for having two capacitors in the sensor and having both in the same position.

3.3.2 Sensor design

A simple position sensor based on these principles presents a good test bed for the readout electronics. A labelled CAD model of the sensor produced can be seen in fig. 3.10. A photograph of the prototype in its test stand can be seen in fig. 3.11. The plates are made of copper and the plastic used for the rods and plunger is polyurethane.

The two outer plates provide the structure within which the important part of the sensor sits. Adjacent to them are two excitation plates, one for a positive excitation and one for a negative excitation. In the centre is a central sensing plate. The two excitation plates are mechanically coupled together by short struts and can move freely along the three long struts that run through all the plates. A plunger is attached to one of the excitation plates, and moves with them. Actuating this corresponds to changing the relative position we wish to measure.

3.3.2.1 Fringe fields

The sense electrode, identified as component **a** in fig. 3.10, is surrounded by a concentric guard electrode. One problem that real capacitors suffer from is the effect of fringe fields. These arise when the fields at the edges of the capacitor plates are no longer homogeneous and constant; see fig. 3.12 for an illustration. This can change the effective capacitance of the capacitor. However, using a guard electrode at the

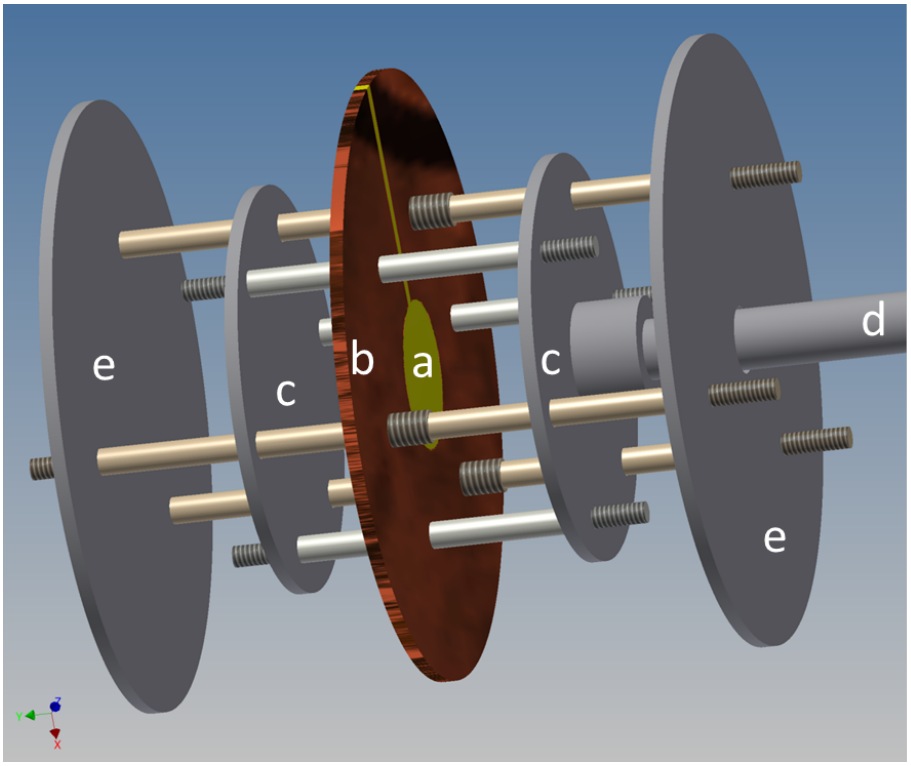


Figure 3.10: CAD model of prototype sensor: **a.** sense electrode, a central circular plate (false-coloured in model) with narrow extension to the edge of the surrounding electrode, **b.** guard electrode, **c.** excitation plates which carry the positive and negative excitations, coupled together, **d.** plunger fixed to the excitation plates, **e.** guard ground plates.

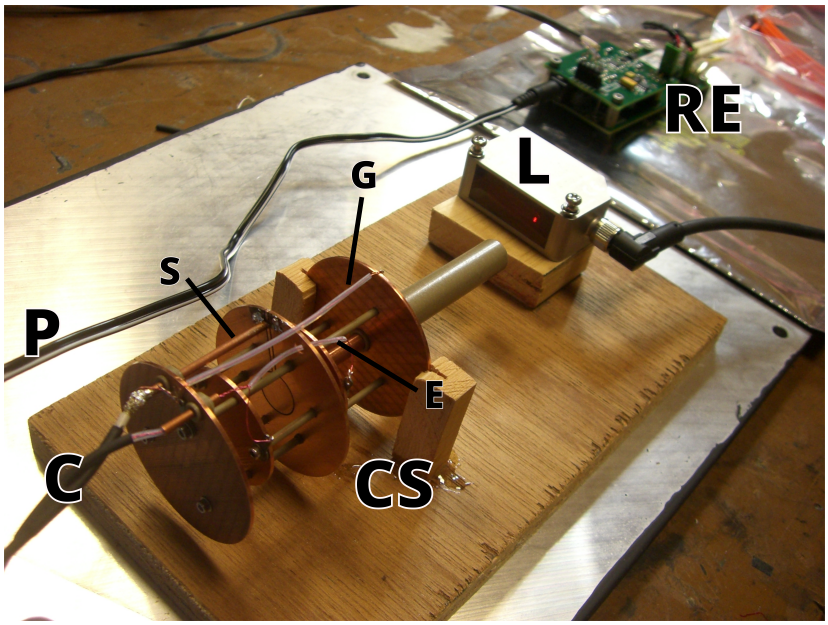


Figure 3.11: Photograph of prototype sensor in a basic test stand. **CS** Capacitive sensor, **L** Laser position sensor, **RE** Readout electronics, **P** Power cable for electronics, **C** Cables for sensor, consisting of: **G** a wire carrying ground to the outer plates, **E** a pair of wires carrying the excitations, and **S** the sense wire, housed in a thin copper tube for shielding.



Figure 3.12: Illustration of fringe fields with and without guard electrode

same potential as the sense electrode minimises the impact of this effect on our measurements. The central electrode is cut from the central disk of copper using a wire saw. The gap is then backfilled with epoxy, providing electrical insulation between the central sense electrode and the grounded guard around it, as well as rigidly supporting the sense electrode within the guard electrode so that it does not need additional structures to hold it in place.

3.3.2.2 Plate configuration

In fig. 3.9, the ground plate is the lower of the three plates and only one plate has an excitation applied. However an alternative is to have a positive excitation on the top plate and a negative excitation on the lower plate. In a case where there are equal capacitances, the central plate sits automatically at ground, assuming that stray fields

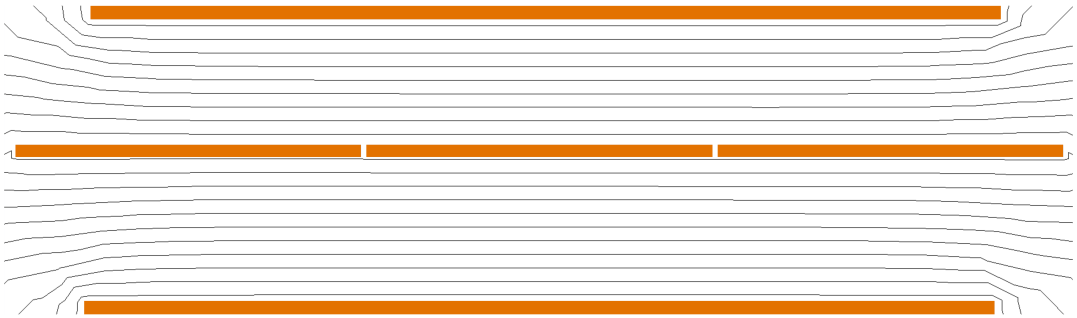


Figure 3.13: A finite element analysis model of the electric field in the central region of the position sensor. The lines indicate equipotentials of the field between the excitation plates and the sense and ground plates.

from the rest of the apparatus are insignificant relative to the fields due to the sensor electrodes. In other configurations, the excitations applied to the upper and lower plates can be altered in real time to ensure that the central plate is always at ground.

A significant advantage of having the central sense plate at ground is that it avoids the need for a driven guard electrode, which would be required if fringe field effects are to be limited. However, if the electronics adjusts the excitations to keep the central plate at ground, the guard electrode can instead be held at ground potential, which makes it much more immune to noise and interference, and reduces the electronic component count. Moreover, a driven guard electrode could result in the potential to cause interference with anything near the sensor, as there would be nothing to prevent the signal being emitted. Therefore avoiding a driven guard by having the sense plate at ground is an important advantage of this design.

In addition to the guard electrode, the two additional large plates at the ends of the sensor will help to shield the sensor. When running the sensor it can also be shielded with a grounded cover to further minimise interference.

3.3.2.3 Calibration

The position sensor design discussed above is relatively simple, so one can be confident of understanding the sensor. Nevertheless, the sensor configuration requires external monitoring in order to associate sensor output with well-defined position values. This was achieved using an OD Mini Prime laser position sensor[1]. This commercial laser position sensor was trained on the plunger of the sensor. It precisely measured the

[1]Details available at https://www.sick.com/gb/en/distance-sensors/displacement-measurement-sensors/od-mini/c/g276251

positions of the moving part of the sensor, outputting its readings on a digital display on the sensor. The output voltages from the capacitive sensor readout could be compared to a true measure of sensor position. The OD Mini Prime can be seen in this set-up in fig. 3.11. Having constructed this testbed, we are in a position to develop, optimise and characterise the readout electronics for the capacitive sensors.

3.4 The readout electronics

The readout electronics developed are to be used not only for the position sensors but also for liquid level sensors, as these are all capacitive sensors with the same form of measurement. The simple position sensor test-bed supported the development of the electronics for all the capacitive sensors. The electronics is designed to monitor a single output voltage from the two capacitors that constitute the sensors. It enables the suppression of the effect of the cable capacitance on the readout such that the cable capacitance does not have an effect at the level of precision required of the readout. The suppression is achieved using a multi-stage feedback circuit in which the gains of amplifiers suppress the effect of the cable capacitance and permit the readout of the sensor capacitance. This is not something that could have been done using a commercial readout chip.

The sections below will explain a range of the features that appear in the final analogue circuit design as a result of this development work. The electronics that will be used in LZ to read out the capacitive sensors is then a further development of this, as part of the analogue circuit is replaced by an FPGA (field-programmable gate array). This will be explored in section 3.13 below. The development of the analogue circuit fed directly into the design of the digital electronics, so understanding this first will provide the basis for understanding the design used in LZ. The final electronics boards have eight channels per board, so each board can read up to eight capacitive sensors.

The signals are read out from the board via a TCP/IP connection that enables the signals from the electronics board to be sent to the 'slow control' system that records monitoring data.

3.5 The feedback circuit

A feedback circuit is used in the readout for the capacitive sensors and the powerful reasons for doing so will be set out below. A feedback circuit uses amplifiers that

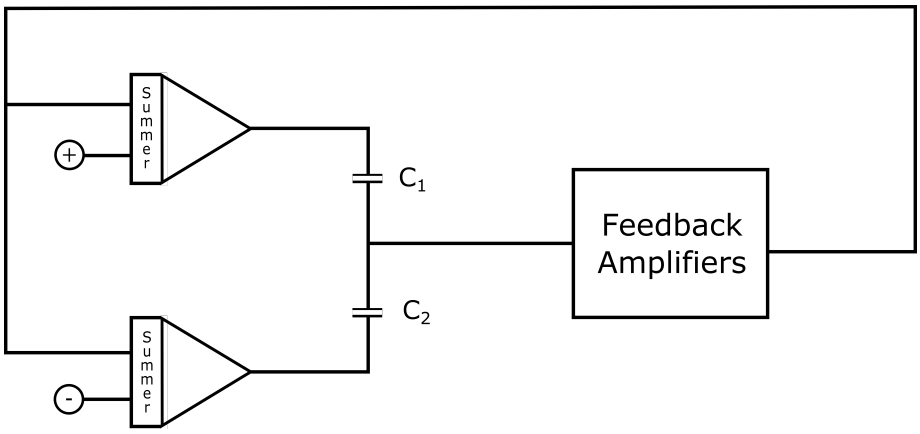


Figure 3.14: A simplified schematic of the feedback loop that forms part of the readout electronics for the capacitive sensors. The sensor consists of capacitors C_1 and C_2.

adapt their output according to the input, which is in turn dependent on the amplifier output: the output feeds back to the input. The capacitors that constitute the sensor sit within this feedback loop. Therefore, by monitoring the output of the amplifier, we can determine the behaviour of the sensor, as the amplifier output will vary according to the capacitances of the sensor. The sensor capacitances will in turn change according to the variable the sensor is designed to measure, such as position or liquid level. This section will explain in more detail how the feedback circuit works.

The essential idea can be found in [79], which discusses the readout configuration required for capacitive sensors. A simplified schematic is given in fig. 3.14. Each sensor consists of two capacitances, C_1 and C_2. Either (a) both of these capacitances can vary, as is the case with the position sensor, or (b) one can change while the other remains a 'reference' capacitor, as happens in the level sensors. In each sensor, the two capacitors share a central plate - the 'sense' plate, which picks up signals from the opposite plates on both C_1 and C_2 that carry positive and negative excitations respectively. Positive and negative fixed excitations are produced by the electronics. Then the output of the amplifiers is added to each of these to produce the positive and negative excitations that are on the outer plates of C_1 and C_2.

The inner plates of C_1 and C_2 are connected so sit at the same potential. If $C_1 = C_2$, and the potential applied to the outer plates is $\pm V$, this central plate (which may be a single plate or may be two separate but connected plates) would naturally be at ground. The potential on this shared plate is fed into the negative terminal of an op-amp (the feedback amplifier), while the positive terminal is held at ground potential.[2] An ideal op-amp brooks no potential difference between the

[2]The unity gain bandwidth of the feedback op-amp is 410 MHz.[15]

positive and negative input terminals, so will alter its output until the connected inner plate of C_1 and C_2 is at ground. The amplifier will thus alter its output until this sense plate is at ground.

The output of the feedback amplifiers is fed into two summing amplifiers - one for each capacitor in the sensor - that add the output to the fixed excitation. The excitation is an AC sine wave with a frequency of 195.3125 kHz and an amplitude of 0.7 V; see section 3.6. These are labelled in fig. 3.15 as '$+\mathrm{V_E}$' (positive) and '$-\mathrm{V_E}$' (negative) to indicate that the two capacitors receive this signal in antiphase, so that when one has 0.7 V, the other has -0.7 V. This summed signal is then what reaches the outer plates of the capacitors C_1 and C_2, creating the signal picked up by the sense plate.

This is a simplification of the process. A fuller version of the circuit can be seen in fig. 3.15 and will be explored in more depth below. The cable capacitance is the capacitance between the core of the signal cable and the grounded sheath that surrounds it. This is modelled as a parasitic capacitance on our signal wire to ground, appearing as C_C before the input to the first feedback amplifier.

3.5.1 Calculating the feedback

The readout electronics provides an output voltage that depends in a known way on the capacitances to be measured. The precise relationship between the capacitances and the output voltage can be determined by analysis of the feedback circuit. Here we will outline the calculation, which can be seen in full in appendix A.

The first step is to analyse the first stage of amplification, which takes the input voltage V_{in} to V_{FS}. This gives

$$V_{FS} = -V_{in}\frac{G}{G+1}\frac{C_I}{C_F+\frac{C_I}{G+1}}\frac{i\omega R_F(C_F+\frac{C_I}{G+1})}{1+i\omega R_F(C_F+\frac{C_I}{G+1})}\,. \tag{3.19}$$

An appropriate choice of components makes it possible to drop the high-pass filter element of eq. (3.19).

The next step is to consider the second stage, which relates V_{FS} to V_{out} via the gain N of the second stage such that $V_{out} = -NV_{FS}$. Hence, relating this to eq. (3.19),

$$V_{out} = NV_{in}\frac{1}{(1+\frac{1}{G})\frac{C_F}{C_I}+\frac{1}{G}}\,. \tag{3.20}$$

The next step is to analyse the circuit at the sense plate. The adder prior to this sums the created excitation to the output signals to generate the potentials fed to

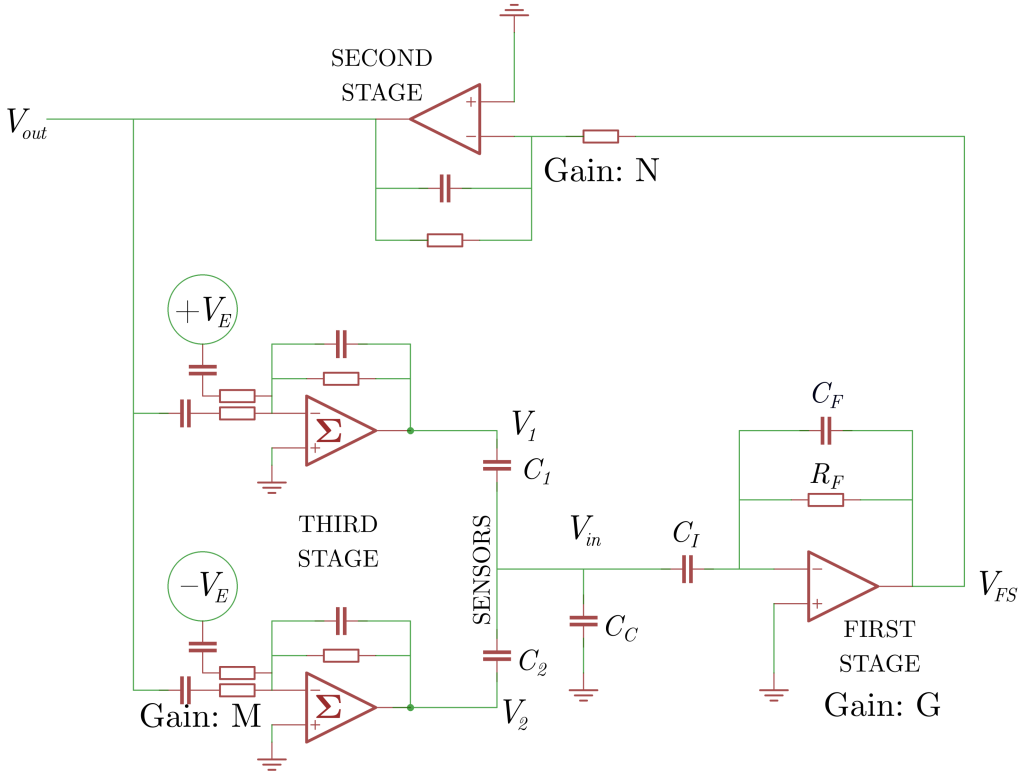


Figure 3.15: A schematic of the feedback loop including the cable capacitance as a stray capacitance to ground and showing a feedback amplifier. A more detailed schematic including component values can be found in appendix A.

the plates 1 and 2 of the sensor. The adder has a gain of M, giving:

$$V_1 = -MV_{out} - V_E \tag{3.21}$$

$$V_2 = -MV_{out} + V_E\,. \tag{3.22}$$

In combination with the previous functions, and with fig. 3.15 for reference, this analysis gives

$$V_{out}\Bigg[- M(C_1 + C_2) - \frac{1}{N}\Bigg((1+\frac{1}{G})\frac{C_F}{C_I} + \frac{1}{G}\Bigg)(C_1 + C_2 + C_C + C_I) + \frac{1}{GN}C_I\Bigg] = V_E(C_1 + C_2)\,. \tag{3.23}$$

This can be rearranged for V_{out}, which is related to the voltage recorded by the gain M' on the ADC as $V_{adc} = M'V_{out}$.

The gain G of the first stage is very large; hence $G + 1 \approx G$. Rearranging and making this substitution gives

$$V_{adc} \approx \frac{M'(C_2 - C_1)}{M(C_1 + C_2) + \frac{1}{N}\Bigg[C_F + (\frac{C_F}{C_I} + \frac{1}{G})(C_1 + C_2 + C_C)\Bigg]}V_E\,. \tag{3.24}$$

We can choose components such that the gain M' on the ADC is matched by the gain on the adder (third stage), i.e. $M' = M$. We can also choose to set $C_F \ll C_I$ such that $\frac{C_F}{C_I} \approx 0$. In addition, the three gains G, M and N are large enough that $1 + \frac{1}{MNG} \approx 1$. Using these approximations,

$$V_{adc} \approx \frac{C_2 - C_1}{C_2 + C_1 + \frac{1}{MN}(C_F + \frac{C_C}{G})}V_E\,. \tag{3.25}$$

Rewriting the gains $MN = H$ and $K = \frac{C_1+C_2}{C_F}$, the output of the readout is

$$V_{adc} \approx V_E \cdot \frac{C_2 - C_1}{C_1 + C_2} \cdot \frac{1}{1 + \frac{1}{HK}\big(1 + \frac{C_C}{C_F G}\big)} \tag{3.26}$$

where V_E is the excitation voltage, $C_{1,2}$ are the measurement capacitors, G is the gain of the first amplifier block, H is the subsequent amplifier gain, C_F is the feedback capacitance of the first amplifier stage, C_C is the capacitance of the signal cable to ground, and $K = \frac{C_1+C_2}{C_F}$.

3.5.2 Cable capacitance suppression

The feedback circuit that forms the readout electronics is designed to suppress the cable capacitance so that the cable capacitance itself and, moreover, changes in the cable capacitance do not have a significant effect on the measured output value. As a result of this, the readout scheme can be used to take data from the capacitive position and level sensors that sit at the heart of LZ, with a 13 m cable between the sensor and the readout electronics.

It is in the third part of this expression that the suppression of the cable capacitance C_C is demonstrated:

$$\frac{1}{1+\frac{1}{HK}\left(1+\frac{C_C}{C_F G}\right)}.$$

The cable capacitance appears in this as

$$\frac{C_C}{HKC_F G}.$$

What this shows is that, although the cable capacitance appears in the output voltage, it does so suppressed by a number of factors. The amplifier gains play a critical role in this suppression. The cable capacitance is initially suppressed by $C_F G$, where C_F is the capacitance of the feedback capacitor on the first stage and G is the overall gain of the first stage. By pushing this gain high, the cable capacitance is directly suppressed. As will be shown in section 3.7.1 below, the gain is dominated by the open-loop gain of the amplifier, which is estimated to be 1778 for the frequency at which the electronics operates.

The cable capacitance is then further suppressed by the factor HK, where H is the product of the second and third stage amplifier gains, and $K = \frac{C_1+C_2}{C_F}$. Because the suppression is spread across all three amplifiers, we can increase the gain of all three to contribute to the cable capacitance suppression. A typical value for H is 10. As the gains on the second and third stages are controlled by the components, these can be modified to push the gain as high as possible without inducing oscillation of the signal, as will be discussed below. However, as the gain on the third stage adder is to be chosen to match the gain in the ADC, the freedom is in choosing the components on the second stage.

The factor K contains the sum of the sensor capacitances; hence the sensor capacitances themselves contribute to the cable capacitance suppression. In this way, the sensor capacitance behaves as a gain within the feedback circuit. The larger the sensor capacitances, the larger the factor K is. Typical sensors have capacitances in the range 1 pF - 20 pF, while $C_F = 10$ pF. At the lower end of this scale, $K \sim 0.2$,

so does not improve the cable capacitance suppression. However, for larger sensors, $K \sim 4$, behaving as an additional gain suppressing the cable capacitance. The position sensors are designed such that $C_1 + C_2$ is constant; however, for the level sensors $C_1 + C_2$ varies over the range of sensor outputs, resulting in varying values for K. Nevertheless, in neither case will K become small enough that it could compromise the suppression of the cable capacitance from the amplifier gains.

The readout must work with all sensors, and they do not all have the same capacitances. As the sensor capacitance plays the role of a gain, the gain from the components in the readout electronics must be chosen to account for the largest sensor capacitance that it will be used with, in order to avoid the risk of oscillation when using a sensor with a higher capacitance.

The cables in LZ are predicted to have a total capacitance of 1.28 nF (see section 3.2), so the readout is required to suppress cable capacitances of this magnitude and to show no variation when this large capacitance varies by up to 100 pF. Figure 3.16 shows the outcome of testing the cable capacitance suppression: increasing the cable capacitance up to 1.35 nF has no systematic effect on the signal.

Nevertheless for cable capacitances well beyond that of LZ, there is some effect on the output signal. At this point the high cable capacitance begins to suppress the signal output, which is the expected behaviour from the form of the equation given in eq. (3.26). As C_C increases, $1 + \frac{1}{HK}\left(1 + \frac{C_C}{C_F G}\right)$ gets larger and so the overall output voltage gets smaller. This effect can be seen for the higher cable capacitances shown in fig. 3.16. However, for the cable capacitances that are present in LZ, the effect of the cable capacitance and any changes it undergoes is negligible. Hence this readout scheme effectively suppresses the cable capacitance and enables the use of capacitive sensors within LZ. The actual component values can be found in the descriptions of the amplifier blocks in section 3.7 below.

3.5.3 Oscillation

In a feedback circuit such as that used in the capacitive sensor readout, if the gain is greater than unity when the phase shift is $180° < \Phi < 360°$, the circuit is in a mode of positive feedback. This arises because if the signal is inverted and shifted by more than 180°, the signal will be summed with something in the same phase. If the gain is greater than unity, the signal is repeatedly amplified, reaching the amplifier's maximum. The output therefore takes the form of the signal oscillating rapidly ($\mathcal{O}$(MHz)) with large amplitude. In this state, the circuit is unusable. The 'phase margin' of the circuit describes how closely below 180° the overall phase shift is. If

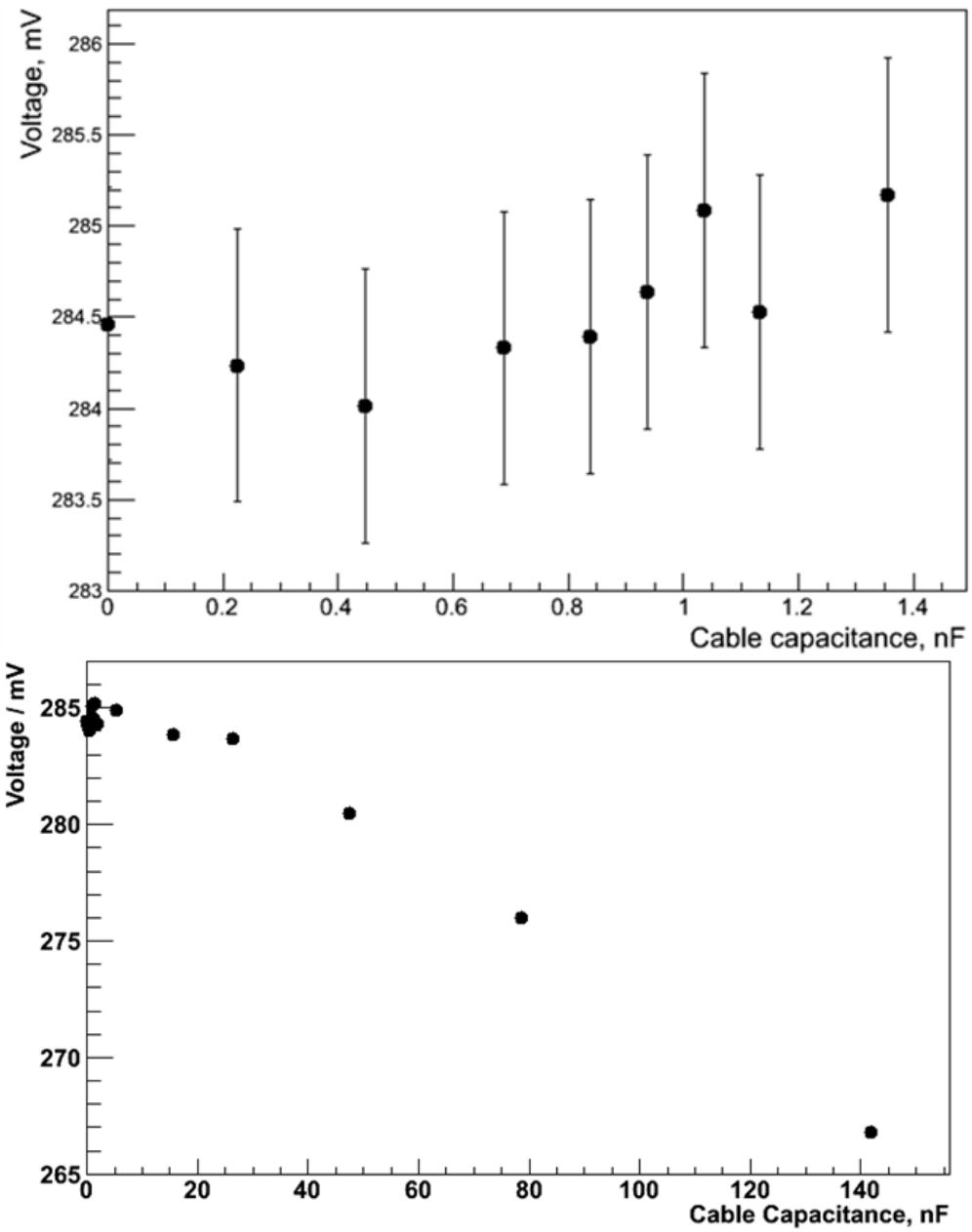


Figure 3.16: Results from an experiment to test the effect on the output of increasing the cable capacitance. A variable capacitor was connected in parallel with the cable capacitance so that the cable capacitance could effectively be altered. The output was recorded for a range of total capacitances. Top: A demonstration of the suppression of the cable capacitance. The output voltage is shown for a fixed pair of capacitors, which is a model for an unchanging capacitive sensor. For additional cable capacitances up to 1.35 nF, there is no systematic effect on the output. Bottom: If the cable capacitance is increased sufficiently, at levels well beyond those found in LZ, the signal begins to be suppressed by the enormous cable capacitances. This is the expected behaviour given the analysis of the feedback circuit.

this is too small and the gain of the feedback loop is too high, the circuit is at risk of oscillating. Hence, optimising the readout electronics is a tradeoff between optimally suppressing the capacitance of the cable carrying the sense signal and maintaining a safety margin that enables immunity to oscillation.

As discussed above, the sum of the sensor capacitances also behaves as a gain in the feedback circuit. Thus the total gain of the feedback loop is a combination of the gains on the different amplifiers and the size of the sensor capacitance. If this is too high, the circuit will oscillate. Hence the gains of the amplifiers and components must be selected with the largest sensor capacitance in mind. Otherwise, when a larger sensor is connected to the electronics, the feedback circuit could be pushed into oscillation. However, the higher the gain, the better the cable capacitance is suppressed. Finding the optimal configuration is thus a matter of pushing the gain up until the circuit is just below the point at which it would oscillate (for the sensor with the highest total capacitance). The component values presented here offer a circuit that does not oscillate under any of the conditions tested. Nevertheless, the challenge of preventing the circuit oscillating is a strong motivation for moving towards a digital readout scheme, as will be described in section 3.13 below.

3.5.4 Phase shift

Because the signals we send to and receive from the capacitive sensors are AC excitations, we have to consider the phase of the signal. This has implications both for the readout and for the circuit design.

The amplifiers can cause a phase shift in the signal, which can be problematic, as noted in section 3.5.3 above. As an example, the open-loop phase of the first stage amplifier ADA4817 can be seen in fig. 3.21. As we are using this amplifier in a configuration where the open-loop gain dominates, we can see from fig. 3.21 that we can expect a phase shift of around $-60°$ at the first stage.

The phase shift will also affect how we turn the AC readout signal into a single value of position. To do this we demodulate the readout signal. However, the point in the signal at which the sampling for demodulation occurs will affect the amplitude of the signal read out. If the signal is read out at anything other than the peak of the sine wave oscillation, it will appear artificially suppressed. To accommodate this, the software used for testing the sensors has an option to alter the phase of where it examines the signal. This can be applied until the signal appears maximised. Hence the phase shift created by the amplifiers can be accommodated in the software. In early designs, this had to be adjusted manually each time. Later on, for more stable

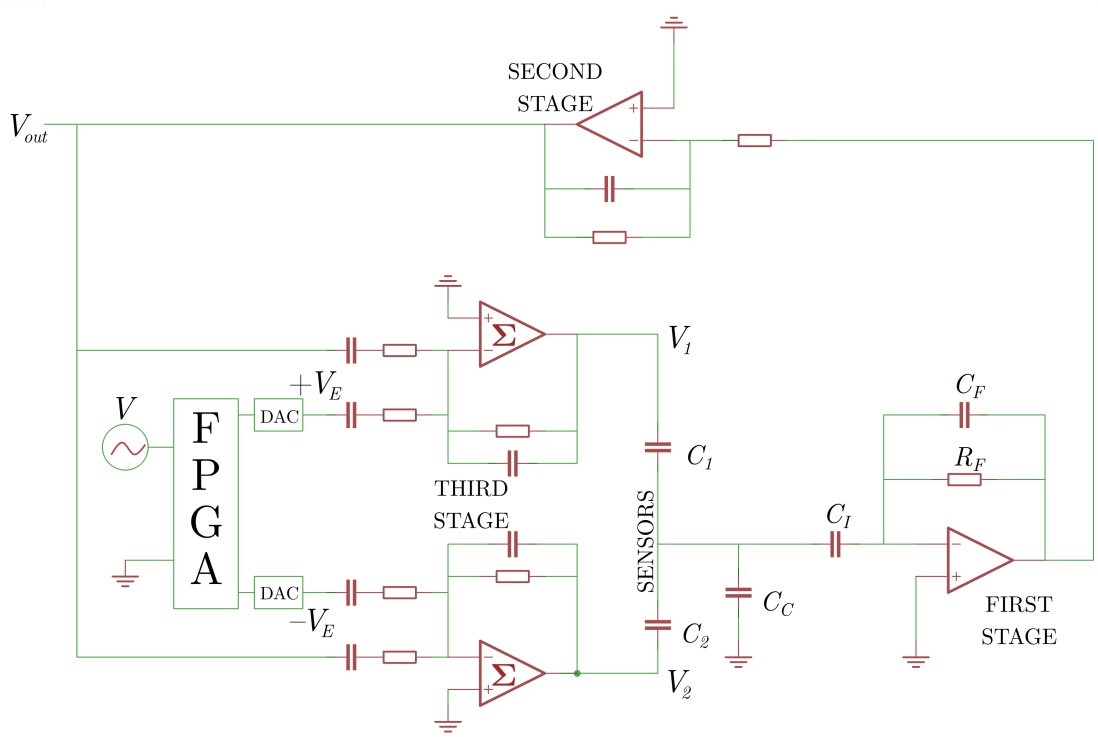


Figure 3.17: A block diagram indicating the FPGA generating the positive and negative excitations for the summer amplifiers.

configurations, the optimum phase change was found and this was pre-programmed. However significant alterations to the electronics (in terms of the components fitted) or the cable or sensor capacitance could necessitate the phase being changed to optimise the signal recorded.

3.6 The excitation

Positive and negative excitations are fed to the outer capacitor plates of the sensor. The proportion picked up by the central plate will depend on the relative capacitances of the two sensor capacitors. The excitation that is provided to the summing amplifiers prior to these plates is a sine wave oscillation with an amplitude of 0.7 V and a frequency of 195.3125 kHz. The choice of this precise excitation as most appropriate for the capacitive sensors in LZ is discussed below. The positive and negative excitations are produced by an FPGA and fed to the summers. This is shown in the block diagram in fig. 3.17.

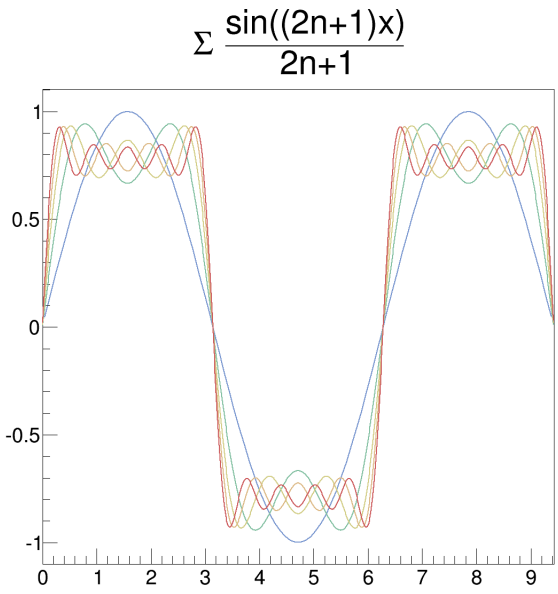


Figure 3.18: The addition of higher harmonics to an initial sine wave leads to an ever more accurate approximation of a square wave, demonstrating the high frequencies present in a square wave.

3.6.1 Excitation shape

The excitation shape used is approximately a sine wave. An alternative would be to use a square wave excitation; this was in fact employed on early versions of the circuit. (The excitations are in reality approximately sinusoidal and generated from an initial square wave.) However, a sine wave is less likely to cause interference with sensitive electrical devices outside the sensor than a square wave. While a sine wave consists only of an excitation at its fundamental frequency, a square wave is made up of many higher frequencies, not just the frequency of the final excitation. An approximation to a square wave can be produced by summing the odd harmonics of an underlying sine wave. For example, the fundamental frequency is given by $y = \sin(t)$, the third harmonic is given by $\frac{\sin(3t)}{3}$, and so on. The more terms summed, the closer the approximation to a square wave, as shown in fig. 3.18.

Consequently, a square wave excitation contains many higher frequencies that are not present in a sine wave excitation. According to Larmor's formula, the power radiated by a charge in motion is proportional to the fourth power of the frequency of that motion. Hence, assuming the movement of the charges with the signal applied, the higher frequencies present in a square wave result in significantly more power radiated, thus increasing the chance that the excitation applied to the sensors could

radiate and interfere with other aspects of the detector such as the signals in the PMTs. Avoiding the introduction of unnecessary higher frequencies by using a sine wave rather than a square wave ameliorates this potential problem.

3.6.2 Frequency

The crystal oscillator in the FPGA produces a 100 MHz clock, enabling the production of a 50 MHz signal. To bring this down, we divide by 2^n. In this case we divide by $2^8 = 256$ as this gives us a frequency in the right range, as discussed below. Hence the chosen frequency is 195.3125 kHz.

From consideration of only the sensor readout, the choice of frequency appears arbitrary. The output is proportional to

$$\frac{C_1 - C_2}{C_1 + C_2} \tag{3.27}$$

which evidently does not explicitly depend on the frequency. There are nevertheless constraints that place limits on what would be a sensible choice.

The excitation should be at a relatively high frequency, as the transfer function for the amplifier has a zero at DC, as can be seen in eq. (3.28) below. The impedance of a capacitive sensor is $Z = \frac{1}{i\omega C}$, so at low frequencies the capacitors that constitute the sensors have high impedances. If the impedance is high, the central plate of the two sensors will not be coupled very strongly to the opposite plates. Hence the central plate is likely to pick up interference from sources other than the excitations, with its potential changing according to incoming noise, rather than being strongly coupled to the rest of the circuit. As a result, it is best for the impedance of the sensors to be relatively low, which suggests a high frequency should be used.

To place some quantitative limits on this, we aim for $\frac{1}{\omega C}$ to be below 1 MΩ. With a sensor of capacitance of a few pF, this suggests the use of a frequency of around 200 kHz. However as noted in the previous subsection, higher frequencies are liable to cause more interference, as radiated power is proportional to frequency to the fourth power. Hence the frequency should not be increased above that required to keep the impedance sufficiently low. These constraints together suggest the use of a frequency of around 200 kHz, and the chosen frequency is as close to this as possible given its attainment by binary division.

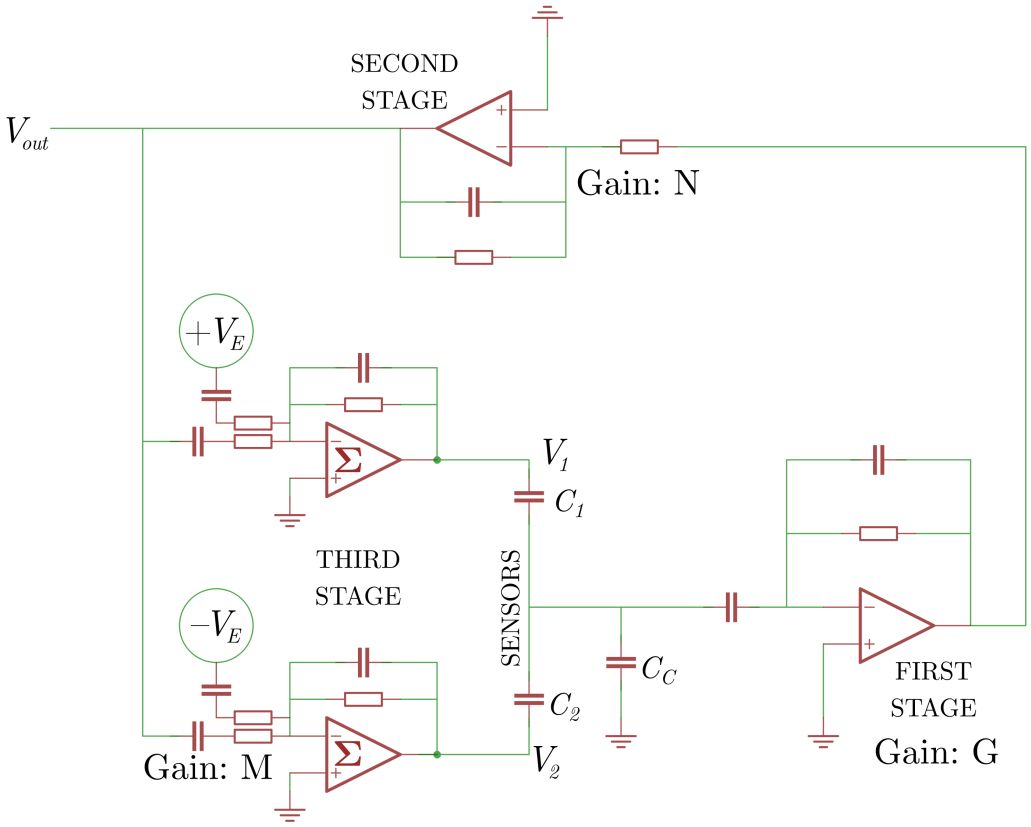


Figure 3.19: A block diagram of the amplifiers in the circuit.

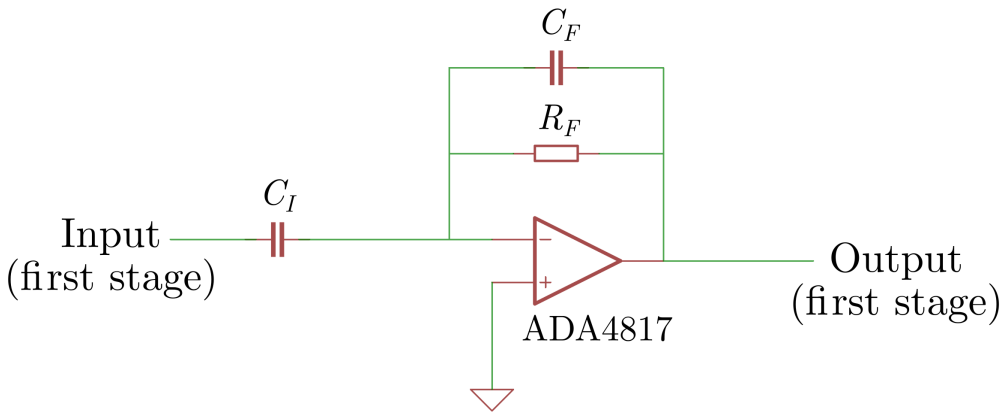


Figure 3.20: The 'first stage' amplifier. This is an ADA4817 dual amplifier.[15] The input capacitor C_I is 1 µF. The feedback loop for the amplifier contains R_F, a 10 MΩ resistor and, in parallel, C_F, a 10 pF capacitor. These feed into the negative input terminal. The positive input terminal is connected to ground. The output will go on to the second stage amplifier.

3.7 The amplifiers

In total, three feedback amplifiers are used in the circuit. This can be seen in fig. 3.19. The output signal is extracted from the feedback loop between the second and third of these. It is sent via the ADC driver to the ADC and is thus read out. This section will examine the different amplifiers used in the readout electronics and why those particular amplifiers are appropriate. The first of the three amplifiers is here called the 'first stage'; this is the first amplifier encountered by the signal from the sense plate. The second is the 'second stage'. The final amplifiers make up the 'third stage', a pair of adders which sum the fixed excitation with the output voltage from the feedback loop, the results of which are fed to the capacitive sensor as the two excitations. The three are connected in that order to create the feedback loop with the sensor capacitors, as shown in fig. 3.19. Each one will be considered in more detail below.

3.7.1 The first stage

The first stage is the first amplifier reached by the sense plate signal entering the readout electronics. The schematic for it can be seen in fig. 3.20. The transfer function of an ideal amplifier (i.e. one that has a high open-loop gain G) in this

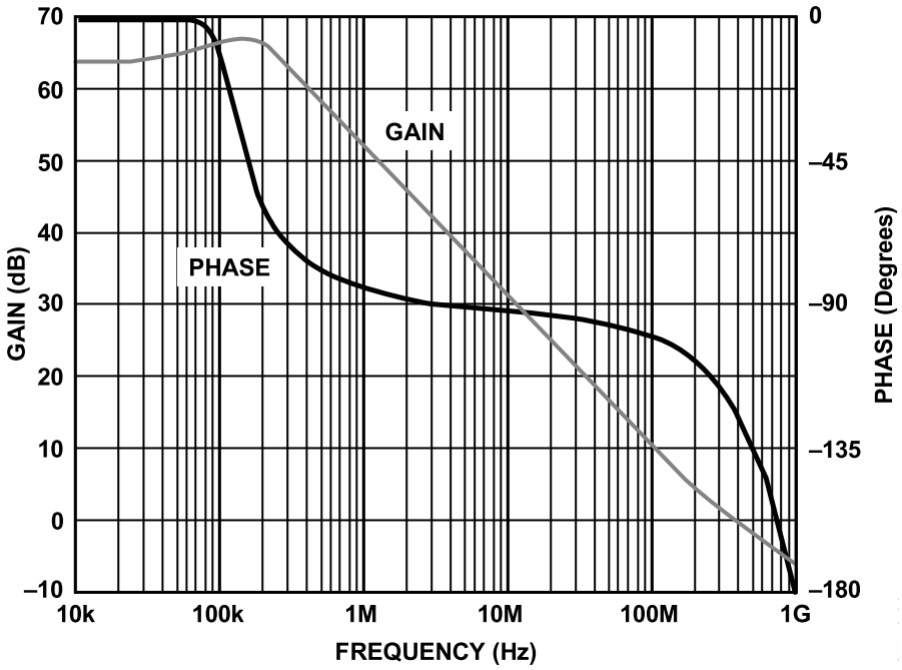


Figure 3.21: The open-loop gain and phase vs. frequency for the ADA4817. In the regime of the first stage, where $C_I/C_F = 10^5$, this gives the gain and phase of the amplifier. From [15]; permission to reproduce this figure has been granted by Analog Devices.

scenario is

$$\begin{aligned} \frac{Z_F}{Z_I} &= \frac{i\omega C_I R_F}{1 + i\omega C_F R_F} \\ &= \frac{C_I}{C_F} \frac{i\omega R_F C_F}{1 + i\omega R_F C_F} \end{aligned} \tag{3.28}$$

where C_I is the input capacitor to the amplifier, and C_F and R_F are the feedback capacitance and resistance respectively, and ω is the frequency of the oscillation. Hence the time constant for this ideal amplifier block is $R_F C_F$ and the closed-loop gain is $\frac{C_I}{C_F}$. The effect of this stage depends on the interplay between the closed-loop gain and the open-loop gain of the amplifier. As we can see from fig. 3.21, at a frequency of around 195 kHz, the open loop gain is around 65 dB. Using the '20 log rule' to convert this to voltage gain:

$$\begin{aligned} 20 \log \left(\frac{V_{out}}{V_{in}} \right) \text{dB} &= 65 \, \text{dB} \\ \left(\frac{V_{out}}{V_{in}} \right) &= 10^{3.25} \\ &= 1778 \, . \end{aligned} \tag{3.29}$$

By contrast, the closed loop gain is

$$\frac{C_I}{C_F} = \frac{1\,\mu\text{F}}{10\,\text{pF}} = 10^5\,.$$

For a general inverting amplifier, the gain is given by

$$\frac{V_O}{V_I} = -\frac{Z_F}{Z_I}\frac{G}{G+1}\frac{1}{1+\frac{1}{G+1}\frac{Z_F}{Z_I}} \tag{3.30}$$

where G is the open-loop gain. It is worth noting that the closed-loop gain is broadly independent of the open-loop gain.

For the first stage, at high frequencies (such as that of the excitation frequency), the high-pass filter element of $\frac{Z_F}{Z_I}$ can be dropped, such that it simplifies to

$$\frac{Z_F}{Z_I} = \frac{C_I}{C_F}\,. \tag{3.31}$$

Hence the gain of the first stage is given by

$$\frac{V_O}{V_I} = -\frac{C_I}{C_F}\frac{G}{G+1}\frac{1}{1+\frac{1}{G+1}\frac{C_I}{C_F}}\,. \tag{3.32}$$

To examine the interplay of the open- and closed-loop gains, one can plot the overall gain (eq. (3.32)) against $\frac{C_I}{C_F}$, as shown in fig. 3.22. At $\frac{C_I}{C_F} = 10^5$, the overall amplifier gain is clearly dominated by the contribution of the open-loop gain. Keeping the component gain high ensures this is the dominant factor in the first stage. This in turn limits the phase shift of the full feedback circuit, as will be discussed below in section 3.7.4.

The gain of the first stage is significantly higher than the gain of subsequent stages. The total gain of the circuit is the sum of the gains at each stage, irrespective of their order. However, putting the largest gain on the first stage improves the potential signal-to-noise ratio of the circuit. If the signal is amplified as much as possible early in the loop, noise added later has a smaller relative impact.

The input component to the first stage is a capacitor, while (as will be seen below) the input to the second stage is a resistor. There are two advantages to this. First, a capacitor does not create any noise on the signal, whereas a resistor would introduce noise at this early stage. (As will be explored further in section 3.9, the voltage noise from a resistor is $V_n = \sqrt{4kTR}$ and the result would then be amplified along with the signal.) Second, an input capacitor prevents any DC getting through to the rest of the circuit. Hence the sensing capacitors can sit at a different overall potential to the

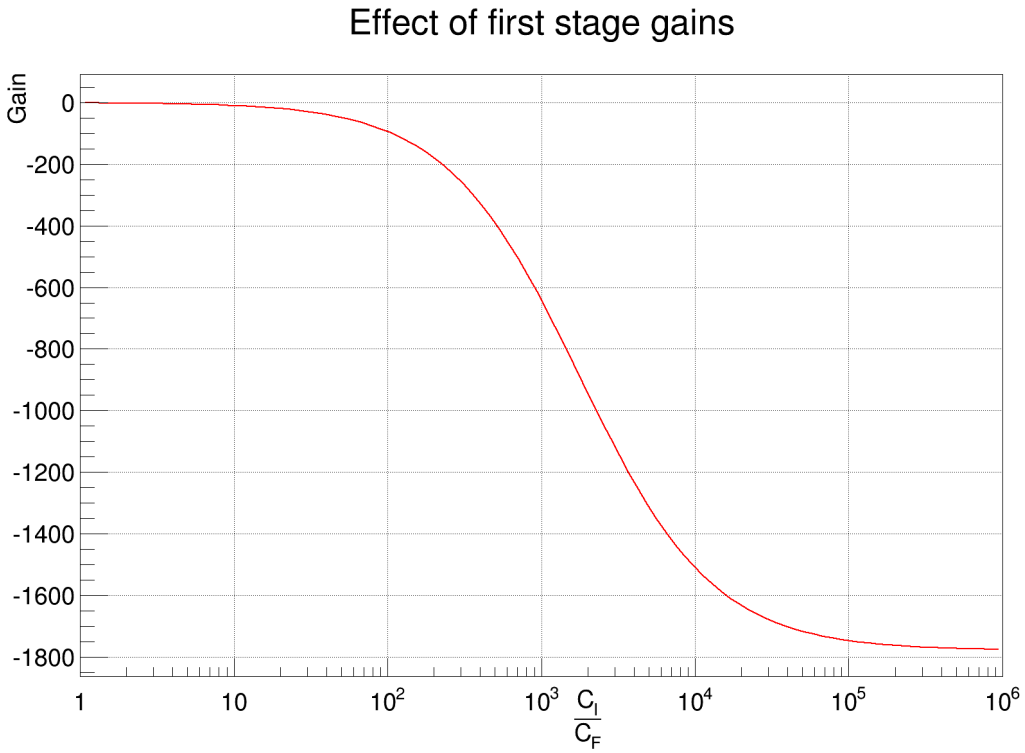


Figure 3.22: The gain of the first stage plotted against $\frac{C_I}{C_F}$. For $\frac{C_I}{C_F} = 10^5$, the gain is clearly dominated by the open-loop gain of 1778.

rest of the electronics, but the readout will only register changes in this, i.e. those caused by the application of the excitation.

The resistor in the feedback loop of the first stage amplifier provides the DC path to the input of the amplifier. This needs to be a large resistor so that it only affects the DC performance of the circuit. This necessitated the choice of an amplifier with a very small input bias current, as that current will flow through the DC path and could result in a significant voltage. For an input bias current of 1 µA and a feedback resistor of 10 MΩ, the potential produced is 10 V. This would quickly push the amplifier to its supply rail. Hence we chose the ADA4817-2 as it offers an input bias current of 2 pA, giving a potential of only 20 µV.

3.7.2 The second stage

The second stage is an inverting amplifier block, and is the second in the loop. As shown in fig. 3.23, it is an LMH6626, which is a dual ultra low noise wideband operational amplifier.[16] The two amplifiers within the dual amplifier are used by two different channels.

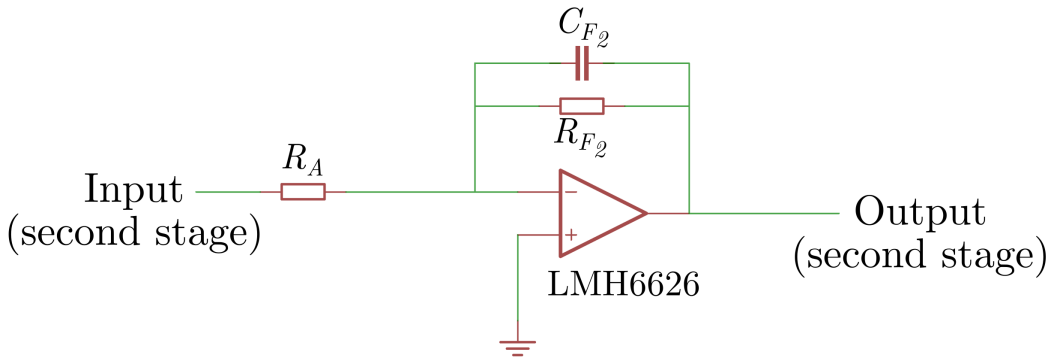


Figure 3.23: The second stage amplifier, an LMH6626.[16] The input to the stage is the output from the first stage. The input to the amplifier features an input resistor, R_A, with a value of 1 kΩ. The feedback loop contains R_{F_2}, which is a 10 kΩ resistor, and C_{F_2}, which is a 10 pF capacitor. As this is configured as an inverting amplifier, the input is to the negative (inverting) input terminal of the amplifier, with the positive input terminal held at ground.

The transfer function for the second amplifier block is

$$\frac{Z_F}{Z_I} = \frac{R_F}{R_I}\frac{1}{1+i\omega C_F R_F}\,. \tag{3.33}$$

Hence the gain of the second stage (using the components detailed in fig. 3.23) is

$$\begin{aligned} -\frac{R_F}{R_I} &= -\frac{10\,\text{k}\Omega}{1\,\text{k}\Omega} \\ &= -10\,. \end{aligned} \tag{3.34}$$

This means the signal is a factor of 10 larger when it leaves this amplifier. After this, the signal is split. One branch is fed to the two summing amplifiers (the third stage), where the fixed excitations are added to this signal (see section 3.7.3). The other branch is the extraction of the signal that constitutes the readout of the sensor, as noted above.

3.7.3 The third stage

The third and final stage features two summing amplifiers. One creates the total positive excitation to be fed to the outer plate of C_1, while the other creates the total negative excitation to be fed to the outer plate of C_2. Both use the fixed excitation voltage generated elsewhere on the board and add to it the output of the feedback loop to create the voltages applied to the capacitors. The amplifier creating the total

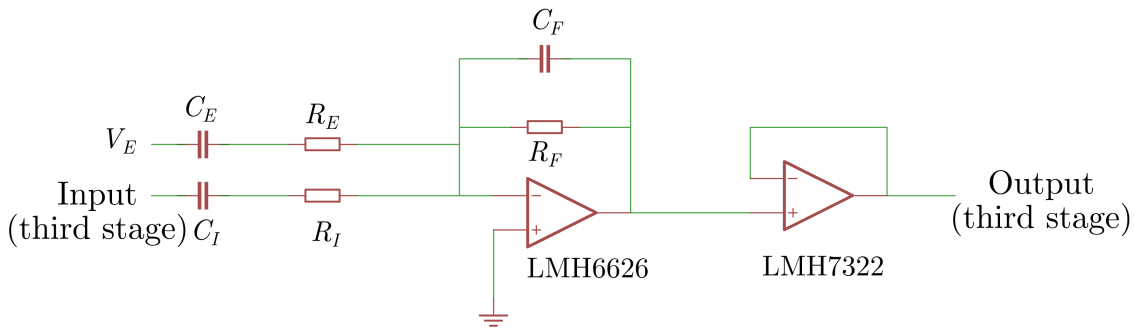


Figure 3.24: The third amplifier stage of the board, an LMH6626,[16] with the additional dual amplifier, an LM7322,[17] to separate off the large capacitive load (see section 3.10). The 'input' is the output from the second amplifier stage. This is fed via input capacitors and resistors to the negative input terminal of the op-amp. This signal is joined in the feedback loop via a capacitor and resistor by either the fixed positive excitation or the fixed negative excitation, dependent on which adder is under consideration. The positive input terminal is at ground. The output is thus the sum of the fixed excitation with the input. The component values are as follows: $C_E = 100\,\text{nF}$, $R_E = 47\,\text{k}\Omega$, $C_I = 100\,\text{nF}$, $R_I = 4.7\,\text{k}\Omega$, $C_F = 10\,\text{pF}$, $R_F = 47\,\text{k}\Omega$.

positive excitation receives the positive fixed excitation while the amplifier creating the total negative excitation receives the inverse, i.e. the negative fixed excitation. Hence the positive plate of the sensing capacitors carries $V_E + V_{out}$ and the negative plate carries $-V_E + V_{out}$.

The adder amplifier is also an LMH6626, the same as the second stage. The configuration in the readout electronics can be seen in fig. 3.24. The output of the third stage goes through a voltage follower amplifier (described in section 3.10 below), before being sent to the excitation plates of the sensing capacitors.

3.7.4 Three stages of amplifiers

All three stages of amplification use inverting amplifiers. (This is clear from the fact that in each case the signal enters the amplifier on the negative input terminal.) Using inverting op-amps in the feedback circuit is useful to keep the transfer function simple; although the same could have been done with non-inverting op-amps the analysis would have been more complicated.

For a negative feedback circuit, a single inversion of the signal is needed, or else positive feedback would occur. This was discussed above in section 3.5.3. The circuit must therefore have an odd number of inverting amplifiers. Due to the limited gain-bandwidth products of real op-amps, good practice in electronics design is to use

multiple stages, each with a lower gain, in order to maintain a high bandwidth, which ensures better phase stability.

In order to limit the possibility of problems arising from phase shifts, the gains of the amplifiers are chosen such that the first stage is dominated by its open-loop gain while the later stages are limited by their closed-loop gain, imposed by the components in the amplifier blocks. As a result, the first stage provides a dominant pole, which ensures the phase shift is minimised. If the amplifier gain is component-limited, the gain roll-off is pushed to a higher frequency than the corner frequency for the open-loop gain. If this were applied to all three amplifiers, there would be no dominant pole, but three poles that each introduce a phase shift of $-90°$. If this happens while the gain is still above unity, the feedback circuit would oscillate. By introducing a dominant pole, the roll-off begins at a lower frequency, but this ensures the gain is below unity by the time the higher-frequency poles are reached.

3.8 Crosstalk

Eight channels occupy the same board and every channel must run independently of the others. The eight channels can be seen in fig. 3.25. Nevertheless, all channels on one board share the same ground plane inside the board. Any change in the potential of this plane can therefore affect all of the channels; the excellent sensitivity of the combination of the readout and sensor is such that just such minor potential shifts were noted in an early electronics design. If current is pushed to ground by components, there can be a potential difference across the ground plane that is picked up by other channels. This results in crosstalk between the channels: when one channel has a large signal, it pushes current to the ground plane and changes the ground level of the other channels, leading to spurious signals in other channels as a result of a true signal in the first.

The early version of the circuit had a resistor to ground from some of the amplifiers and feedback loops, which, although intended to provide DC paths to ground, led to just this sort of unacceptable crosstalk. In the final version, these resistors were removed as often as possible, with the intention of having nothing with a low impedance connection to ground. However, the ADC driver requires a connection via a resistor to ground. To facilitate this without ground return, we introduced a buffer amplifier providing the ground for this connection; see fig. 3.26.

The input impedance of an ideal amplifier is infinite, i.e. no current flows in, and the potential difference between the two inputs is zero. The differential amplifier

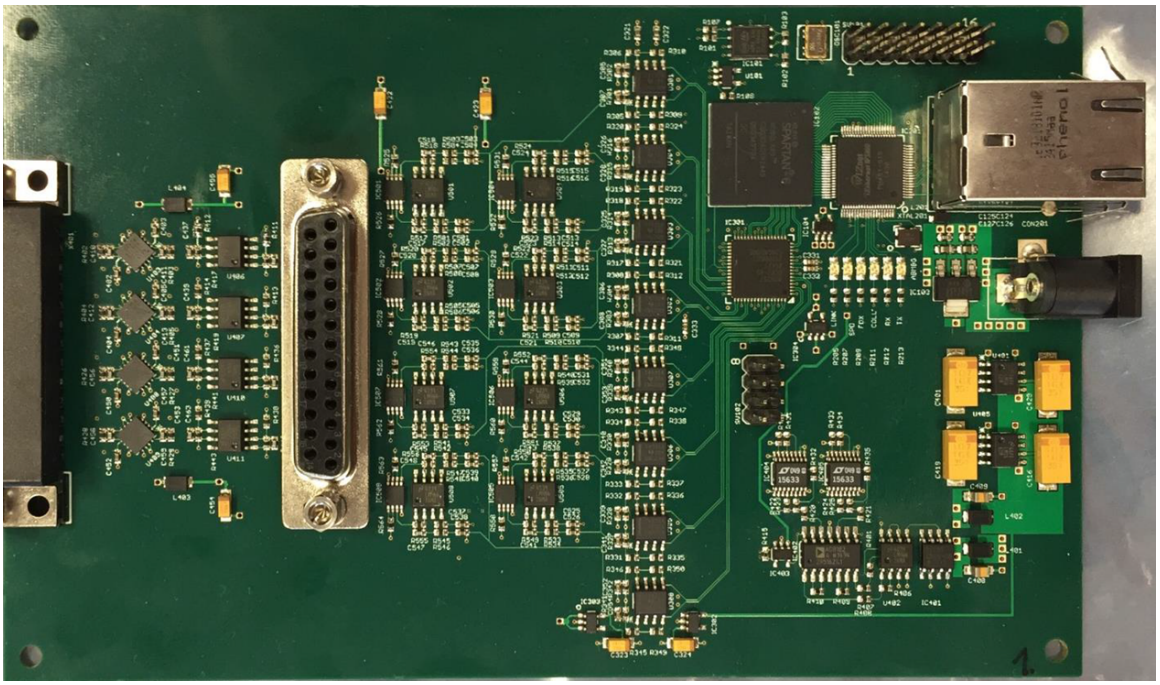


Figure 3.25: The eight channel analogue electronic readout board. Dual amplifiers are used for the first and second stages, so only four are required to run eight channels. These are visible on the left hand side of this image. Each channel uses a single dual amplifier for its two adders that constitute the third stage. These are seen in two rows near the centre of the board.

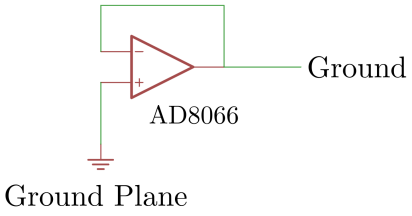


Figure 3.26: The buffer (differential amplifier) that provides a ground without connecting a low impedance source to the ground plane. This helps to prevent crosstalk between channels. The amplifier is an AD8066, a high speed, high slew rate FET input amplifier, with excellent small-signal gain flatness up to frequencies of 10 MHz for a gain of 0 dB.[18]

used as the buffer amplifier (AD8066) is a dual amplifier with an input impedance of 1000 GΩ.[18] It is configured as a voltage follower, meaning that the output should be the same as the input, modulo the amplifier's input offset voltage, which, while zero for ideal amplifiers, can be up to 1.5 mV for the AD8066.[18] The positive input is at ground (i.e. connected to the ground plane). Given that an op-amp aims to have the two inputs at the same potential, the output will be such that the second input is also at ground, with the result that the output will also be at ground. However this ground is created by drawing on the supply rail voltages that are given to the op-amp, rather than drawing it from the ground plane. Hence current is neither drawn from or pushed to the ground plane to provide ground to the ADC driver. The op-amp has only a high impedance connection to the ground plane, as the ground plane is connected to one of the input terminals. This ground is sampled near the early stages of the circuit to ensure the ground used is as uniform as possible across the board. The result of this reconfiguring to have only high impedance connections to the ground plane is the elimination of cross-talk between channels, as demonstrated below.

3.8.1 Results

We can demonstrate that there is no crosstalk between channels using one channel with a varying signal (with input from e.g. a position sensor) and one channel with a fixed signal (with input from a pair of fixed commercial capacitors). The results of this test can be seen in fig. 3.27. The changing readout of the position sensor, from around +250 ADC counts to −250 ADC counts, has no bearing on the readout of the fixed capacitors, which varies by just over 0.1%, irrespective of the signal in the other channel.

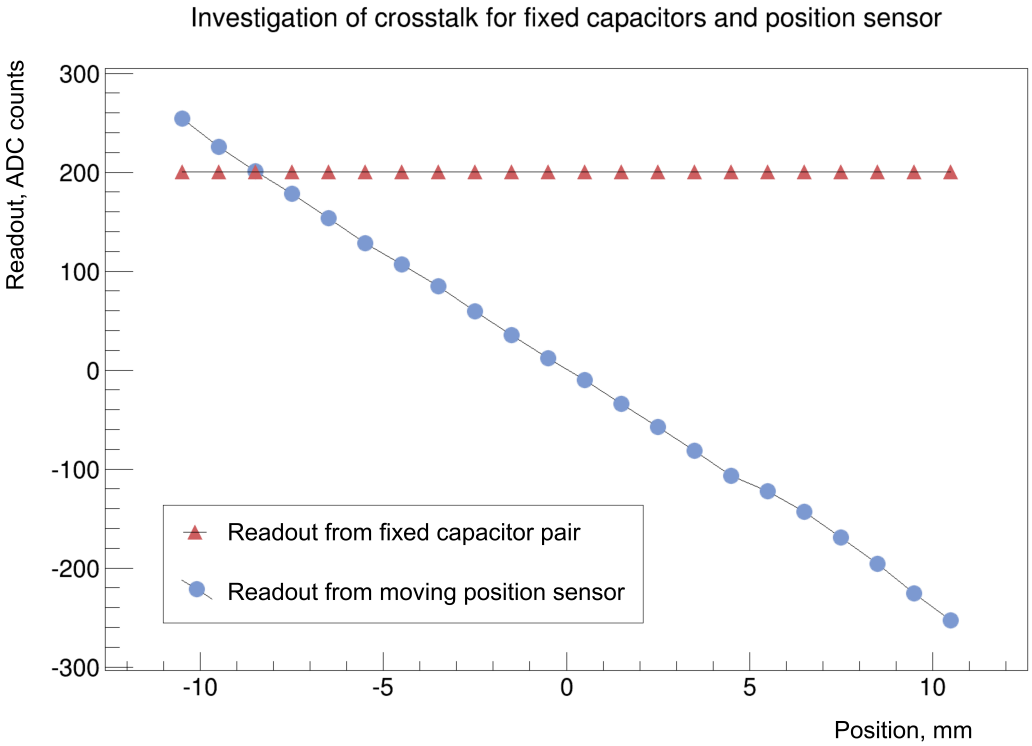


Figure 3.27: A plot showing that there is no crosstalk between different channels on the electronics. The red triangles show the readout from one channel of the electronics, into which was input the signal from a pair of fixed capacitors. The blue circles show the readout from an adjacent channel on the electronics, into which was input a position sensor that moved over a range of 21 mm and accordingly changed its output. If there had been crosstalk between the channels, the varying position sensor signal (blue) would have affected the signal measured for the fixed capacitors (red). As this was not seen, there is no crosstalk between channels. The predicted value of the fixed capacitor channel was 200 ADC counts; the measurement is consistent with this within expected component value variations.

3.9 Noise

There will be some noise present on our signal as a result of the electronics and the cables connecting the sensor. In particular, the large cable capacitance will have an effect on the noise from the feedback amplifiers. Nevertheless, components can be carefully chosen and the signal can be filtered to reduce the noise as much as possible.

3.9.1 Filtering

In order to improve the signal-to-noise ratio, the outgoing signal can be filtered using a digital filter to reduce the appearance of signals at frequencies other than the known excitation frequency. To achieve this, the FPGA in the digital electronics (described below in section 3.13) features a second order bandpass filter centred at 195.3 kHz, with a 30 kHz width. This filters out many unwanted frequencies that are in addition to the excitation, which will include much of the noise.

3.9.2 Noise from the electronics

In section 3.5.2, it was shown that the output signal is practically independent of cable capacitance. Nevertheless, there is a possible contribution to the noise which will ultimately limit the length of cable by reducing the signal-to-noise ratio to unworkable values.

Thermal noise in electronics is caused by the thermal agitation of charge carriers in a conductor, and will be present for all passive resistive components such as resistors and inductors. Amplifiers feature both current noise sources and voltage noise sources. Many of the effects of noise can be reduced by averaging the signal (as is done in the digital electronics discussed below). This is particularly effective when the noise comes from a number of independent sources. Nevertheless it is important to know and understand how noise affects the signal reading, and what we can do to minimise it.

The capacitance of the cable carrying the signal, labelled as C_C in fig. 3.28, will affect the noise of the feedback circuit. In addition to the usual components (the feedback resistor R_F and the feedback capacitor C_F), there is a current noise source I_P just prior to the amplifier, a voltage noise source V_S at the positive terminal of the amplifier, and a voltage noise source V_F to account for the thermal noise of the resistor R_F. The input capacitor C_I is not included as capacitors do not inherently produce noise.

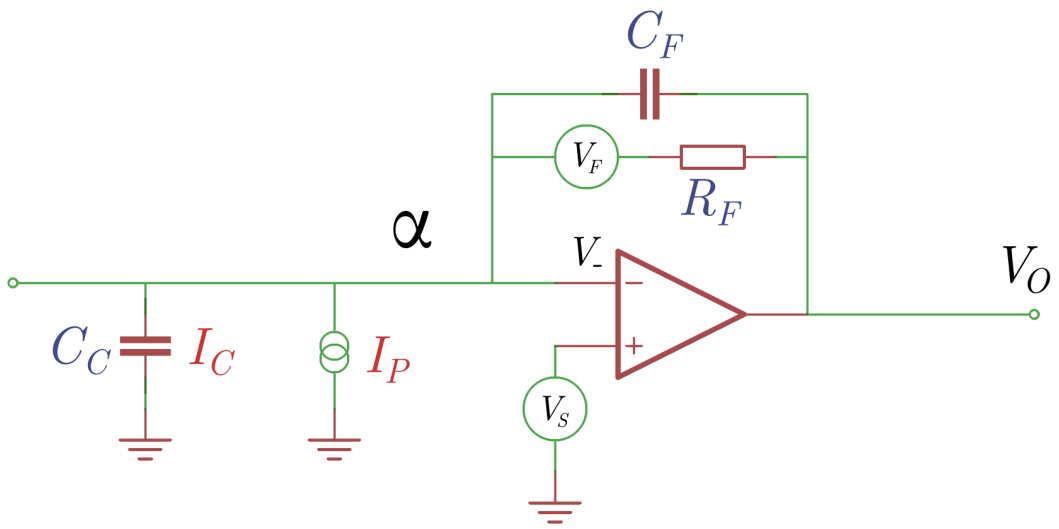


Figure 3.28: Diagram of noise sources at input to feedback loop, for calculation of noise dependence on cable capacitance

The terminals of an ideal amplifier must be at the same potential. The voltage noise source determines the potential of the positive input terminal to be V_S, so the negative input terminal will have the same potential:

$$V_+ = V_S \tag{3.35}$$

$$V_- = V_S\,. \tag{3.36}$$

Consider the currents flowing in and out of the point marked α in fig. 3.28:

$$I_{R_F} + I_{C_F} = I_P + I_C \tag{3.37}$$

where I_C is the current flowing through the cable capacitance, I_P is the current noise of the amplifier, and I_{C_F} and I_{R_F} are the currents flowing through the two branches of the feedback loop. Hence

$$\frac{V_O - V_F - V_-}{R_F} + \frac{V_O - V_-}{Z_{C_F}} = I_P + \frac{V_-}{Z_{C_C}} \tag{3.38}$$

$$\frac{V_O - V_F - V_S}{R_F} + (V_O - V_S) i\omega C_F = I_P + V_S(i\omega C_C)\,. \tag{3.39}$$

Rearranging for V_O gives

$$V_O = \frac{V_F + R_F I_P}{1 + i\omega C_F R_F} + V_S\left(1 + \frac{C_C}{C_F}\frac{i\omega C_F R_F}{1 + i\omega C_F R_F}\right). \tag{3.40}$$

Thus the cable capacitance increases the noise on the signal from the input voltage noise associated with the amplifier. If the cable capacitance is zero, the second term in eq. (3.40) is just V_S; the larger C_C is, the larger that term becomes.

The first stage amplifier is a low noise op-amp (ADA4817-2), which has voltage noise V_S of $4\,\mathrm{nV}/\sqrt{\mathrm{Hz}}$.[15] The cable capacitance is around 1 nF and the feedback capacitance is 10 pF, giving a factor of $\frac{C_C}{C_F} = \frac{1.2\,\mathrm{nF}}{10\,\mathrm{pF}} = 120$. Hence the contribution to the noise on the output signal resulting from the non-zero cable capacitance is

$$V_{C_C} = 480\,\mathrm{nV}/\sqrt{\mathrm{Hz}}\,. \tag{3.41}$$

This should be compared to the sources of noise in the first term of eq. (3.40). The root mean square noise of a resistor is

$$V_n = \sqrt{4kTR} \tag{3.42}$$

where k is the Boltzmann constant ($1.38 \times 10^{-23}\,\mathrm{J/K}$), T is the absolute temperature in Kelvin and R is the resistance of the conductor in ohms. Hence the noise contribution from the feedback resistor is

$$\begin{aligned} V_F &= \sqrt{4 \times 1.38 \times 10^{-23}\,\mathrm{J/K} \times 300\,\mathrm{K} \times 10\,\mathrm{M\Omega}} \\ &= \sqrt{1.656 \times 10^{-13}}\mathrm{V}/\sqrt{\mathrm{Hz}} \\ &= 407\,\mathrm{nV}/\sqrt{\mathrm{Hz}}\,. \end{aligned} \tag{3.43}$$

The current noise of the op-amp is given as $2.5\,\mathrm{fA}/\sqrt{\mathrm{Hz}}$.[15] Hence

$$\begin{aligned} R_F I_P &= 10\,\mathrm{M\Omega} \times 2.5\,\mathrm{fA}/\sqrt{\mathrm{Hz}} \\ &= 25\,\mathrm{nV}/\sqrt{\mathrm{Hz}}\,. \end{aligned} \tag{3.44}$$

Considering the first term of eq. (3.40),

$$1 \ll i\omega C_F R_C$$

so the first term becomes

$$\frac{V_F + R_F I_P}{i\omega C_F R_F} \equiv V_f\,.$$

Using the noise values determined above, this becomes

$$\begin{aligned} V_f &= \frac{432\,\mathrm{nV}/\sqrt{\mathrm{Hz}}}{2\pi \times 195.3125\,\mathrm{kHz} \times 10\,\mathrm{pF} \times 10\,\mathrm{M\Omega}} \\ &= \frac{432\,\mathrm{nV}/\sqrt{\mathrm{Hz}}}{123} \\ &= 3.5\,\mathrm{nV}/\sqrt{\mathrm{Hz}}\,. \end{aligned} \tag{3.45}$$

The total noise from these sources will be

$$\begin{aligned} V_n &= \sqrt{V_f^2 + V_{C_C}^2} \\ &= \sqrt{3.5^2 + 480^2}\mathrm{nV}/\sqrt{\mathrm{Hz}} \\ &= 480.013\,\mathrm{nV}/\sqrt{\mathrm{Hz}}\,. \end{aligned} \tag{3.46}$$

In order to understand the implications of this noise, it must be compared to the signal size. First, consider a wide band, 1 MHz. Then

$$\begin{aligned} V_n' &= 480.013\,\mathrm{nV}/\sqrt{\mathrm{Hz}} \times \sqrt{1\,\mathrm{MHz}} \\ &= 480\,\mu\mathrm{V} = 0.48\,\mathrm{mV}\,. \end{aligned} \tag{3.47}$$

The full-scale signal is

$$0.7\,\mathrm{V} \times \frac{2}{\pi} = 0.45\,\mathrm{V}\,. \tag{3.48}$$

So the noise represents 0.11% of the full range when considering a wide band. However, on the electronics is implemented a band pass filter that is 30 kHz wide. This leads to a noise of

$$\begin{aligned} V_n' &= 480.013\,\mathrm{nV}/\sqrt{\mathrm{Hz}} \times \sqrt{30\,\mathrm{kHz}} \\ &= 83\,\mu\mathrm{V} = 0.08\,\mathrm{mV}\,. \end{aligned} \tag{3.49}$$

This is to be compared to the size of the signal, for which the full scale is 0.45 V. Hence the noise contribution as a result of the cable capacitance does not exceed a signal-to-noise ratio of 5000:1, which is tolerable. Thus, although the large cable capacitance does affect the noise contribution of the amplifier in the feedback circuit, it is at a level that will not cause problems given the bandpass filter implemented on the electronics. Moreover, although this noise on the electronics represents an error of $\sim 0.02\%$ on the position reading, which would correspond to approximately 5 µm, this is subdominant to the sensor error introduced by the cooling of the apparatus, as discussed in section 4.5.2.2 below.

3.9.3 Noise from the cables

In addition to the noise on the electronics discussed above, the cable will introduce further noise, three types of which will be considered here. Nevertheless none of them is a dominant source of noise on our signal.

The first to examine is the thermal noise that arises as a result of the cable resistance. This is the same type of noise analysed in the previous section, but this time arises from the non-ideal nature of the cable, rather than from an intended

component. The cable has a nominal linear resistance of $3512\,\Omega/100\,\mathrm{m}$, which gives $457\,\Omega$ for our length of cable. The maximum noise due to this is

$$\begin{aligned} V_n &= \sqrt{4kTR} \\ &= \sqrt{4 \times 1.38 \times 10^{-23}\,\mathrm{J/K} \times 300\,\mathrm{K} \times 457\,\Omega} \\ &= \sqrt{7.6 \times 10^{-18}}V \\ &= 2.8\,\mathrm{nV}/\sqrt{\mathrm{Hz}}\,. \end{aligned} \tag{3.50}$$

This is a small contribution, and will be even smaller at lower temperatures, i.e. while the experiment is running.

The second additional cable noise source is current noise from 'microphonic' effects. As the cable cools, its capacitance will change, and this change will provide a source of noise:

$$I_n = V\frac{dC}{dt}\,. \tag{3.51}$$

Hence this noise is proportional to the rate of change of capacitance. As the cooling of LZ will be very gradual (over a number of days), the small, expected capacitance change of the cables will also be slow, so this will not pose a significant additional noise source.

The third cable noise source to discuss results from the triboelectric effect, which causes signal generation within the cable. When two different materials come into frictional contact, an exchange of charge can occur. This can result in discharges between the two materials that do not occur in a controlled fashion. As LZ cools, the cables will cool and shrink. Because the extruded FEP layer within the cable will shrink more along its length than the copper core or braided copper sheath, there will be friction between the core and insulation, and the insulation and sheath. This can result in the transfer of negative charge to the polypropylene from the copper, and the discharges from this will provide signal noise. The insulation is estimated to shrink by around 140 mm more than the core over the length of the cable. This noise is expected to only occur during cooldown, so will only affect the position sensors. Moreover, it will appear sporadically, so the averaging of the signal will greatly reduce its effect.

We have considered a range of noise sources that could affect our signal. Those that result directly from the cable are relatively small and do not cause concern. The voltage noise from the amplifier is amplified by the large cable capacitance, but the overall signal-to-noise ratio remains acceptable. Finally, the digital electronics (as

discussed in section 3.13) averages readout signals over one period of the excitation, and much of the noise will be reduced in this process.

3.10 Isolation of amplifiers

The long cables that connect the sensor capacitors to the readout electronics have, as noted above, a large capacitance, on the order of 1 nF. Although in developing the feedback circuit we focused on the effect of the capacitance of the signal cable (as this would potentially affect the signal readout), the excitation cables will have the same large capacitance. Although this does not directly change the excitation, there is scope for it to affect the third stage amplifier's ability to respond if the large capacitance is connected directly to the output of the amplifier.

The impedance of a capacitor is $Z = \frac{1}{i\omega C}$, so at high frequencies, capacitors have a low impedance. Hence a large capacitive load will draw a large current from the amplifier. A large capacitor also requires a very high output voltage, as the voltage charges the capacitor. Charging the large capacitance of the cable before the amplifier gets feedback can result in phase shifts of the signal and hence oscillation of the feedback circuit.

To combat this, an additional voltage follower amplifier is introduced after the third stage to isolate the internals of the feedback circuit from what we connect on the outside, namely the excitation cables and sensing capacitors. This can be seen in fig. 3.24. The amplifier chosen is an LM7322, which is a high-output current and unlimited capacitive load operational amplifier.[17] It is thus well placed to send excitation signals to the sensing capacitors via the long cables.

3.11 Power supply

The electronics uses a linear power supply to provide the required voltage to the amplifiers. In contrast, early designs of the electronics used switch-mode power supplies. However, variation in the supply voltage owing to the switching interfered with the output signal: the same double-peaked waveform with a period of around 32 ms could be seen on both the voltage output from the power supply and the signal. This is shown in fig. 3.29 and fig. 3.30. As a result, the final design uses a linear power supply to avoid this source of interference.

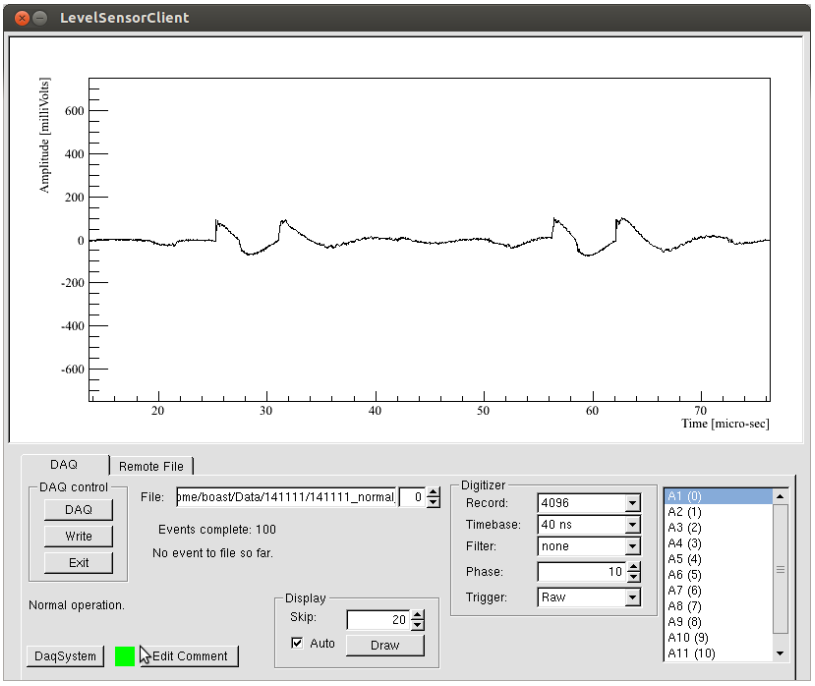


Figure 3.29: The interference from the switching power supply



Figure 3.30: The output from the switching power supply

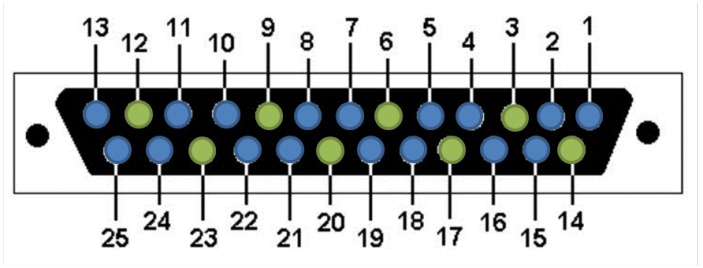
3.12 Shielding and connectors

In this section, we will explore the opportunities for shielding the sensors' signals, from the sensors themselves, through the connectors, to the electronics and on the board itself. Shielding the signal from both external influences and interference by the sensor excitations is of paramount importance. Without sufficient shielding, the signal cable can pick up interference from any nearby emitters. This will produce noise on the signal and could also cause the signal to have longer term deviations from the true value. This is particularly likely to be caused by pick-up of additional excitation voltage owing to interference between the excitation and signal once it has left the sensing capacitor plates. Moreover, any additional interference of this sort will not be filtered out - it will just distort the sensor readings.

Coaxial cables are used for the signal and excitations, ensuring that the core carrying the signal is surrounded by a grounded sheath. This limits leakage of the excitation into other systems and protects the signal from interference. In many designs of the sensors, including those used in the system test described in section 4.5, coaxial connectors to the sensors were also used to maintain this ground surrounding the signal. Some prototype connections to the electronics did not use coaxial connectors so failed to maintain the ground around the signal, which led to unacceptable interference.

Design constraints imposed by LZ mean that the final sensor does not in fact use coaxial connectors at either end of the cables. There are two main reasons that commercial, coaxial connectors cannot be used in the xenon space of LZ. All connectors examined featured materials that would present too high a background contribution. These were generally spring materials in the clip of the connector receptacle that would accept the pin from the other half of the connector. Secondly, these connectors mostly have complicated internal structures that could provide spaces for xenon to become trapped. In order to maintain purity, the xenon must be continuously cycled through the detector and purification systems. Trapped volumes are thus to be avoided. Together, these considerations counted strongly against using commercial coaxial connectors. It could have been possible to design and create our own coaxial connectors in-house, but they would have been costly to produce, as they would have been small and potentially complicated.

As a result, coaxial connectors are not used for the connection of the cable to the sensor. Instead, there are two single signal pins inserted into receptacles beside each other, mounted on a PCB base. The pins and receptacles are the same as those used



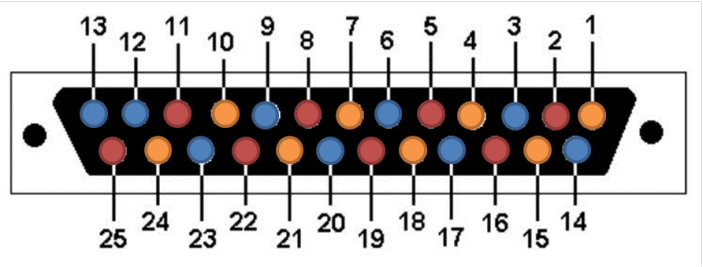


Figure 3.31: The pinout for the DB25 connectors for the capacitive sensors.

for the PMTs, which reduces the component count in LZ. It also ensures that the pins and receptacles we use meet the required standard of radiopurity for use in LZ.

The feedthroughs that carry the signals from the xenon space to vacuum and then to air are fitted with DB25-type connectors. These consist of 25 single pins so are again not coaxial. However, the potential detriment this poses is mitigated by ensuring the pin-out design for these connectors minimises interference and cross-talk between channels by surrounding each signal pin with a set of ground pins. This design can be seen in fig. 3.31. There is one DB25 for the capacitor sensor signal connectors and a separate one for the excitations to minimise pick-up of the excitations by the signal wires at this stage. The connector for the excitations follows a similar pattern to that of the signals but can do so with fewer ground pins. This allows the carrying of 16 excitations plus shielding on a single DB25. The excitation pin-out is far less critical as the potentials are driven and thus are not subject to interference in the same way as the sensor signals.

Unwanted interference on the board can also be limited by physically separating the sensitive signal connector from the emitting components on the board. Some early boards with multiple channels placed the signal and excitation connections too close together, which resulted in additional interference between the excitation and signal. In the final design this is mitigated by using two separate DB25 connectors, one for the signals and one for the excitations, that are physically apart from each other on the board. Furthermore, the components on the board that are liable to emit radiation that could interfere with the signal are placed at the other end of the

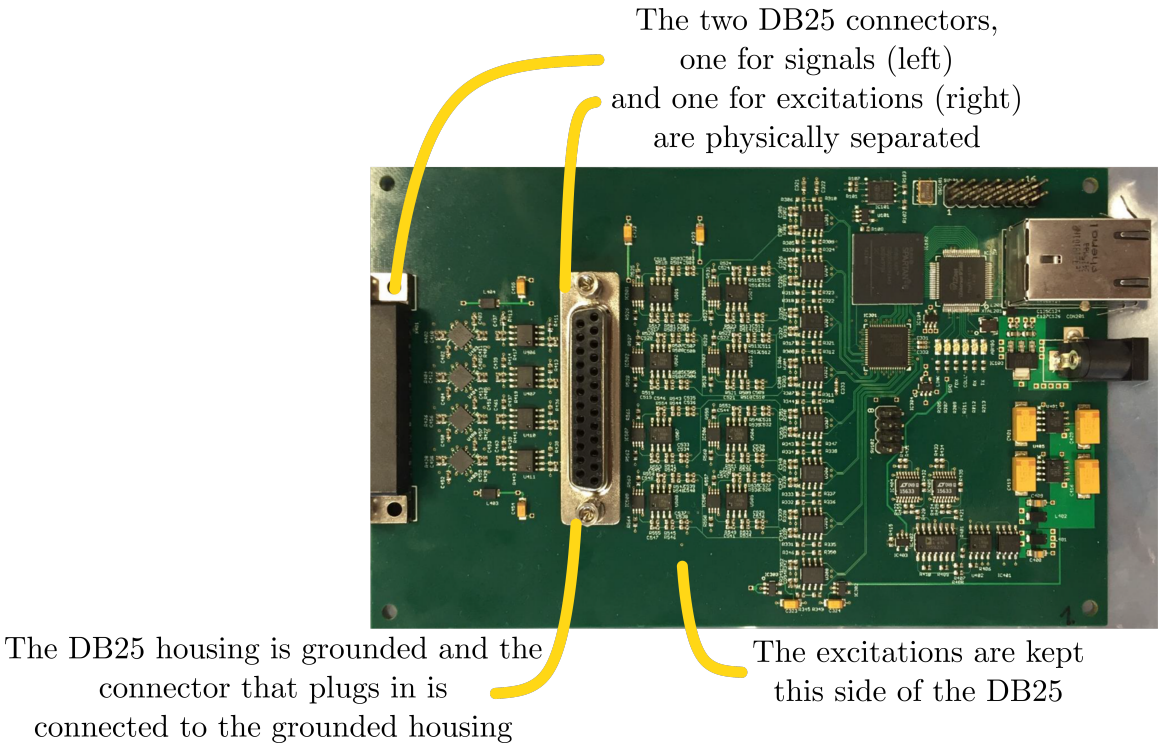


Figure 3.32: The eight channel electronics board, with features to ensure the signals do not experience interference from the excitations or other external sources.

board from the signal connector. Finally, it is important to ensure that the shell of the DB25 connector is grounded, as this does not automatically happen but without it the signals are susceptible to interference. In conclusion, there are many strategies that can be adopted to ensure that the signals are well shielded. These have been optimised on the capacitive sensor readout, within the constraints imposed by the LZ detector requirements.

3.13 Digital electronics

Although all of the above has been discussed in terms of analogue electronics, the same overall outcome can be achieved using digital electronics. Indeed, the readout for the capacitive sensors in LZ will use the digital electronics discussed below. In this section we will describe how this functions before exploring some of the advantages of using a digital readout for the capacitive sensors in LZ.

The effect of reading out the difference of capacitances while unaffected by the cable capacitance is possible via the judicious programming of a field-programmable gate array (FPGA). The first stage of the feedback loop discussed above is still present and remains analogue, with the same amplifier and set-up as described in section 3.7.1;

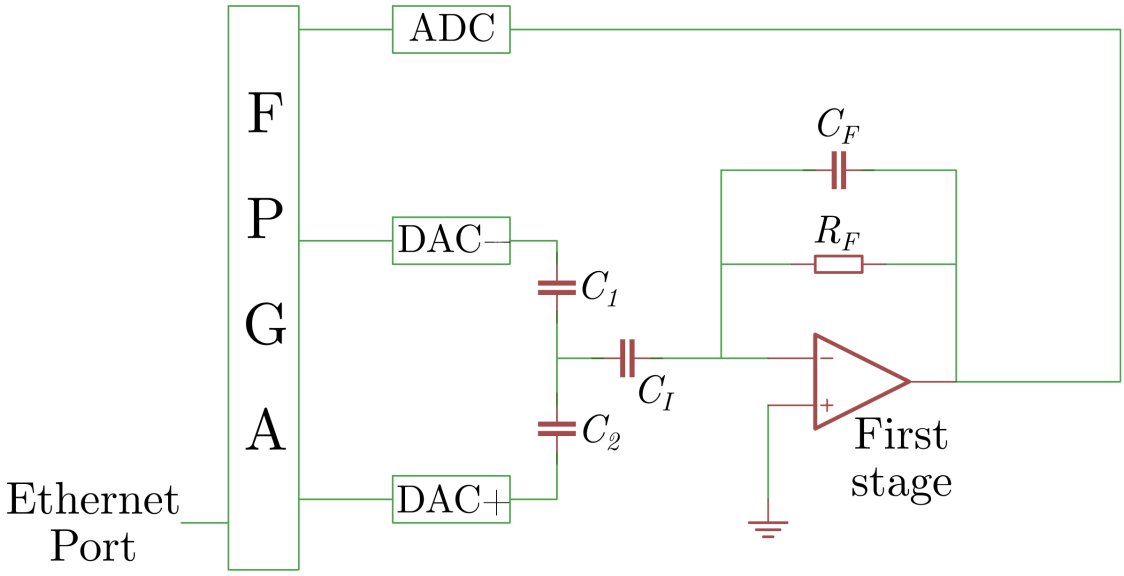


Figure 3.33: A block diagram of the digital electronics feedback loop.

however, beyond that, the feedback circuit is constructed digitally. This be seen in fig. 3.33.

The FPGA interfaced to the ADC reads in the sense signal, emits a sensor value and creates the excitation potentials to send to the capacitor plates. The FPGA accumulates measurements of the sensor output over one period of the excitation. Because it generates the excitations that are applied to the outer capacitor plates, it knows how many points it must take for one period of the excitation. The FPGA then averages these points to determine the baseline for that period of signal. According to how far from zero the baseline is, the FPGA adjusts the amplitude of the excitations it outputs such that on the next cycle the averaged value of the signal should be closer to zero. Although the sense reading determines the change implemented by the FPGA, the signal itself is not part of the feedback loop in the way it was in the analogue circuit. The sense-plate signal can thus be subjected to very high gains because it is not directly part of the feedback circuit so the gains applied to it will not affect the feedback.

This adjustment is done only in small steps of around 1 - 2%. This restriction ensures that the circuit cannot oscillate as was the case with the analogue circuit. Any large, rapid changes are limited to small changes per cycle. Because the digital electronics is not liable to oscillation, we can drive the gain up much higher than we could on the analogue circuit.

The digital electronics features a filter centred at the excitation frequency, 195.3 kHz,

as discussed in section 3.9.1. This will limit the noise that might be created by the digital electronics.

3.13.1 Readout speed

The digital electronics is inherently slower than the analogue electronics, which updates instantaneously according to variations in input. Two factors slow the digital electronics down. The first is due to the averaging over periods of the excitation. The output will only update after a complete period has been sampled so a change in sensor capacitance cannot have an instantaneous effect on the feedback so will not immediately appear in the output. The second factor that slows the digital electronics is akin to a low amplifier slew rate and arises because of the limited stepwise adjustment of the output excitation. If the ratio of capacitances were to change instantaneously by, for example, 20%, the electronics would take up to 20 cycles to match that change, because each incremental change in output is limited and the output can only change by that much once per cycle.

A rate of 195.3125 kHz means that the small, incremental changes will happen every 5.12 µs; 20 cycles (as suggested above) would be completed in 102.4 µs, which is well within the requirements placed on the readout. Moreover, the changes that the position and liquid level sensors are monitoring will be fairly slow, and certainly slow on the timescale of cycles of the electronics. The fastest possible change we might want to measure are surface waves on the liquid xenon. The speed of sound in liquid xenon is around 620 m/s, and surface waves will travel much slower than this.[80] For waves of wavelength 5 mm, which is around the size of the level sensor, the corresponding frequency is 124 kHz. The surface waves will accordingly have a lower frequency. Thus the electronics will be able to handle the variations associated with these waves. On the position sensors and long level sensors, the changes are expected to happen over timescales of order seconds, so the digital electronics is easily fast enough to respond to changes in those sensors.

3.13.2 Digital output

The final output signal of the digital electronics is shown in appendix B to be

$$f = \frac{C_2 - C_1}{C_2 + C_1}\,. \tag{3.52}$$

This is a ratio of capacitances as was sought in the analogue case and therefore gains all the benefits of cancellation between terms. However, as is evident from this

formula, the cable capacitance and gain do not directly appear in this expression. As such, varying the cable capacitance should have no impact on the output measurement and suppressing it is therefore of less importance. The effect of C_C on the circuit can be seen in the calculations in appendix B.

Moreover, the output of the electronics in eq. (3.52) does not contain the excitation voltage. This is a major advantage over the output voltage of the analogue electronics, as given in eq. (3.26), whereby the output voltage is proportional to the excitation voltage. If the excitation voltage changes for any reason, the change will not affect the output of the sensor.

3.14 Conclusion

This chapter has explored the features of the readout electronics designed for use with the capacitive sensors (specifically the position and liquid level sensors) in LZ. The above examined details of the feedback circuit enable the successful suppression of the cable capacitance such that the capacitive sensors can be precisely run. This includes increasing the amplifier gains while avoiding oscillations of the signal. The transition from the analogue to the digital electronics offers many advantages. As a result of these, the final readout uses an analogue first stage with the feedback loop completed in an FPGA. This readout fulfils all the requirements imposed by the design of LZ and enables us to accurately and reliably take data with the capacitive sensors to be installed in the experiment.

Chapter 4

Position Sensor Design

The LZ detector consists of a time projection chamber (TPC), inside two nested, titanium cryostat vessels. In order to measure the movement of the TPC inside the inner cryostat vessel, a system of capacitive position sensors will be installed in LZ. Their design is motivated by the experimental requirements of precision as well as restrictions on the available technologies and materials, owing to the nature of a xenon low-background experiment. This chapter will examine some of the options for position sensors, explore the design chosen for the position sensors in LZ, and discuss some of the tests run on the sensors.

4.1 Motivating position sensors

A cooldown procedure will be instituted to bring LZ down to its operation temperature of around $-100\,^{\circ}\mathrm{C}$. During this, the TPC is expected to shrink. It is important to monitor how it contracts or moves during cooling, as, in case of departures from the expected motion, the cooldown procedure may be modified. At the top of the TPC is the top PMT array, fixed to a titanium truss. The shrinking of the TPC results from the contraction of the material it is made from, but there is also scope for the TPC to tilt, twist or tip, affecting the position of the PMT array. The majority of event data are created in the TPC and collected by the arrays of PMTs at the top and bottom of the TPC. The behaviour of the TPC and top PMT array is therefore very important. As the PMT array sits on top of the TPC without any additional support, any movement of the TPC will affect the position of the PMT array, and therefore can affect the data taken by the experiment. The PMT array is critical to the success of the experiment, so understanding its final location is important. This is information that the position sensors will provide.

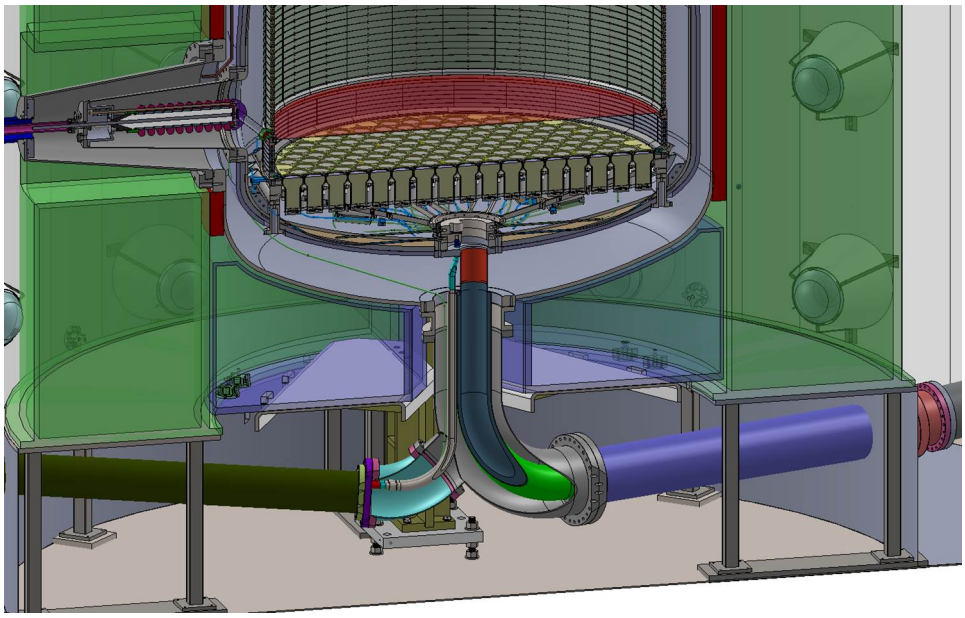


Figure 4.1: The bottom of the detector, with the TPC supports on the ICV and the titanium PMT frame visible

4.1.1 The shrinking of the experiment

The TPC is made of PTFE and titanium, so, during cooling, the size of the TPC is expected to change as the PTFE shrinks. The TPC is connected to the rest of the detector structure at its base via a titanium frame and support points; see fig. 4.1. Hence as the TPC shrinks, the top of the TPC will move downwards with respect to the vessels surrounding it. The vessel immediately around the TPC is known as the 'inner cryostat vessel' or ICV. This is a titanium pressure vessel designed to contain the liquid xenon and support the internal structure of the detector.

The TPC is composed of interlocking rings of PTFE interspersed with rings of titanium. The titanium 'field shaping rings' provide the field gradient along the height of the TPC, while the segmented PTFE rings separate them; see fig. 4.2. The PTFE and titanium rings stack on top of each other, with each layer interlocking with those immediately above and below it.

As the PTFE will shrink in all dimensions, in addition to the vertical shrinking noted above, the rings could shrink inwards too. However, although PTFE has a greater coefficient of linear thermal expansion (CLTE) than titanium, the composite structure of the TPC means the shrinking of the PTFE rings will be constrained by the titanium rings they sit on. Nevertheless, the position of the top PMT array will not be affected by this radial PTFE shrinking, as the structure supporting it is titanium, and PTFE is relatively soft so will not compress the titanium frame. In

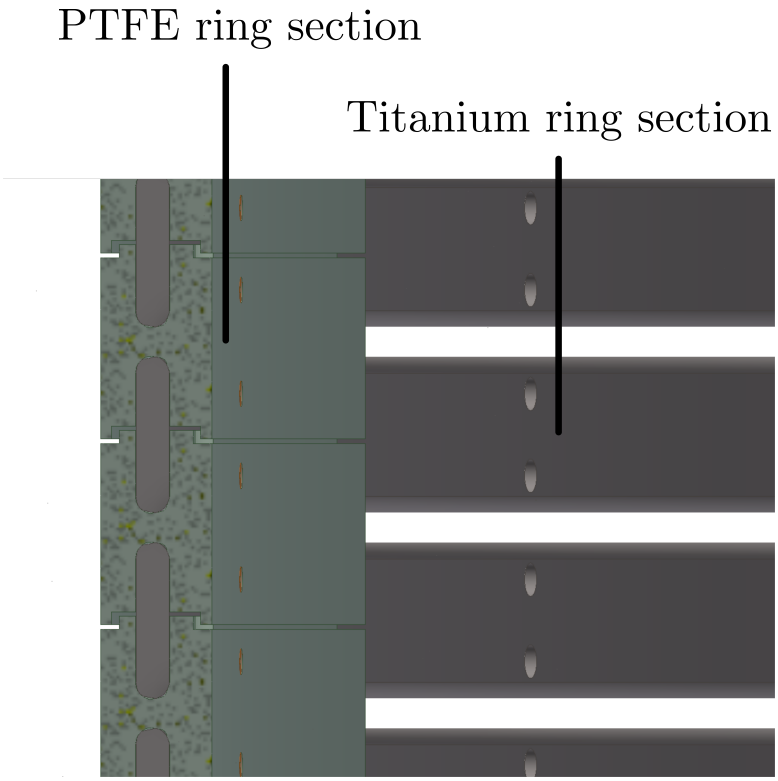


Figure 4.2: A cross-section view through the TPC rings, as they feature in the CAD model of the detector. One set of segments of the PTFE rings is shown in pale green. The titanium rings are extended round to the right.

addition, the PTFE segments that make up the rings can separate, so will not place undue stress on the titanium.

4.1.1.1 Vertical Shrinking

There is expected to be some vertical shrinking of the TPC owing to the shrinking of the PTFE. Again, this will be moderated by the titanium that sits between the PTFE rings, as seen in fig. 4.2. In fact, as the shrinking is measured relative to the titanium ICV, there is no net shrinking due to the titanium in the stack of rings. The total height of PTFE in the stack is 328 mm: 58 pieces of 4 mm height in the forward field region, 7 pieces of 10 mm height in the reverse field region, and 26 mm in the bottom grid region. The expected fractional shrinkage of the PTFE from room temperature (construction temperature) to experimental temperature is 1.5%, given the CLTE of PTFE and a temperature change of 130 K. This gives a total expected measurable shrinking of

$$328\,\mathrm{mm} \times 0.015 = 4.9\,\mathrm{mm}\,. \tag{4.1}$$

It is necessary also to account for the shrinking of this height of titanium, as measurements are made with respect to the ICV, so only relative changes are measurable. Over a cooling of 130 K, 328 mm of vessel height would shrink by

$$0.328\,\mathrm{m} \cdot 9 \times 10^{-6}\,\mathrm{m/m/K} \cdot 130\,\mathrm{K} = 0.3\,\mathrm{mm}\,. \tag{4.2}$$

This gives us an expected measurable vertical shrinking of the TPC with respect to the ICV of 4.6 mm. As measurements will be made against the ICV, any calculations of absolute position of the top of the TPC need to account also for the shrinking of the ICV. However, understanding the relative position of the two is the most important information and that value results from the cancelling out of the shrinking of the ICV and the titanium in the stack of TPC rings. The details of this will be discussed further in section 5.5.5 in light of the connected system of sensors used in LZ.

Although it is important to monitor the vertical shrinking of the TPC as it cools, to ensure it does so uniformly, the final height of the TPC has relatively little effect on the S1 and S2 response of the detector to electron and nuclear recoils. A change in TPC height of 10 mm alters the number of photoelectrons for S1 and S2 signals by less than 3.3×10^{-4}. This is a greater change in height than could reasonably be expected, and illustrates the relative unimportance of the height of the TPC for the size of the event signals in LZ. The height change does affect the drift field, as the voltages are spread across a different length. However, the changes in question are

not significant in terms of the expected signals. Hence the main role of the position sensors will be during the cooling of the detector.

4.1.2 Other movements

The shrinking of the TPC is expected and predicted, but it is not the only possible movement that can affect the position of the PMT array. Because the TPC is connected to the surrounding cryostat vessel only at the base, the top could tilt or tip to one side, moving one side of the PMT array closer to the wall of the vessel. This could occur if the cooling of the TPC is uneven so that one side shrinks more than the other.

Any tipping of the top of the TPC could be critical because of the very limited space between the edge of the PMT array plate and the cryostat vessel; see fig. 4.3. Near the top of the TPC are components that are charged to the same potential as the gate and anode voltages. The ICV is by contrast at ground potential. Therefore if the top of the TPC is to move towards the ICV on one side, the fields in that region will increase. If the field were to get high enough, electrical breakdown could occur, resulting in sparks and discharges.

In order to limit the scope of this movement and hence the risk of discharges, buffers are being built into the edge of the structure that supports the PMT array plate. These fill in the gap between this and the ICV wall, with up to around 2 mm clearance remaining. This clearance allows vertical movement and enables the insertion of the TPC structure into the ICV. The position sensors can provide a useful check on this, confirming that the TPC is moving within these constraints.

Although the height of the TPC has relatively little effect on the overall signals from LZ, any tipping or tilting of the PMT array can be significant. The size of an event's S2 signal depends on the gas gap through which the electrons are accelerated. Although the gate and anode are a fixed distance apart, the gas gap will depend on where the liquid level falls between the two. The liquid level is controlled only by liquid overflow into the weir. Thus if the liquid level is higher or lower within the gate-anode gap, the signal will change. A uniform change of gas gap by only 50 µm can result in a change of S2 signal of almost 1%. In the case of a TPC tipped to one side, the change in gas gap would not be uniform. The liquid surface will remain perpendicular to vertical irrespective of the configuration of the TPC. Hence the liquid will be much closer to the anode at one side than the other. The variation of signal size would thus be spatially dependent across the detector, and events would appear larger or smaller than they actually are. This effect would need correcting

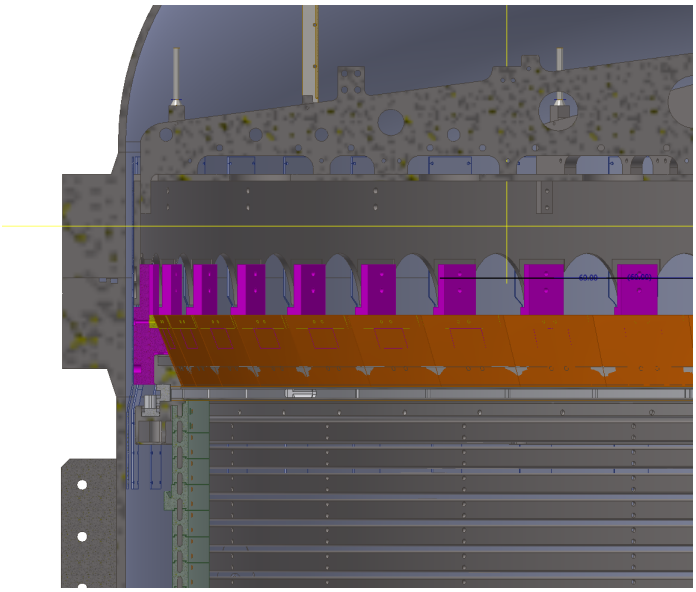


Figure 4.3: A CAD cross-section through the TPC and cryostat vessels around the top corner of the detector. Note particularly the limited space between the ICV (the OCV is not shown) and the structures at the top of the TPC.

out in the data from the PMTs, as the relative size of S1 and S2 signals is a critical parameter in categorising events.

In order to avoid this problem, it is important to keep the TPC as vertical as possible. To this end, levelling devices are installed between the ICV and the OCV so that the ICV position can be corrected after installation to make sure that the TPC is vertical. The levelling process relies on the sensors that monitor the liquid level in the overflow weir, and on measuring the S2 response of the detector and how it varies across the diameter of the TPC. Both of these measures require the detector to be filled with liquid xenon. By contrast, the position sensors can provide useful information about the location of the TPC prior to this levelling process, as they do not require liquid in the detector.

In the design of the TPC, there is no system to ensure the TPC rings remain aligned in their initial positions: although their design makes sure they stay stacked on top of one another, they are free to shift horizontally with respect to one another. It would be possible for the rings to all twist a small amount in the same direction, adding up to a significant torsional (twisting) effect at the top of the TPC. There is no other system that can measure whether this occurs, so the position sensors are essential for understanding this. If the PMT arrays are misaligned, it is possible that event locations could be misidentified, and a correction would need to be included in

the reconstruction and analysis of the data. Measurement of any axial movement of the PMT array is therefore an important role for the position sensors.

Once part of the integrated system described in chapter 5, the position sensors will be able to measure movements associated with vertical shrinking, radial displacement and torsion of the top of the TPC with respect to the inner cryostat vessel.

4.2 Choosing capacitive sensing

The importance of knowing the position of the PMT array and the shrinking of the TPC has been established, so a sensor is required that can fulfil this need. Commercial sensors are not appropriate, as will be explained below. Capacitive sensing, with a sensor designed in-house, is found to be the best option. The merits and demerits of different ways to create a capacitive position sensor will also be considered in this section.

4.2.1 Material considerations

The constraints on our choice of materials for the sensors are two-fold. First, radioactivity around the TPC must be kept to an absolute minimum. Any radioactive elements could decay and this decay could result in a signal in the PMTs. In order to be able to spot an event as rare as a proposed WIMP interaction, background events must be kept to a minimum. The causes and effects of possible decays were explored in depth in section 2.5 above.

Second, the purity of the xenon is essential for the continued running of the experiment. Any impurities decrease the average electron drift length: particle interactions with a xenon target liberate electrons, which are then drifted to the liquid-gas interface. Any ions (i.e. impurities) are liable to capture these electrons. Hence fewer reach the liquid-gas interface, resulting in a smaller S2, thus decreasing the relative S2/S1 signal ratio from the event. The emission of these ions from materials is known as outgassing. As the sensors will be in the xenon gas, and hence able to contaminate the xenon, any materials used must have a very low rate of outgassing. This limits the possible materials from which the sensors can be built, as the xenon purity must not be compromised.

Together, these restrictions on materials effectively prohibit the use of commercial sensors. The likelihood of materials used commercially being appropriately radiopure and xenon-friendly is very low, as the list of appropriate materials is highly restricted. This requirement motivates the design and production of sensors in-house, where all

of the materials used in the sensors can be appropriately understood, controlled and tested.

4.2.2 Sensing modalities

There are many different techniques that could be used to create a position sensor, but the nature of the LZ experiment places restrictions on the kinds of sensors that could be used. For example, it is not possible to use reflected laser light to obtain a position measurement, even though this generally can provide a reliable sensor and is used commercially. The laser light that would be used would be likely to be picked up by a PMT. This could then render the PMT inoperable, if not through saturation then through the increase of the single photoelectron rate, which would impact the efficiency of the detector trigger. Nevertheless, the time during which the position sensor is most critical is during cooldown, when the PMTs will not be required. However, designing a position sensor that interferes with the PMTs not only risks damaging the PMTs but also means there is no scope for using the sensor during detector operation. As such, a laser position sensor is not an option that suits our requirements for the system of position sensors in LZ.

As noted above, considerations of radiopurity and xenon-friendliness mean the position sensors must be something we can design and build in-house. This rules out the possibility of using relatively complicated technologies such as ultrasound, which would be difficult to construct and operate with the limited materials and in-house expertise available. There are, however, two widely used sensing modalities that could form a sensor that would fit the needs of LZ. These are capacitive sensors and inductive sensors. Below are considered variations of each of these as methods to measure position.

4.2.2.1 Capacitive sensors

One common method of measurement used in commercial position sensors such as digital calipers employs the variation of a capacitance. This option, as has been discussed in chapter 3, facilitates the management of material radiopurity and xenon non-toxicity. Moreover a basic capacitor is simple enough for in-house design and manufacture to be feasible. Below in section 4.2.4, the options for how the capacitance variation could be instantiated are considered.

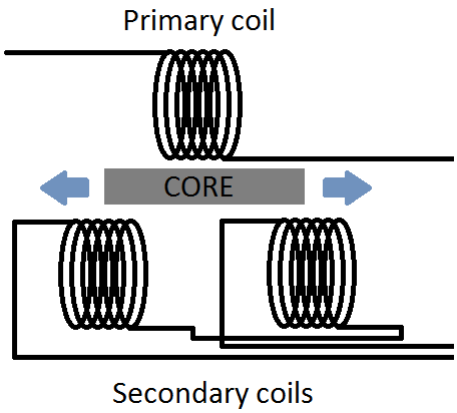


Figure 4.4: A diagram of a linear variable differential transformer that can be used as a position sensor.

4.2.2.2 Inductive sensors

Linear variable differential transformers (LVDTs) can provide an inductive position measurement, whereby the variation in an induced voltage is dependent on the position of the sensor's components. In a typical inductive sensor, the primary windings of the LVDT, as seen in fig. 4.4, are supplied with a fixed-amplitude, alternating voltage. They produce an alternating field, inducing a signal in the secondary coils, the strength of which depends on the position of the core (armature). The core would be attached to the component that we want to measure the position of, and the coils attached to the component with respect to which we would be measuring. The level of the signal induced in each secondary coil can then be used to determine the position of the core. The two secondary coils can be connected in opposition; then, when the armature (core) displacement is zero, the signals are equal and so give a total reading of zero. Movement of the armature results in an increase in the signal in one secondary coil and a decrease in the signal in the other, which gives an output from the sensor. The direction of the displacement can be determined from the phase of the signal, since the secondary coils are connected in opposition.

4.2.3 Merits and demerits of sensing methods

Inductive position sensors and capacitive position sensors have similar advantages. Both can be made to be quite robust as they have fairly simple components. For the same reason, both can be manufactured in-house from relatively simple materials, so could be constructed to comply with the materials restrictions imposed by LZ. Neither inherently involves friction between the moving parts, so should not result in

the creation of dust or particulates from rubbing, which might contaminate the xenon. Importantly, neither demands electronics at the point of the sensor and any signals can be carried away, which makes them easier to incorporate into a low-background experiment. Electronics are generally radioactively hot, so it would be undesirable for them to be in close proximity to the liquid xenon volume.

As much as they share many advantages, inductive and capacitive position sensors also share a significant disadvantage: both are in some way mechanically susceptible to temperature changes causing mis-readings. LVDT sensors will suffer some variation as they shrink due to cooling, as the lengths of the core and coils will decrease. In the case of capacitive sensors, the plate area will shrink with cooling and, depending on the sensor design, the plate spacing could change too. Nevertheless in either case, a thermometer mounted near the sensor could allow us to compensate for this in our calibration by knowing the expected shrinking and its effects. On a different note, the electric and magnetic properties of capacitive and inductive position sensors respectively are also liable to change with temperature. For the case of a capacitive sensor, the capacitance is dependent on the relative permittivity of the dielectric between the plates. As the xenon gas cools, its relative permittivity will change a tiny amount. In addition, if an extra dielectric is used, the permittivity of this too can change. Equivalently, on cooling the inductive sensor, the permeability of the core can vary, dependent on the material it is made of.

Nevertheless the two modalities are not equally good for our application. The significant disadvantage of inductive sensors is that, to prevent the sensor picking up or emitting of any stray, time-varying electromagnetic fields, the sensor would require magnetic shielding. In contrast, a capacitive sensor uses only electric components of fields, so the shielding is comparatively easy. Importantly, any magnetic fields leaking from the position sensors could be detrimental to the PMTs, the top array of which is very close to the position sensors. Their mechanism of amplification is dependent on there being no magnetic fields in the volume of the tube. Although capacitive sensors do require shielding, they do not generate magnetic fields that would need to be contained so do not present this particular problem.

Above all, the sensors must not interfere with the running of the detector, of which the PMTs are an essential part. The risk to the PMTs associated with the magnetic fields of inductive sensors is not a risk worth taking. Thus a capacitive design for the position sensors in LZ was chosen.

4.2.4 Varying capacitance

There are many different ways of varying the capacitance of a capacitor in such a way that the change can be coupled to a changing position. The most obvious and theoretically most straightforward options are spacing variation and area variation. A spacing variation sensor was used for characterising the electronics and was described in section 3.3. However, instead of varying the plate spacing or area, the plates can be left as they are and what lies between them changed instead. This results in either a capacitor whose dielectric varies with position, or a sensor in which the capacitance is variously split. This final option best overcomes the difficulties associated with working within the confines of LZ.

4.2.4.1 Spacing variation

Spacing variation capacitive sensors were discussed in section 3.3.1 and used for developing the readout electronics. With an appropriate plate spacing, such a sensor can be very sensitive to small spacing changes, measuring along the axis perpendicular to the faces of the plates.

4.2.4.2 Area variation

The principle for area variation sensors is similar to that for spacing variation sensors: we couple the capacitor plates to the components whose position we wish to measure in such a way that movements of the components translate into variations in the effective area of the capacitor. The effective area of a parallel plate capacitor is given by the overlap of the two plates. Hence by moving one plate with respect to the other, the overlapping area of the two plates can be changed, thus changing the capacitance of the sensor. This could again be done in a three-plate configuration to enable a ratiometric output. The relative sensitivity of spacing variation and area variation sensors depends upon the chosen values for length, width and spacing; neither is inherently more sensitive.

4.2.4.3 Dielectric variation

The relative permittivity of the material or materials between the capacitor plates directly affects the capacitance. Hence by changing the material that fills the gap, the capacitance can be changed; coupling the material change to a relative position change creates our position sensor.

A simple way of changing the material according to position is to have a slider that covers part of the capacitor plates with a dielectric. As the slider moves, a different fraction of the capacitor is filled with the dielectric, and so the position changes create a change in capacitance that can be measured.

A clear advantage of this style of sensor over area or spacing variation sensors is that none of the electrically connected parts of the capacitor need to move. The dielectric slider needs to be physically connected to the component whose position is being measured, but does not need any wiring. This greatly simplifies the sensor design and makes the electrical connections more robust and less likely to fail.

However, there is a challenge associated with dielectric variation sensors that is particular to our application. For LZ, the sensor is most critical while the detector is cooling down by around 130 K. As this occurs, the sensor itself, including the dielectric slider, will also cool. This temperature change will change the relative permittivity of the slider. Hence there will be two effects changing the capacitance at once: the position change due to the shrinking of the TPC, which is required, and the changing relative permittivity of the dielectric slider. The two effects are not separable, as they are both simply changing the capacitance of the sensor. (It is worth noting that the relative permittivity of xenon gas varies very little with temperature, so it is only in cases of dielectric variation sensors that this change is a concern.)

It would be possible to correct for the changing relative permittivity in calibration. This would require a thermometer to be mounted very near the sensor. The thermometer would read out the temperature around the sensor, which could be assumed to be the temperature of the dielectric slider. The changing relative permittivity can then be corrected for by knowing exactly how it changes with temperature. However, this relies not only on a knowledge of the variation of the relative permittivity, but also on the assumption that the thermometer reading can provide a good approximation to the temperature of the dielectric. During periods of temperature change, the gas temperature may change more quickly than the temperature of the materials in the gas. All in all, it would be difficult to be sure that the supposed position change the sensor measured was truly that and not a variation of the relative permittivity of the material between the sensor plates.

For a sensor with a design in this vein, as used in the System Test and described in section section 4.5.1.1, a change of relative permittivity of 10% causes a 6% change in sensor output. Such a change would be not unexpected over 130 K of temperature variation. This would be a dominant systematic for the sensor. Hence if position is

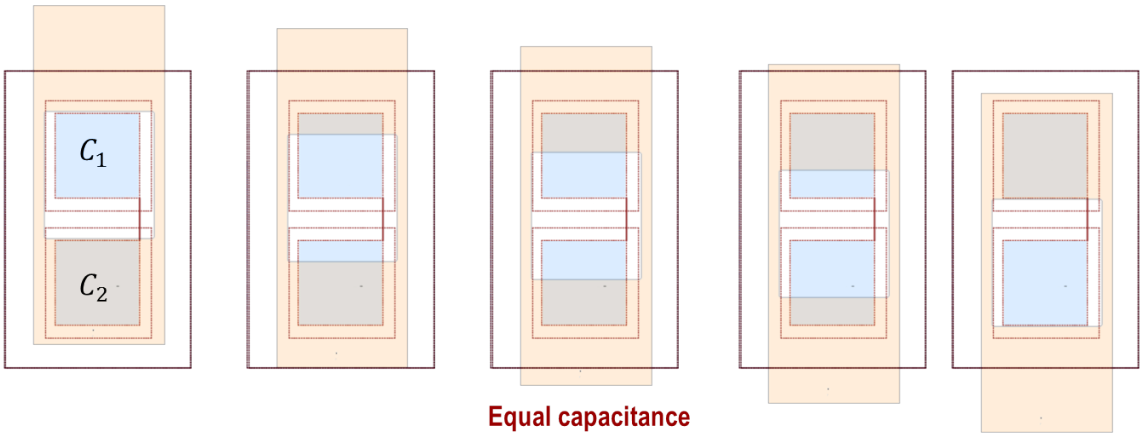


Figure 4.5: The movement of a dielectric slider (orange) between the plates of capacitors C_1 and C_2. The hole in the slider effectively changes the relative permittivity between the capacitor plates, thus changing the capacitance. When the slider is in the centre, the two capacitors have the same amount covered and uncovered, so they have equal capacitance. The two ends illustrate the two opposite extremes.

to be measured by moving a dielectric, there must be an accurate model of the sensor that matches the data. Otherwise it will not be possible to include corrections.

4.2.4.4 Splitting capacitors

Inserting a metal block between two capacitor plates has the effect of splitting that capacitor into two capacitors with smaller plate spacings in series. Effectively, a metal block is a dielectric block with an infinite relative permittivity. In this case, the metal block would pick up a potential according to the field in which it sits; this potential would be the same on all surfaces of the block. The opposite faces of the metal block behave as two capacitor plates connected in series. If a metal block is used in a parallel-plate capacitive sensor as described earlier, one capacitor forms between the excitation plate and one face of the metal block, and another forms between the opposite face of the metal block and the sense plate. This is illustrated in fig. 4.6. The thicker the block is, the more different the sum of the two new spacings is from the original spacing, so the greater the change in capacitance is. Partially inserting the block will divide the original capacitor into three: one that has the original plate spacing but a fraction of the area and two that cover the remaining fraction of the area but with smaller plate spacings. This can be seen in fig. 4.7. As the block moves through, the total capacitance from these three capacitors will change; this is the fundamental basis for our capacitive position sensors.

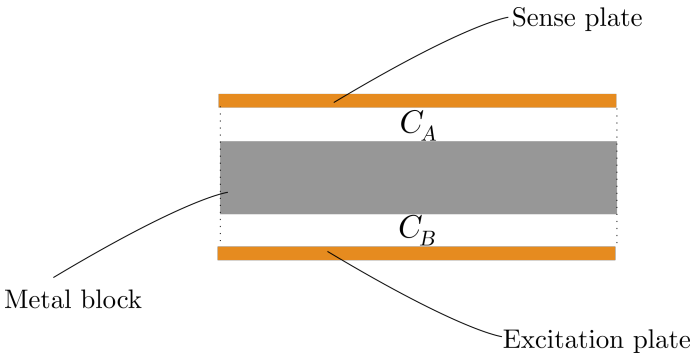


Figure 4.6: The insertion of a metal block into the original capacitor divides it into two capacitors, labelled here as C_A and C_B. They are connected via the metal block such that they effectively share a capacitor plate. Equally they can be considered as two capacitors in series.

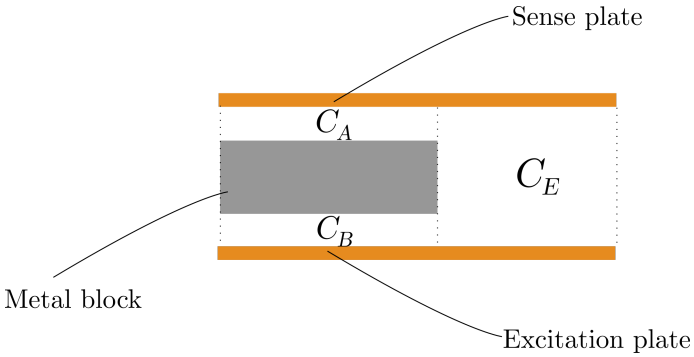


Figure 4.7: The insertion of a metal block that partly shields the sense plates from the excitation plates results in the division of the original capacitor into three capacitors. The section without the metal block in (labelled here as C_E) takes the full width of the original capacitor. The remaining sections, labelled C_A and C_B, have much smaller plate spacings. As the block moves into the capacitor, the relative ratios of C_E, C_A and C_B change. To find the total capacitance, add C_A and C_B in series, and then add this series sum in parallel with C_E.

4.2.4.5 Conclusion on capacitance variation

As set out above, there are many ways to vary the capacitance of a position sensor. Spacing variation sensors are limited by the fact that if the plate separation becomes too large relative to the plate size, they cease to behave in a way that approximates an ideal capacitor. It can therefore be difficult to make them appropriately compact, as a large measurement range demands a large plate size. Additionally, at least one of the moving parts of a spacing variation sensor must be electrically connected.

As noted above, dielectric variation sensors trump spacing or area variation sensors in precisely this way: the only moving part in a dielectric variation sensor is the dielectric block, which needs no wiring. The plates remain stationary with respect to each other while the block moves in and out of the gap between them. This advantage motivated the use of a dielectric variation sensor in the first runs with the LZ System Test at SLAC; see section 4.5 for details. However, while this design works well in unchanging conditions, it is liable to error in conditions where temperatures are varying. The point at which the position sensors will be most important is while temperatures are changing and the TPC is cooling and shrinking. Hence it is difficult to justify using a design that is least reliable when it should be most useful.

However, if the dielectric block is replaced with a metal block, as explored in section 4.2.4.4, a capacitance is created that changes because it is split into three capacitors that vary their capacitance as the metal block moves. This has the advantage of needing no moving wiring, while avoiding the problem of varying relative permittivities with temperature. Hence this is the most appropriate form of capacitive position sensing for use in LZ.

4.3 Sensor design

4.3.1 Design process

In order to develop the electronics, we created a spacing variation sensor. This is described in more detail in section 3.3. This simple design permitted easy evaluation of the electronics in a realistic setting, and allowed us to demonstrate that the readout worked well. However, LZ requires a more robust sensor design that doesn't demand movement of the cables. This led to the development of the sensor with a dielectric slider to control the change of capacitance. This was used in the early System Test runs at SLAC. However problems with the changing relative permittivity of the di-

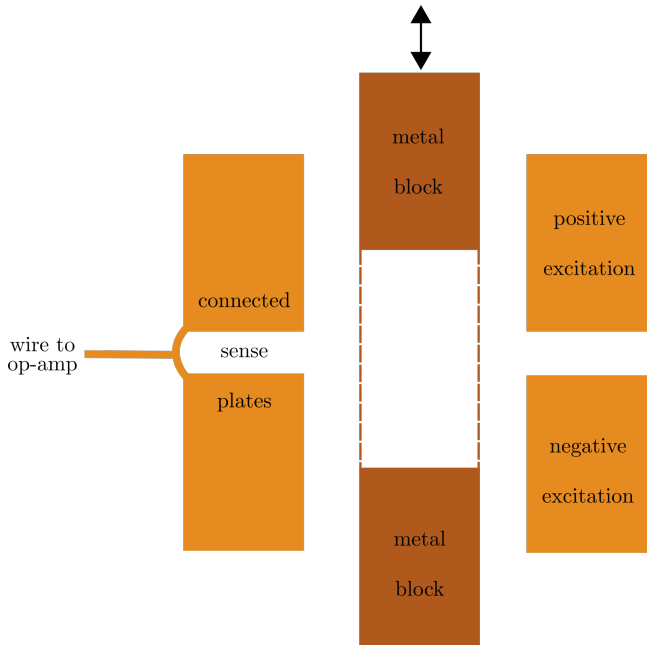


Figure 4.8: The essential parts of the sensor: the two excitation plates, with the connected sense plates opposite them, and the (mechanically but not electrically) connected metal blocks in between.

electric motivated the shift to a metal block to control the change of capacitance. This final design is explored in detail below.

4.3.2 Sensor geometry

The main body of the position sensor consists of two parallel-plate capacitors that share one plate; see fig. 4.8 for a schematic illustration. The shared plate is the 'sensing' plate, while of the other two, one carries a positive excitation and the other carries a negative excitation. A pair of mechanically coupled metal blocks move within the two capacitors, dividing the capacitance as explained above. This can be seen in an exploded view in fig. 4.9. The relationship between the plates, blocks and capacitances can be seen in fig. 4.10.

Of course, many different geometries are possible for creating a capacitor. All that is required is two conductors separated by a dielectric. However, design constraints motivated the choice of a parallel plate capacitor as the basis of the position sensor. The sensor needs to be mechanically robust, and, since it is being constructed in-house, should be as simple as possible, to keep down the cost of machining the required parts. Both of these considerations suggest a parallel plate geometry as a sensible solution. However, an ideal parallel plate capacitor should be infinitely large.

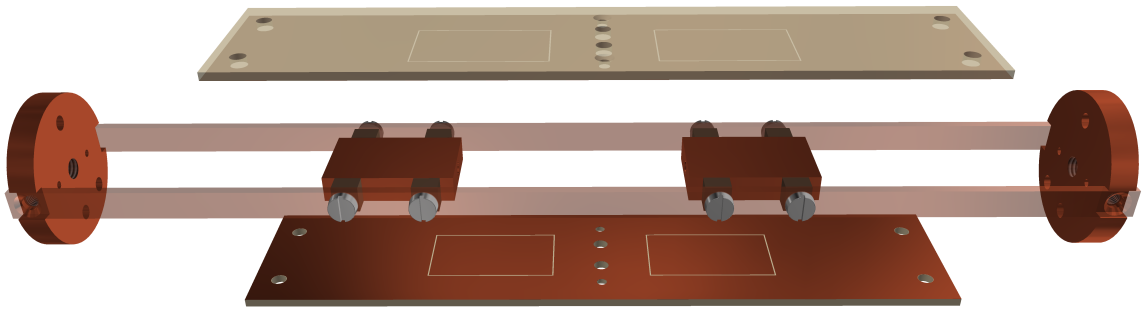


Figure 4.9: An exploded view of the sensor plates with sense and excitation electrodes, with the moving metal blocks between.

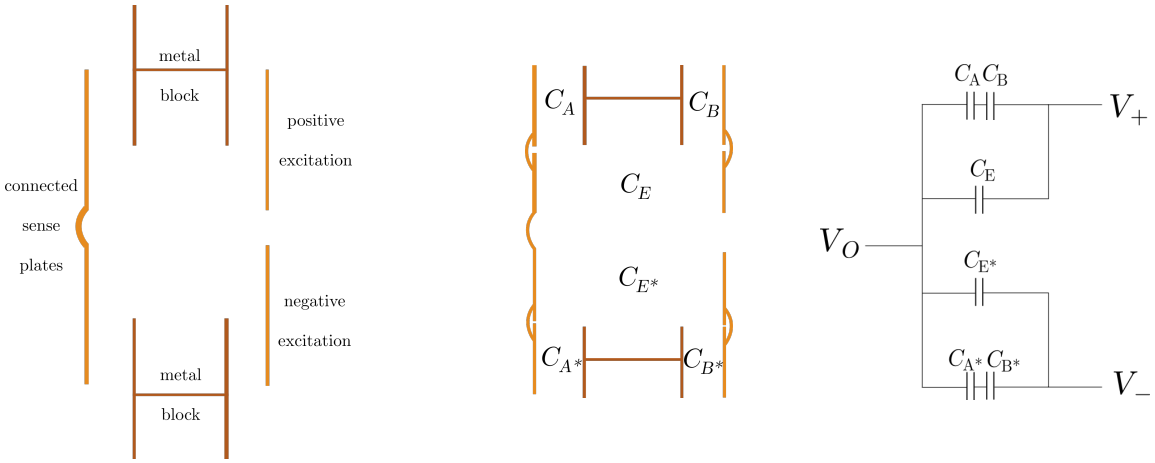


Figure 4.10: Abstractions from the sensor design seen in fig. 4.8, to show the capacitances that are present in the sensor. C_A, C_B and C_E together constitute C_1, with the other capacitors forming C_2.

Although the space constraints on the sensor are not very tight, (as there is nothing else occupying the space above the PMT array), infinite plate sizes are clearly not something we could accommodate. Introducing edges to the capacitor plates introduces fringe fields, which are non-uniformities in the field present at each edge of the capacitor plates. This is mitigated by the inclusion of guard electrodes around the sense plates. Some of the problems associated with fringe fields could also be allayed by the use of a cylindrical geometry; however this presents substantial engineering challenges that are discussed further in appendix E.

Anchoring the two plates of the capacitor is simple as the plates on both sides are directly accessible. The actuated metal blocks can also be connected from the sides without disturbing the integrity of the capacitor plates. Additionally, if the metal blocks stray from their central position, the changes in capacitance cancel each other out of the measurement, as will be shown below. Furthermore, the shape of the capacitor plates can be etched onto a copper-clad substrate, which makes construction of a guard electrode very simple: it can consist of the rest of the copper on the substrate.

4.3.3 Design details

The inner workings of the sensor are housed in a cylindrical copper tube, which provides stability and shielding to the sensor. A CAD image of the sensor is shown in fig. 4.11. The main features of the sensor are the capacitive plates and moving metal blocks. The plates are made from copper-clad Cirlex, a polyimide substrate with a copper layer deposited on top; more detail on Cirlex is given in section 4.4.1. Parts of the copper are removed by photolithography to give the shapes of the capacitor plates required. The design for this can be seen in fig. 4.13. The moving metal blocks are pieces of copper which attach at the sides (via PEEK spacers) to flat copper rods that control their movement. The rods are held in the right place with short cylindrical pieces of copper at each end, to ensure that the moving copper blocks do not electrically connect to the Cirlex plates and short the sensor. The Cirlex plates are held apart at each end and in the centre by copper spacers. These are all connected to the outer tube, which is grounded, so all share the same ground. Additional rods running through PEEK spacers keep everything aligned. The engineering drawings for all of these parts can be found in Appendix F.



Figure 4.11: A CAD model of the sensor, viewed from the outside

4.3.4 Sensor output

The position sensor consists of two capacitors, C_1 and C_2, that are connected in series. Consider the moving metal block as offset by an amount x from the central zero position, as shown in . Each electrode picking up the signal has a length l. Consider the capacitor which contains more block when it moves by an amount x. In this case, $\frac{l}{2} + x$ of the capacitor contains the metal filler, and $\frac{l}{2} - x$ is empty. This is treated as two capacitors in parallel.

The empty section has capacitance $C_E = \frac{\varepsilon_0 A_E}{d} = \frac{\varepsilon_0 w\left(\frac{l}{2}-x\right)}{d}$ where w is the width of the plates and d is the distance between them; see fig. 4.15. The block thickness is denoted by h. With the block lying directly in the centre of the gap, one can then treat the full section (C_F) as one capacitor (A) of spacing $\frac{d-h}{2} \equiv D$ and one capacitor (B) of spacing D, both with area

$$A_A = A_B = \left(\frac{l}{2} + x\right) \times w\,. \tag{4.3}$$

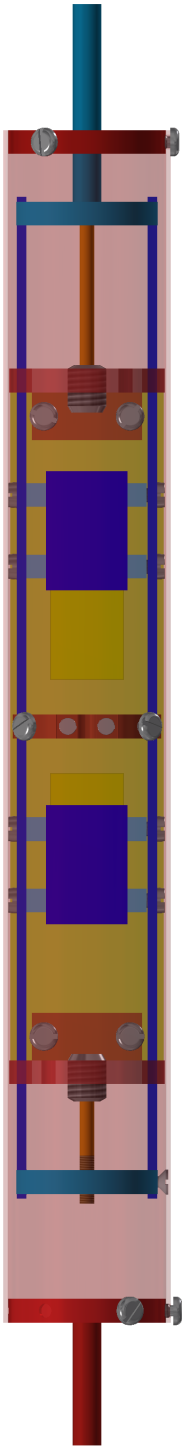


Figure 4.12: A cross-section through the sensor, with the parts artificially coloured for clarity. All of the blue parts move together when the rod at the top of the image is actuated. The yellow parts are the Cirlex boards.

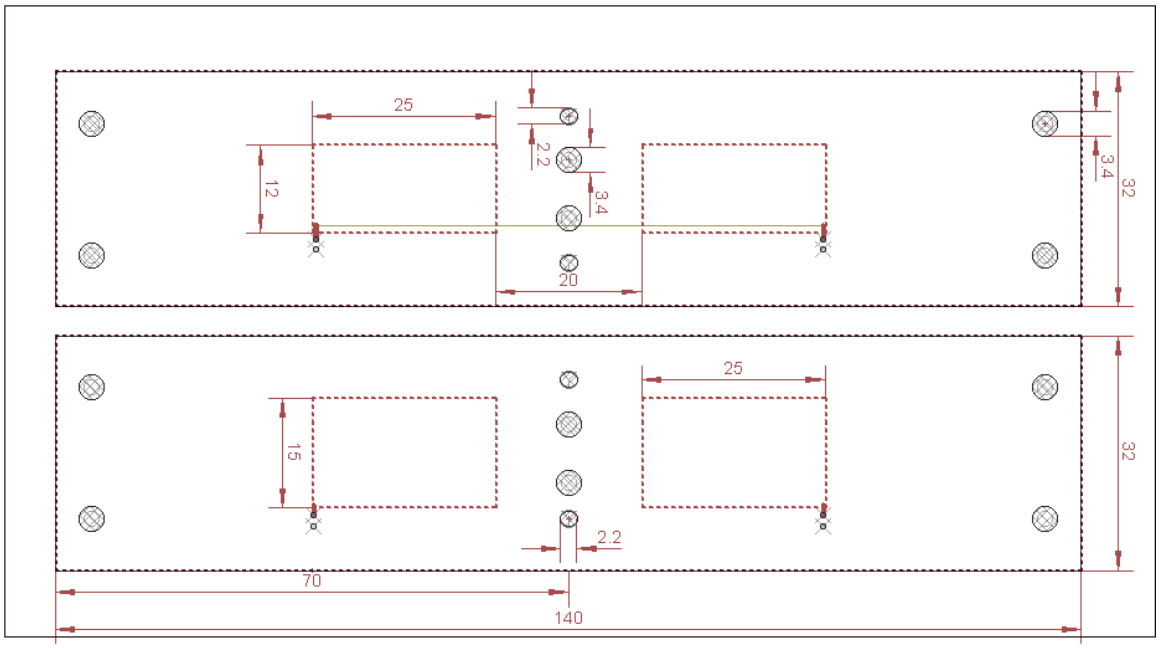


Figure 4.13: The dimensioned drawing of the design for the sensor plates. This is used to produce a photolithography mask that is in turn used to create the appropriate shapes of copper on the Cirlex.

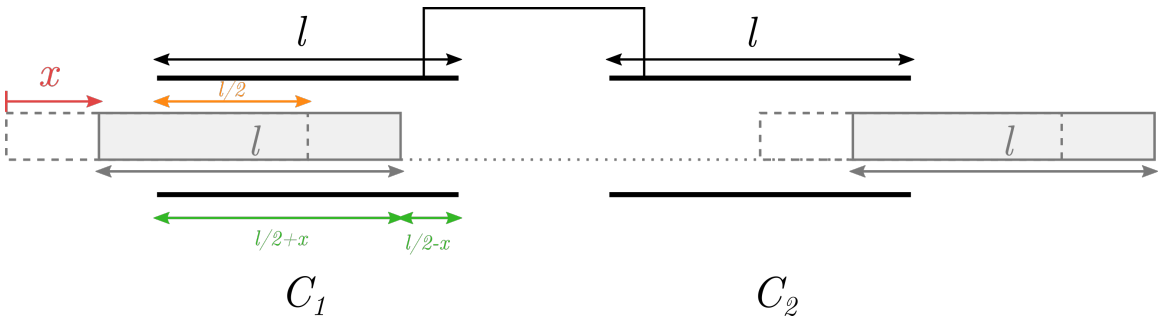


Figure 4.14: The definitions of the sensor lengths and sections, and the sense of motion as used in the calculation of sensor output.

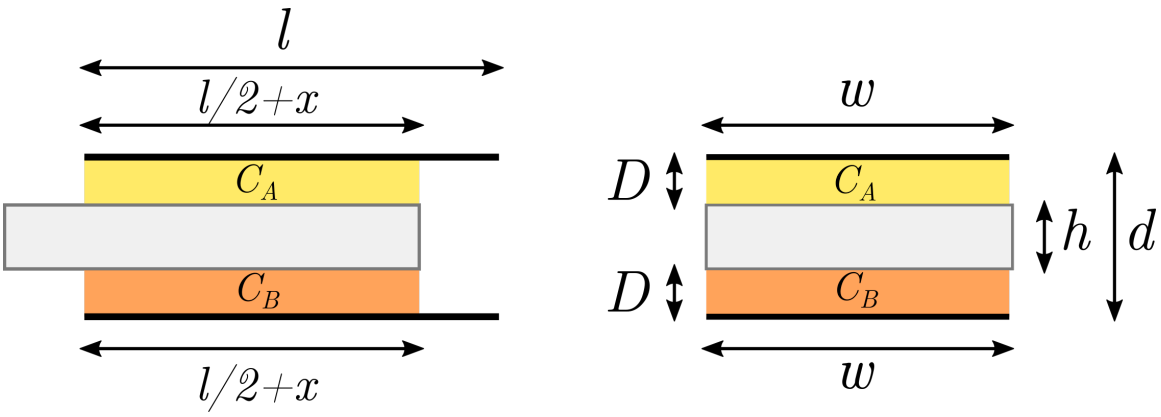


Figure 4.15: A diagram to illustrate the terminology used to calculate the sensor output.

So

$$\begin{aligned} C_F &= \frac{C_A C_B}{C_A + C_B} \\ &= \frac{\varepsilon_0^2 \varepsilon_r^2 A_A A_B D}{D^2 \varepsilon_0 (A_A + A_B)} \\ &= \frac{\varepsilon_0 \varepsilon_r w (\frac{l}{2} + x)(\frac{l}{2} + x)}{D(l + 2x)} \\ &= \frac{\varepsilon_0 \varepsilon_r w \left(\frac{l}{2} + x\right)}{d - h} . \end{aligned} \tag{4.4}$$

Combining the two parts of this half gives

$$\begin{aligned} C_1 &= C_E + C_F \\ &= \frac{\varepsilon_0 \varepsilon_r w \left(\frac{l}{2} - x\right)}{d} + \frac{\varepsilon_0 \varepsilon_r w \left(\frac{l}{2} + x\right)}{d - h} . \end{aligned} \tag{4.5}$$

For the other half of the device, a similar schema applies, except that the filler fills a portion $\frac{l}{2} - x$, and $\frac{l}{2} + x$ is left empty. Hence

$$\begin{aligned} C_2 &= C_{E*} + C_{F*} \\ &= \frac{\varepsilon_0 \varepsilon_r w \left(\frac{l}{2} + x\right)}{d} + \frac{\varepsilon_0 \varepsilon_r w (\frac{l}{2} - x)}{d - h} . \end{aligned} \tag{4.6}$$

The sum and difference of these two will be required for the final readout.

$$\begin{aligned} C_1 + C_2 &= \frac{\varepsilon_0 \varepsilon_r w l}{d} + \frac{\varepsilon_0 \varepsilon_r w l}{d - h} \\ &= \varepsilon_0 \varepsilon_r w l (\frac{1}{d} + \frac{1}{d - h}) \\ &= \varepsilon_0 \varepsilon_r w l \Delta^+ \end{aligned} \tag{4.7}$$

where

$$\begin{aligned}\Delta^{+} &= \frac{1}{d} + \frac{1}{d-h} \\ &= \frac{2d-h}{d(d-h)}\,.\end{aligned} \tag{4.8}$$

Hence

$$\begin{aligned}C_2 - C_1 &= \frac{2\varepsilon_0\varepsilon_r wx}{d} + \frac{\varepsilon_0\varepsilon_r w\,(-2x)}{d-h} \\ &= 2\varepsilon_0\varepsilon_r wx\left(\frac{1}{d} - \frac{1}{d-h}\right) \\ &= 2\varepsilon_0\varepsilon_r wx\Delta^{-}\end{aligned} \tag{4.9}$$

where

$$\Delta^{-} = \frac{1}{d} - \frac{1}{d-h} \tag{4.10}$$

$$= \frac{-h}{d(d-h)}\,. \tag{4.11}$$

The readout on the digital electronics board is given by

$$\begin{aligned}f &= \frac{\Delta C}{\Sigma C} \\ &= \frac{C_2 - C_1}{C_1 + C_2} \\ &= \frac{2x}{l}\frac{\Delta^{-}}{\Delta^{+}}\,.\end{aligned} \tag{4.12}$$

Consider

$$\begin{aligned}\frac{\Delta^{-}}{\Delta^{+}} &= \frac{\frac{1}{d} - \frac{1}{d-h}}{\frac{1}{d} + \frac{1}{d-h}} \\ &= \frac{1}{1 - \frac{2d}{h}}\,.\end{aligned} \tag{4.13}$$

Hence the overall sensor output is given by

$$f = \frac{2x}{l}\frac{1}{1 - \frac{2d}{h}}\,. \tag{4.14}$$

4.3.4.1 Optimising the dimensions

The sensor electronics is able to read out between 1024 and -1024 in single bit steps. Therefore in order to maximise the sensitivity of the sensor readout, it is important to maximise the output range of the sensor within these limits. This is done by

optimising the values of d and h within the constraints of making a mechanically viable sensor.

For any given combination of dimensions, the sensor output can be modelled and one of those dimensions can be altered. By building an understanding of the different roles the variables play on the overall output, the final dimensions can be chosen to together maximise the possible sensor output range. Below are figures exploring these variables.

From fig. 4.16 and fig. 4.17, one can see that the maximal output is obtained for a sensor with as small a difference between the plate spacing and block thickness as possible. However, mechanical considerations are the limiting factor here. Engineering and machining tolerances in the parts produced limit the precision it is sensible to expect. We cannot risk the block touching either plate, but it is not reasonable to expect perfect alignment. It is therefore prudent to allow a little tolerance for possible misalignments. To this end, a gap of 0.5 mm between the face of the block and the face of the capacitor plate was chosen. This gives some room for error while still ensuring a reasonably high potential output.

With the gap size chosen, it is still possible to change the total spacing between the capacitor plates (or equivalently the block thickness, which will be 1 mm less than the plate spacing). The possible outputs for this are shown in fig. 4.18. From this, it is apparent that the larger the overall spacing, the larger the potential maximum sensor output. However, the larger the spacing between the capacitor plates, the further the design is from the approximation to an ideal capacitor and the more susceptible the sensor is to non-ideal effects such as fringe fields and other non-uniformities. Therefore the plate spacing should not be increased further than is strictly necessary.

The final dimensions must be a compromise between the optimisation (maximisation) of the output signal and the mechanical feasibility of the design. Together, these factors suggest a maximum readout of around $\frac{700}{1000}$ units, which is attained at the extremes of the sensor range. Given the model shown in fig. 4.18, this suggests a plate spacing of around 6 mm, with a block thickness of 5 mm. For such a sensor, the range of outputs expected with variation of position are shown in fig. 4.19.

4.3.5 Cooling and shrinking

When the system cools, everything will shrink; indeed, the shrinking of the TPC is what the sensors will be measuring. However this shrinking also applies to the sensor itself. The position sensor design is optimised to limit the effect this has on the output

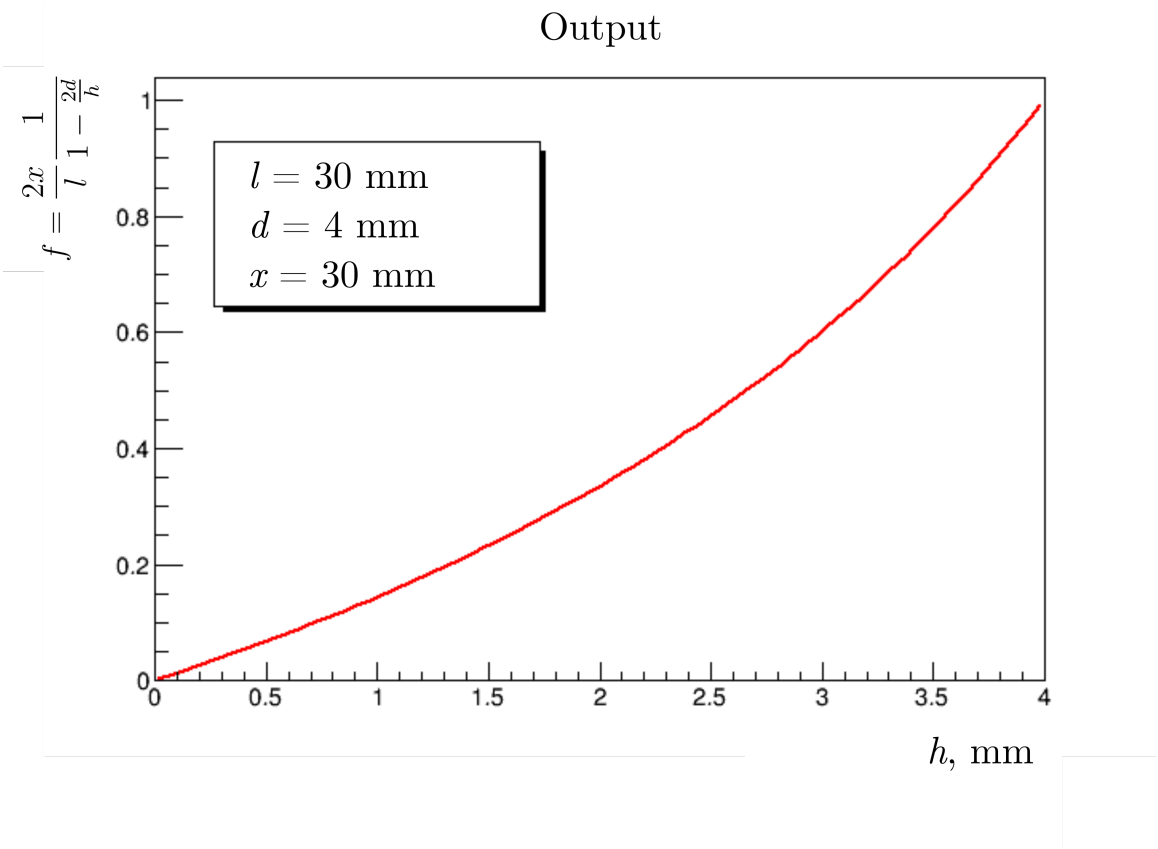


Figure 4.16: A model of the sensor output, changing the thickness of the metal block between the plates between 0 mm and 4 mm. In this model, the metal block sits in a gap of 4 mm between the plates.

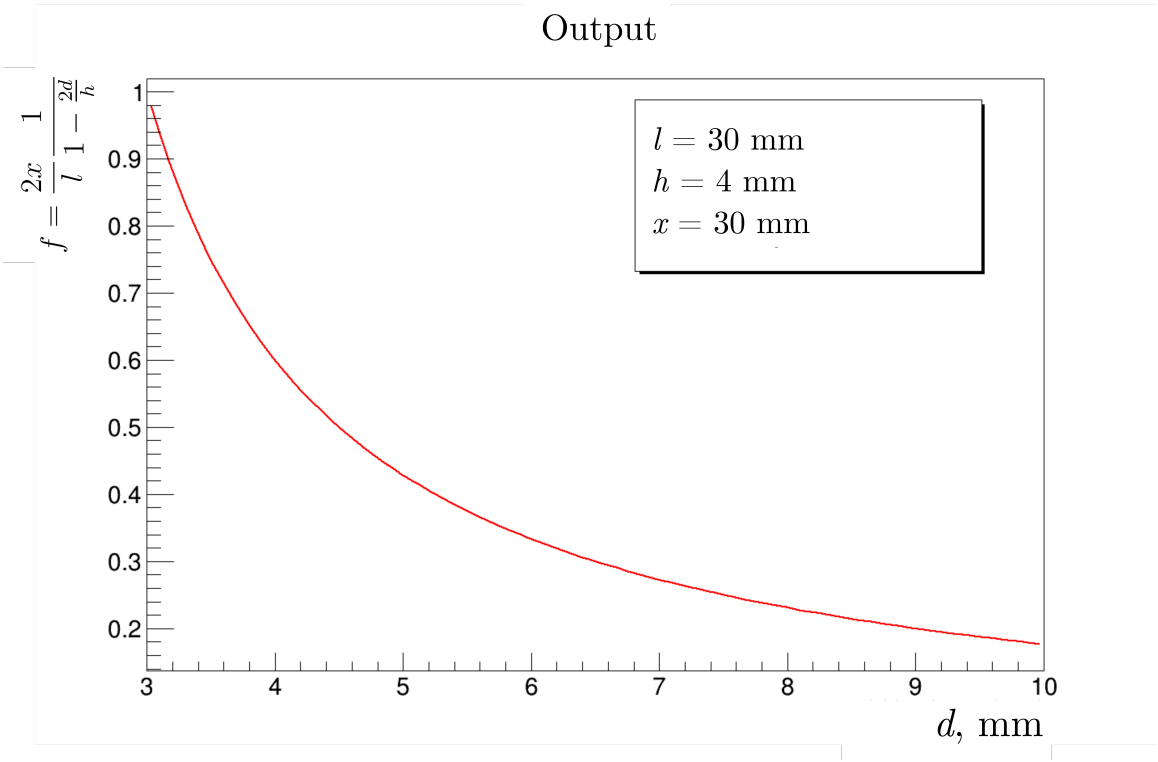


Figure 4.17: A model of the sensor output, changing the spacing between the capacitor plates between 3 mm and 10 mm. In this model, the metal block has a thickness of 3 mm.

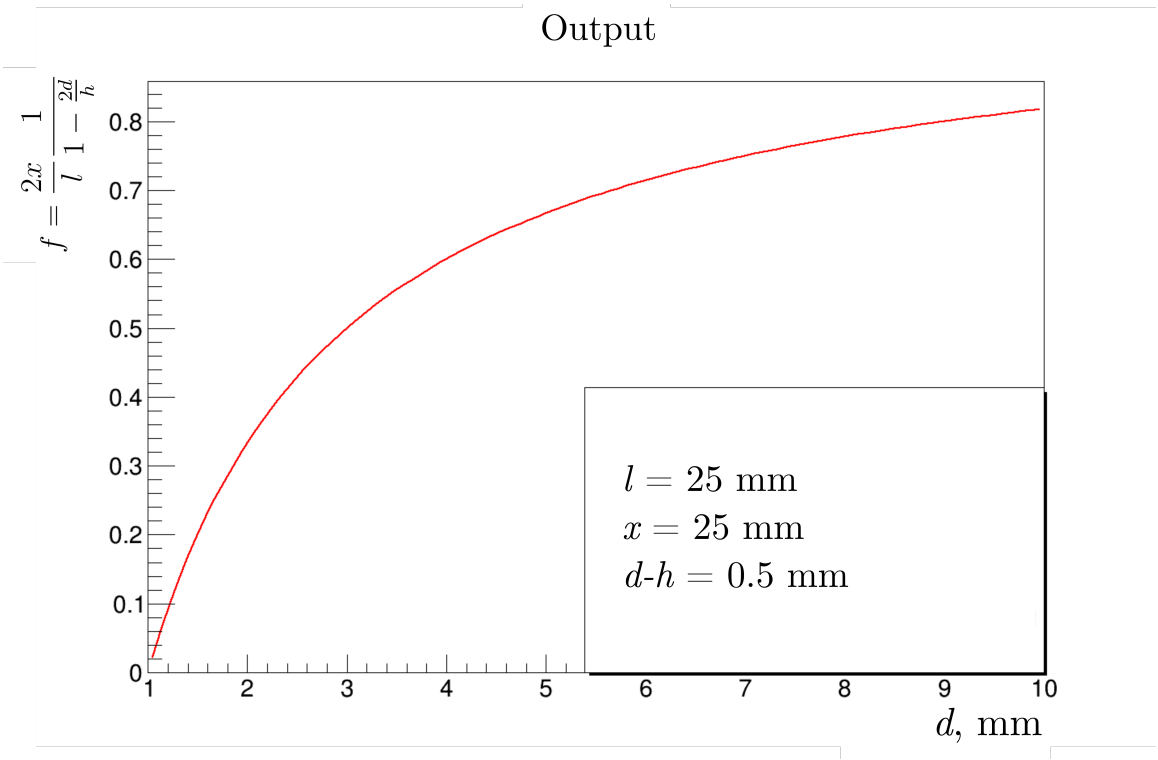


Figure 4.18: A model of the sensor output with a fixed gap of 0.5 mm between the block face and plate face, but changing the total spacing between the capacitor plates. As shown, the larger the spacing, the greater the output of the sensor. This change is steepest for small spacings, and as the spacing increases further, the gain in output is less significant.

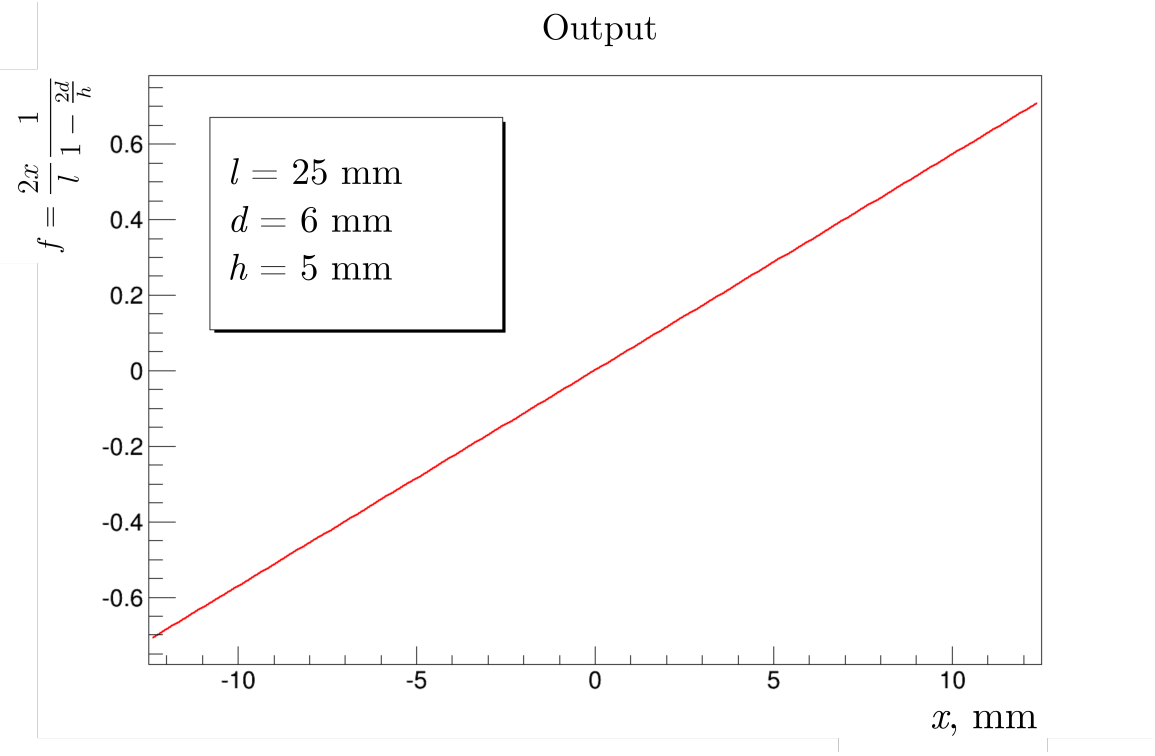


Figure 4.19: The output of the optimised sensor, according to the simple model. The sensor 'sense' plate is 25 mm long and the range of the sensor is 25 mm, i.e. 12.5 mm in each direction. The anticipated measurable vertical shrinking was calculated in section 4.1.1.1 to be 4.6 mm. If we suppose a worst-case scenario, we might anticipate an additional 10% shrinking. This would lead to an expected sensor length change of 4.0 mm, with the sensors in the system as described in chapter 5. In addition to this shrinking, the TPC could move outwards by up to 2 mm (see section 4.1.2). If this is also included, the sensor length change becomes 5.2 mm. Any twisting of the platform would result in further sensor extension. The sensor is expected only to operate in the central portion of its range.

of the sensor. This section will consider the various ways cooling and shrinking affect the sensor, and demonstrate the ways it has been designed out where possible.

4.3.5.1 Dielectric variation

Because the sensor will be using a metal block rather than a dielectric block as the moving part, the changes the temperature causes are all mechanical rather than electrical. The dielectric in the sensor is xenon gas throughout. The relative permittivity of xenon gas will vary very slightly with temperature, but this will not have an effect on the output of the sensor. The sensor output is given by eq. (4.15) below. Evidently no changes in ε_r, that is, in the relative permittivity of the xenon gas, will have any effect on the output, because ε_r, although included in the calculation, appears nowhere in the final expression for a sensor in which the dielectric in all capacitors is the same.

4.3.5.2 Through-thickness shrinking

From section 4.3.4, the readout is given by

$$f = \frac{2x}{l}\frac{\Delta^-}{\Delta^+} \tag{4.15}$$

where

$$\Delta^- = \frac{-h}{d(d-h)} \tag{4.16}$$

and

$$\Delta^+ = \frac{2d-h}{d(d-h)}\,. \tag{4.17}$$

Consider a case where d (the gap between the plates) and h (the thickness of the block) both change by a certain fraction δ, such that $d \to d \pm \delta d = d(1 \pm \delta d/d)$ and $h \to h \pm \delta h = h(1 \pm \frac{\delta h}{h})$. This is what might happen during the cooling of the sensor. Then

$$\frac{\Delta^-}{\Delta^+} = \frac{1}{1-\frac{2d}{h}}\,. \tag{4.18}$$

That is, if d and h change by the same fractional amount, the overall value of $\frac{\Delta^-}{\Delta^+}$ will not change, and thus the total readout value will not change. Hence so long as the material that holds apart the capacitor plates is the same as the material that the block is made from, any through-thickness shrinking will have no effect, as the block and the gap will change in the same way. In the position sensor, the capacitor plates are held apart by a piece of copper, and the blocks that move between the plates are also copper, fulfilling this requirement. Hence any through-thickness shrinking will not affect the sensor.

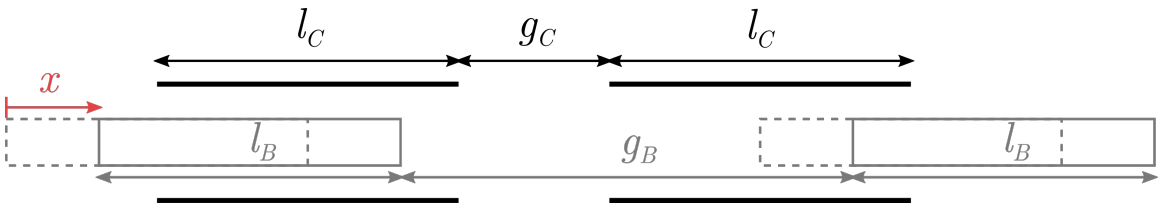


Figure 4.20: A diagram to show the lengths of electrodes, blocks and gaps, as used in the calculation of the effect shrinking has on the sensor. The top pair of black lines represent the sense electrodes. The dashed grey block indicates the 'central' position of the block.

4.3.5.3 In-plane shrinking

The Cirlex that makes up the capacitor plates will shrink differently from the copper blocks that move. The in-plane CLTE of the Cirlex is 30 ppm/K and the CLTE of copper is 16.6 ppm/K. Hence the differential shrinking between the Cirlex and the copper is 13.3 ppm/K; this is how much more the Cirlex will shrink than the copper. Let us assume a temperature change of 130 K. Hence the Cirlex will shrink by 3.9 µm/mm and the copper would shrink by 2.2 µm/mm. Equivalently, the Cirlex shrinks by 1.69 µm/mm more than the copper.

In the earlier calculation of the sensor output, it was assumed that the length l of the moving block was the same as the length l of the capacitor plate. Although they can be designed to be so at one temperature, because the block and capacitor plates are made of different materials, they will shrink differently so cannot be always the same length. In order to account for this, here follows a re-examination of the calculation in section 4.3.4, without making this assumption.

The position sensor consists of two capacitors, C_1 and C_2, that are connected in series. Consider the metal block as offset by a distance x from the central position in which the metal block fills half of the capacitor, as shown in fig. 4.20. Let the initial (room) temperature lengths be indicated by a superscript 0. Each sense electrode has a length l_C. There is an in-plane gap between the two electrodes, separating them by a distance g_C. The moving copper blocks each have length l_B and are separated by a gap g_B, controlled by copper.

As the temperature drops, the relative shrinking of the Cirlex will decrease the length of the capacitor plates and the gap between them. Below is repeated the earlier calculation of the sensor response considering the different behaviours of Cirlex and copper at low temperature.

The position sensor consists of two capacitors, C_1 and C_2, that share one plate. Consider the moving metal block as offset by an amount x from the central zero

position. Consider the capacitor which contains more block when it moves by an amount x. In this case, $l_C + \frac{g_C}{2} - [\frac{l_B+g_B}{2}] + x$ of the capacitor contains the metal filler block. If $l_C = l_B$ and $g_C = g_B$, this simplifies to $\frac{l}{2} + x$ as before. The amount empty and the amount full must total l_C. Hence the empty part of the sensor is given by $-\frac{g_C}{2} + \left[\frac{l_B+g_B}{2}\right] - x$. This is treated as two capacitors in parallel.

The empty section has capacitance

$$\begin{aligned} C_E &= \frac{\varepsilon_0 A_E}{d} \\ &= \frac{\varepsilon_0 w \left(-\frac{g_C}{2} + \left[\frac{l_B+g_B}{2}\right] - x\right)}{d} \end{aligned} \tag{4.19}$$

where w is the width of the plates and d is the distance between them. Suppose the block has thickness h. Suppose also the block lies directly in the centre of the gap. The full section (C_F) can then be treated as two capacitors (A and B) of spacing $\frac{d-h}{2} \equiv D$ with areas

$$A_A = A_B = \left(l_C + \frac{g_C}{2} - \left[\frac{l_B + g_B}{2}\right] + x\right) \times w\,. \tag{4.20}$$

The total full capacitance is given by

$$\begin{aligned} C_F &= \frac{C_A C_B}{C_A + C_B} \\ &= \frac{\varepsilon_0^2 \varepsilon_r^2 A_A A_B D}{D^2 \varepsilon_0 (A_A + A_B)} \\ &= \frac{\varepsilon_0 \varepsilon_r w^2 \left(l_C + \frac{g_C}{2} - [\frac{l_B+g_B}{2}] + x\right)\left(l_C + \frac{g_C}{2} - [\frac{l_B+g_B}{2}] + x\right)}{Dw(2l_C + g_C - [l_B + g_B] + 2x)}\,. \end{aligned} \tag{4.21}$$

This simplifies to

$$C_F = \frac{\varepsilon_0 \varepsilon_r w \left(l_C + \frac{g_C}{2} - [\frac{l_B+g_B}{2}] + x\right)}{(d-h)}\,. \tag{4.22}$$

Combining the two parts of this half gives

$$\begin{aligned} C_1 &= C_E + C_F \\ &= \frac{\varepsilon_0 \varepsilon_r w \left(-\frac{g_C}{2} + [\frac{l_B+g_B}{2}] - x\right)}{d} + \frac{\varepsilon_0 \varepsilon_r w \left(l_C + \frac{g_C}{2} - [\frac{l_B+g_B}{2}] + x\right)}{(d-h)}\,. \end{aligned} \tag{4.23}$$

For the other half of the device, the schema is similar, except that the block fills a portion $\left(l_C + \frac{g_C}{2} - [\frac{l_B+g_B}{2}] - x\right)$, and $\left(-\frac{g_C}{2} + [\frac{l_B+g_B}{2}] + x\right)$ is left empty. Hence

$$\begin{aligned} C_2 &= C_{E*} + C_{F*} \\ &= \frac{\varepsilon_0 \varepsilon_r w \left(-\frac{g_C}{2} + [\frac{l_B+g_B}{2}] + x\right)}{d} + \frac{\varepsilon_0 \varepsilon_r w \left(l_C + \frac{g_C}{2} - [\frac{l_B+g_B}{2}] - x\right)}{d-h}\,. \end{aligned} \tag{4.24}$$

Next, find the sum and difference of these two, as this will be required for the final readout.

$$C_1 + C_2 = 2\varepsilon_0\varepsilon_r w \left[\frac{\frac{-g_C}{2} + \left\lfloor \frac{l_B+g_B}{2} \right\rfloor}{d} + \frac{l_C + \frac{g_C}{2} - \left\lfloor \frac{l_B+g_B}{2} \right\rfloor}{d-h} \right] \tag{4.25}$$

$$\begin{aligned} C_2 - C_1 &= \frac{2\varepsilon_0\varepsilon_r wx}{d} + \frac{\varepsilon_0\varepsilon_r w\,(-2x)}{d-h} \\ &= 2\varepsilon_0\varepsilon_r wx \left(\frac{1}{d} - \frac{1}{d-h} \right). \end{aligned} \tag{4.26}$$

The readout on the digital electronics board is given by

$$\begin{aligned} f &= \frac{\Delta C}{\Sigma C} \\ &= \frac{C_2 - C_1}{C_1 + C_2} \\ &= \frac{2\varepsilon_0\varepsilon_r wx \left(\frac{1}{d} - \frac{1}{d-h}\right)}{2\varepsilon_0\varepsilon_r w \left[\frac{\frac{-g_C}{2} + \left\lfloor \frac{l_B+g_B}{2} \right\rfloor}{d} + \frac{l_C + \frac{g_C}{2} - \left\lfloor \frac{l_B+g_B}{2} \right\rfloor}{d-h} \right]} \\ &= \frac{x \left(\frac{1}{d} - \frac{1}{d-h}\right)}{\left[\frac{\frac{-g_C}{2} + \left\lfloor \frac{l_B+g_B}{2} \right\rfloor}{d} + \frac{l_C + \frac{g_C}{2} - \left\lfloor \frac{l_B+g_B}{2} \right\rfloor}{d-h} \right]}. \end{aligned} \tag{4.27}$$

Given this expression for the overall sensor output, the behaviour of the output with changing temperature can now be determined. At low temperature, considering the CLTEs given above, $l_C = 0.9961 l_C^0$ and $g_C = 0.9961 g_C^0$, while $l_B = 0.9978 l_B^0$ and $g_B = 0.9978 g_B^0$. These factors enter the readout value as follows:

$$\begin{aligned} f &= \frac{x \left(\frac{1}{d} - \frac{1}{d-h}\right)}{\left[\frac{\frac{-0.9961 g_C}{2} + \left\lfloor \frac{0.9978 l_B + 0.9978 g_B}{2} \right\rfloor}{d} + \frac{0.9961 l_C + \frac{0.9961 g_C}{2} - \left\lfloor \frac{0.9978 l_B + 0.9978 g_B}{2} \right\rfloor}{d-h} \right]} \\ &= x \times \frac{\left(\frac{1}{d} - \frac{1}{d-h}\right)}{\left[\frac{-0.9961 \frac{g_C}{2} + 0.9978 \left\lfloor \frac{l_B+g_B}{2} \right\rfloor}{d} + \frac{0.9961 \left(l_C + \frac{g_C}{2}\right) - 0.9978 \left\lfloor \frac{l_B+g_B}{2} \right\rfloor}{d-h} \right]}. \end{aligned} \tag{4.28}$$

The effect these cooling factors have can be explored by substituting in typical values for d, h, l and g. In the main sensor design, $d = 6\,\text{mm}$, $h = 5\,\text{mm}$, $l = 25\,\text{mm}$ and $g = 20\,\text{mm}$. At the warm (construction) temperature, the value of the distance

scale factor is

$$\begin{aligned}
&\frac{\left(\frac{1}{d}-\frac{1}{d-h}\right)}{\frac{-\frac{g_C}{2}+\left[\frac{l_B+g_B}{2}\right]}{d}+\frac{\left(l_C+\frac{g_C}{2}\right)-\left[\frac{l_B+g_B}{2}\right]}{d-h}} \\
&= \frac{\left(\frac{1}{6}-\frac{1}{6-5}\right)}{\frac{-\frac{20}{2}+\left[\frac{25+20}{2}\right]}{6}+\frac{\left(25+\frac{20}{2}\right)-\left[\frac{25+20}{2}\right]}{6-5}} \\
&= -0.05714\,.
\end{aligned} \tag{4.29}$$

For the case where the shrinking is included, the scale factor is

$$\begin{aligned}
&= \frac{\left(\frac{1}{6}-\frac{1}{6-5}\right)}{\left[\frac{-0.9961\frac{20}{2}+0.9978\left[\frac{25+20}{2}\right]}{6}+\frac{0.9961\left(25+\frac{20}{2}\right)-0.9978\left[\frac{25+20}{2}\right]}{6-5}\right]} \\
&= -0.05749\,.
\end{aligned} \tag{4.30}$$

There is a very small difference between these two values: when the full-size sensor is cold, the readout value is expected to increase by around only $(0.05749-0.05714)\div 0.05714 = 0.6\%$. This is not a dominant contribution to sensor error.

4.3.5.4 Conclusion on shrinking

Overall, these calculations above demonstrate that shrinking should have a negligible effect on the output of the sensor. That the sensor design behaves in this way is demonstrated for a real sensor in section 4.5.2.2.

4.3.6 Deviations

The expected output of the sensor, as described in section 4.3.4 is given by

$$\begin{aligned}
f &= \frac{2x}{l}\frac{1}{1-\frac{2d}{h}} \\
&= \frac{2x}{l}\frac{\Delta^-}{\Delta^+}\,.
\end{aligned} \tag{4.31}$$

In the calculation of this, it was assumed that the block was in the centre of the gap between the main capacitor plates. If the block is off-centre, i.e. closer to either the excitation plates or sensor plates, the distances between the capacitor plates for the two capacitors in the 'full' section of each half will be different. As shown earlier,

$$\begin{aligned}
C_F &= \frac{C_A C_B}{C_A + C_B} \\
&= \frac{\varepsilon_0 \varepsilon_r A_A A_B}{A_A D_B + A_B D_A}\,.
\end{aligned} \tag{4.32}$$

There should be no situation in which the areas of the two capacitors are be different, as they both feature the same metal block as one plate of the capacitor and a Cirlex plate as the other. Hence $A_A = A_B = A$.

$$\begin{aligned} C_F &= \frac{\varepsilon_0 \varepsilon_r A^2}{A\left(D_A + D_B\right)} \\ &= \frac{\varepsilon_0 \varepsilon_r A}{D_A + D_B}\,. \end{aligned} \tag{4.33}$$

Any offset of the central block will result in an increase to either D_A or D_B and a decrease to the other of the same amount. The sum of the two distances, however, is unchanged by an offset. Hence the capacitance of the 'full' parts of the capacitors will be unchanged by offsetting the blocks. As such a move would not change the capacitance of the empty sections of the capacitor either, as the metal block is by definition not in that section, the total capacitances and hence the overall output would remain unchanged. This is a very useful feature of the sensor design, in combination with the readout scheme, as small inaccuracies that may be present in the machining or assembly of the sensor do not feed into the final sensor output.

4.3.7 Sensor integration

The individual sensors do not directly measure the changing space between the ICV dome and the PMT truss. Although to measure the vertical change with a single sensor would be possible, it would be extremely difficult to design a sensor to measure radial movement of the PMT truss with respect to the cryostat vessel for the following reasons. The sensors all sit above the PMT truss, the top of which is above the level of the flange that connects the main body of the inner ICV to the dome of the ICV; see fig. 4.3. This means any sensor connection to the ICV must be to the dome, and not to the main body of the ICV. Once the dome is lowered onto the main body, there is very limited access to the inside of the vessel, which complicates the connection of sensors. Radial sensors would need to press outwards against the dome of the ICV, but this will not be in place when the sensors are installed. Although it would be reasonably straightforward to have a sprung vertical sensor that compressed as the dome was lowered, it is difficult to create analogues of this for radial or torsional sensors, given the assembly procedure of lowering the dome last.

A further consideration is that each individual sensor would need to be free to move along the surface of the ICV dome, though would also need to be held against it. A position sensor is sensitive along only one direction, and therefore able to move in only one direction. Movement in other directions would put stresses on the sensor that

would be liable to break it. Hence the sensors would need to be free from constraint in the directions in which they were not measuring.

All in all, this gives a very tangled and confused system of sensors and assembly considerations. However, almost all of these challenges can be overcome by connecting six sensors into a system known as a 'Gough-Stewart Platform Mechanism' (GSPM), or more colloquially as a 'hexapod'. The sensors would form a single unit of two platforms connected by six sensors, capable of measuring all six degrees of freedom of movement of one platform with respect to the other. This avoids the need for individual sensor connections to the ICV. The hexapod can be connected as a unit to the PMT truss and the dome; see section 5.5.2 for further discussion of how this is done. More details of the general theory of GSPMs, our particular use, and the geometry and algebra involved are in Chapter 5.

4.4 Materials

4.4.1 Capacitor plate substrate

The plates in the sensor that form the parallel plates of the capacitors are made of copper-clad Cirlex. Cirlex is a composite material manufactured by US company Fralock.[1] It consists of copper deposited on a polyimide, adhesiveless laminate. The laminate in turn consists of many layers of Kapton, a polyimide sheet material manufactured by DuPont. Cirlex was used in the LUX experiment and will be used in LZ for the PMT base plates, onto which the essential circuit components for the PMTs are soldered. Cirlex is therefore well known within the experiment and has been appropriately screened and tested for use in xenon.

Cirlex is described by the manufacturer as having 'good integrity at extreme temperatures', and its previous use in LUX demonstrates its ability to withstand the low temperatures of two-phase xenon dark matter experiments. Its coefficient of linear thermal expansion (CLTE) in-plane is closely matched to that of polyether ether ketone (PEEK): 30 ppm/K for Cirlex, and 26 ppm/K for PEEK.[81] For comparison, the CLTE of copper is 16.6 ppm/K. However, the through-thickness CLTE of Cirlex is quoted as 118 ppm/K by the manufacturer, Fralock.[81] The dielectric constant at 10 kHz and 25 °C is given as 3.45. It is not known at low temperatures but is expected to change, as in general the dielectric permittivity of polymers is a strong function of the temperature; see fig. 4.21. However, as the Cirlex does not feature

[1] http://www.fralock.com/semiconductor/Cirlex/

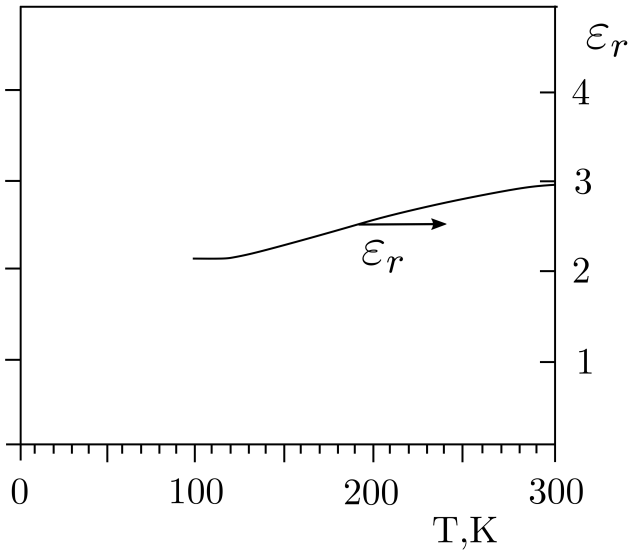


Figure 4.21: The dielectric permittivity of polymers in general as a function of temperature. These are difficult data to find, as although materials are regularly tested at high temperatures, there is less information about the behaviour of polymers, particularly their electric properties, at low temperatures. Adapted from [19].

within the capacitors, the change in relative permittivity will not affect the sensor measurements.

The radioactivity of Cirlex was measured by the screening programme at Boulby Underground Laboratory, in the high-purity germanium detectors; this is discussed further in section 4.4.6 below. The following results were found, where 'early' and 'late' refer to the first and second parts of the relevant decay chains, as discussed in section 2.5.1.

Item	U early (mBq/kg)	U late (mBq/kg)	Th early (mBq/kg)	Th late (mBq/kg)	Co60 (mBq/kg)	K40 (mBq/kg)
Cirlex	23.88	19.13	3.19	3.19	0.63	15.08

As some early designs featured a slider made of dielectric, an alternative substrate was considered that potentially had a smaller change in relative permittivity with temperature. CuFlon, manufactured by PolyFlon, consists of copper deposited on PTFE. It has been used by the GERDA neutrinoless double-beta decay experiment and was assessed for used by NEXT-100, another double-beta decay experiment, which suggests it may be appropriate for use in LZ. Pertinently, the relative permittivity of PTFE (2.1) remains virtually unchanged between $-40\,°C$ and $-250\,°C$ and 5 Hz to 10 GHz, which suggests that CuFlon would be highly appropriate in a sensor with a dielectric slider. (The slider should be made of the same material as the plate

substrate in order for geometric changes during cooling to cancel.) Nevertheless, having a smaller relative permittivity (2.1 rather than 3.45) would mean that the change in capacitance for a sensor that operates on a changing dielectric would be smaller, leading to a less sensitive sensor.

However CuFlon suffers from significant size changes during cooling, which moreover are different for clad and unclad CuFlon. For bare CuFlon, the CLTE is 129 ppm/K, while copper-clad CuFlon has CLTEs of 26.1 ppm/K in plane and 194 ppm/K through-thickness. A further disadvantage of CuFlon is the relative softness of PTFE. The capacitor plates may not end up being rigid enough, and any small deviations could result in unwanted changes in capacitance of the sensors. Nevertheless, it would stand to be radiopure enough for use in LZ. The screening of CuFlon by NEXT-100 gave the following backgrounds in mBq/kg:

Element	Activity (mBq/kg)
U-238	<33
Rn-226	<1.3
Th-232	<1.1
Th-228	<1.1
U-235	<0.6
Co-60	<0.3
K-40	4.8 ± 1.1
Cs-137	<0.3

This suggests that CuFlon would contribute less to the radioactive background than the same amount of Cirlex would.

An alternative to either of these is to use a sheet of metal as the capacitor plate, and avoid having any substrate at all. However this makes engineering the sensor significantly more difficult, as there is not a straightforward way to hold the plate without introducing something that complicates its capacitance. It is also more difficult to design a guard electrode in this case. To do so, a separate piece of metal would need to be insulated from the sense plate but held very close to it. Using copper deposited on a substrate simplifies this and makes the mechanical design of the sensor much easier. It also permits the use of photolithography, as will be described below.

Ultimately, Cirlex was chosen for the sensor plates because of its previous use within the LUX experiment and its planned use for the PMT bases in LZ. The relevant expertise for sourcing, working with and cleaning Cirlex are already within the collaboration, so additional investigations would not be required.

4.4.1.1 Photolithography

Photolithography is the process of removing some copper from a substrate using light-sensitive chemicals, masks and light. It can result in very precise designs in the shape of the remaining copper. This process is used to shape the copper on the Cirlex of the position sensors, and is also being used for creating the pads and wiring on the Cirlex PMT bases.

There are two common ways to remove copper and leave behind the appropriate shapes on the substrate. One is photolithography; the other is mechanical etching. Mechanical etching should leave no residue after cleaning, and there is no risk of any chemicals being absorbed by the substrate. Hence this method was chosen for etching the sensor shapes for the System Test sensor as described below. However the laminate nature of Cirlex means it is not an easy material to neatly mechanically etch, as the layers are scratched up by the drill bit used for this. This can result in a rough surface on the etched Cirlex that risks pieces of Cirlex 'dust' detaching into the xenon during the experiment. Care was taken for the System Test sensor that the sensor was well cleaned and the Cirlex was polished to remove roughness as far as possible. However the challenge this posed was a key driver towards using photolithography in the final design.

To use photolithography to produce the sensor, the first step is to draw the designs that are used to create the photomask. These designs mark out which sections of copper should be removed and which sections should be kept. From these the photomask is produced, on which the sections where copper should be removed are clear and the sections where the copper should remain are dark. Using a light-sensitive emulsion on a film, the mask can be produced with a resolution of 4000 dpi. The Cirlex is coated with a photo-resistive layer before the mask is put in place and exposed to light. The light hardens those parts of the photo-resistive layer that are visible through the mask. An acid is then used to remove those parts of the copper that are not protected by the hardened photoresist, resulting in an image of the mask in the copper on the Cirlex. This image can be very precise, which means complicated parts like the bases for the PMTs can be produced relatively easily. The use of photolithography for other parts of LZ reinforced the decision to use it for the position sensors. The sensor photolithography design can be seen in fig. 4.22.

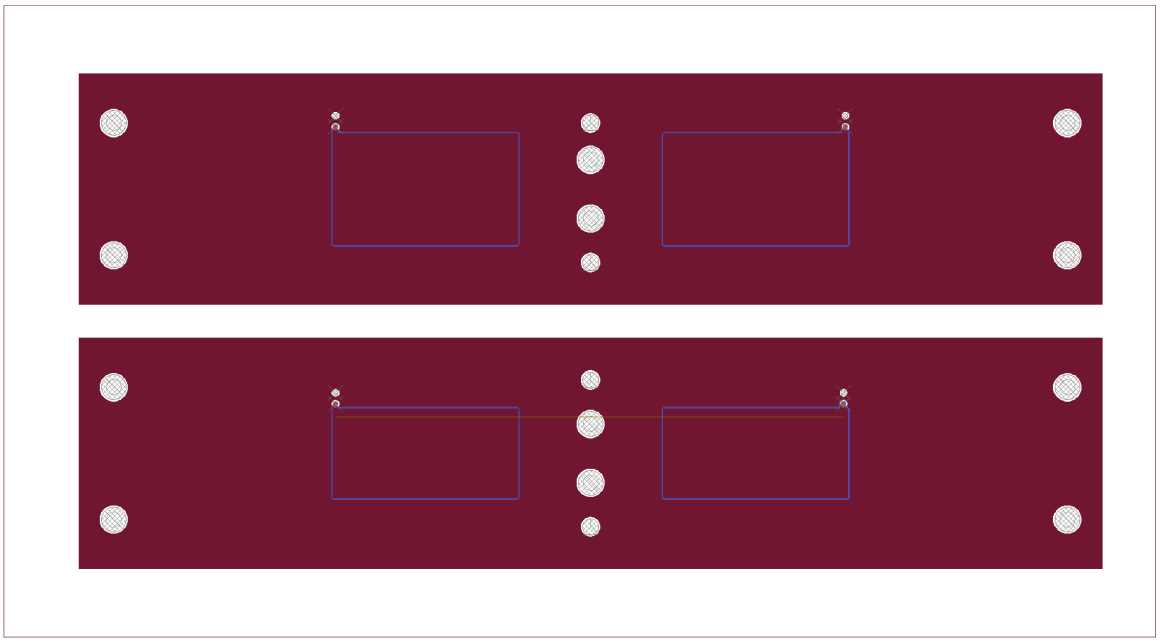


Figure 4.22: The image used to create the photolithography mask for producing the electrode design on the copper-clad Cirlex.

4.4.2 Copper

The outer casing of the sensor is a commercially available copper tube: a Wednesbury copper pipe with a 35 mm outer diameter and an inner diameter of 33 mm. This provides rigidity and structure to the sensor. Copper was chosen for the shielding material because it is generally suitable for use in low-background experiments. Nevertheless, to be sure this particular copper is appropriate, sections of the tube were screened at Boulby Underground Laboratory using high purity germanium detectors. The purpose of screening is to determine the radiopurity of the material, as described in section 2.5. The results of the screening are given below and confirm that this tube is suitable for use in LZ.

4.4.2.1 Copper screening

The screening process described below as an example is that undergone by the copper tube; all of the materials used in LZ will have undergone something very similar.

Following procurement of the Wednesbury tube, ten 10 cm lengths were cut from it to be screened. The procurement included enough material for this, a new System Test sensor and the six final sensors. Hence screening part of this batch should be representative of the material that goes into the final detector. These ten short sections were then cleaned according to the LZ-internal cleaning protocol. This included

immersing them in a 6 % solution of Citranox (a weak acid cleaner), treatment in an ultrasonic bath using both acetone and IPA, and repeated wiping with IPA-soaked lint-free cloths. All of this took place in a cleanroom. Once suitably clean, the tube sections were triple-bagged in radon-impermeable bags, and sent to the team at Boulby Underground Laboratory.

The screening involved placing the ten sections of tube in a high-purity germanium detector, which was able, over a period of a week, to determine the quantities of certain radioactive elements present. These are given below.

Element	Activity (mBq/kg)
U early	21.4
U late	2.5
Th early	4.0
Th late	2.6
Co60	1.1
K40	28.0

From these values, it is possible to calculate the total radioactivity for each component, which means multiplying the activity per unit mass by the component's mass. (For example, it might be acceptable to have something tiny with a relatively high radioactivity, or equally if a component has a relatively high mass, the radiopurity requirements would be much more stringent.) For the copper tube, the total mass is 1.43 kg for all six sensors. The tube alone therefore contributes an expected neutron yield of 0.02 neutrons per year. Further sensor contributions are given in section 4.4.6.

4.4.2.2 Copper machining

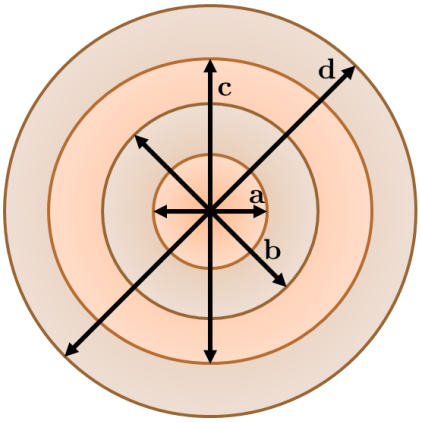
Copper parts machined from a block are used for the metal structures within the sensor. Some of these have a structural role, for example holding the sensor plates in the right position. In each sensor, two copper blocks are actuated and cause the change in capacitance. These blocks and the parts holding the sensor plates need to be made from the same material to ensure they behave in the same way when the temperature changes, as explained in section 4.3.5 above. Copper was chosen for these parts as high purity copper is easy to procure (and hence is relatively cheap) and will not contribute significantly to the background radioactivity from the sensors. A large block of copper will be used to create all of these parts, plus some of those for the level sensors. This will minimise the length of time that the final sensor surface area will have been in contact with air; if the surface is in air for any considerable length of time, lead plate-out on the surface is likely, as discussed in section 2.5.

4.4.3 PEEK

Polyether ether ketone (PEEK) is a polymer known to be suitably non-radioactive and non-toxic to the xenon purity. The stoppers at the end of the sensors will be made of this, as will the screws that hold some parts together. As PEEK is a relatively hard polymer, it is fairly easy to machine, so can be used for parts where the dimensions must be precise, such as screws. As with the copper discussed above, large blocks of PEEK will be used to produce a number of sensor components across the position and level sensors. This material has been screened and found to be acceptable for use in LZ.

4.4.4 Wiring

The cables used for the position sensor are the same as those for the PMT signals, as these are guaranteed to be acceptable for use in LZ. These will be provided by another group in LZ, pre-fitted with the connectors discussed in section 4.4.5. The cable is a specially created coaxial cable from the company Axon, with a copper core and braid, and extruded FEP as the dielectric and outer coating. A diagram of the cable can be seen in fig. 4.23.



a: 0.254 mm, bare copper core (r = 0.127 mm)
b: 0.83 mm, extruded FEP dielectric (r = 0.415 mm)
c: bare copper shield (woven)
d: 1.3 mm, outer jacket, extruded FEP

Figure 4.23: The dimensions of the cable used for the position sensors, as produced by Axon.

The main cable will connect between the flange (on the other side of which is the electronics) and the 'connector box' described in section 4.4.5, which is just above the sensors. This cable will be around 13 m in length. In addition to the long cable, a short cable will interface between the connector box and the sensor plates. This enables the connection to the sensor to be made by soldering the short cable onto

the coppered Cirlex. The short cable will be the same Axon coaxial cable as the long cable.

4.4.5 Connectors

To connect the long, main cables to the short sensor cables, the same Harwin pins and receptacles as the PMT cables and bases will be used. These were found to be far less radioactive than many commercial connectors, though they do still make some contribution. However the number of pins and receptacles used for the sensors is a tiny fraction of the overall total, so the sensors do not contribute significantly to the background from the connectors.

The connectors are housed within a grounded copper 'castle' that provides shielding and strain relief for the cable connections. Each cable is split onto two pins: one for the signal and one for the grounded sheath. The main cable that runs from the connectors to the flange is coaxial, as is the short cable from the connectors to the sensor. Each cable is split across two pins and the corresponding two receptacles combine into a single coaxial cable. The grounded copper structure around the connectors will provide much-needed shielding to protect the signal when it is split out of the ground sheath of the coaxial cable.

4.4.6 Total radioactivity

The process of screening was described for the copper tube in section 4.4.2.1 above. A similar procedure was undertaken for all of the materials and components that will feature in the position sensors.

Item	Number	Unit mass (g)	Total mass (kg)	U early (mBq/kg)	U late (mBq/kg)	Th early (mBq/kg)	Th late (mBq/kg)	Co60 (mBq/kg)	K40 (mBq/kg)
Copper Tube	6	237.834	1.427	21.400	2.500	4.000	2.600	1.100	28.000
Copper	6	238.118	1.429	14.500	1.700	1.300	1.200	0.400	7.000
Cirlex	6	22.688	0.136	23.880	19.130	3.190	3.190	0.630	15.080
Stainless Steel	6	70.560	0.423	59.000	26.000	1.300	1.300	10.000	6.000
PEEK	6	11.239	0.067	14.000	4.600	5.000	3.000	0.200	19.000
PEEK Screws	6	5.060	0.030	14.000	4.600	5.000	3.000	0.200	19.000
Copper Screws	6	6.368	0.038	14.500	1.700	1.300	1.200	0.400	7.000
Solder	6	0.050	0.000	58.190	11.840	10.670	10.670	2.240	31.810

Based on these values, the total expected neutron yield per year can be calculated for each material in the sensors. Summing all of these gives the expected neutron background due to the sensors.

Material	neutron yield total (n/yr/material)
Copper	0.03
Cirlex	0.16
PEEK	0.04
Stainless Steel	0.17
Solder	0.00
Total	0.40

By way of comparison, the TPC thermometers are expected to produce a total of 1.8 neutrons per year, the wire grid holders are expected to produce 20.71 neutrons per year, and the cryostat vessel itself 159 neutrons per year. The position sensors therefore do not contribute significantly to the neutron background in LZ. This is as a result of having carefully chosen a design that could be made of appropriate materials and subsequently having screened those materials. Hence the sensors meet the requirements to be able to operate in a low-background environment.

4.5 System Test at SLAC

The LZ System Test was created at the Stanford Linear Accelerator Center (SLAC) to explore, optimise and verify the designs of many aspects of the LZ detector, from the structure of the wire grids to the xenon flow system. The system that was run for Phase 1 of these tests used a narrow PTFE TPC inside stainless steel cryostat vessels, operating as a two-phase xenon system. This enabled us to install and test a position sensor in the environment in which it will run in LZ. The first phase of the System Test had multiple 'runs' in which we installed position sensors. Runs 3 - 6 used an early position sensor design (April - June 2016), described in section 4.5.1. A sensor very similar to the final design and discussed in section 4.5.2 was produced for Run 7 of the System Test.

4.5.1 The early runs

4.5.1.1 Design

The position sensor in the System Test demonstrated that the technology created to measure the significant thermal contraction of the field-cage system functioned as expected. To achieve this in the early runs of the System Test, the position sensor was connected between the top of the TPC and the structure above it that was directly connected to the cryostat vessel; see fig. 4.24. When the detector was running, the

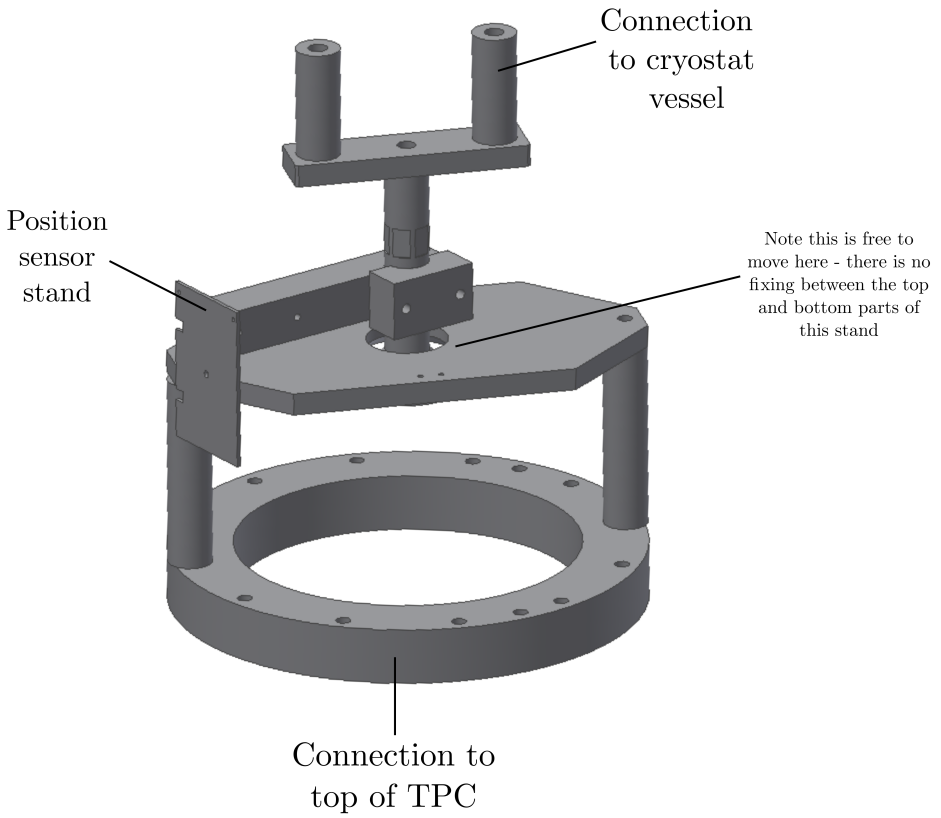


Figure 4.24: CAD model showing how position sensor is connected to cryostat vessel and TPC

weight of the TPC was resting on the bottom of the cryostat. As the system cools to operating temperature, the material of the TPC cools and shrinks towards the base on which it is supported. Hence the distance between the top of the TPC and the structure attached to the cryostat vessel increases, and this would be measured by the position sensor. Although in LZ there will be six position sensors connecting the top of the TPC and the cryostat vessel, there was not space for this in the System Test, and one sensor was deemed to be enough to determine the success of the design.

The main body of the sensor is made from Cirlex, as described in section 4.4.1, with the electrode shapes etched into the copper on the surface of the Cirlex. The operating principle of the position sensor used in the System Test is based on picking up linear travel via a slider that moves a dielectric between two adjoining parallel plate capacitors. The copper surfaces of the Cirlex form the two plates of the capacitor, while a piece of blank Cirlex with a cut-out hole is the dielectric slider; see fig. 4.25.

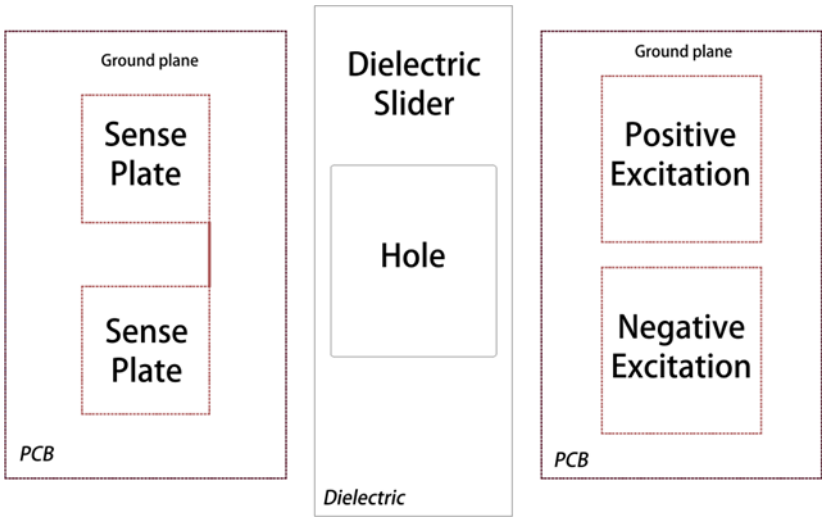


Figure 4.25: A schematic of the electrodes and dielectric slider for the position sensor in the SLAC system test

The whole sensor is then screwed into a specially designed holder, which has space for the cables and connectors, and which holds the sensor upright. All of these can be seen in the solid model images in fig. 4.26. The sensor is held in place with a single screw through the centre that pulls it onto the steel support. The Cirlex sensor and the steel support will shrink by different amounts during cooling. Hence if more than one screw was used, tensions would be introduced to the sensor owing to this differential shrinking, which could result in warping or damage to the sensor. This motivated the design using a single, central screw. To avoid the sensor rotating about this screw, the stand has raised sides that run along the edges of the sensor, with cut-outs to allow egress for the three cables.

The separate parts of the sensor are held together using a special epoxy, Masterbond EP29LPSP. This is a certified low out-gassing, low-temperature epoxy. Hence it is suitable for use in two-phase liquid xenon experiments. This epoxy is used in large volumes elsewhere in LZ. The main use is for fixing the grid wires in place within the grid ring. The epoxy used for the sensor is a comparatively small quantity. The use of epoxy ensured that through-thickness shrinking of the sensor was controlled only by the shrinking of the Cirlex, and not other materials or items such as screws. The constructed sensor was tested in liquid nitrogen prior to shipping to SLAC to ensure that it would operate when cooled. The slider has a copper extension, which rests on top of a structure directly connected to the top of the TPC. The body of the sensor in its holder is attached to a bar connected to the cryostat vessel. These are the two parts that will move with respect to each other as the TPC cools and shrinks. The

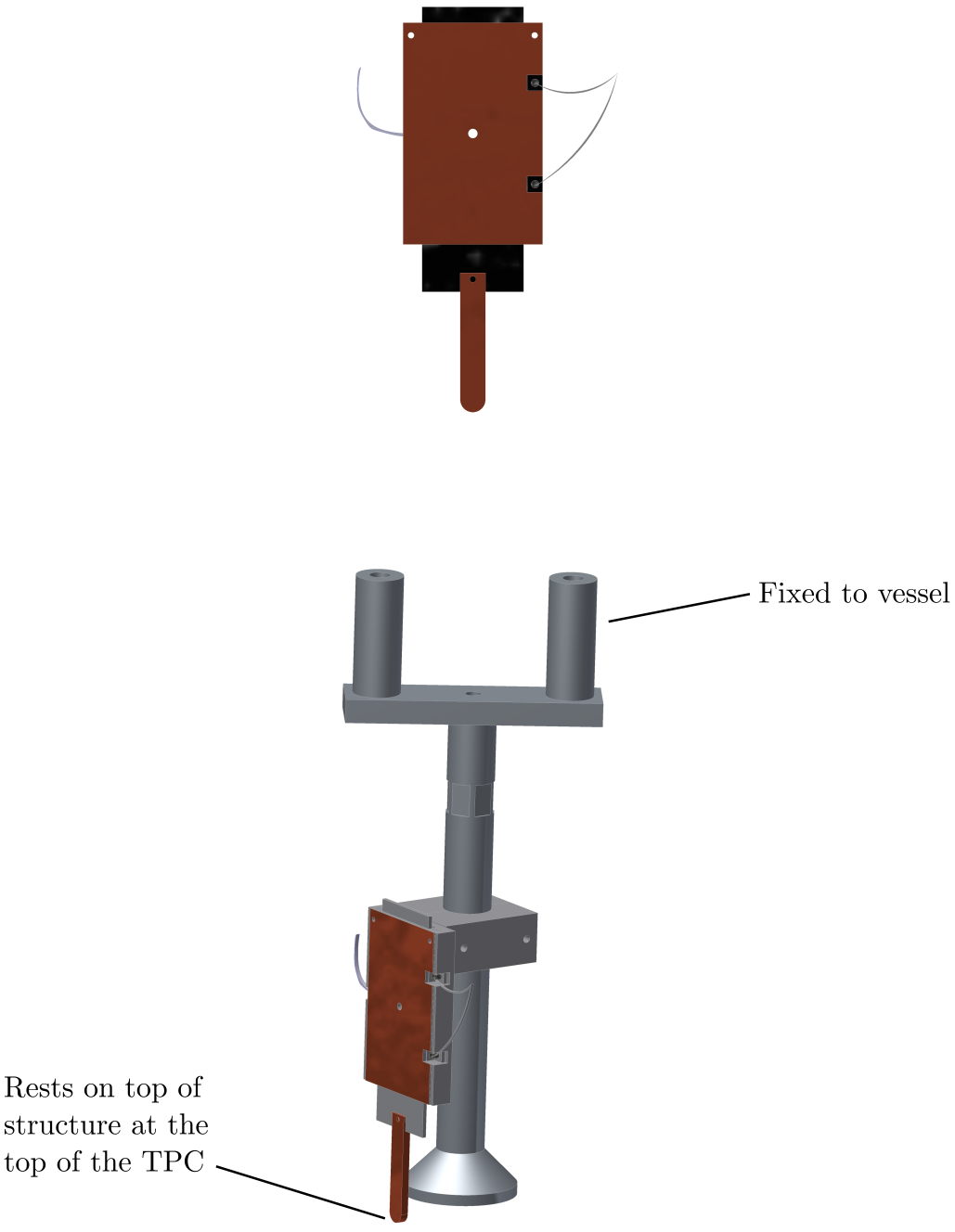


Figure 4.26: Solid models showing the design of the position sensor and its stand for the system test.



Figure 4.27: The position sensor for the early runs of the system test.

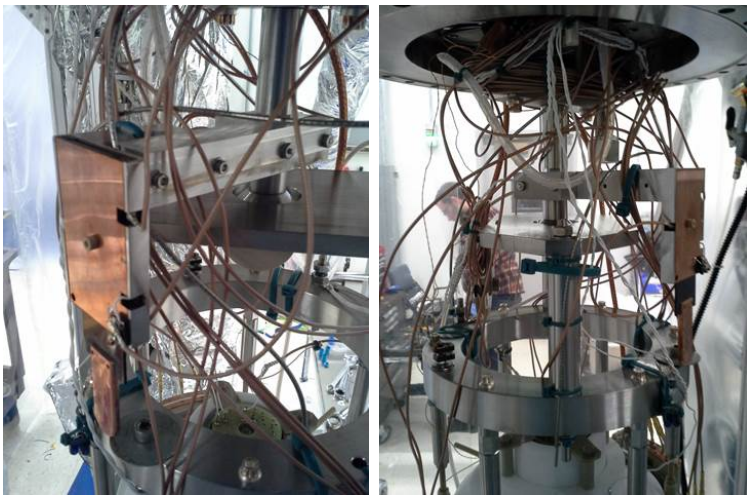


Figure 4.28: Photographs of the position sensor in place in the system test

installed sensor can be seen in fig. 4.28.

The position sensor and level sensors share the same readout board; all readout is via coaxial cables that connect from the sensor to a feedthrough onto which the readout board is mounted. The readout is an early version of the analogue feedback circuit described in Chapter 3. It minimises the effect of the cable capacitance on the sensor output.

4.5.1.2 Operation

In order to be mounted, an additional arm had to be added to the position sensor stand, as the design of the top of the detector changed between the position sensor being produced and it being installed. This can be seen in fig. 4.28. The cables are connected to the sensor with surface-mounted U.FL connectors, which are very small, press-on, coaxial connectors. Before the sensor could be mounted in the vessel, one of these connectors became detached from the Cirlex plate on which it was mounted. As a result, no signal could be read out. An ingenious fix using some spare components available at SLAC enabled an additional connector to be added to restore the sensor's functionality; see fig. 4.29. It was in this fixed state that the sensor went into the System Test.

The position sensor was operated during the very short Run 3 of the System Test, as well as throughout the longer Run 4 (April - June 2016). The results of these runs are discussed in section 4.5.1.4

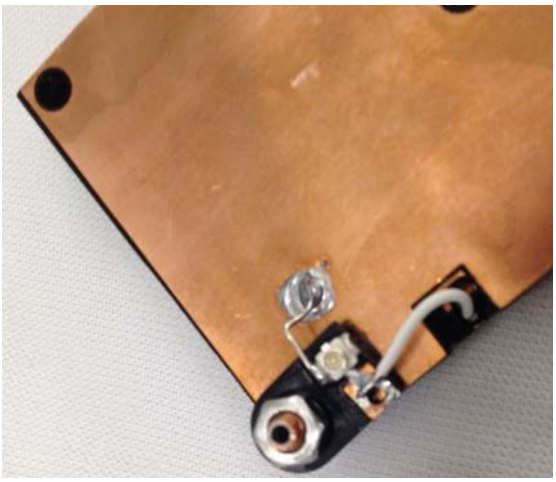


Figure 4.29: The fixing of the connector on the position sensor

4.5.1.3 Calibration

The sensor was constructed in Oxford and data was taken with it before it was sent to SLAC; see fig. 4.30. This consisted of taking data through the sensor readout, with the sensor in its holder and the sensor plunger resting on a platform that moved up and down. We thus had a set of data where a readout sensor value corresponds to a measured position, which could be used to demonstrate the linearity of the sensor.

An *in situ* calibration of the position sensor was undertaken at SLAC within the confines of the cleanroom, with the position sensor in place above the TPC. A series of washers of known heights were stacked one by one under the position sensor plunger, while the sensor took data through the system test's slow control system. This resulted in a set of readout sensor values and corresponding changes in height. The gradient of a plot of sensor values against height can then be used as a calibration factor. The y-offset of the graph is not meaningful as the zero does not necessarily bear any similarity to the zero of the previous data. The data can be seen in fig. 4.31. The calibration factor of $-0.0187\,\mathrm{mm/unit}$ can convert a differential reading from the sensor in ADC counts to a difference in height in mm. The higher the sensor reading, the less height was added, i.e. the further out the plunger is. Hence an increasing reading corresponds to the TPC shrinking away from the sensor.

If no offset is used, the zero position corresponds to a zero reading on the sensor, which is designed to be when the plunger is right in the centre. However a more useful offset when the detector is cooling and running is to have set to zero the position when the experiment is warm and the sensors have been installed. The sensor reading is then the differential shrinking of the TPC. This results in a calibration

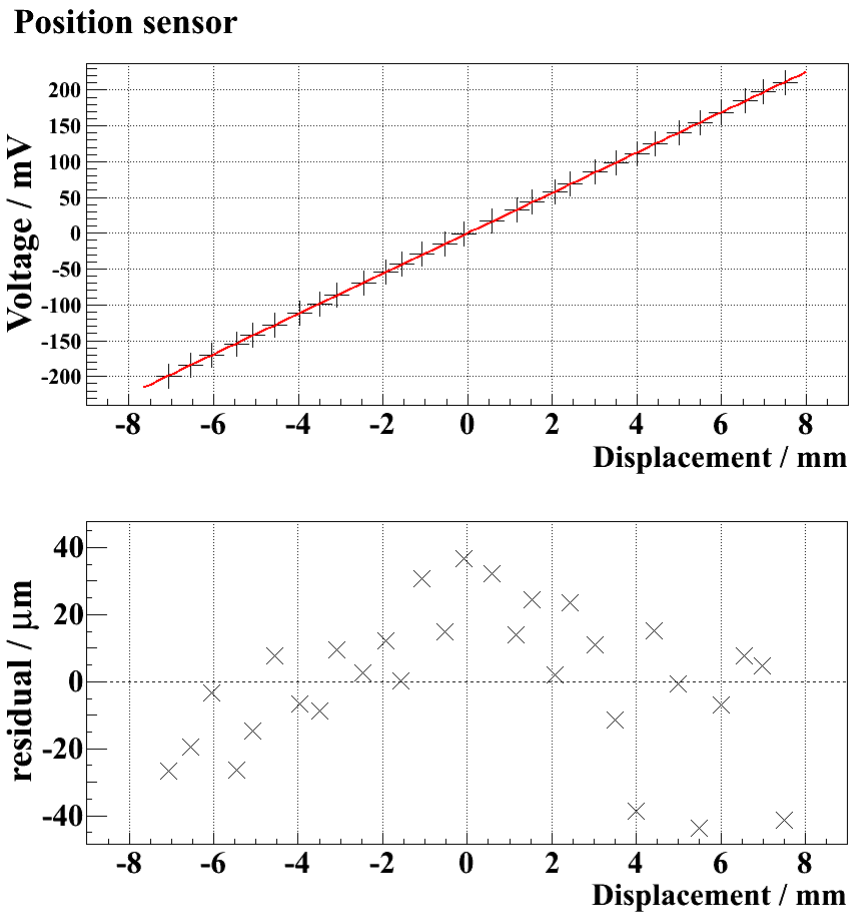


Figure 4.30: Data taken with the position sensor before it was taken to SLAC. This is a demonstration of the linearity of the sensor. The residual is compared to a straight line fit, shown in red in the top plot. This suggests that the conversion factor between sensor reading in mV and position reading in mm is 0.034 mm/mV.

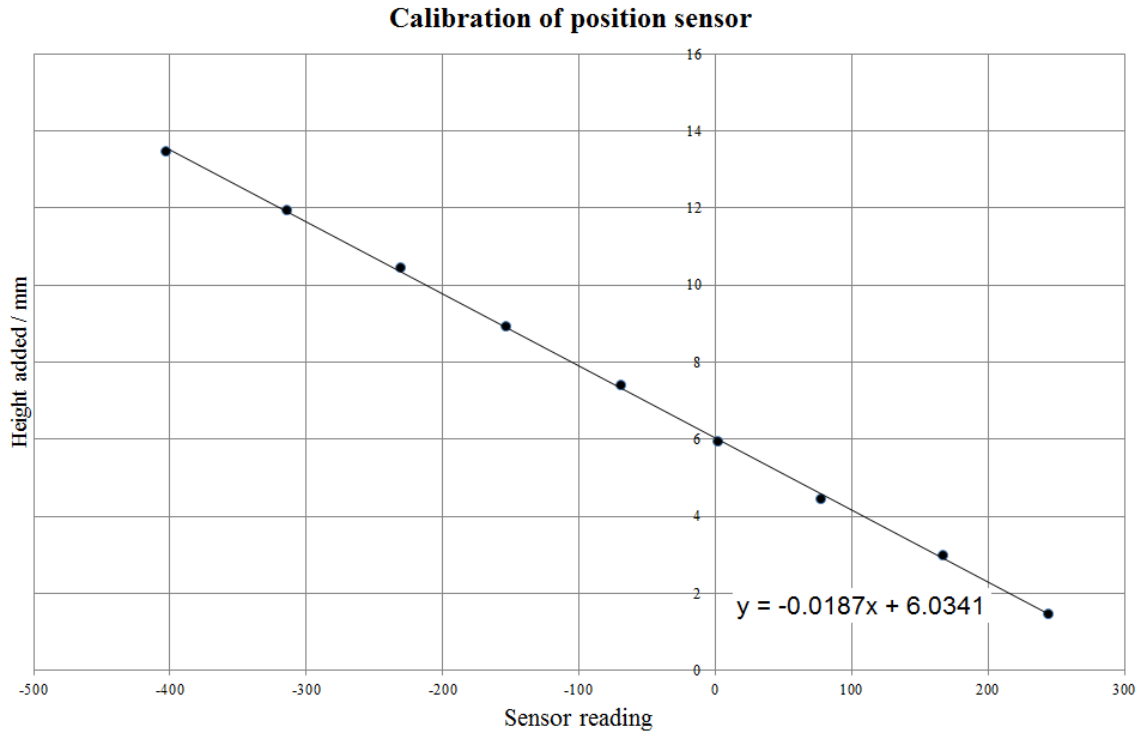


Figure 4.31: The calibration of the position sensor used in Runs 3 - 6 in the SLAC System Test. The height was added by inserting washers under the plunger, pushing the plunger into the sensor with each step. This was undertaken at ambient temperature while the system was open, and used the cables (2.3 m long) and electronics created for this run of the System Test. Uncertainties are not given here as this is not the final sensor configuration.

factor of $-0.0187\,\mathrm{mm/unit}$ to convert from sensor readings in ADC counts to position measurements in mm. It is this calibration factor that is applied to the data in section 4.5.1.4.

4.5.1.4 Results

The position sensor ran well during Runs 3 and 4. The data from the cooldown of Run 3 can be seen in Figure 4.32. The temperature drops from around 290 K to around 170 K and approximately stabilizes at that level. During this cooling, the top of the TPC moves down by around 1.2 mm. Further small changes happened as the temperature fluctuated around its final value. It should be noted that in this data no correction has been made for the changing dielectric constant of the material used as the dielectric slider. This is likely to have some effect on the output, though this has not been quantified. Nevertheless, the existence of this effect led to the use of a different sensor design for future iterations.

The position sensor showed that as the temperature periodically rose and fell, the sensor would measure the growing and shrinking of the TPC. In fig. 4.33, we see the correlation between temperature and position over around three weeks. Some of the variation in this measurement will arise because of the temperature gradients across the detector: the measured temperature may not correspond to a constant temperature across the PTFE of the TPC, so we would not necessarily expect a changing temperature to correlate perfectly with an exact position change.

The position sensor was also installed for Runs 5 and 6, but the sensor was accidentally disconnected between Run 4 and Run 5. The cable was pulled, which disconnected the U.FL plug on the cable from the socket on the sensor, and this was not noticed until after the outer vessel was closed. The vessel was not re-opened until after Run 6, so the sensor could not be reconnected until that point. This means no useful data was taken during Runs 5 and 6. However once the sensor was reconnected, it ran well, though there were no further experimental runs with this design, so no scope to take more data than that taken during Run 4.

The sensor generally functioned well, although subsequent designs avoided the use of U.FL cable connectors, as they were responsible for both the initial loss of sensor function and later loss of data-taking capability. Continuing to use them would have introduced too much risk of failure. After this design, we also moved away from using a dielectric slider as the means of changing the relative permittivity in the capacitors, as being unable to distinguish changes in relative permittivity from changes in position limited the precision and accuracy of the sensor.

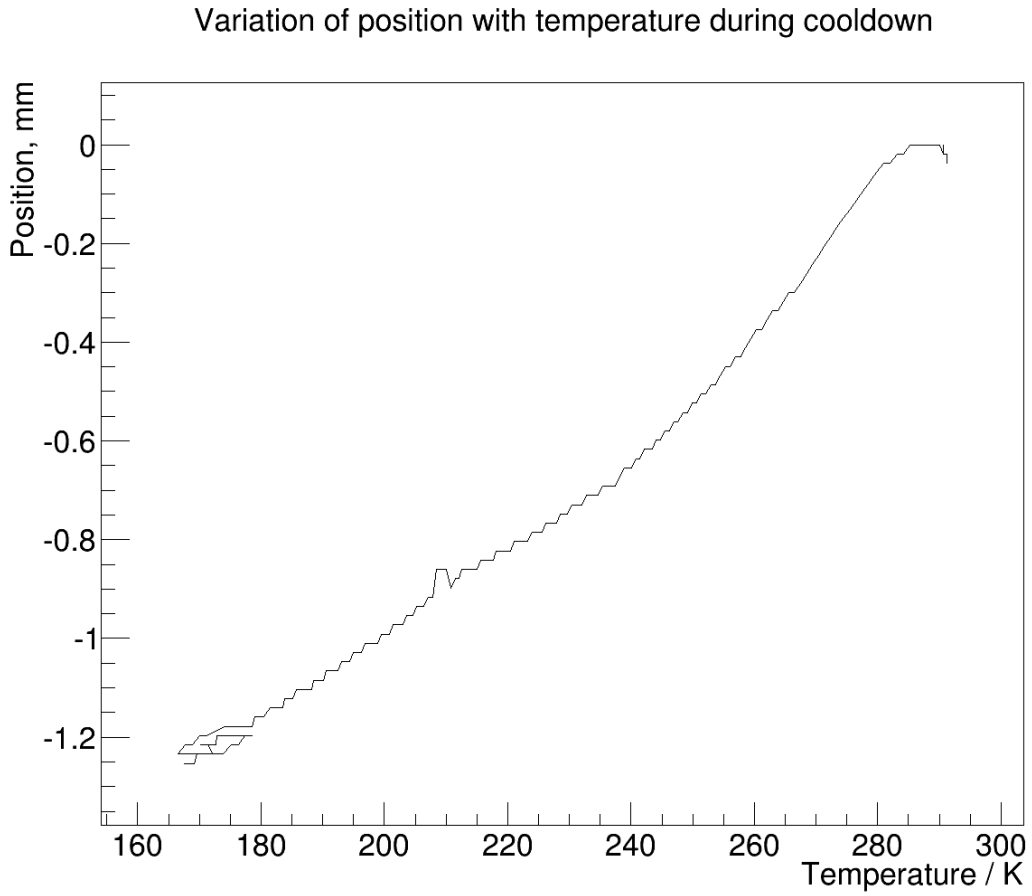


Figure 4.32: Data from first cooldown with position sensor. Nulled at room temperature (2.4 mm). As temperature drops, TPC cools and shrinks, dropping away from the position sensor. The small, brief rise at around 230 K was due to some interference on the electronics, and the same feature was seen on the other sensors that shared the position sensor's readout board. Once the system reaches around 180 K, the temperature fluctuates between 166K and 178K over 20 hours of operation. These fluctuations take time to propagate through materials and cause small amounts of shrinking and expansion. The calibration factor determined after the run is applied here.

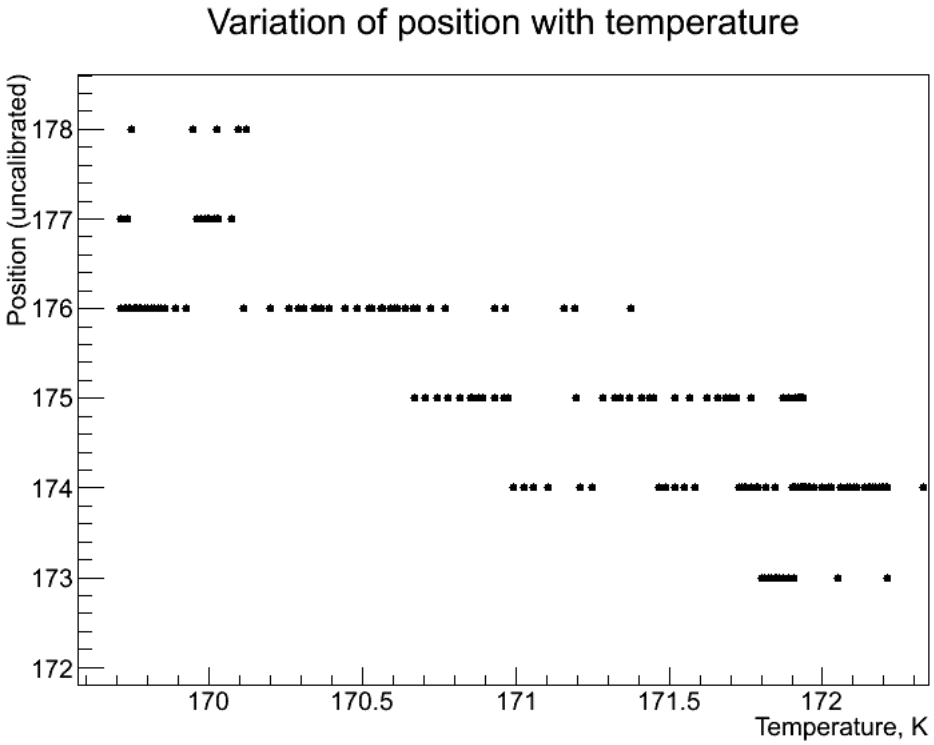


Figure 4.33: Three weeks of data taken during Run 4 in which the temperature varied as measured by a thermometer attached to the TPC. The slight variations in position at each temperature are not unexpected, as the thermometer measures only one small point, and the heat will take time to diffuse throughout the material, causing different amounts of shrinking in different places resulting in different TPC sizes for the same measured temperature. The data here is given in uncalibrated ADC counts from the position sensor. The apparent 1 deg quantisation arises from the signal moving between distinct ADC bits. This suggests that we should perhaps have used a different gain; however the temperature changes and hence position changes here are tiny: the calibration factor is $-0.0187\,\mathrm{mm/count}$, so these movements are on the order of only $20\,\mu\mathrm{m}$. Hence this level of quantisation is not a concern.

4.5.2 Run 7

4.5.2.1 Design

The vessel was fully opened between Runs 6 and 7, permitting the installation of a new sensor. The design to be tested in Run 7 used the cylindrical design optimised for final use in LZ. Additional attachments allowed it to be fitted to the existing sensor stands with minimal alterations. It had been hoped to fix the sensor at both ends, in order to keep the final test design as close to that used in LZ as possible: in the final, real sensor design, the Gough-Stewart Platform Mechanism that supports the sensors fixes both ends to ball and socket joints. However there were concerns that the relative movements of the TPC and xenon vessel between sensor installation and the running of the experiment were not fully understood. One procedure, known as the 'lifting' of the TPC could result in the TPC swinging with respect to the xenon vessel. If the sensor was rigidly fixed at both ends, it would not be able to accommodate this movement and the stresses on the sensor would be liable to cause it damage.

One possible solution was to add joints to the connection points of the sensor. However the space in which the position sensor sits is quite constrained. Adding joints (for example the ball and socket joints that will be discussed in the following chapter) would have taken up too much space.

As no solution could be found that permitted the sensor being connected at both ends, which would have been desirable to more closely replicate the sensor conditions in LZ, it was decided to resort to the design in previous runs where the plunger rests on a piece that is connected to the TPC, while the main body of the sensor is connected to the central rod that is connected to the xenon vessel. However, the new sensor design (as compared with earlier System Test runs) meant that it was relatively straightforward to add a pair of springs to the inside of the sensor, running along the rods, that would ensure the plunger is always held against the piece it is resting on. The springs were chosen to optimise the diameter and length (to fit within the sensor design) for an appropriate force. Using a compression spring results in the pushing apart of the sensor faces without requiring the addition of any attachment or containment structure. The chosen springs are stainless steel and are rated to work at $-100\,^{\circ}\mathrm{C}$, which is around the expected operating temperature of the detector.

It was decided that the sensor should have a range of 10 mm. This is much longer than the expected shrinking, which is anticipated to be the same as was seen during the cooldown for Run 3, i.e. around 1.2 mm. The additional range allows for

movement other than shrinking of the TPC after the sensor is installed. The TPC lift in Run 3 spanned a measured 1.6 mm but is predicted to cover up to 4.6 mm. Having a range of 10 mm thus can accommodate all of this movement with some range to spare. However there is not sufficient space within the vessel to make the sensor's active range any longer than this.

4.5.2.2 Calibration

The sensor was calibrated at room temperature in Oxford prior to shipping to SLAC. The results of running the sensor can be seen in fig. 4.35.

The sensor results are fitted with the following function:

$$\frac{a + bx}{c + dx + ex^2} \tag{4.34}$$

where the parameters are:

- $a = -9.19\,\mathrm{mm}^2$
- $b = -88.871\,\mathrm{mm}$
- $c = 0.4698\,\mathrm{mm}^2$
- $d = 0.002\,11\,\mathrm{mm}$
- $e = 0.00791.$

When fitted with this function, the results fall within 11.4 counts of the curve. An error of up to 11.4 counts in a total range of 1385 gives an error on the data of less than $11.4 \div (698.5 + 686.3) = 11.4 \div 1384.8 = 0.8\%$. Inverting this function enables the position to be determined from the sensor output.

The sensor was also tested at low temperatures to ensure successful operation in the System Test environment. The results of this can be seen in fig. 4.37. The sensor was immersed in liquid nitrogen, which evaporated and then the sensor returned to room temperature. The temperature was measured using a PT100 resistive thermometer with a four-wire measurement. This was placed half way down the sensor. A copper block was placed inside the top part of the sensor mechanism (as viewed in fig. 4.34) to push the slider out to a fixed, constant length; the springs in the lower part of the sensor held it against this block. This ensured that the sensor was measuring the same 'position' throughout the test.

A comparison of the initial and final levels of the sensor show that the low temperature affected the sensor only in a very small way. The initial sensor reading (when



Figure 4.34: Inside the position sensor used in Run 7 of the System Test at SLAC. The copper blocks that change the capacitance can be seen between the pair of Cirlex plates. The central copper block holds these plates together while the central, rounded blocks outside the plates are used to fix the surrounding copper tube; the tapped holes for this can be seen. The stainless steel rods are fixed to the very top and bottom copper discs, and run through PEEK bushes in the interior copper discs. At the lower ends of the rods, the springs can be seen, holding apart the end and interior copper discs. The copper blocks move with the outer copper discs; a pair of flat rectangular rods (one can be seen at the back of the image, the other is removed) connect the blocks to the top and bottom discs.

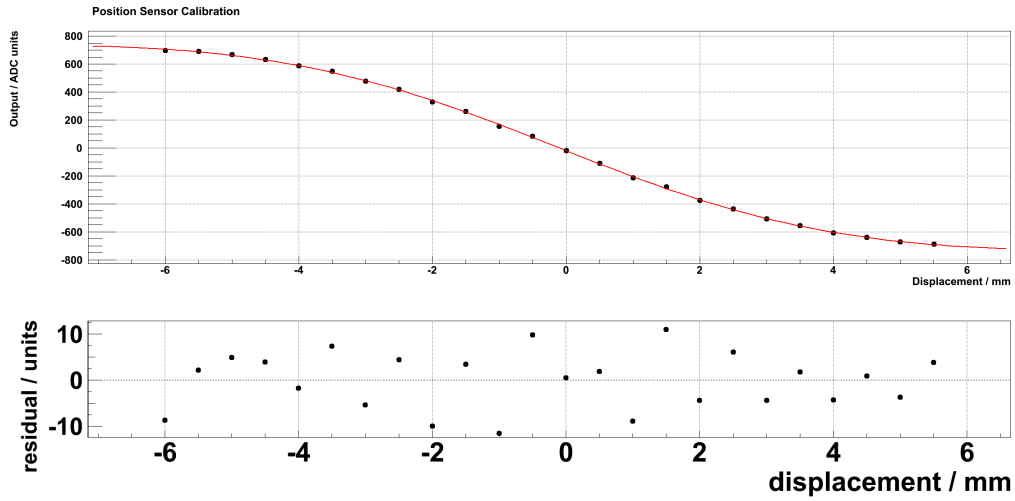


Figure 4.35: Data from calibrating the system test Run 7 position sensor. The sensor was moved and its position measured on a Vernier scale while the output was recorded. An arbitrary x-offset has been removed from the data by hand. The data has been fitted with a fractional function with a linear numerator and quadratic denominator. The residual differences between this fit and the data are shown in the lower half of the plot. This curve is non-linear by comparison to fig. 4.30, but the data presented here are from a very different sensor design to that used for fig. 4.30, employing variation of capacitance by the movement of metal blocks to split the capacitance rather than by the movement of a slider that changes the dielectric in the capacitors.

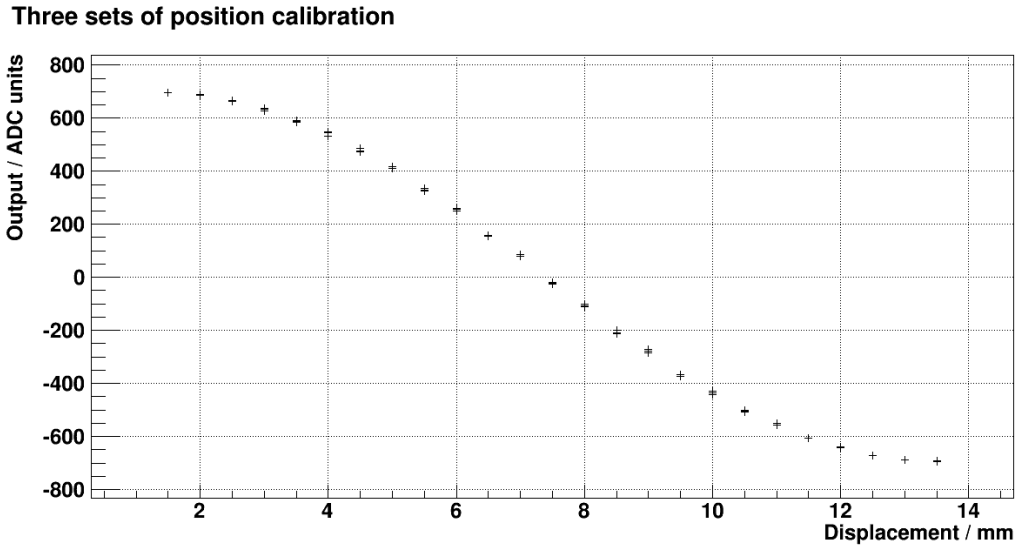


Figure 4.36: Calibration data for three runs of the sensor. The negligible differences between the repeated points demonstrates the reliability of the sensor measurements.

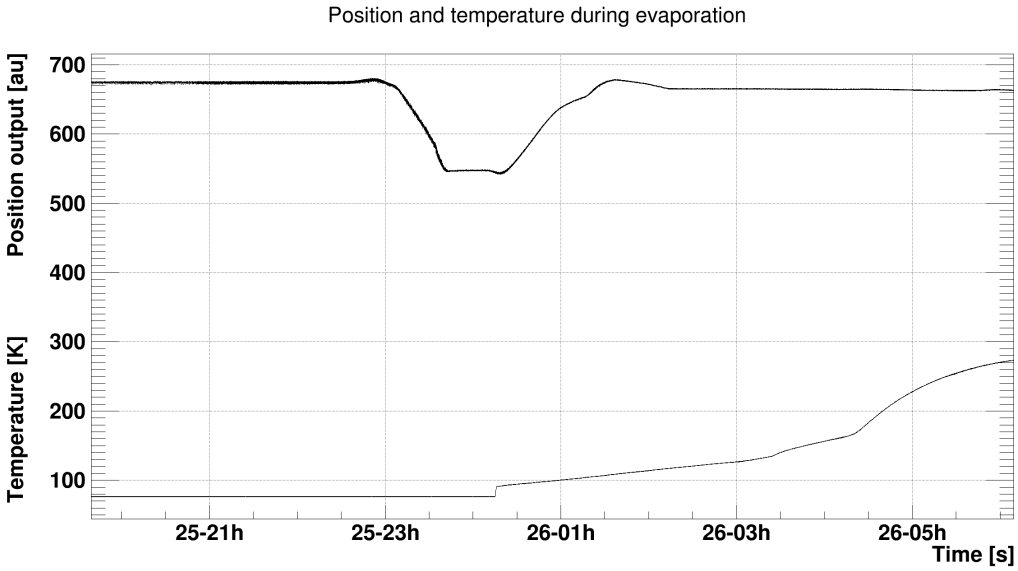


Figure 4.37: Measurements by the position sensor as liquid nitrogen evaporates, reducing the liquid level in the sensor. This is plotted against the temperature as measured at the centre of the sensor. The sensor output drops after around three hours; at this point the sensor is partly filled with liquid nitrogen and partly filled with air. The mismatch in dielectric constants between the two halves of the centre cause this lower reading. Once the conditions revert to having the same dielectric in both halves of the sensor, the reading returns to its original level.

stably filled with nitrogen) is around 675; see fig. 4.38. The final reading when empty and warm is around 663, giving a change of around 12 ADC counts during warming. The total range of the sensor is 1385 ADC counts (see fig. 4.35). This therefore suggests that any error due to the cooling of the sensor is of the order of less than 0.9%. This demonstrates that the sensor operates at low temperature and shows only a negligible change in sensor output due to this low temperature.

The features of the sensor readout during warming arise from the change in liquid level in the sensor. When both halves of the centre are full of the same dielectric (whether air or liquid nitrogen), the relative permittivities of the dielectric cancel out from the expression that gives the output. However, while the nitrogen is boiling off, the liquid level in the sensor changes. The sensor was vertical, so the liquid level emptied out of first one half and then the other. The thermometer was mounted halfway down the sensor. The point at which a temperature rise is seen is when the liquid level reaches the thermometer. This corresponds to the sensor being half full of nitrogen, which tallies with the changes we see in sensor readout. As the position sensors will operate only in gas in LZ, this will not be a feature of the sensor measurements.

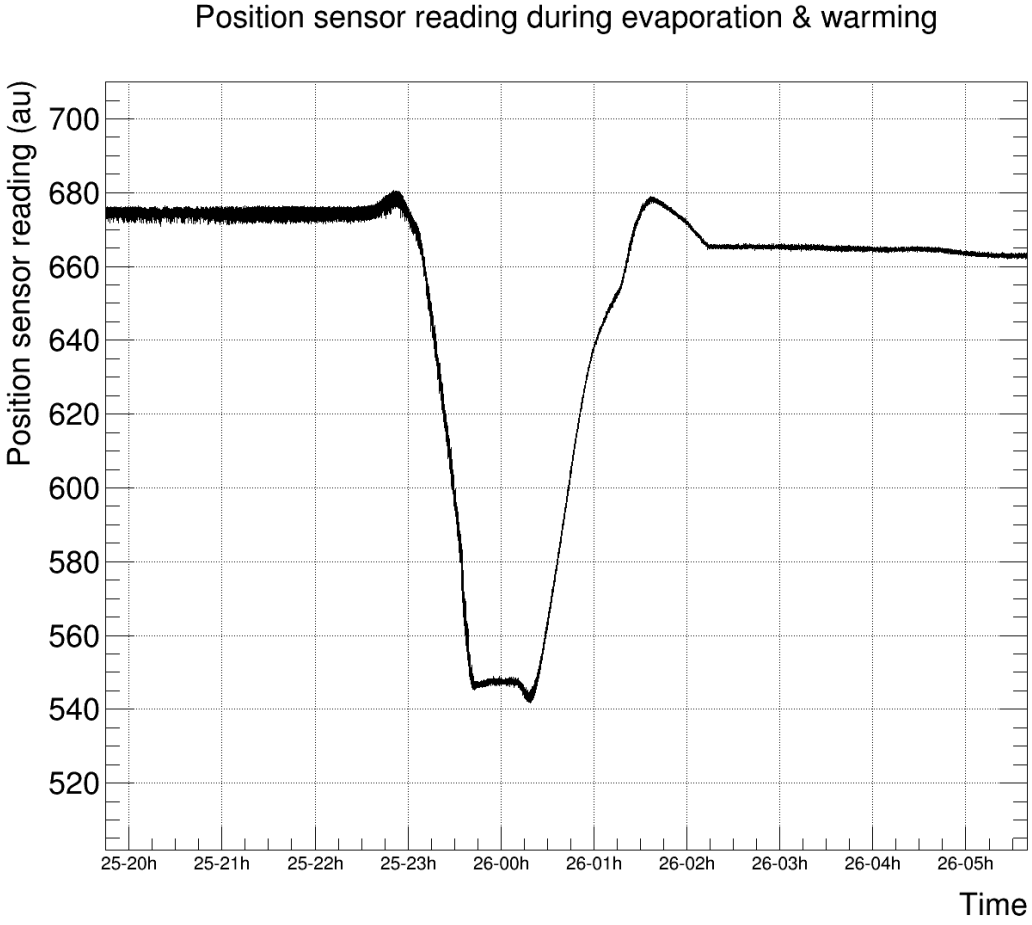


Figure 4.38: The detailed response of the sensor as liquid nitrogen boils off, reducing the liquid level in the sensor. The initial sensor reading (when stably filled with nitrogen) is around 675. The final reading when empty and warm is around 663, giving a change of around 12 ADC counts during warming. Between these level points, the sensor reading changes as the liquid level in the sensor changes. When one half of the sensor is filled with a different dielectric, the relative permittivities of the two halves will appear in the expression for the output, resulting in a deviation from the expected behaviour.

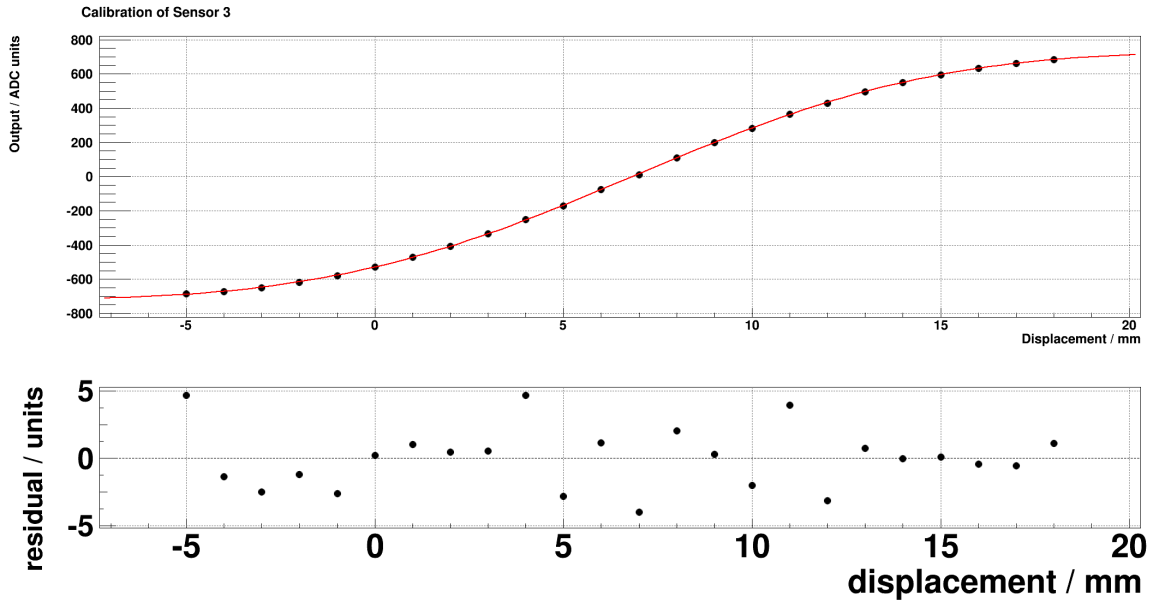


Figure 4.39: Data from calibrating one of the six 'final design' sensors built, fitted with a polynomial curve, against which the residuals in the lower plot are determined.

4.6 Final sensor

The final sensor design is as discussed in section 4.3. Six of these sensors were built for testing. The calibration data for one typical sensor, taken in the same way as that for the Run 7 System Test sensor, is shown in fig. 4.39. The range of the data for this sensor is 1369.27 ADC counts over 23 mm. The largest residual is 4.67 ADC counts, giving an overall estimate of the sensor error as 0.078 mm, equivalent to around 0.3% of the full sensor scale.

4.7 Conclusion

In this chapter we have discussed in depth the design of the position sensor for the LZ experiment. We have explored the shrinking of LZ and why it is important that we understand this. We have also shown why this design of position sensor is appropriate, and have explored the advantages it has. In the next chapter we will explain how the position sensor will interface with the experiment via an interconnected system known as a Gough-Stewart Platform Mechanism, or 'hexapod'. The sensor used for this is the final design as explored in this chapter.

Chapter 5

A connected system of sensors

In LZ, the position sensors will not be operated on an individual basis, but will provide information as part of a connected system of position sensors. This system is known as the 'hexapod', and brings together the readout described in Chapter 3 and the sensor design explored in Chapter 4, alongside an algorithm that ties together the outputs of six interconnected sensors. The design is known as a 'Gough-Stewart Platform Mechanism', and the details of this will be described in this chapter. The use of a hexapod enables the position measurements required in LZ that could otherwise be difficult given the physical constraints of the detector system.

5.1 Using individual sensors

As discussed previously, it is important to know the position of the PMT truss, which is an integral part of the top of the TPC. The TPC itself is made of interlocking stacked rings of PTFE. It is possible for the PMT truss to move vertically (the TPC shrinking towards its base support), radially (the TPC shrinking unevenly and pushing one side of the PMT truss towards the cryostat wall) and torsionally (the PMT truss twisting as a result of movement of the PTFE rings) with respect to the inner cryostat vessel (ICV). Any given individual position sensor can measure only the changing distance between two points, and this alone cannot determine the nature of the relative movement. Hence a system of sensors is required that can monitor different aspects of the relative motion of the cryostat dome and the PMT truss.

It might have been possible to connect individual sensors to measure each of the possible movements, for example three vertical sensors to monitor the vertical change, three radial sensors to monitor any tipping and so on. However, this is not a feasible option, for reasons explored below.

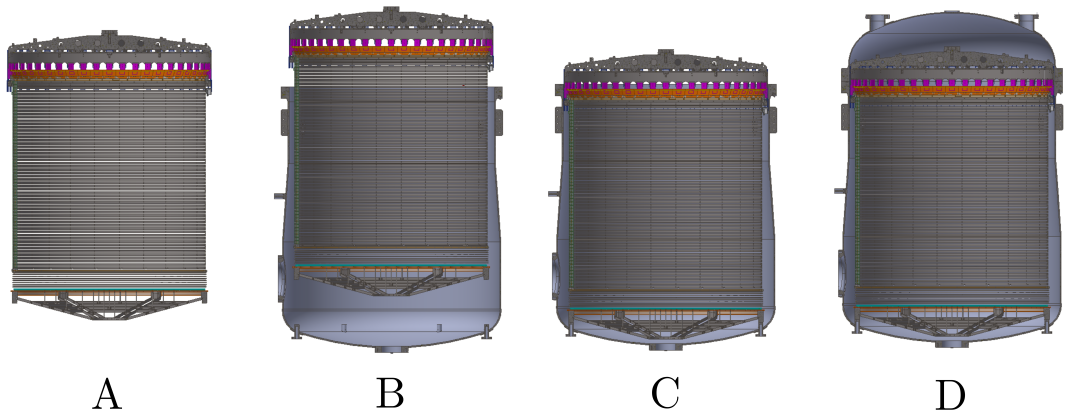


Figure 5.1: (A) The TPC is assembled, before (B) being lowered into the ICV, until the base of the TPC is at the bottom of the ICV (C). The cryostat dome is then lowered onto this (D) and secured in place.

5.1.1 Assembling the detector

The TPC consists of a series of interlocking PTFE rings and titanium rings that are stacked one on top of another; they are not screwed or glued in place. The TPC sits within the inner cryostat vessel, and is fixed at the base. This assembly is shown in fig. 5.1. The TPC is separately assembled before being lowered into the ICV. The cryostat dome will then be suspended above the TPC and main vessel. The dome will then be lowered and the flange that connects the main vessel and the dome will be bolted closed, sealing the inner cryostat vessel. The sensors need to be installed once the TPC is in the cryostat vessel. At the top of the TPC is the PMT truss, a titanium structure that supports the top array of PMTs. It consists of a large plate with cut-outs for the PMTs windows, plus three bars that cross the plate and connect in the centre; see fig. 5.2. The sensors are intended to measure the movement of the TPC and PMTs, and the PMT truss is used as a proxy for this. Thus the sensors need to connect the PMT truss to the inside wall of the inner cryostat vessel. However, the PMT truss sits quite a long way above the flange where the main vessel and dome join; see fig. 5.3. This means that the inside wall of the main cryostat vessel is difficult to reach from the PMT truss; it would be significant challenge to connect a sensor between the PMT truss and the wall of the cryostat vessel. Hence all of the sensors will need to connect between the PMT truss and the dome of the cryostat.

It is possible to imagine this working for a vertical sensor, (for example, a sensor that sticks straight upwards and is supported with springs that the dome compresses

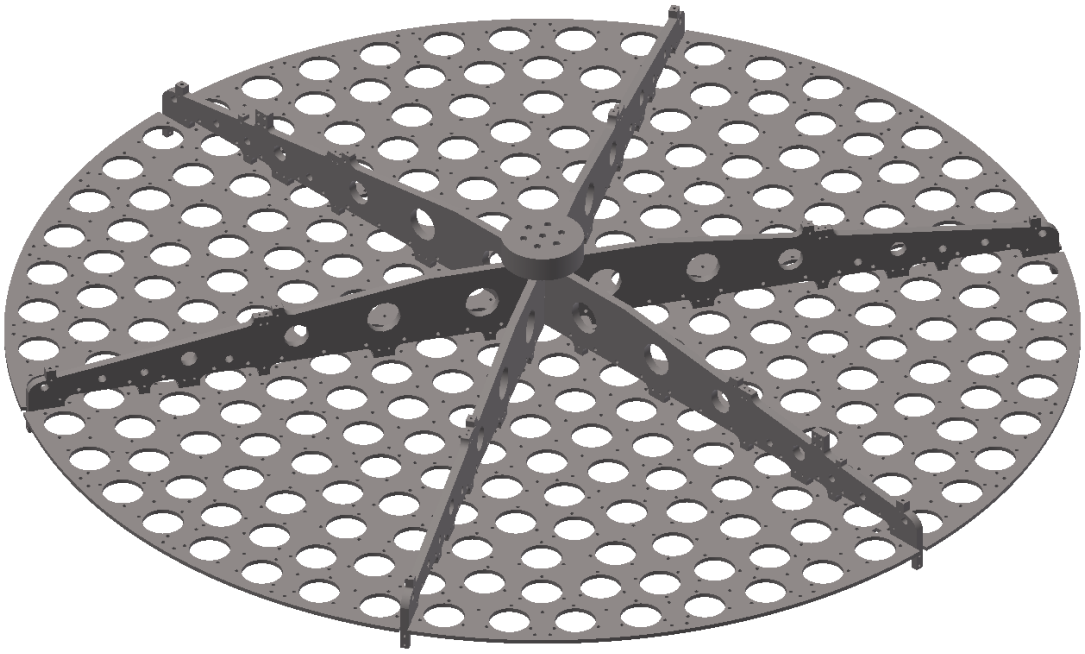


Figure 5.2: The titanium structure that supports the array of PMTs.

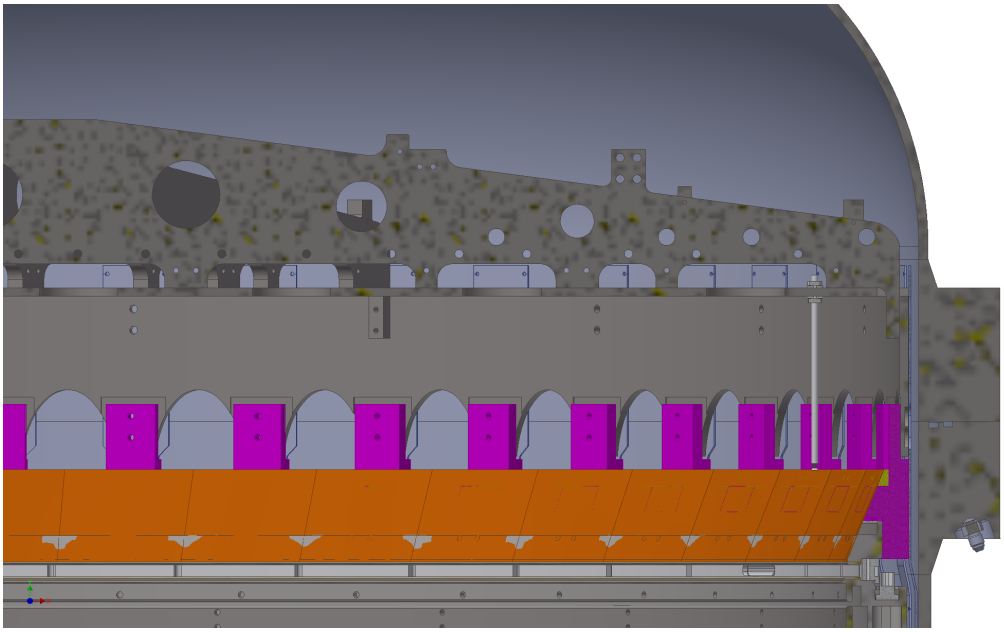


Figure 5.3: A CAD model of the top corner of the detector, showing the PMT truss above the level of the flange at which the ICV main body and dome are connected.

as it is lowered). Nevertheless, the fact that the interior is inaccessible once the dome is in place means creating an analogous design for sensors that measure rotational or radial movement, which seems unfeasible. It is moreover not possible to instrument the TPC below the PMT truss because of the high electric field in that region between the TPC and ICV.

To avoid these challenges associated with using multiple individual sensors, it was suggested that we use a 'hexapod': a system of six interconnected sensors. This circumvents the problem of needing radial sensors to measure radial movement and torsional sensors to measure rotational movement, as it combines all of the axes into a single system. Known more formally as a 'Gough-Stewart Platform Mechanism' (GSPM), this is the solution that will be used in LZ and discussed in depth below.

5.2 Gough-Stewart platform mechanisms

5.2.1 Introduction

A Gough-Stewart Platform Mechanism (GSPM) is a six-degree-of-freedom parallel manipulator: a top platform can move in all six degrees of freedom (x, y, z, pitch, roll and yaw) with respect to a base platform, and the movement arises from the actuation of joints connecting the two platforms that extend parallel to their length.[82] The general structure is not a new idea: the French mathematician Cauchy studied the rigidity of an 'articulated octahedron' in the 19th century.[83] In the 1950s and '60s, the prevailing style of GSPM was created and studied by Eric Gough and D. Stewart.[20] Because of the six jacks that connect the two platforms, GSPMs are often known as 'hexapods' for their six legs, though this term is also prevalent in robotics, where it is used to describe a machine with (unsurprisingly) six legs.

GSPMs are used in a range of scenarios where precisely controlled positioning is vital. For example, the Dark Energy Spectroscopic Instrument (DESI) is a ground-based telescope that will use a GSPM for positioning the barrel of the telescope.[84] Parallel manipulators have also been used at, among other places, the European Synchrotron Radiation Facility (ESRF), for positioning samples, which demanded repeatability of better than 0.1 µm with a load of 230 kg.[85] Commercial hexapods are also available. More details, examples and images of hexapods can be found in appendix D.

5.2.2 Our application

The examples in the previous section and in appendix D demonstrate the wide-ranging use of GSPMs across physics and engineering. However, there are few examples of the use of GSPMs that are parallel to the use in LZ. The examples discussed above are all cases of GSPMs being used to actuate and position one platform (and whatever is attached to it) relative to another. By contrast, the LZ hexapod will use a GSPM as a measuring device. In this case, one GSPM platform will be moved with respect to the other by external forces, specifically the shrinking of components of the experiment. The GSPM is effectively positioned between the two platforms to measure how much the platforms are moved by. Instead of actuated jacks, the struts connecting the top and bottom platforms will be position sensors that monitor their own extension. Specifically, they will be the position sensors discussed in detail in Chapter 4. From these six measurements, we can determine the position of one platform relative to the other. The two platforms in question will be the two components of the experiment that we want to understand the relative position of, namely the PMT truss at the top of the TPC and the dome of the ICV. Using a system of six sensors connected as a GSPM enables the measuring of movement in all six degrees of freedom, without having to have sensors devoted to particular axes.

The GSPM employed in LZ is in the form of a '6-3' platform, which is to say that the base has 6 distinct joints while the top platform has 3. Alternatives include a 6-6 platform, which has six connections on both platforms, or a 3-3 platform, which has three on each.

5.3 Tripods

5.3.1 Motivation

While a hexapod is mathematically very difficult to analyse, a tripod is much simpler and provides a useful starting point. It consists of a system of three sensors connected at a single point at the top, with each sensor connecting to one point of an equilateral triangle that forms the base.

5.3.2 Design

A tripod and software were constructed to convert the individual position sensor measurements into a measurement of the position of the tripod's point; this enabled an initial demonstration of a system of connected sensors being used as an overall

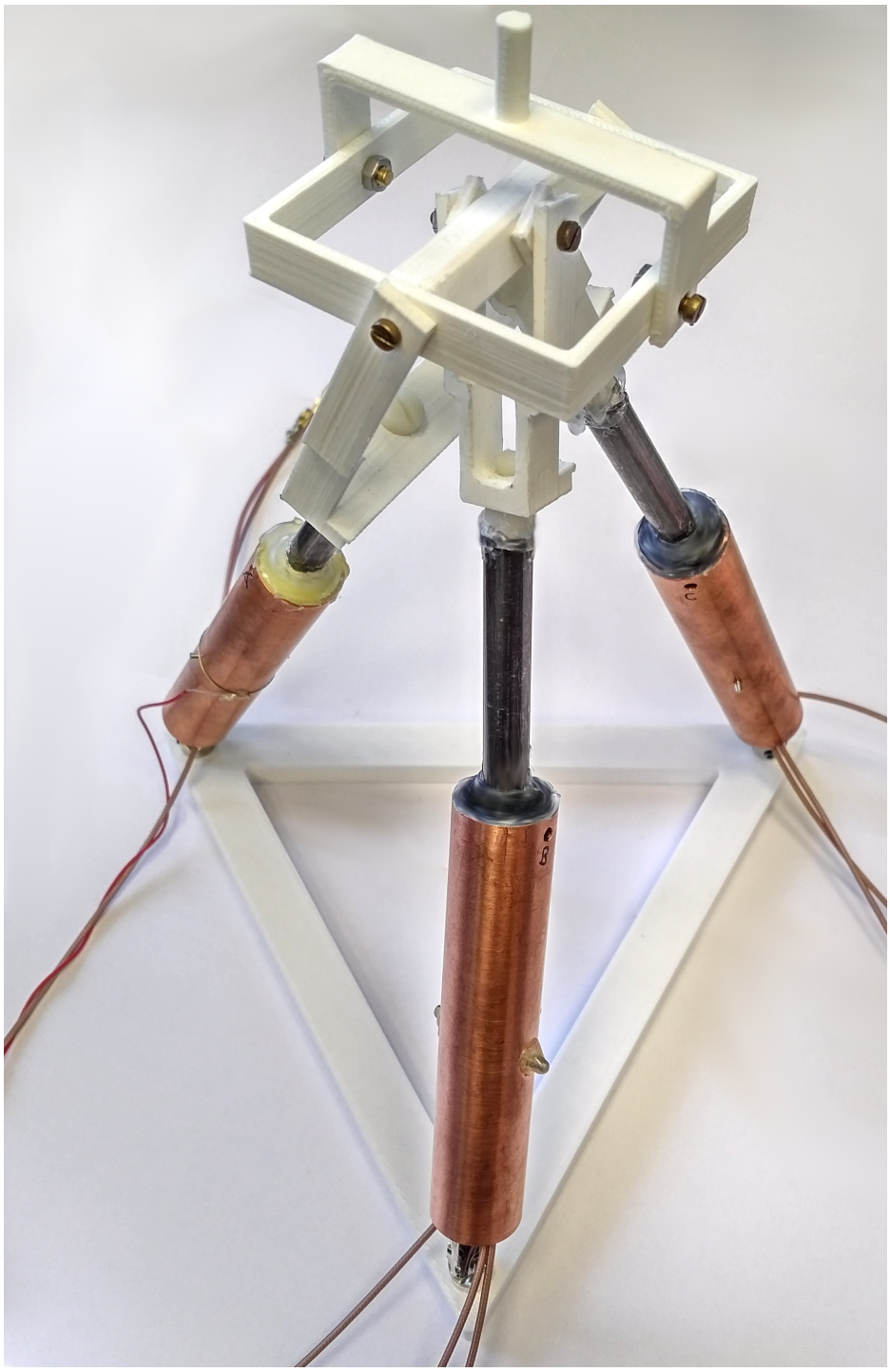


Figure 5.4: A photograph of the demonstrator tripod. At the base of each sensor, a universal joint can be seen. This allows the sensor to move freely in any direction. At the top, the connection of the three sensors is extended to allow them to effectively meet at a single point, which is required for the geometric analysis.

measuring device. As this was only a proof of principle device, 3D-printed parts were used for both the tripod stand and for parts of the sensors that went into it. A photograph of the final tripod can be seen in fig. 5.4. The top of the tripod consists of an arrangement of joints that together have the effect of the three sensors meeting at a single point. This is essential for the tripod analysis to work precisely, as the analysis treats the tripod as a tetrahedron.

The sensors are a concentric design with moving metal blocks to measure position. A CAD model of this sensor can be seen in appendix E, where there is also an exploration of the challenges associated with this design. Each sensor was individually calibrated to give an equation for the straight line that its data should lie approximately along. This calibration enabled a conversion from sensor readout to sensor length. In a change from the calibrations completed for the System Test sensors, in this case the full length of the sensor from end to end must be known, as this distance is required for the geometric calculations that will be described below. The sensors are calibrated by fitting a curve to a data set for each sensor that covers that sensor's full range. From this, a sensor reading can be converted to a length measurement.

5.3.3 Analysis

The tripod structure consists of an equilateral triangular base with three triangular faces that meet at the top point. These faces have sides that change in length - they are the position sensors.

Consider the base triangle to consist of three points A, B and C about the origin O; see fig. 5.5. Each side has length ℓ and the radius of the circle is r, with each of A, B and C sitting on that circle.

The coordinates of the points on the base are given by

- **A** $\left(-\frac{\ell}{2}, -\ell\frac{\sqrt{3}}{6}, 0\right)$
- **B** $\left(0, \ell\frac{\sqrt{3}}{3}, 0\right)$
- **C** $\left(\frac{\ell}{2}, -\ell\frac{\sqrt{3}}{6}, 0\right)$.

Let D be the point at the apex of the tripod, with coordinates (x, y, z). Then the squares of the distances from the base points A, B and C to the apex D are given

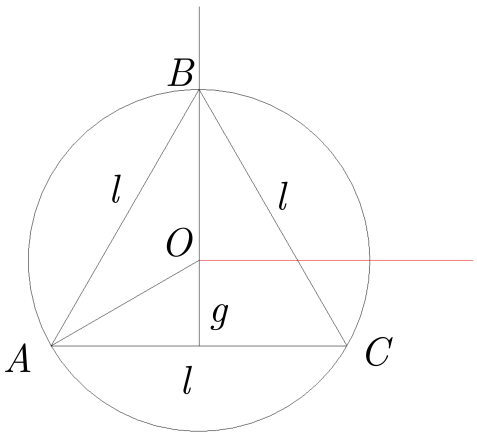


Figure 5.5: A diagram showing the points and distances that constitute the base of the tripod.

by:

$$AD^2 = \left(x + \frac{\ell}{2}\right)^2 + \left(y + \ell\frac{\sqrt{3}}{6}\right)^2 + z^2 \tag{5.1}$$

$$BD^2 = x^2 + \left(y - \ell\frac{\sqrt{3}}{3}\right)^2 + z^2 \tag{5.2}$$

$$CD^2 = \left(x - \frac{\ell}{2}\right)^2 + \left(y + \ell\frac{\sqrt{3}}{6}\right)^2 + z^2\ . \tag{5.3}$$

These can be combined to extract x, y and z. First,

$$AD^2 - CD^2 = 2x\ell\,. \tag{5.4}$$

Hence

$$x = \frac{AD^2 - CD^2}{2\ell}\,. \tag{5.5}$$

The difference of the first two of the equations gives

$$AD^2 - BD^2 = x\ell + \sqrt{3}\ell y\,. \tag{5.6}$$

From this and the solution for x, y can be found as

$$y = \frac{1}{\sqrt{3}\ell}\left[\frac{AD^2}{2} - BD^2 + \frac{CD^2}{2}\right]\ . \tag{5.7}$$

Finally, the third coordinate of the top point is

$$z^2 = \frac{1}{3}\left(AD^2 + CD^2 + BD^2 - \ell^2\right) - \frac{1}{4\ell^2}\left(AD^2 - CD^2\right)^2 - \frac{1}{3\ell^2}\left(\frac{AD^2}{2} - BD^2 + \frac{CD^2}{2}\right). \tag{5.8}$$

Hence the three coordinates (x, y, z) of the top of the tripod can be given in terms of the lengths of the sensors AD, BD, CD, and the length ℓ of the base sides. Using this, an algorithm can be implemented that converts the sensor lengths in real time to a value for position.

5.3.4 Data

In order to test the tripod, the system of sensors as shown in fig. 5.4 was run through a series of movements, with the three sensors' outputs being recorded. These outputs were then transformed into measurements of length, and the three lengths were input into calculations that use the geometry described in section 5.3.3 to reconstruct the x-,y- and z-coordinates of the point at the top of the tripod. Three sets of movements panned through the x, y and z ranges of the tripod, and in each case the changing reconstructed coordinate is compared to the measured change in the position of the base. The top of the tripod was clamped in a stationary position, while the base was moved. The inverse nature of the changes is therefore accounted for in the analysis of the data. The results can be seen in fig. 5.6 and fig. 5.7.

In each of these, the data is fitted with a straight line, which results in the following gradients:

- x **movement:** 1.01 mm/mm
- y **movement:** 0.92 mm/mm
- z **movement:** 0.99 mm/mm.

The data for the x and z movements shows that the position can be well-reconstructed, with 1 mm changes in platform position resulting in 1 mm changes in reconstructed position, to within 1%, as demonstrated by the fitted line gradients of 1.01 mm/mm and 0.99 mm/mm respectively. The y-changes are reconstructed to within around 10%.

There are many sources of error in the tripod and its data. The joints at the top of the tripod have a significant amount of play in them, which can affect measurements if the direction is changed. To minimise this effect, all data was taken for the

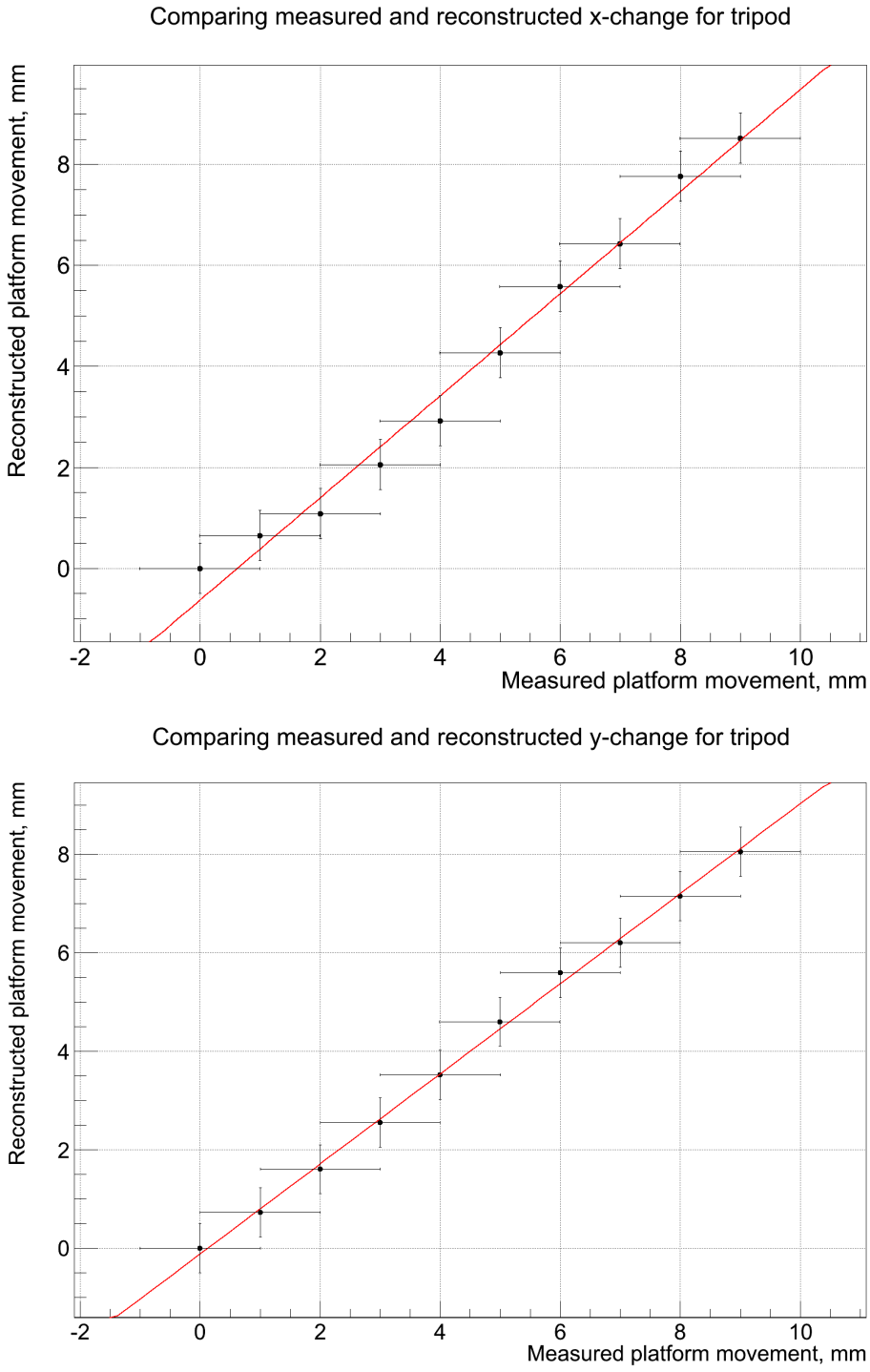


Figure 5.6: A comparison of measured and reconstructed movements along the x- and y-axes. The displacement of the platform carrying the tripod was measured by comparing a marked point on the platform to a mm-scale ruler. This simple method of measuring the changing position gives rise to the horizontal error bars in these plots.

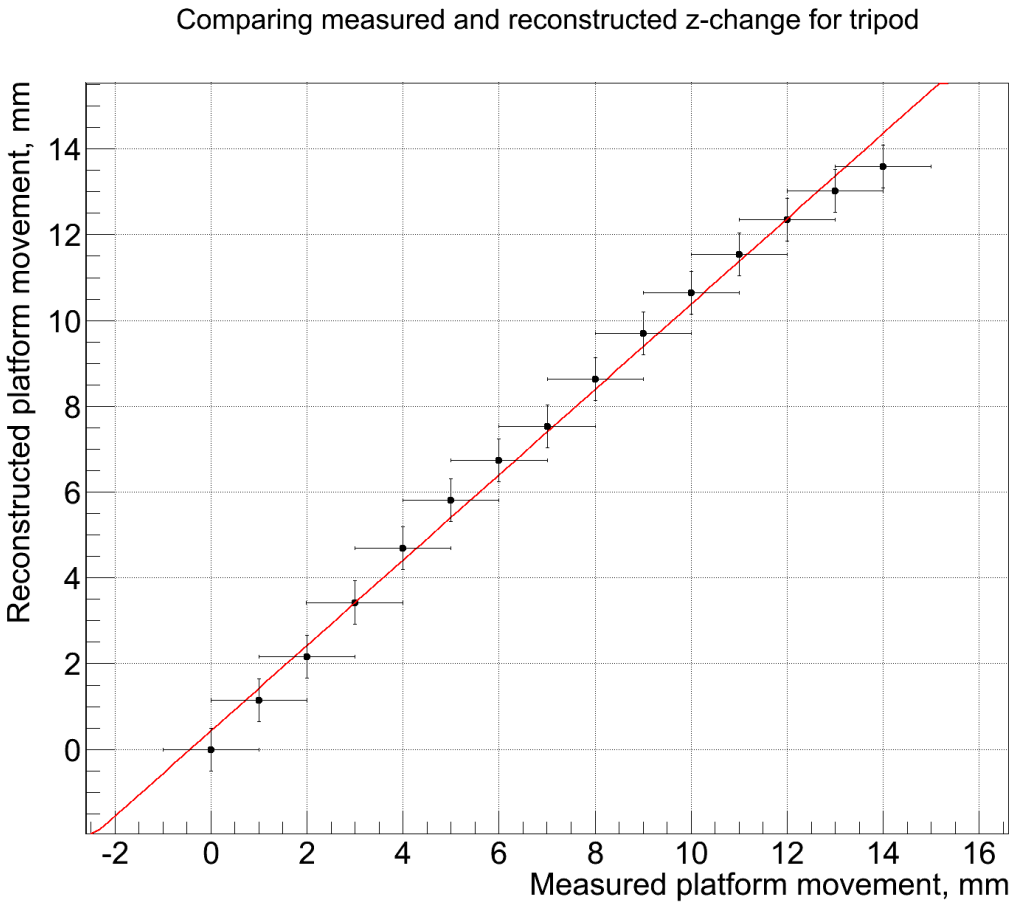


Figure 5.7: A comparison of measured and reconstructed movements along the z-axis.

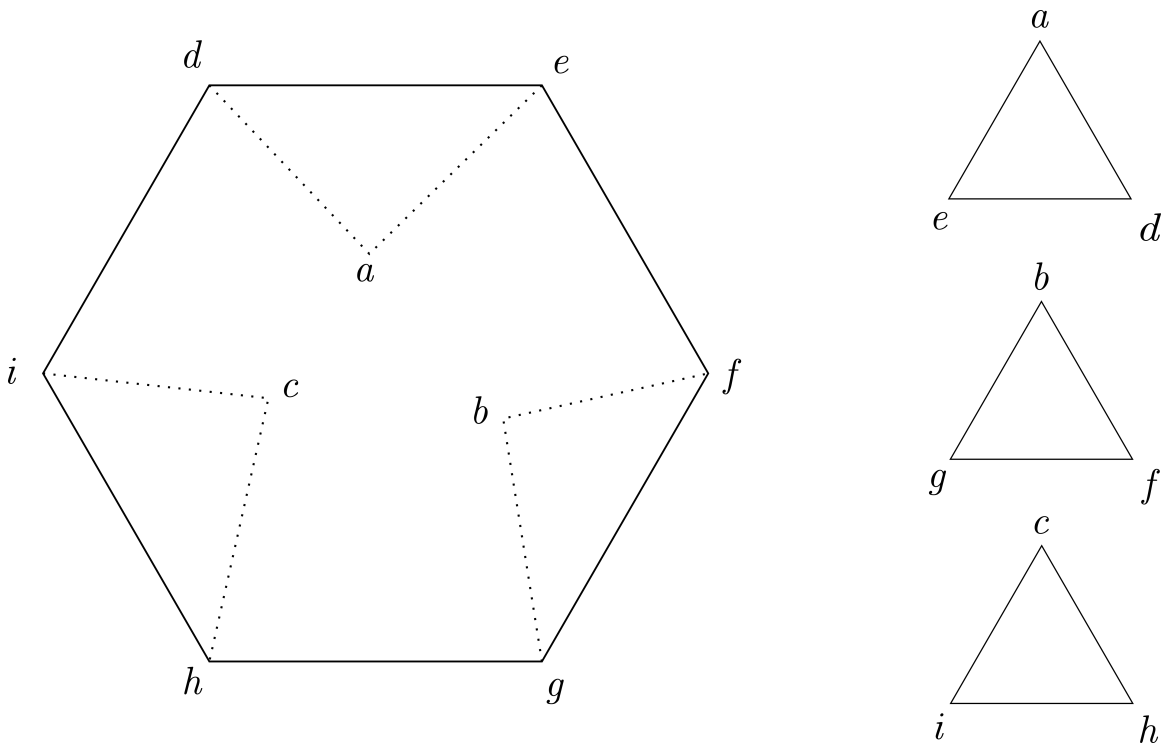


Figure 5.8: A diagram showing the points on the base of the hexapod and the associated triangles

central range of movement, with the position being changed in only one direction. In addition, the sensors exhibited some hysteresis on occasion, sometimes moving less than was strictly required for the tripod to assume the new position indicated by the measurement. Nevertheless, the x and z data from the tripod indicate a good initial standpoint from which to develop the more complicated technology and analysis required for the successful running of a hexapod system of position sensors.

5.4 Hexapods

5.4.1 The geometry

The hexapod base consists of six points in a plane, which do not have to be regularly spaced, but will form a hexagon. Let these be labelled d, e, f, g, h and i. Each of these six base points is the attachment point for one end of one sensor. The points are paired such that the line between an adjacent pair of points forms the base of a triangle, with the other two sides of that triangle consisting of position sensors that are joined pairwise at the top. The top points - the sensor triangle tips - are labelled a, b and c. Hence the triangles to be considered (with two sensor sides and a base

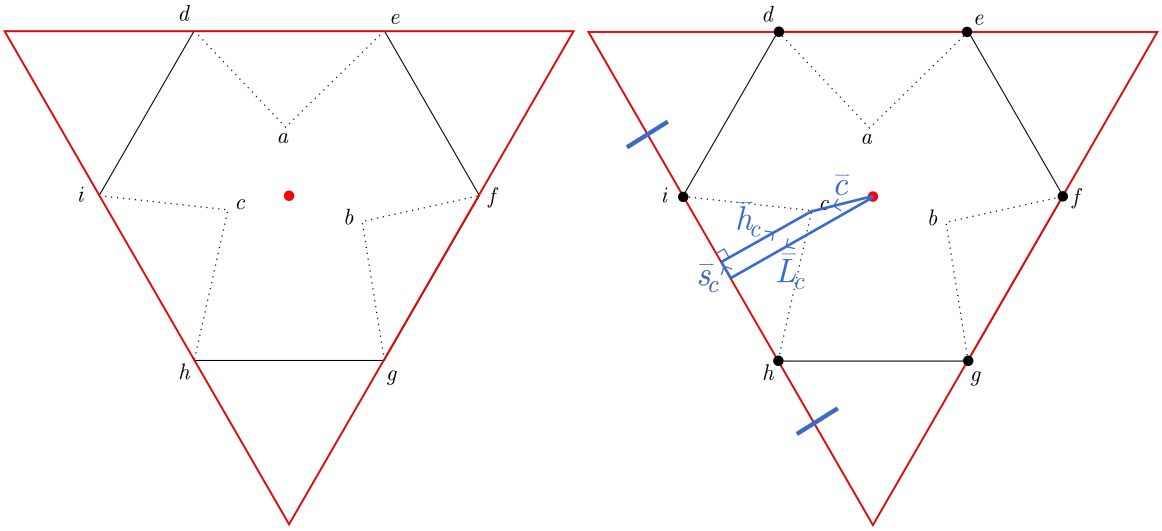


Figure 5.9: Left: A diagram showing the points on the base of the hexapod and the definition of the centre of the base. Right: with the addition of the vectors used to describe the position of point c, projected onto the base plane. Alternate views of these vectors are shown in fig. 5.10.

side) are dae, fbg and hci. These can be seen in fig. 5.8.

The origin of the base is defined as the centroid of the triangle created by extending lines de, fg and hi, as shown in fig. 5.9. The base plane defines the x-y plane of the coordinates. The x and y axes can be defined in any way within this.

Consider vectors from the origin to the points a, b and c. Each vector can be split as follows:

- A vector $\vec{L}$ that runs from the origin to the midpoint of the triangle base line
- A vector $\vec{s}$ that runs from the midpoint of the baseline to the base of the triangle height line. The triangle height line is a line from the tip of the triangle (i.e. the final point) that meets the baseline perpendicularly.
- A vector $\vec{h}$ that runs up the height of the triangle in the triangle's plane

A diagram of these three vectors is shown in fig. 5.10. Hence, for example, the vector from the origin to the top of the triangle hci is $\vec{c} = \vec{L_c} + \vec{s_c} + \vec{h_c}$.

The vector $\vec{L}$ will depend only on the positions of the base points so is fixed by the hexapod design. The vector $\vec{s}$ depends on the positions of the base points plus the position sensor lengths, i.e. the lengths of the triangle sides. The vector $\vec{h}$ depends on the triangle side lengths (i.e. the base points and the sensor lengths) and the inclination angle of the triangle with respect to the base plane.

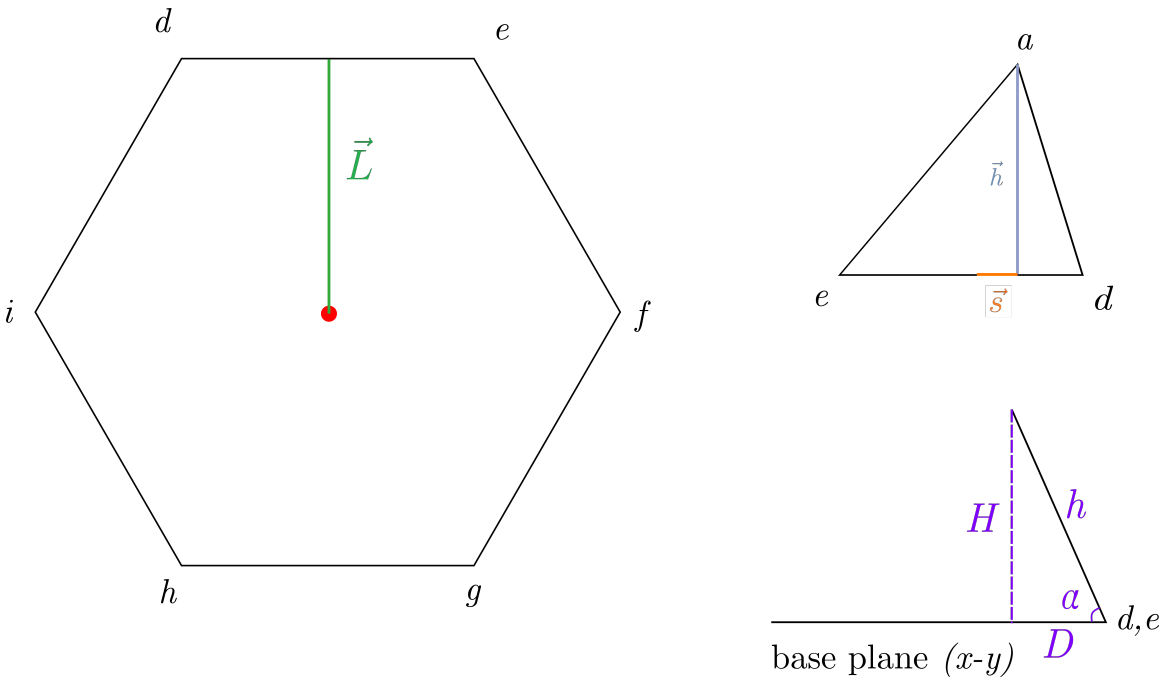


Figure 5.10: A diagram showing the definitions of the three vectors that constitute the vector from the origin to the top of a triangle.

The distances between points a, b and c are fixed and known, as the three points form the top platform of the hexapod. Hence the lengths ab, bc and ca are known.

Evidently $|\vec{b}-\vec{a}| = ab$, $|\vec{c}-\vec{b}| = bc$ and $|\vec{a}-\vec{c}| = ca$. That is, the vectors describing the positions of a, b and c in terms of the respective vectors $\vec{L}$, $\vec{s}$ and $\vec{h}$ can be connected to the known distances between those points.

In all of the definitions so far, the only unknowns are the angles of inclination of the triangle faces, that is, the angle between the plane of the triangle and the z-axis. All other values are known and fixed or measured. We have three triangles, so we have three unknown angles of inclination, and three equations in which they are contained - the three equations for ab, bc and ca. However, each of these three equations contains a pair of the angles: the equation for $\vec{a}$ contains the angle of inclination of triangle dae and the equation for $\vec{b}$ contains the angle of inclination of triangle fbg, so the equation for ab contains two unknown angles of inclination. Therefore solving these three simultaneous equations for the three angles of inclinations requires consideration. An example of one of these three equations is as follows:

$$\vec{c} = \begin{pmatrix} L_h \cos\chi + s_c \cos\chi' + D_c \sin\chi' \\ L_h \sin\chi + s_c \sin\chi' - D_c \cos\chi' \\ H_c \end{pmatrix} . \tag{5.9}$$

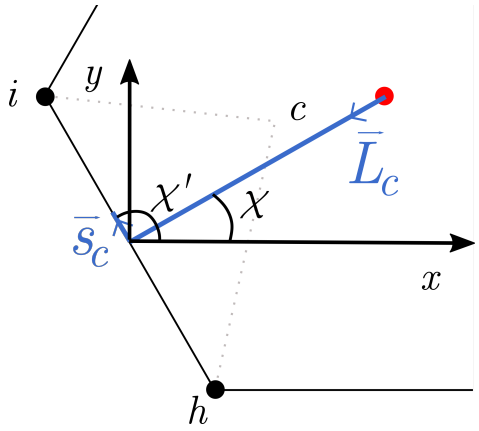


Figure 5.11: A diagram showing the definitions of the angles χ and χ' in the base plane.

In this equation, χ' is the angle between the base of the triangle and the chosen x-axis, while χ is the angle between the line from the origin to the base midpoint and the x-axis; these are shown in fig. 5.11. L and s are defined as before. In addition,

$$D_c = h_c \cos\gamma \tag{5.10}$$

$$H_c = h_c \sin\gamma \tag{5.11}$$

where h_c is defined as above and γ is the angle of inclination of the triangle *hci*. All of these parameters except γ can be determined *ab initio*. In order to solve the resulting simultaneous equations, they need to be written in terms of a single variable, $\cos\gamma \equiv \mathbb{C}$. Then

$$D_c = \mathbb{C}h_c \tag{5.12}$$

$$H_c = \sqrt{1-\mathbb{C}^2}h_c\,. \tag{5.13}$$

Hence the equation for $\vec{c}$ contains only $\mathbb{C}$ as an unknown variable, and the equation for *ca* contains $\mathbb{C} \equiv \cos\gamma$ and $\mathbb{A} \equiv \cos\alpha$, where α is the angle of inclination of the triangle *dae*.

5.4.2 An analytical solution

An analytic solution of these equations is not obvious. Trying to extricate the individual angles quickly creates long and complicated equations because of the way they feature. Although it is technically possible to solve analytically - after all, we have three simultaneous equations in three unknowns - it is far from straightforward to do so.

Significant literature exists on the problem of the forward displacement analysis of GSPMs (which is what we are attempting) and it is widely acknowledged as a thorny problem. The inverse problem of kinematic analysis (determining what length the sides should be to put the platform in a given position) is relatively straightforward.[86] However, solving the problem outlined above quickly becomes difficult. A number of works have demonstrated that the analysis of a 6-3 platform mechanism (such as that we are using) results in a polynomial of order sixteen.[87, 88, 89] There are therefore sixteen possible solutions to the equations, or sixteen possible configurations of the platform for a given set of sensor lengths. The sixteenth-order polynomial, which itself is non-trivial to find from the simultaneous equations, would have to be solved to find these, and then the correct solution from among these determined from previous information about the platform configuration. This is an extremely complex analysis to do and therefore does not present a realistic option for the hexapod in LZ.

5.4.3 A numerical solution

Although a complete analytic solution is not feasible, the outcome of the geometrical analysis can be used to form the basis of a numerical solution. In describing the geometry of the hexapod in a general way, three simultaneous equations were attained that contain three free parameters in pairs.

Nevertheless, for the purposes of the hexapod in LZ, an analytical solution is not needed. It is sufficient to instead solve the three equations numerically, iterating over possible values for the three free parameters until a triplet is found that makes all three equations true. There are 16 such triplets that could possibly solve these equations. The solution picked out by the method below depends up the initial values used. As the hexapod will only make slow, small movements, using the previous correct solution will result in the correct triplet being found, as the hexapod will not go through any of the 'zeroes' of the equations, such as the top and bottom platform being in a plane.

For this numerical solution, we use the Newton-Raphson method, which converges on a solution that is accurate enough to meet the requirements of LZ after around six iterations. The three equations are formed into a vector

$$\vec{f} = \begin{pmatrix} f(a,b) \\ f(b,c) \\ f(c,a) \end{pmatrix} \tag{5.14}$$

where $f(a,b)$ is the equation that connects the top points a and b, and hence contains the angles of inclination $\mathbb{A}$ and $\mathbb{B}$. The Jacobian for this vector is given by

$$\vec{J} = \begin{pmatrix} \frac{\partial f(a,b)}{\partial \mathbb{A}} & \frac{\partial f(a,b)}{\partial \mathbb{B}} & 0 \\ 0 & \frac{\partial f(b,c)}{\partial \mathbb{B}} & \frac{\partial f(b,c)}{\partial \mathbb{C}} \\ \frac{\partial f(c,a)}{\partial \mathbb{A}} & 0 & \frac{\partial f(c,a)}{\partial \mathbb{C}} \end{pmatrix} . \tag{5.15}$$

The optimisation function is given by

$$\begin{pmatrix} \mathbb{A} \\ \mathbb{B} \\ \mathbb{C} \end{pmatrix}_{\text{new}} = \begin{pmatrix} \mathbb{A} \\ \mathbb{B} \\ \mathbb{C} \end{pmatrix}_{\text{old}} - \vec{J}^{-1} \begin{pmatrix} f(a,b) \\ f(b,c) \\ f(c,a) \end{pmatrix} . \tag{5.16}$$

In each iteration, $\vec{J}^{-1}$ is recalculated using the new values of $\mathbb{A}$, $\mathbb{B}$ and $\mathbb{C}$. The process is set to continue until the following criterion is met:

$$(\mathbb{A}_{\text{new}} - \mathbb{A}_{\text{old}})^2 + (\mathbb{B}_{\text{new}} - \mathbb{B}_{\text{old}})^2 + (\mathbb{C}_{\text{new}} - \mathbb{C}_{\text{old}})^2 < 1 \times 10^{-18} . \tag{5.17}$$

This results in values for $\mathbb{A}$, $\mathbb{B}$ and $\mathbb{C}$, giving the inclinations of all three triangles. Once these inclinations are obtained, there is only one possible configuration of the hexapod. Therefore once the three angles are known, the x, y and z coordinates of the corners of the top, triangular platform can be calculated.

With this numerical method, the six position sensors in the hexapod can be used to find the position of the top platform (the top of the TPC) with respect to the base of the hexapod (the inside of the ICV). This style of solution, whereby three constraint equations undergo simultaneous solution via the Newton-Raphson method, is advocated in [90]. A similar approach is taken in [91]; however a simpler geometry enables the substitution of variables such that the three simultaneous equations become a single equation to be solved numerically.

5.4.4 Multiple solutions and singularities

It was noted above that, for a set of simultaneous equations describing the hexapod, there are sixteen possible solutions corresponding to sixteen possible hexapod configurations for a given set of sensor lengths. The configurations these correspond to are explored in fig. 5.12. Of these sixteen possibilities, only one is an option for the hexapod we are considering, as reaching the other configurations from our starting point would demand going beyond the possible range of movement for the hexapod. The other fifteen solutions moreover do not pose a concern for our numerical solution for the LZ hexapod. Following McAree, with *a priori* knowledge of the assembly at

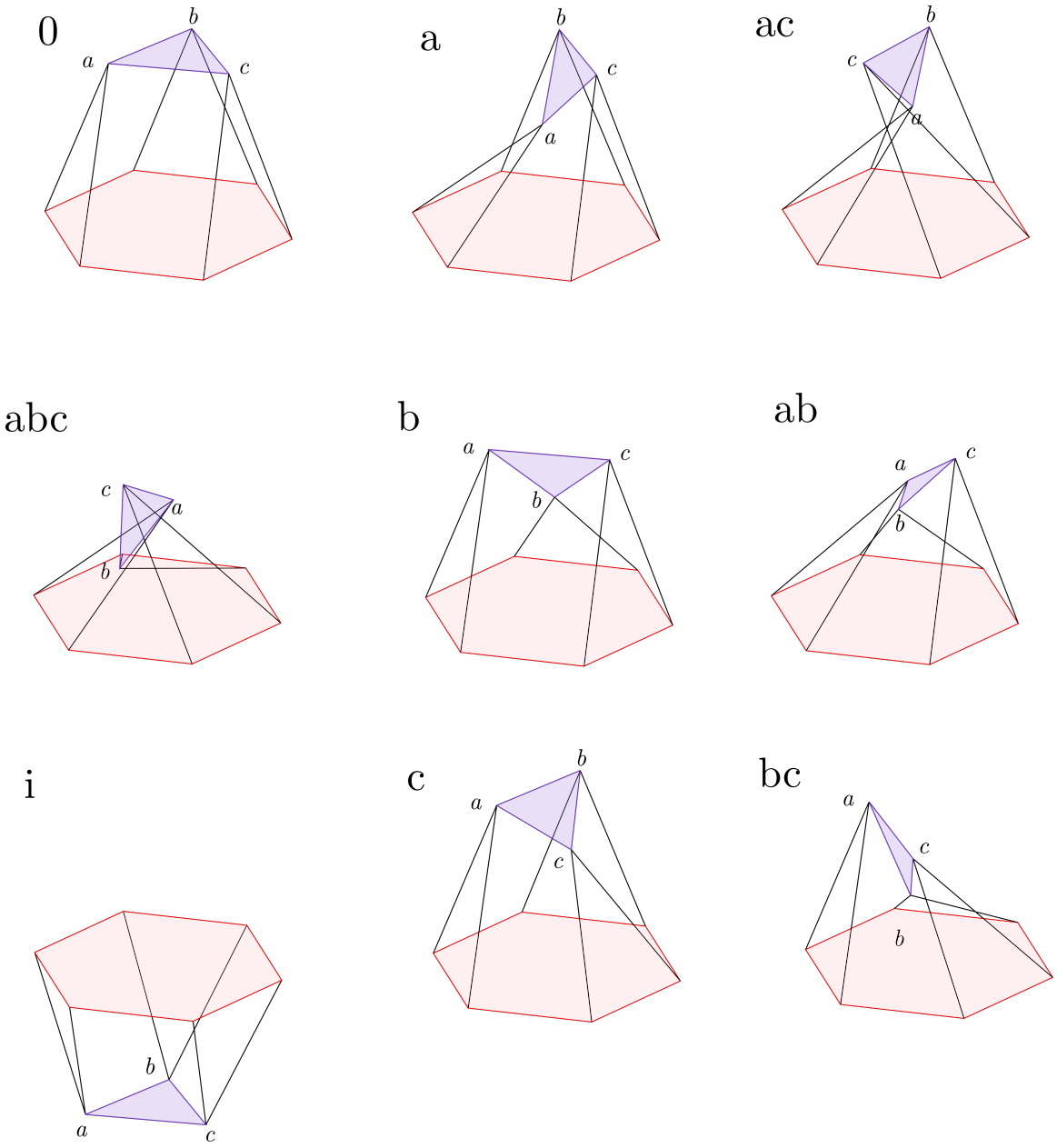


Figure 5.12: An illustration of some of the different hexapod configurations that constitute the sixteen possible solutions to the simultaneous equations. In every case, the leg lengths are the same, as are the lengths ab, bc and ca. (0) is the original, correct solution. (a), (b), (c) are the solutions where the corresponding vertex has been 'folded' through to the other side such that the triangle abc can still be constructed. (ab), (ac), (bc) have two sides 'folded' in this way. (abc) has all three sides 'folded' through. These eight configurations represent all the possible architectural solutions where the top platform is above the bottom platform. However, for each of these there is also an equivalent solution where the top platform is inverted below the bottom platform. The simplest of these is (i), and the remainder can be similarly constructed.

some initial time, it is possible to track the motion of the platform unless or until it reaches a singular configuration.[90] This is a configuration in which the kinematic constraint equations are poorly conditioned, such as the 'base' platform being coplanar with the 'upper' platform. In such a case, Newton-Raphson-based algorithms will invariably fail.[90] However, none of the singular configurations in question are within the working range of the hexapod, so the algorithm will not be required to run near such singularities. Hence the equations will remain well conditioned and the initial estimate in each iteration will be near the true solution, so the Newton-Raphson algorithm to be used will provide good convergence.[90]

The initial configuration of the hexapod will be known: once installed, the hexapod can be observed through a cable port to ensure it is in place as expected. An estimate of the initial lengths and configuration can be determined from the CAD model of the hexapod in the detector. These can be used as the input for the first solution. From there, all movements will be small. Hence if the previous solution is used as the starting point on each occasion, the correct solution will be attained.

5.5 Hexapod design

The hexapod is designed to measure the movement of the top of the TPC with respect to the inner cryostat vessel. It is thus fixed between the ICV dome and the PMT truss. The hexapod will be able to measure the position of the PMT array in terms of its x,y and z position, as well as its pitch, roll and yaw. This means that the orientation of the PMT array will be known; this information is only available with the hexapod. In the following subsections we will review the design of the hexapod and explain the choices made in that process.

5.5.1 The design

The hexapod needs one platform to which six sensors connect and another platform to which three sensors connect. However neither of these platforms needs to be a standalone or separate structure as far as the hexapod is concerned. The platforms can be virtual structures, conceived as the planes in which the sensor connections exist. Nevertheless, the sensor connections do, of course, have to be physical. In order to minimise the amount of material the hexapod introduces to the detector, the sensors will connect directly to the dome, so this upper platform is virtual. However the lower platform is real. It consists of a hexagon of six titanium bars with corner

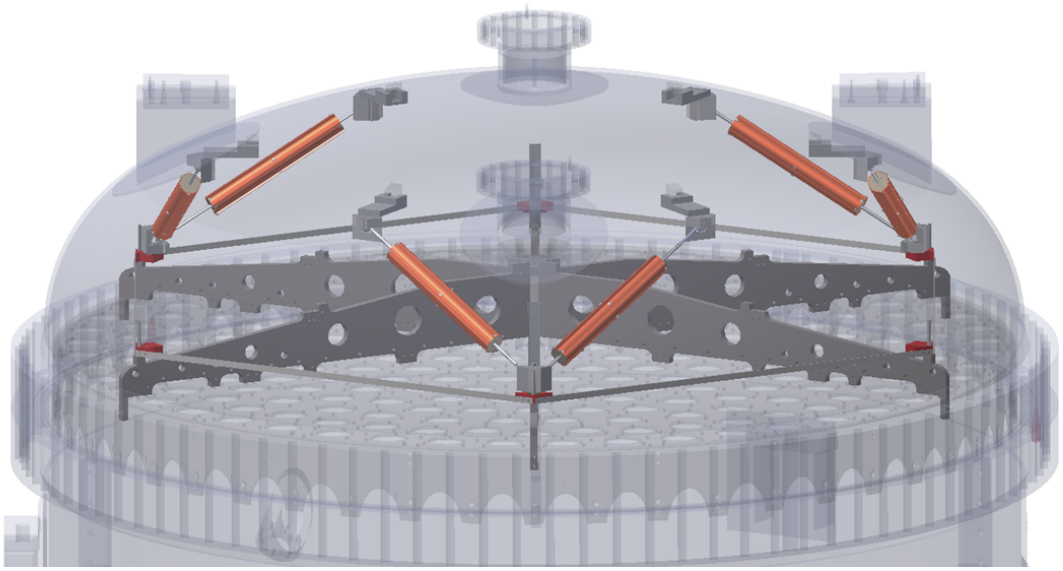


Figure 5.13: A CAD image showing the hexapod in place between the PMT truss and ICV dome. The hexapod will measure the position of the PMT truss with respect to the ICV, particularly during the cooling of the experiment, when the PMT truss is expected to move. This does not give the position of the PMTs with respect to the liquid xenon height, but gives valuable information about the movement and final position of the PMTs.

connectors that are aligned with the six struts of the PMT truss. The sensors connect the two platforms, as shown in fig. 5.13.

5.5.1.1 Mounting points

There will be six mounting points on the inside of the dome and three on the PMT truss. Part of the motivation for this is conceptual. The motivation for the hexapod is knowing how the PMT truss moves with respect to the ICV, which is our frame of reference. The algorithm finds the position of the top platform (which has three sensors connected to it) with respect to the base (which has six sensors connected to it). Hence the base should be the ICV dome, with six sensors and the upper platform should be the PMT truss with three sensors. It is worth clarifying that the base is thus physically above the 'upper' platform.

The mounting posts themselves will be welded onto the inside of the ICV dome after its construction. The posts are rectangular to enable the alignment of the hexapod when connecting to them; see fig. 5.14. One side is curved to match the curve of the inside face of the dome; the precise shape of this curve depends upon the radius at which the posts are placed. Small errors in the placement of the mounting

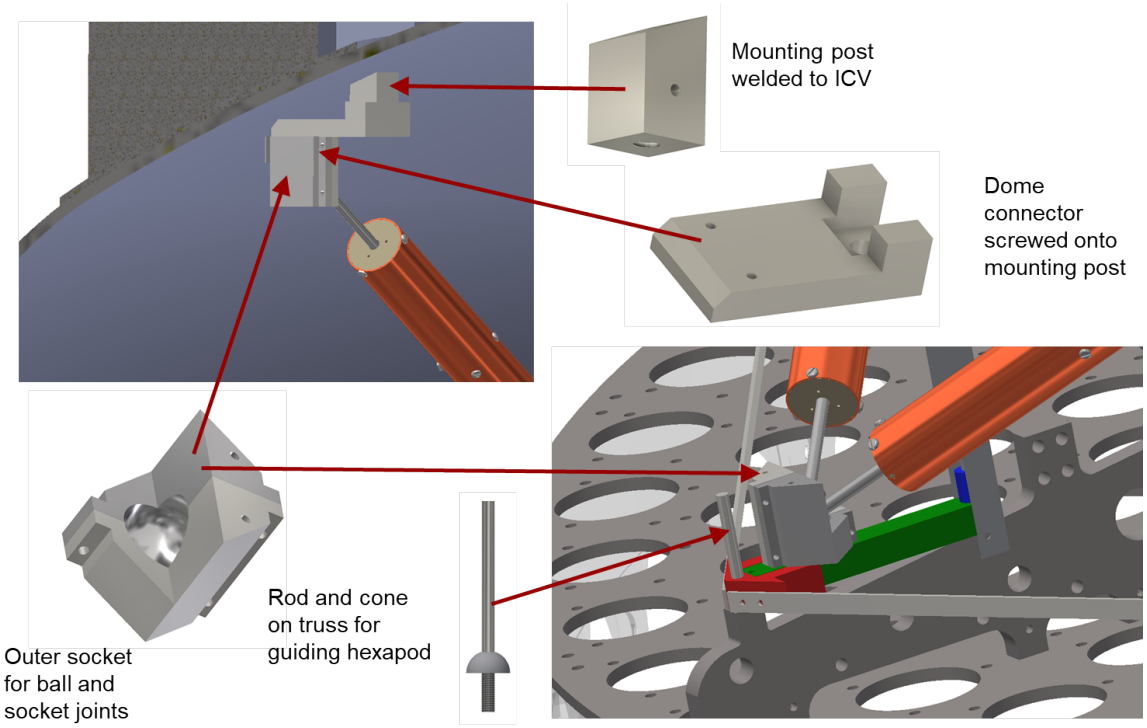


Figure 5.14: Parts of the hexapod and connections

posts will not be a big problem so long as they are well measured. The algorithm needs to know exactly where the connection point is, but can deal with irregular placements so long as the final connections to the sensors are all in a plane. Once the mounting posts are welded in place, the inside of the dome will be scanned by a laser to measure precisely the inside surface and the positions of the mounting posts. Adjustments can then be made to the dome connectors that will screw onto them to ensure that the ball and socket joint will sit at exactly the right height to put all the sensor connections in a plane.

5.5.1.2 Bars

The platform that connects to the PMT truss consists of six titanium bars that connect with specially designed corner pieces. These bars are taller than they are wide so that they will not flex downwards. Only two corners will be bolted down, as will be explained in section 5.5.1.4, so it is important that there is no vertical flex in the hexapod. If there were scope for such motion, as the TPC shrinks and falls away, it could be possible for the hexapod to not move with the truss. The hexapod therefore would not measure the position of the truss. However, using bars with an upright cross-section essentially eliminates this possibility. Titanium is chosen for the

bars and corner pieces for two main reasons. First, the material stands to introduce a substantial additional mass to the detector. In order for this not to greatly impact the background contribution of the sensors, the material must be highly radiopure. The titanium sourced for creating the cryostat vessels is particularly radiopure, so the material leftover from this was a good option. In addition, using the same material for the hexapod bars as is used for the PMT truss eliminates any concerns about differential shrinking between the hexapod and the PMT truss.

5.5.1.3 Platform corners

The corner pieces are designed to connect pairs of bars with pairs of stainless steel screws. Two screws at each end of the bar will ensure that the bars are correctly aligned and the hexapod cannot be constructed with any deformation to the platform. The corner pieces also have a hole and countersunk cone cut from the base. This is to align each corner of the hexapod with the correct point on the PMT truss, on which there are corresponding rods with spheres at their bases. A CAD model of the design can be seen in fig. 5.15. The radius of the sphere and the angle of the cone will affect how the two pieces interact, which in turn affects what height the hexapod sits at. In order to make the most of the maximised sensitivity, these numbers are known and included in the appropriate calculations of hexapod height.

5.5.1.4 Screwing down the hexapod

The hexapod needs to be firmly attached to the PMT truss to ensure that when the TPC shrinks away from the ICV dome, the hexapod platform moves with it and measures this change in position. The complication is that the hexapod will not sit in the right position until the dome is lowered and once the dome is in place, the interior is no longer accessible.

To solve this challenge, the hexapod will be constructed above its final position and lowered into place with the dome. It will then be secured with screws that connect the hexapod to the PMT truss. These screws sit directly below the cable ports in the dome and this is how we will access them. An additional sleeve is inserted into the port, which features a small hole directly above the screw. A very long Allen key will be inserted through this hole and used to turn the screw, fixing the hexapod onto the PMT truss.

The two parts to be screwed together are an ‘extender’ that comes out of a hexapod corner connector and the top of a flat boss on the PMT truss. The screw used for this is designed to be held in a stand on the extender so that it cannot fall out as

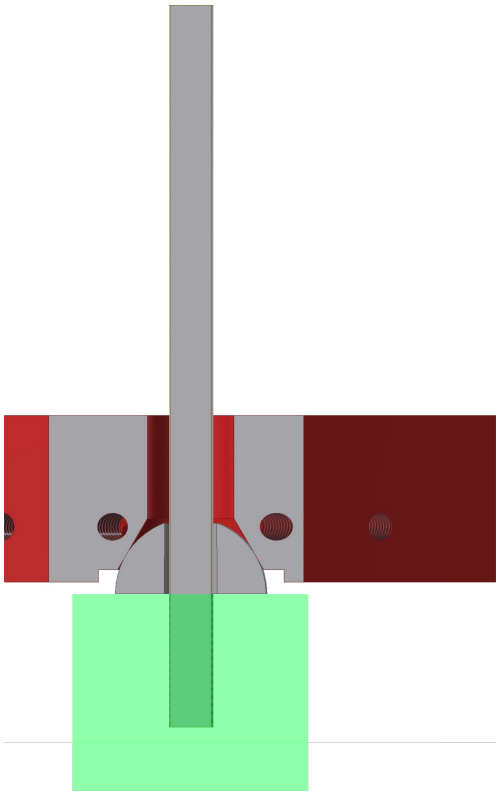


Figure 5.15: A CAD image showing a section through the rod and sphere attached to the PMT truss (location shown by green square), with the corresponding cone-shaped cutaway in the corner connection piece of the hexapod.

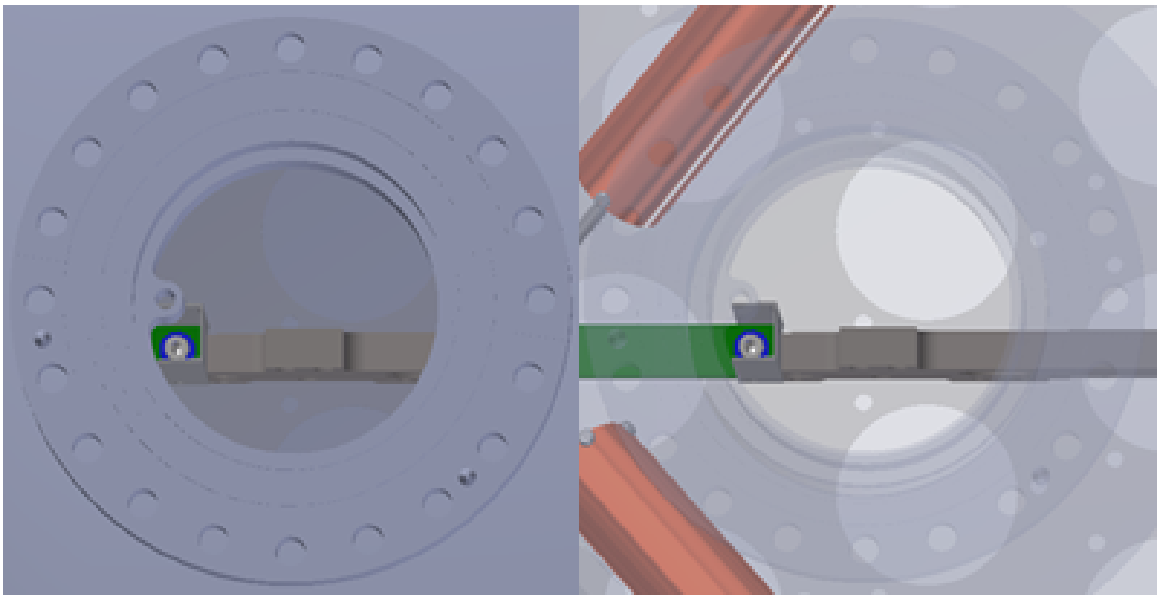


Figure 5.16: A CAD image of the view directly down through the cable port at the top of the ICV. The attachment point for the hexapod can be seen straight through it. On the right, the cryostat vessel has been greyed out to make the interior clearer. The additional sleeve provides the small circular hole visible on the left hand side of the port. At the end of the green arm, a square guard can be seen, which will prevent the arm rubbing against the cables as it moves into place.

the hexapod is lowered. If this were to happen, the system would have to be opened up and potentially disassembled to remove the screw, so this is a small but critical detail. It is also designed so that if it is accidentally loosened rather than tightened while being accessed from the cable port, it will not unscrew and fall out, as this would cause the same problem. The stand for the captive screw is shown in fig. 5.17.

5.5.1.5 Sensor connections

At the point where the sensor connects to the platform, it must do so via a joint to allow movement of the platform without applying strain to the sensor. For the single sensor connections (to the '6' platform), it makes sense for these to be simple ball and socket joints, as they allow appropriate freedom of movement. They are machined from titanium with PEEK inserts such that a titanium ball (with a rod attached) moves inside a PEEK socket, which in turn moves inside a titanium socket. The use of the PEEK insert should reduce the friction between the ball and socket, which might be a problem if adjacent surfaces were titanium.

The connections for the pairs of sensors to a single point are more complex. In

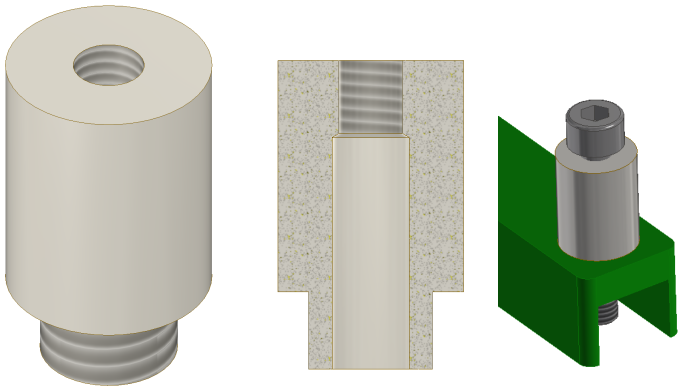


Figure 5.17: Left and Centre: CAD images of the stand for the captive screw. This is fixed into the extender bar runs from a corner of the hexapod along the PMT truss. The screw is what holds the hexapod in place on the truss. The screw is screwed through the stand before assembly of the hexapod. The long unthreaded core of the stand means that if the screw (which has a thread only on its lowest section) is unintentionally unscrewed rather than tightened, it will not unscrew from the stand. Right: The screw, stand and extender bar.

order for the geometry posed in the algorithm to hold true, the two sensors must meet at a point. This point can be virtual, that is, the two sensors do not need to literally be connected at a point. However, the connection point must not move when the sensors move.

One way to achieve this is with a double ball and socket joint where the two ball and socket pairs are concentric, that is, they are constructed around one another. This may be an inappropriate solution for some hexapods because such a ball and socket joint is very difficult to construct in a way that allows unconstrained movement of both balls. However, for the small range of motion we anticipate, these restrictions do not pose a concern. As such a double ball and socket joint will work well.

An alternative considered was a set of hinges organised to allow the required motion while maintaining a single coincident point for the sensors. However the hinges would have to be built from scratch using low-background materials and without any lubricant such as oil or grease. Adding PEEK inserts would be complicated and it was felt that machining the parts would be expensive as a result of this complexity. Without them, the risk is that the joint would be too tight and seize up as a result of metal-on-metal friction, or would be too loose and the play in the joint would compromise precision movement and measurement. Thus the double ball and socket joints were selected instead.

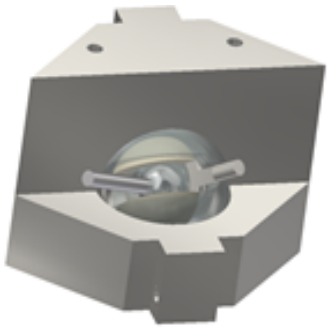


Figure 5.18: A CAD image showing the double ball and socket joint. These are the connection between the PMT truss and a pair of position sensors.

The PEEK inserts in the double ball and socket joint ensure the surfaces in contact are not both metal, so they should reduce friction. The shape of the inserts is non-trivial, however, as they must permit as much movement as possible while not allowing the joint to fall apart. If the pieces that make up the insert are smaller than the gap in the socket housing, in certain situations a piece of lining could fall out. Once one piece goes, the whole socket finds new and unwanted axes of motion and is likely to completely disintegrate. Hence the PEEK inserts consist of one complete hemisphere and one hemisphere with an angled slot cut out of part of it. This slot gives space for the rod to the other ball to move. Greatest freedom of movement would be achieved if the slot bisected the hemisphere; however the pieces of lining are then too small. Hence a single piece is used with an angled slot. All of the engineering drawings for the ball and socket joints can be found Appendix F.

5.5.2 Installation

The ICV has six welded mounting points on the inside of the dome. The sensors are attached to these while the dome is suspended high above the TPC, before the whole hexapod is lowered onto the PMT truss. The hexapod is built by connecting together pairs of sensors and constructing the titanium hexagon. The cable from each sensor runs up to the dome. The construction of the hexagon must avoid the cables that will run from the PMT truss to the ports in the ICV dome, that is, through the centre of the hexapod. Once built, the hexapod will be sitting in the right place and will be electrically connected, but it has no mechanical connection to the PMT truss. Once the dome is in place, a long Allen key will be inserted through a gap in a sleeve in the dome ports. This will be used to screw the hexapod base frame onto the PMT truss. It is not safe to leave the two pieces unconnected as the assembly is done above

ground, before the detector is tipped for transport below ground. This tipping could result in the hexapod slipping out of place if not bolted down.

5.5.3 Electrical connection

The electrical connection is made once the hexapod is constructed and hanging from the dome. The cables will exit the sensor at the end nearest the dome and will make their way to a connector using the Harwin pins and receptacles described in Chapter 4. The cables that exit this connector will run along the inside of the dome of the ICV to the port, where they will join other cables in exiting the vessel.

The cables are fixed solidly to the Cirlex plates in the sensor, both by the connection to the active sensor plates as well as by additional solder on the back of the plates to hold the sheath of the cable firmly. The Cirlex plates are in turn fixed to the copper tube. In order for the cable length not to need to change when the hexapod compresses as the dome is lowered, the rod that connects to the single ball and socket joints and hence to the ICV will be screwed into the disk that connects directly with the outer tube of the sensor. The moving inner copper blocks are actuated by the rod that comes out of the lower end of the sensor, attached to the double ball and socket joints and hence the PMT truss.

During this compression and later movements of the sensor, the cables will move with respect to the copper cylinder that fixes the square rods holding the blocks apart. The holes in this are as large as possible to minimise friction between the cables and sensor. However, routing the cables as just described minimises the number of parts that will move with respect to the cables, and also removes the need for the cables to bend or change length during the installation or running of the hexapod.

5.5.4 Sensitivity

The hexapod is intended to measure the change in relative position of the TPC and the inner cryostat vessel (ICV) in three axes: vertically, radially and axially. Vertical motion will separate the two hexapod platforms and axial motion will rotate them with respect to each other. The design of the hexapod will affect the sensitivity to the three different axes of measurement. The two that are most critical and most interesting are the vertical movement (which is expected) and the radial movement (which could be significant if it occurs). The axial movement is expected to be zero; it is measured to ensure that it is so. Thus the hexapod is designed to be equally

sensitive to the vertical and radial movement, which constrains some aspects of the hexapod design.

The sensitivity of the hexapod can be framed in terms of how much extension the sensors undergo for a given movement. To illustrate, consider one of the triangles formed by a pair of hexapod sensors. Let this triangle have vertices A, B and C, with AB and AC consisting of sensors, with a solid base BC. The taller the triangle is, that is, the higher vertex A is above the base BC, the less sensitive the sensors will be to vertical movements: for a height change of a fixed amount, the sensor length will change much more for a shorter triangle than a taller one. Hence the shape of the hexapod, in terms of the relative sizes of the base and height, determines how sensitive the hexapod will be to different motions.

A kinematic analysis of the hexapod can be used to determine the leg lengths required for a given platform position. From this, the leg length change for a given movement of the top platform can be calculated.

In order to fulfil the criterion of equal sensitivity to radial and vertical movements of the platform, the average leg length change should be equal for 300 µm vertical movement and 300 µm radial movement of the centre of the top platform with respect to the centre of the base. (These are the smallest movements we are required to measure with the hexapod.) This demand is used as a proxy for equal sensitivity to vertical and radial movement. The set of six leg lengths is calculated for the original platform placement and recalculated for the displaced platform. The average change of leg length is calculated as $\frac{1}{6}$ of the sum of the squares of the change of leg lengths.

In designing the hexapod, there is not total freedom to choose the base radius, height and top platform radius. Prior mechanical constraints exist resulting from the placement of the hexapod between the PMT truss and the dome of the ICV. This limits the height and radius of the hexapod, as it must fit in this space. In fact, there is no point within the dome for which we can attain equal sensitivity to both vertical and radial movement - the hexapod needs either to be taller or have a larger radius than the dome permits at any point. This is demonstrated by the fact that the lines in fig. 5.19 do not cross. As a compromise, the radius of the base (upper) platform is chosen to be that for which the two lines are closest. This determines the location of the welded mounting posts in the dome. This is at a height of 215.1 mm, which corresponds to a radius of 486.1 mm

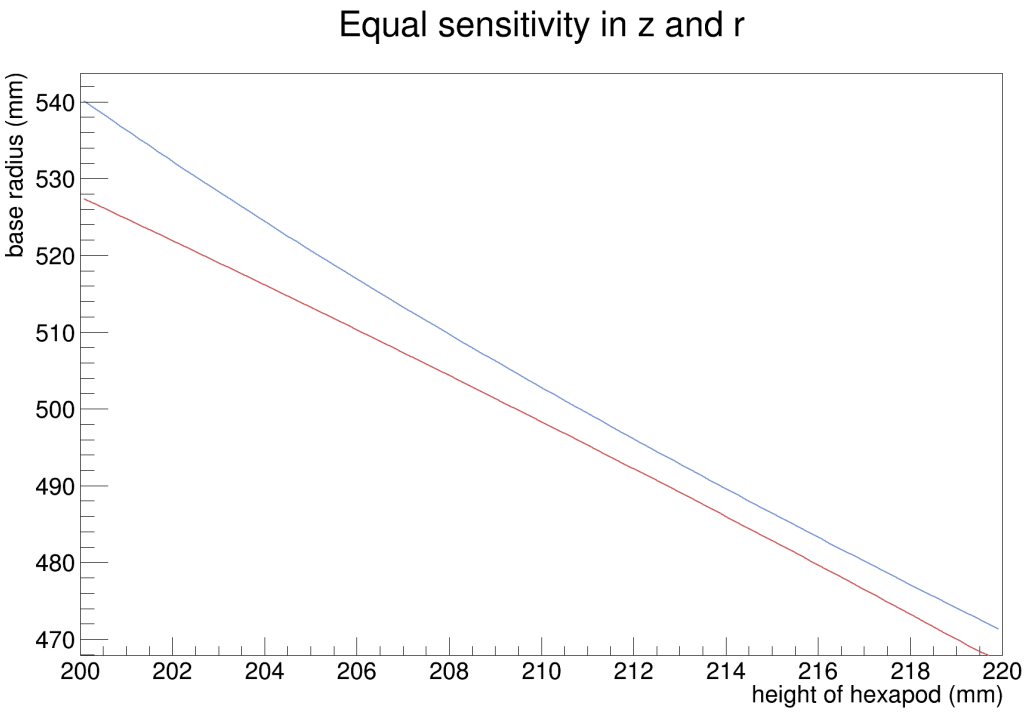


Figure 5.19: The outcome of the hexapod sensitivity optimisation. The blue line (upper) shows the heights and radii for which the hexapod is equally sensitive to vertical and horizontal movements. The red line (lower) shows the available heights and radii given the mechanical constraints of the ICV dome. The point of closest approach of these two lines is at a height of 215.1 mm, with a corresponding radius of 486.125 mm. This is where the hexapod will most closely approximate being equally sensitive to radial and vertical movements.

5.5.5 Temperature effects

Both platforms of the hexapod will shrink radially with cooling. The upper (base) platform is effectively made of titanium, as it is the ICV dome. The lower (top) platform is a titanium ring. Therefore the two platforms will both shrink, and will do so by the same proportion as the ICV and field-shaping rings. The size of the base platform is used in the calculation of the position of the top platform, so a factor for its shrinking must be included in the calculations. The temperature of the ICV will be known, as it is well-instrumented with thermometers, so its shrinking can be precisely calculated. The same applies to the radial shrinking of the PMT truss, which determines the three distances between the three top points of the hexapod. These shortening lengths will be inputs into the algorithm that calculates the position of the PMT truss with respect to the ICV.

In addition, the titanium rods that connect the sensor to the ball and socket joints will shrink as they cool. The shrinking rods will not pull the ball-and-socket joints closer together so will instead affect the length measured by the sensor by extending it. However, this can be corrected for if the additional sensor length in the algorithm is modified with temperature, as per the other lengths discussed above.

5.5.6 Error propagation

The sensors cannot be perfectly precise or accurate. It was shown in Chapter 4 that the maximum error on a sensor's measurement is around 0.3%. Errors in the sensor measurements of length will propagate through the algorithm for the hexapod and result in errors in the reconstructed positions of the top platform points. This can be modelled numerically, considering the error in hexapod output given a known error in input. The maximal error in the reconstructed height of the platform corresponds to the worst-case scenario of all six sensors being wrong by the maximum estimate of 78 µm.

If everything is constructed precisely according to the CAD models of the detector, the hexapod will have a triangular lower (top) platform with radius 695.8 mm and a hexagonal upper (base) platform with radius 541.5 mm, separated by a vertical height of 195.5 mm. All of the sensors have length 403.7 mm. All of these lengths are measured to the centres of the ball and socket joints, which is where the edges meet. If we run the hexapod algorithm with these sensor lengths, base coordinates and top platform separations, the coordinates output (all in mm) are as follows:

- A: $(0.0, -695.8, 195.5)$

- B: $(602.6, 347.9, 195.5)$
- C: $(-602.6, 347.9, 195.5)$.

Together, these give the coordinates of the centre of the top platform (the PMT truss) as $(0.0\,\text{mm}, 0.0\,\text{mm}, 195.5\,\text{mm})$ with respect to the centre of the base platform (the ICV dome), where positive z is in the direction of the bottom of the detector.

In the case of the sensors all having the maximal error of 78 µm, we can add this to all the sensor lengths and investigate the outcome of the algorithm. Inputting all the sensor lengths as 403.7 mm gives an output (in mm) from the algorithm as:

- A: $(0.0, -695.8, 195.6)$
- B: $(602.6, 347.9, 195.6)$
- C: $(-602.6, 347.9, 195.6)$.

Hence the new z-coordinate of the centre of the platform is 195.6 mm. The difference between this new coordinate and the old coordinate is 0.1 mm. As all the sensors were lengthened by the same amount, this is the only coordinate that changed. However, the procedure can be repeated changing any number of sensors. In each case, no coordinate changes by more than 200 µm.

Certain combinations of sensor errors can reinforce to produce other maximal errors, which can be explored as above. If the sensor errors act to produce an apparent rotation of the top platform compared with its true position, the constraint of no coordinate being mis-reconstructed by more than 200 µm results in a mis-reconstruction of the yaw of the platform by up to 0.02 deg. Similarly, the pitch and roll can be mis-reconstructed due to sensor error by up to 0.02 deg.

The process shows that the hexapod provides an acceptable level of accuracy for LZ. The baseline sensitivity expected of the sensors by the experiment is that the system should measure position to a precision of better than 300 µm. If they do not achieve this, they will not be considered appropriate for use in LZ by the collaboration. However, in each test case here, the output changed by an amount less than the required sensitivity of the position sensors. With these sensors and the hexapod algorithm, possible sensor errors lead to an error of less than 200 µm on the position as reconstructed from the sensor measurements. Thus the propagation of sensor errors through the hexapod algorithm does not pose a problem, and the hexapod fulfils the requirement placed on the position sensors by LZ.

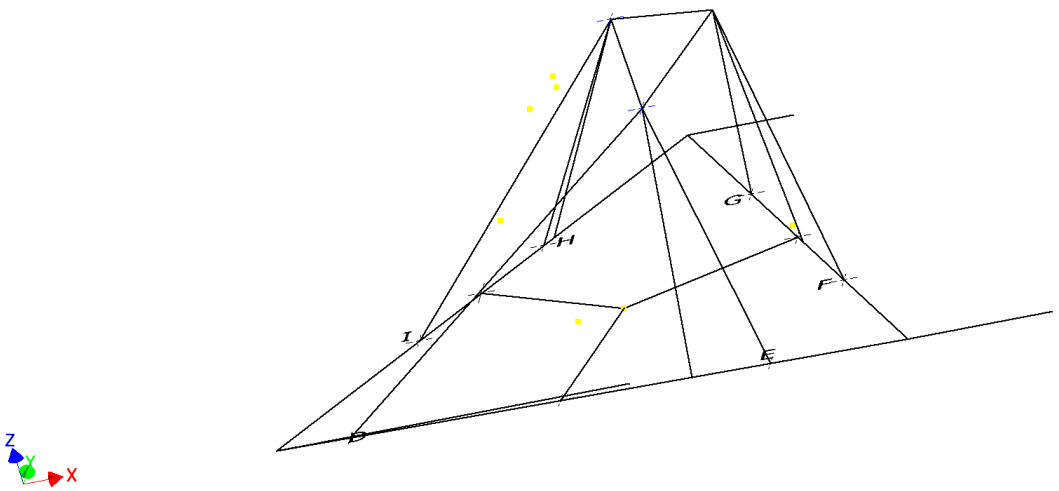


Figure 5.20: A CAD model of an arbitrary 6-3 GSPM structure. The CAD software was used to measure the lengths of the 'sensors', and this was an input to the algorithm. The algorithm produced the estimated positions of top platform, and this was compared to the positions in the CAD software.

5.6 Testing the hexapod

5.6.1 CAD models

The first stage of testing the hexapod algorithm used a CAD model shown in fig. 5.20. This model has an irregular hexagonal base and an irregular triangular top platform at an angle to the base. The base coordinates, top platform point separations and sensor lengths were measured in the CAD programme used to create this model. They were found to be as follows (all given in mm):

d: $(-619.607, -437.759, 0)$

e: $(433.036, -470.623, 0)$

f: $(560.573, -78.479, 0)$

g: $(245.435, 508.9, 0)$

h: $(-263.149, 442.696, 0)$

i: $(-514.961, 36.379, 0)$

$ab = 399.353$

$bc = 292.156$

$ca = 492.926$

$da = 1075.079$

$ea = 680.176$

$fb = 715.309$

$gb = 750.181$

$ch = 752.994$

$ic = 913.006$

With these inputs, the hexapod algorithm was run, with the following outputs:

- A: $(243.511, -212.322, 600.000)$
- B: $(380.260, 159.541, 650.000)$
- C: $(106.760, 260.304, 630.000)$

giving an overall set of coordinates for the top centre point as $(243.510, 69.174, 626.667)$. The coordinates for the three top points correspond exactly to those measured in the CAD model, showing that the hexapod algorithm is able to handle an irregular hexapod and produce correct results.

5.6.2 Hexapod test stand

The second stage of testing the hexapod is to build one and demonstrate that the algorithm produces results matched by those measured in another way. For this, we created a smaller version of the hexapod, with a base diameter of 0.6 m, as a hexapod the size of that in LZ would not fit onto the 3-dimensional metrology table in the department's mechanical workshop. The model hexapod was built with full-size position sensors. The ball and socket joints were 3D-printed in plastic, and the top and base platform were created from plywood. These aspects can be seen in fig. 5.21.

The height of the triangular platform above the base could be adjusted, as well as the platform rotated. The metrology system could be aligned to record the position of a chosen point. This was chosen to be a point directly above one of the three points reconstructed by the algorithm; the algorithm reconstructs the positions of

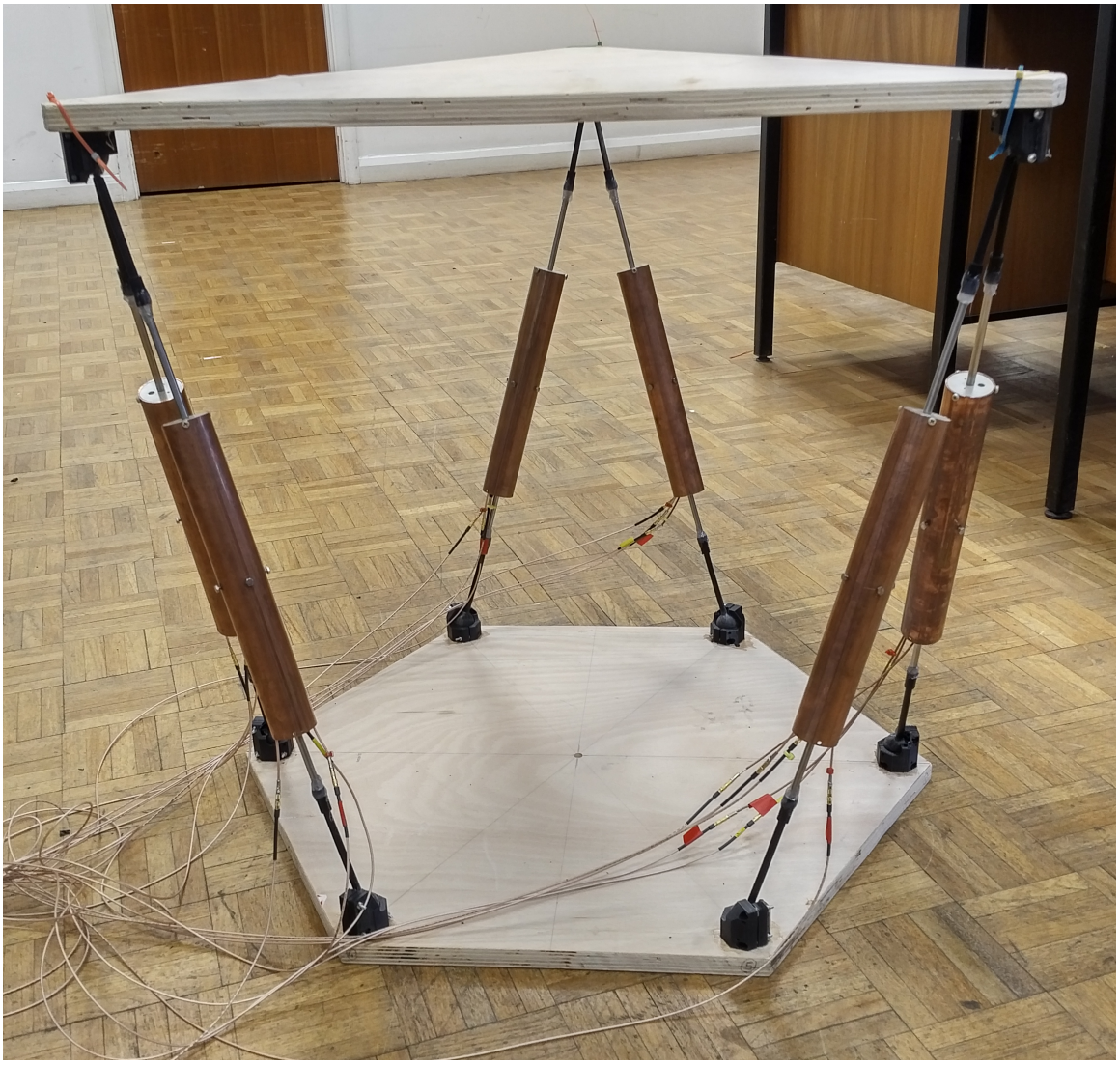


Figure 5.21: The hexapod test stand constructed as a proof-of-principle model for the system of sensors and reconstruction algorithm.

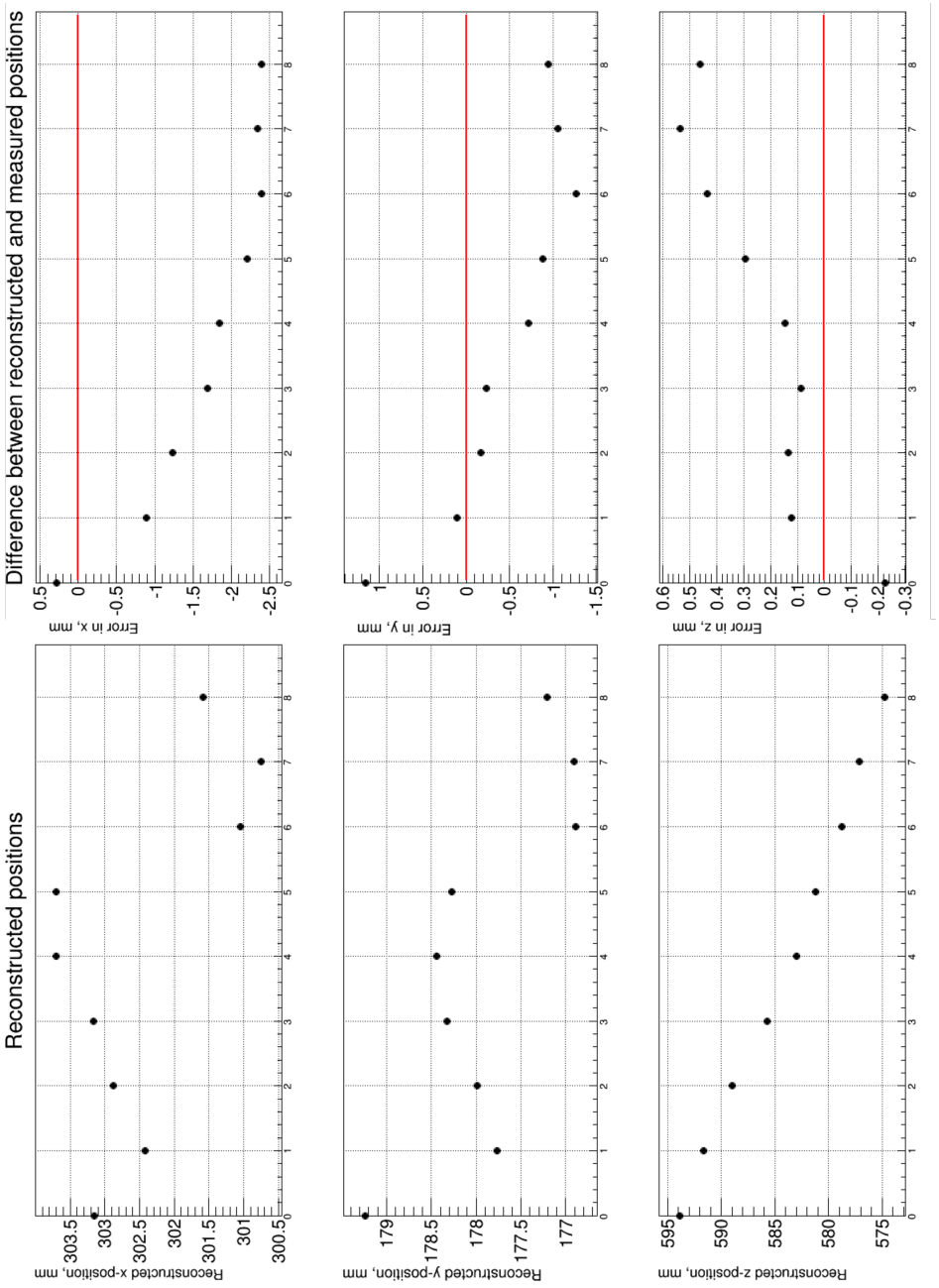


Figure 5.22: Data from the hexapod test stand during a run of movement that moved the top platform vertically. Shown is the reconstructed position (left) and the differences between the reconstructed and measured positions (right). The actual motion was measured with a coordinate-measuring machine (CMM) that measured the position of a point on the top of the top platform. From this, the position of the centre of the ball and socket joint was inferred. Some error was introduced by this process, as the CMM had to be aligned with the point by eye, and this could not always be accurate. This introduces some errors into the 'measured position' value. In addition, the theoretical centre of the ball and socket joint, which is the point reconstructed by the algorithm, is unattainable, so the translation from the point on the top of the platform to the point at the centre of the joint can only be estimated. This introduces further errors into the 'measured' values.

the centres of the ball-and-socket joints, as these are the corners of the geometry. The position of this point is extrapolated from the measured position.

Figure 5.22 shows a series of measurements made at a range of heights with the reconstructed position and the corresponding error between the reconstructed and measured positions. Some error is to be expected in this system. The 3D-printed ball-and-socket joints offer far less precise movements than the real joints will, and play in the joints will directly affect the accuracy of the measurements. In addition, although every care was taken to align the pin of the metrology system with the point to be measured, this was done in the x-y plane by eye, so errors in these coordinates are particularly likely. Nevertheless, the data shows good agreement between the reconstructed and measured positions for the z-direction. Although the overall errors are generally greater than the 300 µm precision required for LZ, the additional error is attributable to the test stand itself and not the underlying technology. Hence the hexapod test stand demonstrates the system of position sensors that will be used in LZ to monitor the position of the PMT array.

5.7 Conclusion

The hexapod is determining with high precision the position of the PMT array. The requirement placed upon it is to measure with an accuracy of better than 300 µm. The hexapod design explored in this chapter will be able to reach this requirement, enabling a precise understanding of the position of the PMT array. Hence, during cooldown, the movements of the TPC can be well understood, and the final position of the PMT array will be known. This is achieved through the combination of the design of the capacitive sensor readout discussed in Chapter 3, the accurate sensor design discussed in Chapter 4, and the hexapod design and reconstruction algorithm explained in this chapter, all of which are dedicated to fulfilling the requirements imposed by running in a large, low-background detector. Together, these aspects create a successful position-sensing system for the top PMT array in the LUX-ZEPLIN dark matter experiment.

Current Status

As of spring 2018, the LUX-ZEPLIN experiment is under construction. Cryostat fabrication has recently been completed and assembly of the PMT array began in March 2018. Xenon handling, installation and commissioning will start this autumn, as will some of the underground installation. The TPC construction and installation is planned to begin in spring 2019, with xenon liquefaction to start in winter 2019. The first physics data are expected in spring 2020.

The position sensors and hexapod will fit within this schedule. The hexapod is firmly fixed as a part of the experiment design and is included in the official engineering drawings. The position sensor components have been machined and cleaned, and the sensor construction has begun. The hexapod engineering designs have been finalised, and the titanium parts will soon be constructed. Installation will follow that of the TPC, so can be expected to be in spring 2019.

The Xenon1T experiment recently announced new results that further extend the range of cross-sections and masses in which dark matter has not been found.[92] The potential thus remains for a discovery to be made, and the LUX-ZEPLIN experiment will be well placed to lead this race to solve one of the greatest outstanding questions in physics.

Appendices

Appendix A

Analysing the analogue feedback circuit

The readout electronics provides an output voltage that depends in a known way on the capacitances to be measured. The precise relationship between the capacitances and the output voltage can be determined by analysis of the feedback circuit. Here is a fuller version of the calculation than was given in Chapter 3.

The first step is to analyse the first stage of amplification, which takes the input voltage V_{in} to V_{FS}.

$$\frac{V_{FS} - V^*}{Z_F} = \frac{V^* - V_{in}}{Z_I} \tag{A.1}$$

where

$$Z_F = \frac{R_F}{1 + i\omega R_F C_F} \tag{A.2}$$

and

$$Z_I = \frac{1}{i\omega C_I}\,. \tag{A.3}$$

Consider the gain of the first stage. In the regime in which the first stage amplifier is operating, the open-loop gain G is large (~ 1778) and dominates over the closed-loop gain of this stage such that the overall gain is approximately G. Hence, with an open-loop gain of G on the first stage,

$$V^* = -\frac{1}{G} V_{FS}\,. \tag{A.4}$$

Substituting these in,

$$V_{FS}\left(\frac{1}{Z_F} + \frac{1}{GZ_F}\right) = -\frac{V_{FS}}{GZ_I} - \frac{V_{in}}{Z_I} \tag{A.5}$$

$$V_{FS}\left(\frac{1}{Z_F} + \frac{1}{GZ_F} + \frac{V_{FS}}{GZ_I}\right) = -\frac{V_{in}}{Z_I}\,. \tag{A.6}$$

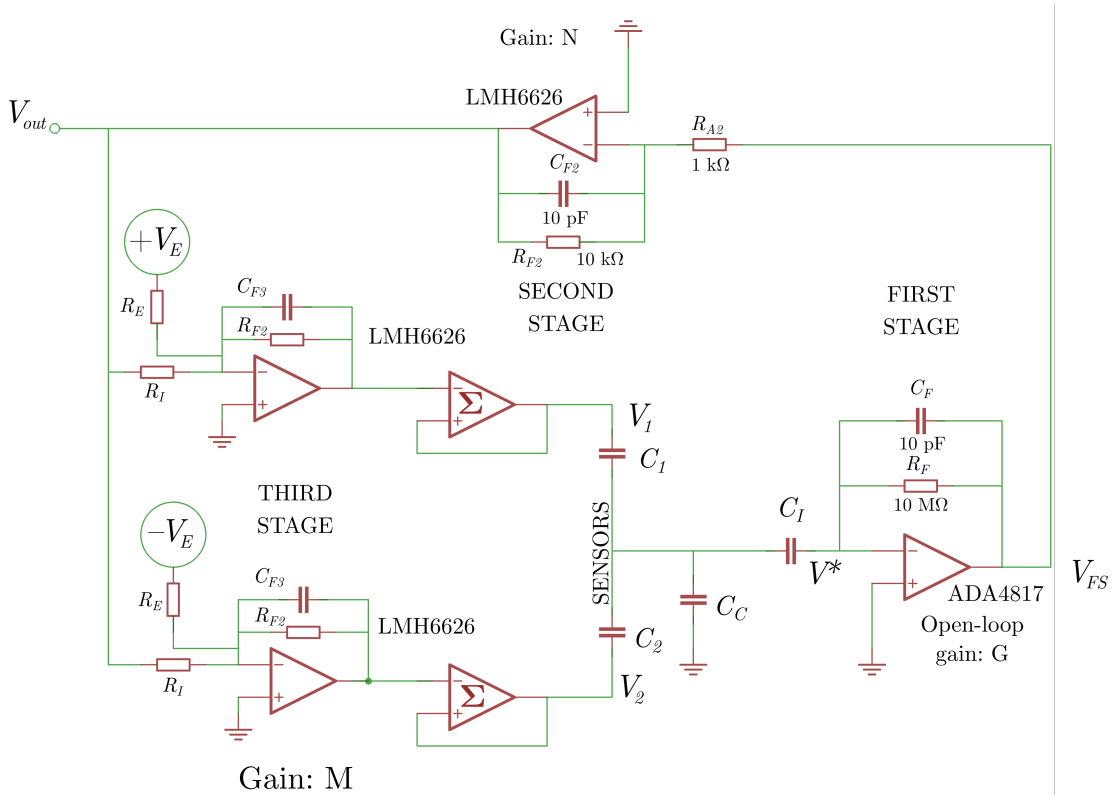


Figure A.1: The analogue feedback circuit to be analysed.

This can be rearranged for V_{FS}:

$$\begin{aligned} V_{FS} &= \frac{-V_{in}}{\frac{Z_I}{G}\left(\frac{G+1}{Z_F}+\frac{1}{Z_I}\right)} \\ &= \frac{-V_{in}}{\frac{1}{i\omega C_I G}\left(\frac{G+1}{R_F}(1+i\omega R_F C_F)+i\omega C_I\right)} \\ &= -V_{in}\frac{G}{G+1}\frac{i\omega C_I R_F}{1+i\omega R_F\left(C_F+\frac{C_I}{G+1}\right)}\,. \end{aligned} \tag{A.7}$$

Rearranging to put this into the form of a high-pass filter gives

$$\begin{aligned} V_{FS} &= -V_{in}\frac{G}{G+1}\frac{C_I}{C_F+\frac{C_I}{G+1}}\frac{i\omega R_F(C_F+\frac{C_I}{G+1})}{1+i\omega R_F(C_F+\frac{C_I}{G+1})} \\ &= -V_{in}\frac{G}{G+1}\frac{C_I}{C_F+\frac{C_I}{G+1}}\frac{i\omega\tau}{1+i\omega\tau}\,. \end{aligned} \tag{A.8}$$

where $\tau = R_F(C_F+\frac{C_I}{G+1})$. An appropriate choice of components (effectively neglecting the zero at DC) makes it possible to drop the high-pass filter element of eq. (A.8).

Hence

$$V_{FS} = -V_{in}\frac{G}{G+1}\frac{C_I}{C_F + \frac{C_I}{G+1}}\,. \tag{A.9}$$

The next step is to consider the second stage, which relates V_{FS} to V_{out} via the closed-loop gain N of the second stage such that $V_{out} = -NV_{FS}$. Hence, relating this to eq. (A.9),

$$\begin{aligned} V_{out} &= -NV_{FS} \\ &= NV_{in}\frac{1}{(1+\frac{1}{G})\frac{C_F}{C_I} + \frac{1}{G}}\,. \end{aligned} \tag{A.10}$$

This can be rearranged for V_{in}:

$$V_{in} = \frac{1}{N}\left[\left(1+\frac{1}{G}\right)\frac{C_F}{C_I} + \frac{1}{G}\right]V_{out}\,. \tag{A.11}$$

The next stage involves analysis of the circuit at the sense plate. The adder prior to this sums the created excitation to the output signals to generate the potentials fed to the plates 1 and 2 of the sensor. The adder has a gain of M, giving:

$$V_1 = -MV_{out} - V_E \tag{A.12}$$

$$V_2 = -MV_{out} + V_E\,. \tag{A.13}$$

Beginning where V_{in} is marked in fig. A.1, we can analyse the currents flowing. The potentials V_1 and V_2 are the potentials on the excitation plates of the capacitors. This analysis gives

$$\frac{V_1 - V_{in}}{Z_1} = \frac{V_{in} - V_2}{Z_L} + \frac{V_{in}}{Z_C} + \frac{V_{in} - V^*}{Z_I}\,. \tag{A.14}$$

Substituting in for V_1 and V_2, this gives

$$(-MV_{out} - V_E - V_{in})C_1 = (V_{in} + MV_{out} - V_E)C_2 + V_{in}C_C + (V_{in} - V^*)C_I \tag{A.15}$$

$$-MV_{out}(C_1 + C_2) - V_{in}(C_1 + C_2 + C_C - C_I) + V^*C_I = V_E(C_1 - C_2)\,. \tag{A.16}$$

We can substitute in for V^* using eq. (A.4) and for V_{in} using eq. (A.11). Hence

$$\begin{aligned} V_{out}\Bigg[&- M(C_1 + C_2) - \frac{1}{N}\left(\left(1+\frac{1}{G}\right)\frac{C_F}{C_I} + \frac{1}{G}\right)\left(C_1 + C_2 + C_C - C_I\right) \\ &+ \frac{1}{GN}C_I\Bigg] = V_E(C_1 - C_2)\,. \end{aligned} \tag{A.17}$$

This can be rearranged for V_{out} as follows:

$$V_{out} = \frac{C_2 - C_1}{M\big(C_1 + C_2\big) + (C_1 + C_2 + C_C + C_I)\frac{1}{N}\left[\big(\frac{G+1}{G}\big)\frac{C_F}{C_I} + \frac{1}{G}\right] - \frac{1}{GN}C_I} V_E \,. \quad \text{(A.18)}$$

Rearranging this gives

$$V_{out} = \frac{1}{1+\frac{1}{G}} \cdot \frac{C_2 - C_1}{\frac{1}{1+\frac{1}{G}}M\big(C_1 + C_2\big) + (C_1 + C_2 + C_C)\frac{1}{N}\big[\frac{1}{G+1} + \frac{C_F}{C_I}\big] + \frac{C_F}{N}} V_E \,. \quad \text{(A.19)}$$

V_{out} is related to the voltage recorded by the gain M' on the ADC as $V_{adc} = M'V_{out}$. Hence we can rewrite eq. (A.19) in terms of V_{adc}:

$$V_{adc} = M' \cdot \frac{1}{1+\frac{1}{G}} \cdot \frac{C_2 - C_1}{\frac{1}{1+\frac{1}{G}}M\big(C_1 + C_2\big) + (C_1 + C_2 + C_C)\frac{1}{N}\big[\frac{1}{G+1} + \frac{C_F}{C_I}\big] + \frac{C_F}{N}} V_E \,. \quad \text{(A.20)}$$

The gain G of the first stage is very large; hence we make the approximation $G + 1 \approx G$. Rearranging and making this substitution gives

$$V_{adc} \approx \frac{M'(C_2 - C_1)}{M(C_1 + C_2) + \frac{1}{N}\left[C_F + (\frac{C_F}{C_I} + \frac{1}{G})(C_1 + C_2 + C_C)\right]} V_E \,. \quad \text{(A.21)}$$

We can choose components such that the gain M' on the ADC is matched by the gain on the adder (third stage), i.e. $M' = M$. Hence

$$V_{adc} \approx \frac{(C_2 - C_1)}{(C_1 + C_2) + \frac{1}{MN}\left[C_F + (\frac{C_F}{C_I} + \frac{1}{G})(C_1 + C_2 + C_C)\right]} V_E \,. \quad \text{(A.22)}$$

We can also choose to set $C_F \ll C_I$ such that $\frac{C_F}{C_I} \approx 0$.

$$\begin{aligned} V_{adc} &\approx \frac{(C_2 - C_1)}{(C_1 + C_2) + \frac{1}{MN}\left[C_F + \frac{C_1+C_2+C_C}{G}\right]} V_E \\ &\approx \frac{(C_2 - C_1)}{(C_1 + C_2)(1 + \frac{1}{MNG}) + \frac{1}{MN}\left[C_F + \frac{C_C}{G}\right]} V_E \,. \end{aligned} \quad \text{(A.23)}$$

In addition, the three gains G, M and N are large enough that $1 + \frac{1}{MNG} \approx 1$. Hence,

$$V_{adc} \approx \frac{C_2 - C_1}{C_1 + C_2 + \frac{1}{MN}(C_F + \frac{C_C}{G})} V_E \,. \quad \text{(A.24)}$$

Rewriting the gains $MN = H$ and $K = \frac{C_1+C_2}{C_F}$, the output of the analogue electronic readout is

$$V_{adc} \approx V_E \cdot \frac{C_2 - C_1}{C_1 + C_2} \cdot \frac{1}{1 + \frac{1}{HK}\left(1 + \frac{C_C}{C_F G}\right)} \tag{A.25}$$

where V_E is the excitation voltage, $C_{1,2}$ are the measurement capacitors, G is the open-loop gain of the first amplifier block, H is the subsequent amplifier gain, C_F is the feedback capacitance of the first amplifier stage, C_C is the capacitance of the signal cable to ground, and $K = \frac{C_1+C_2}{C_F}$.

Appendix B

Analysing the digital electronics

The output of the electronics is

$$f = \frac{C_1 - C_2}{C_1 + C_2}\,. \tag{B.1}$$

Here we will show how that result is derived.

Consider the currents flowing in and out of point A, where V_S is the sense plate potential, V_1 and V_2 are the potentials on the excitation plates, and V_+ and V_- are the potentials at the terminals of the amplifier:

$$\begin{gathered} I_1 + I_2 = I_C + I_I \\ \frac{V_1 - V_S}{Z_{C_1}} + \frac{V_2 - V_S}{Z_{C_2}} = \frac{V_S}{Z_{C_C}} + \frac{V_S - V_-}{Z_{C_I}} \\ \frac{V_1 - V_S}{\frac{1}{i\omega C_1}} + \frac{V_2 - V_S}{\frac{1}{i\omega C_2}} = \frac{V_S}{\frac{1}{i\omega C_C}} + \frac{V_S - V_-}{\frac{1}{i\omega C_I}} \end{gathered} \tag{B.2}$$

if we consider AC excitations only. Hence

$$(V_1 - V_S)C_1 + (V_2 - V_S)C_2 = V_S C_C + (V_S - V_-)C_I\,. \tag{B.3}$$

Rearranging this gives

$$V_1 C_1 + V_2 C_2 = V_S(C_1 + C_2 + C_C + C_I) - V_- C_I\,. \tag{B.4}$$

V_{out} is the output of the amplifier. So

$$V_{out} = G(V_+ - V_-) \tag{B.5}$$

and at high frequency

$$V_- = -\frac{V_{out}}{G}\,. \tag{B.6}$$

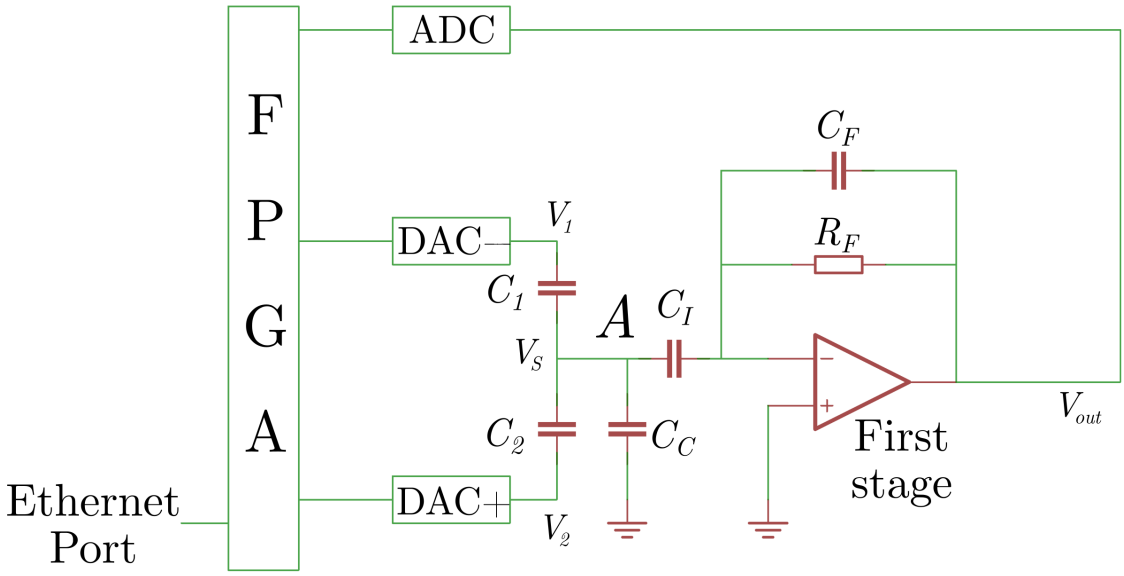


Figure B.1: The analogue feedback circuit to be analysed.

Considering the feedback loop around the amplifier:

$$\frac{V_S - V_-}{Z_I} = \frac{V_- - V_{out}}{Z_F} \tag{B.7}$$

$$\frac{V_S - V_-}{\frac{1}{i\omega C_I}} = \frac{V_- - V_{out}}{\frac{R_F}{1+i\omega C_F R_F}}\,. \tag{B.8}$$

Rearranging:

$$\frac{i\omega C_I R_F}{1 + i\omega C_F R_F}\left(V_S + \frac{V_{out}}{G}\right) = -\left(1 + \frac{1}{G}\right)V_{out}\,. \tag{B.9}$$

Hence

$$V_S + \frac{V_{out}}{G} = -\frac{1 + i\omega C_F R_F}{i\omega C_F R_F}\left(1 + \frac{1}{G}\right)V_{out}\,. \tag{B.10}$$

Rearranging for V_S gives

$$V_S = -\left[\frac{1 + i\omega C_F R_F}{i\omega C_F R_F}\left(1 + \frac{1}{G}\right) + \frac{1}{G}\right]V_{out}\,. \tag{B.11}$$

Multiplying out the RHS gives

$$V_S = -\left[\frac{1 + i\omega C_F R_F + \frac{1}{G}(1 + i\omega C_F R_F + i\omega C_I R_F)}{i\omega C_I R_F}\right]V_{out}\,. \tag{B.12}$$

Rearranging eq. (B.4) gives

$$V_S = \frac{V_1 C_1 + V_2 C_2 + V_- C_I}{C_1 + C_2 + C_C + C_I}\,. \tag{B.13}$$

Substituting this back in and rearranging gives

$$V_1C_1 + V_2C_2 = -\left[\frac{1 + i\omega C_F R_F + \frac{1}{G}(1 + i\omega C_F R_F + i\omega C_I R_F)}{i\omega C_I R_F}\right] \times V_{out}(C_1 + C_2 + C_C + C_I) - V_{-}C_I \quad \text{(B.14)}$$

$$V_1C_1 + V_2C_2 = -\left[\frac{1 + i\omega C_F R_F + \frac{1}{G}(1 + i\omega C_F R_F + i\omega C_I R_F)}{i\omega C_I R_F}\right] \times V_{out}(C_1 + C_2 + C_C + C_I) + \frac{C_I}{G}V_{out}\,. \quad \text{(B.15)}$$

Multiplying this out gives

$$V_1C_1 + V_2C_2 = -\frac{1}{i\omega C_I R_F}\Bigg[- i\omega C_I R_F\frac{C_I}{G} + 1 + i\omega C_F R_F + \left(\frac{1}{G}(1 + i\omega C_F R_F + i\omega C_I R_F)\right)\big(C_1 + C_2 + C_C + C_I\big)\Bigg]V_{out}\,. \quad \text{(B.16)}$$

If we operate at a high frequency such that $\frac{1}{\omega} \sim 0$, then we effectively need keep only the terms with frequency dependence. Hence we find

$$V_1C_1 + V_2C_2 = \Bigg[\frac{C_I}{G} - \frac{C_F}{C_I}\big(C_1 + C_2 + C_C + C_I\big) - \frac{1}{G}\big(\frac{C_F}{C_I} + 1\big)\big(C_1 + C_2 + C_C + C_I\big)\Bigg]V_{out}\,. \quad \text{(B.17)}$$

Rearranging for V_{out} and grouping terms gives

$$\begin{aligned} V_{out} &= \frac{V_1C_1 + V_2C_2}{\left[\frac{C_I}{G} - \big(\frac{C_F}{C_I} - \frac{1}{G}\big(\frac{C_F}{C_I} + 1\big)\big)\big(C_1 + C_2 + C_C + C_I\big)\right]} \\ &= -\frac{V_1C_1 + V_2C_2}{\frac{C_F}{C_I}\big(1 + \frac{1}{G}\big)\big(C_1 + C_2 + C_C + C_I\big) + \frac{1}{G}\big(C_1 + C_2 + C_C\big)} \\ &= -\frac{V_1C_1 + V_2C_2}{\frac{C_F}{C_I}\big(1 + \frac{1}{G}\big)\big(C_1 + C_2\big) + \frac{1}{G}\big(C_1 + C_2\big) + \frac{C_F}{C_I}\big(1 + \frac{1}{G}\big)\big(C_C + C_I\big) + \frac{1}{G}C_C}\,. \end{aligned} \quad \text{(B.18)}$$

Rearranging the denominator gives

$$V_{out} = -\frac{V_1C_1 + V_2C_2}{(C_1 + C_2)\left[\frac{C_F}{C_I}\big(1 + \frac{1}{G}\big) + \frac{1}{G}\right] + C_F\big(1 + \frac{1}{G}\big) + C_C\frac{C_F}{C_I}\big(1 + \frac{1}{G}\big) + \frac{1}{G}C_C}\,. \quad \text{(B.19)}$$

The voltage on the first and second capacitor plates is the sum of the fixed excitation plus the created voltage V_C.

$$V_1 = V_E + V_C \tag{B.20}$$

$$V_2 = -V_E + V_C \tag{B.21}$$

Inserting this and rearranging gives:

$$\begin{aligned} V_{out} &= -\frac{\big(V_E + V_C\big)C_1 + (-V_E + V_C)C_2}{(C_1 + C_2)\big[\frac{C_F}{C_I}\big(1 + \frac{1}{G}\big) + \frac{1}{G}\big] + C_C\big[\frac{C_F}{C_I}\big(1 + \frac{1}{G}\big) + \frac{1}{G}\big] + C_F\big(1 + \frac{1}{G}\big)} \\ &= -\frac{\big(C_1 - C_2\big)V_E + (C_1 + C_2)V_C}{(C_1 + C_2)\big[\frac{C_F}{C_I}\big(1 + \frac{1}{G}\big) + \frac{1}{G}\big] + C_C\big[\frac{C_F}{C_I}\big(1 + \frac{1}{G}\big) + \frac{1}{G}\big] + C_F\big(1 + \frac{1}{G}\big)} \,. \end{aligned} \tag{B.22}$$

Cancelling out $C_1 + C_2$ gives

$$V_{out} = -\frac{(\frac{C_1 - C_2}{C_1 + C_2}V_E + V_C)}{\Big[1 + \frac{C_C}{C_1 + C_2}\Big]\Big[\frac{C_F}{C_I}\big(1 + \frac{1}{G}\big) + \frac{1}{G}\Big] + \frac{C_F}{C_1 + C_2}\big(1 + \frac{1}{G}\big)} \,. \tag{B.23}$$

Let $\Delta C = C_1 - C_2$ and $\Sigma C = C_1 + C_2$. Then

$$V_{out} = \frac{\frac{\Delta C}{\Sigma C}V_E + V_C}{\Big[1 + \frac{C_C}{C_U + C_L}\Big]\Big[\frac{C_F}{C_I}\big(1 + \frac{1}{G}\big) + \frac{1}{G}\Big] + \frac{C_F}{\Sigma C}\big(1 + \frac{1}{G}\big)} \,. \tag{B.24}$$

The goal of the FPGA is to make the output zero and it adjusts the signal V_C accordingly. Hence

$$\frac{\Delta C}{\Sigma C}V_E + V_C = 0 \,. \tag{B.25}$$

The voltage V_C that is added to the fixed excitation before being applied to the capacitor plates is a function f of the excitation voltage:

$$V_C = f \times V_E \,. \tag{B.26}$$

So

$$\frac{\Delta C}{\Sigma C}V_E + f \times V_E = 0 \,. \tag{B.27}$$

This f is the value the readout presents us with. Hence the readout from the digital electronics is

$$f = -\frac{\Delta C}{\Sigma C} = -\frac{C_1 - C_2}{C_2 + C_1} \,. \tag{B.28}$$

Appendix C

Materials List

Item	Material
Tubes (sensor shielding)	Copper
PCBs (electrodes)	Copper-coated Cirlex
Rods	Stainless steel
Multiple sensor parts, including: Internal structure caps Plate separators Moving blocks Connector between blocks Screws	Copper
Multiple sensor parts, including: End caps Electrical insulation blocks Screws	Polyether ether ketone (PEEK)
Hexapod structure parts, including: Ball and socket joints Bars Corner pieces	Titanium
Coaxial cable	Axon coaxial cable
Solder	Lead-free solder (ELSOLD, Sn + 0.3% Cu)
Connectors	Harwin H8504-05 receptacles Harwin H3185-05 receptacles Harwin H2175 pins Harwin H2105 pins

Appendix D

On hexapods

Although frequently named after D. Stewart, who published his plans for a platform with six degrees of freedom in 1965, a platform actuated by six jacks was created by Eric Gough in the 1950s.[20] Gough's platform was used for testing tyres, while Stewart saw the potential of his as a flight simulator, having no fixed axes relative to the ground and hence able to simulate banking.

GSPMs have indeed been used in flight simulators, as Stewart suggested. They are also used in a range of scenarios where precisely controlled positioning is vital. The Dark Energy Spectroscopic Instrument (DESI) is a ground-based telescope that will use a GSPM for positioning the barrel of the telescope [84]. A large example of a GSPM is the base of the AMiBA radio telescope, which studies the Cosmic Microwave Background. The 6 m carbon fibre hexapod is used for positioning the telescope dish to within $0.2''$ and has a lightweight structure which can be easily disassembled, relocated and reassembled.[21]

GSPMs benefit from being light relative to the loads they can carry - the weight of a load on the platform is approximately equally distributed on all links. Prototypes exist of GSPMs that weigh as little as 35 kg bearing loads of up to 600 kg.[85] Parallel manipulators have also been used at the European Synchrotron Radiation Facility (ESRF), for positioning samples, which demanded repeatability of better than 0.1 µm with a load of 230 kg,[85] and for the positioning of a number of the x-ray mirrors on the synchrotron's beamlines.[93] They are also available commercially from companies such as SYMÉTRIE, who make a range of hexapods to suit a variety of applications.[1]

[1] http://www.symetrie.fr/en/home/

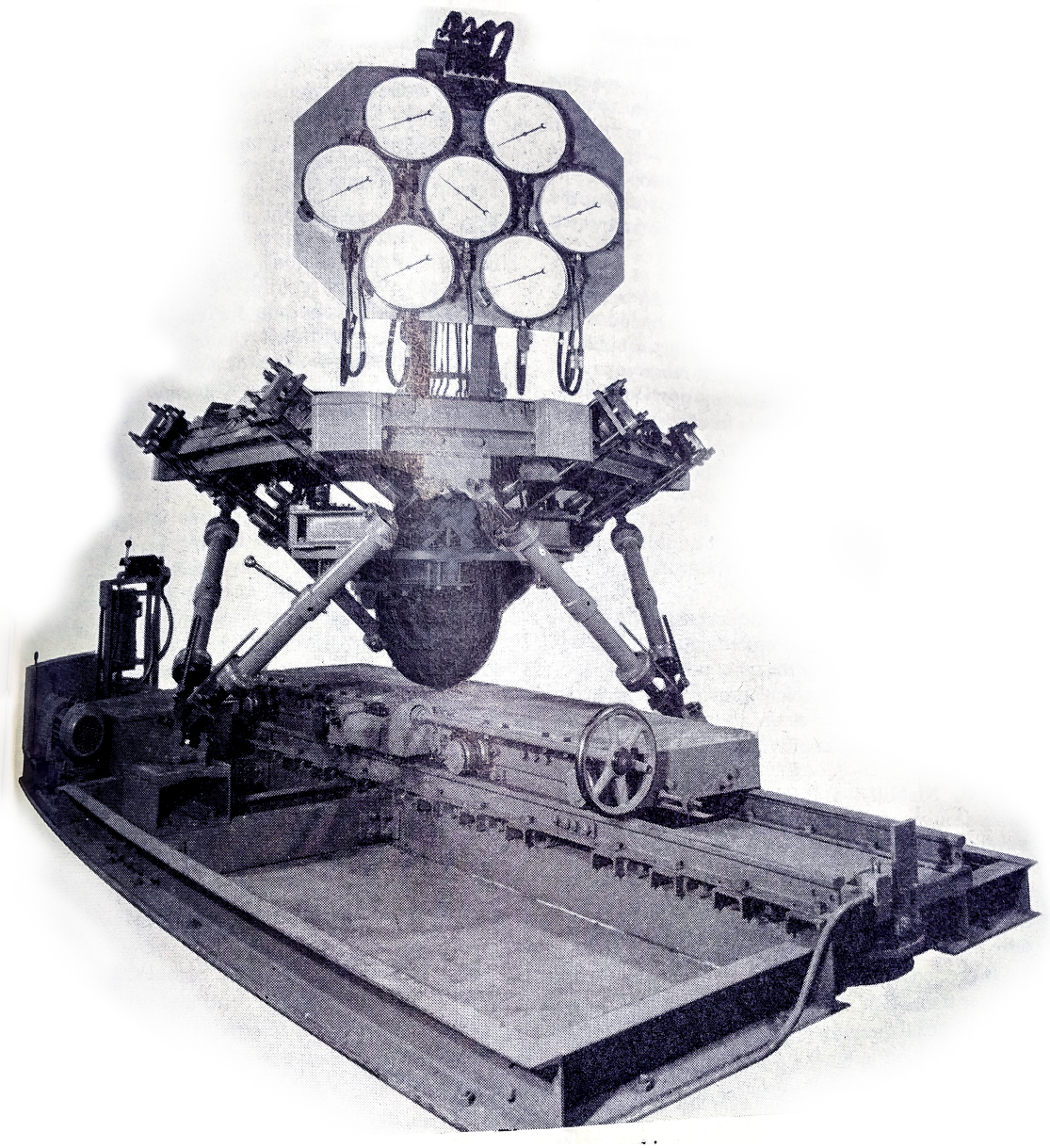


Figure D.1: The tyre-testing platform created by Eric Gough in the 1950s. Image from [20]. Permission to reproduce this image has been granted by SAGE Publications.

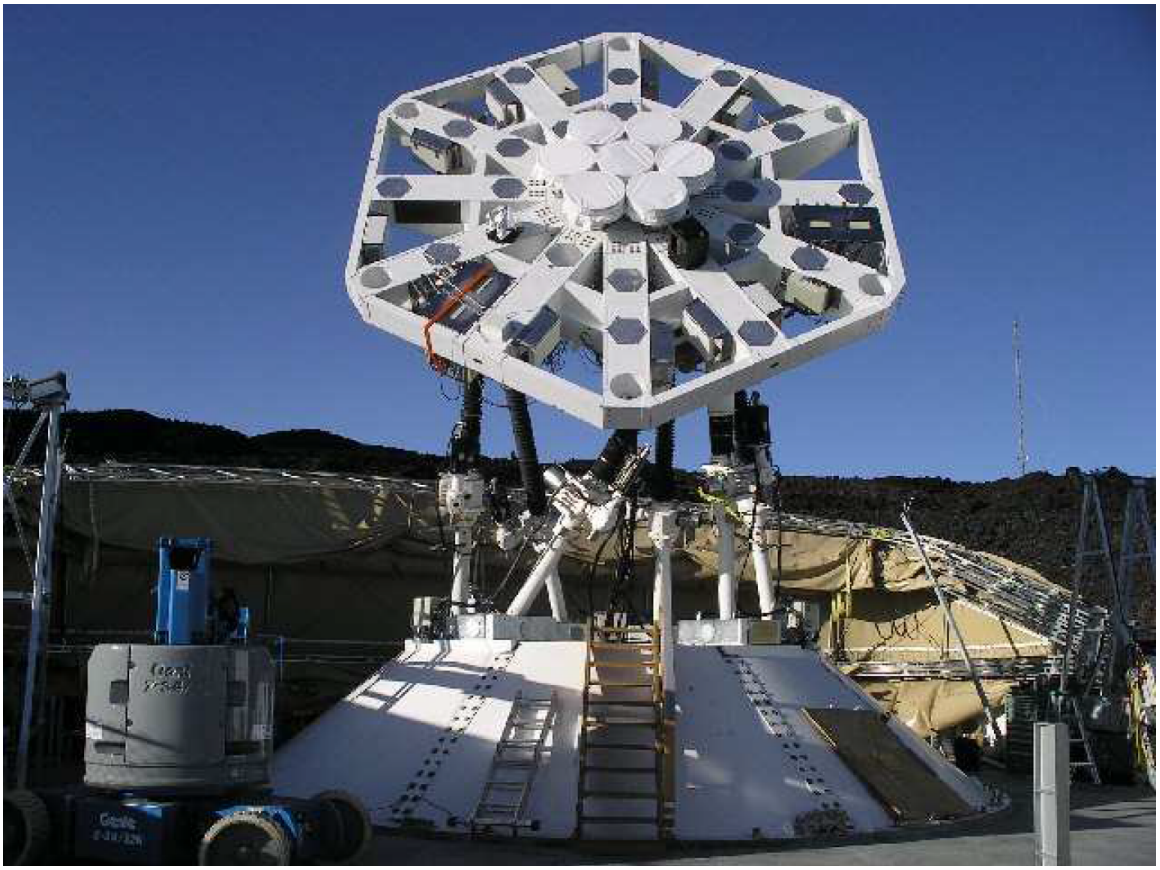


Figure D.2: The GSPM used for positioning the AMiBA telescope. This is, of course, much larger than the hexapod that will feature in LZ. Figure from [21], AAS. Reproduced with permission.

Appendix E

Cylindrical sensor design

Many different geometries are possible for creating a capacitor. For any parallel plate capacitor, introducing edges to the capacitor plates introduces fringe fields, which are non-uniformities in the field present at each edge of the capacitor plates.

One set of fringe fields can be eliminated if, instead of using a parallel plate capacitor, a concentric cylindrical geometry is used. In this case, a central wire or rod forms one of the conducting parts of the capacitor and a tube around it forms the other. The gap between the two is the dielectric. In this case, there are fringe fields to contend with at the ends of the rod and tube, but not along their lengths. By comparison, a parallel plate sensor has fringe fields along all four edges. In addition, a cylindrical geometry makes for a potentially neat and compact sensor. These were the motivations for using a cylindrical sensor design when producing a set of three sensors for the test tripod discussed in section 5.3.

However, the design complexity quickly increases when trying to make a cylindrical sensor very precise. If the central rod strays from its position down the centre of the tube, the capacitance can change considerably. Hence the rod needs to be held very securely. Nevertheless, we wish to avoid having a dielectric in the sensor if at all possible, as the relative permittivity of this would change with temperature and affect the sensor readings, as discussed in section 4.2.4.3. Care would therefore need to be taken regarding fixing the rod inside the tube, as the non-conductive component used for this must not behave as an additional dielectric in the capacitor, or the problem of the sensor reading changing with temperature would arise again. Hence the connection would need to be somewhere beyond the sensitive (measuring) part of the rod. Furthermore this applies not only to the central 'sensing' rod but also to the metal blocks that will vary the capacitance according to their position. These would also be tubes, and would be inserted between the rod and the outer tube. However constructing a system to move them is complicated. Any dielectric that supports

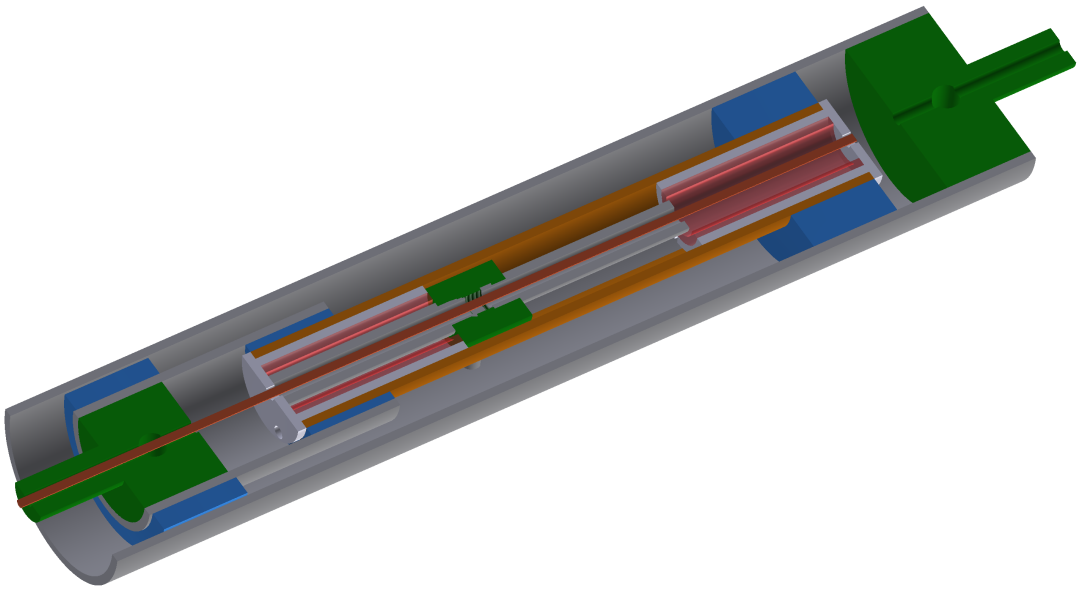


Figure E.1: The CAD model of the cylindrical sensor designed for use in the tripod.

them from the ends would then cause dielectric variations in the sensor in addition to the changes from the moving metal block. However trying to move the metal blocks from the side would mean cutting gaps into the surrounding tube, which would create additional non-uniformities in the fields.

What has so far been called the 'outer tube' would in fact be not one but two tubes as there are two excitations to be picked up by the sensing rod. These two tubes would need to be held very carefully in place, as any deviations from concentricity with the rod would change the capacitance. However this would again need to be done without adding dielectric materials between the tubes and the sense rod, while also keeping them electrically isolated. In addition, there would need to be yet another tube around those two to act as a shield, and prevent the excitations radiating from the sensors and potentially interfering with other devices in the detector. One is thus left with one central rod with three layers of concentric tubes and no straightforward ways to connect them.

In addition, it is more difficult to retain axial symmetry in a concentric design than it is to retain parallel surfaces in a parallel plate design. This is compounded by the challenge of accessing the central conductor noted above.

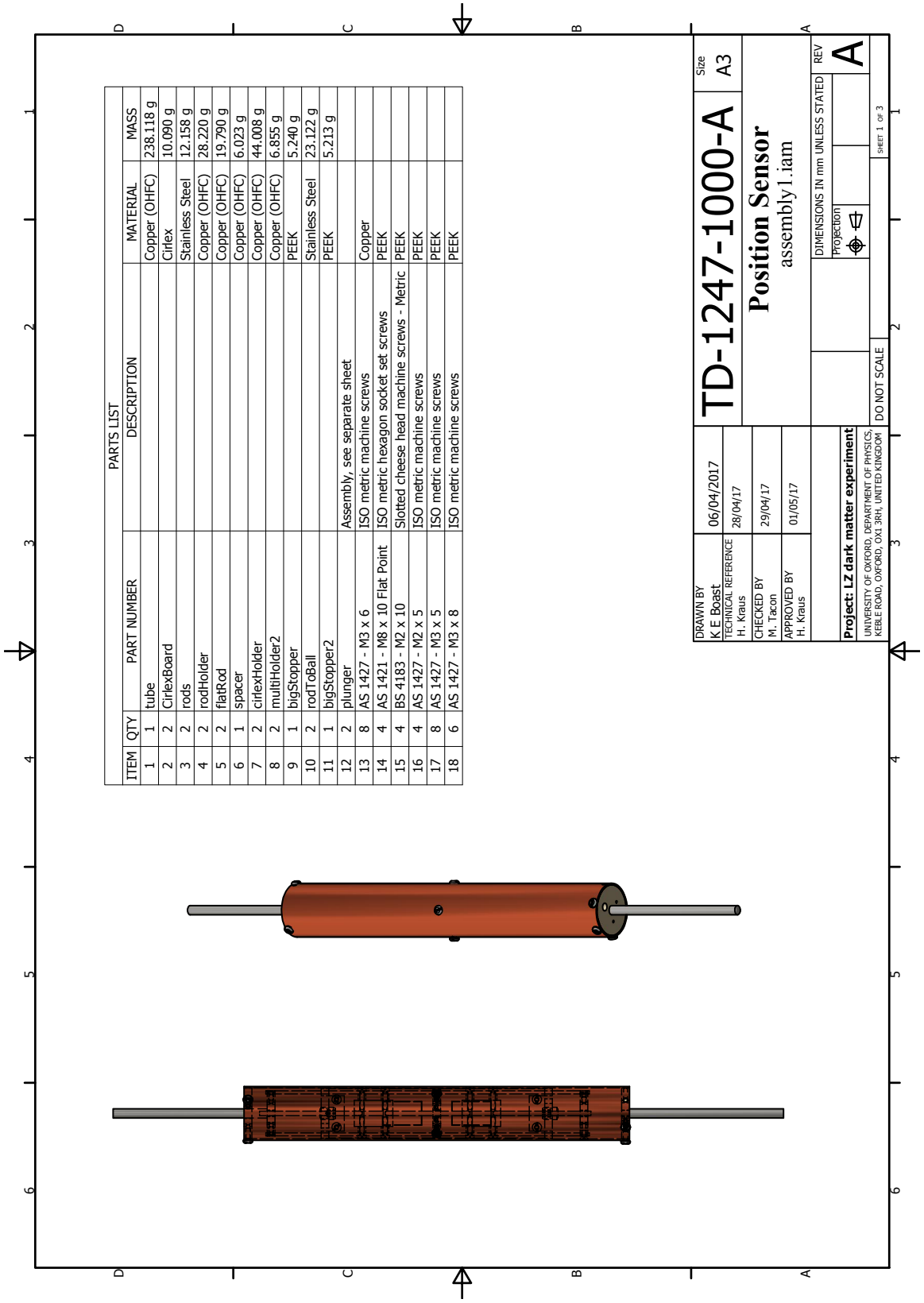
In the design for the tripod sensors, we used plastic pieces to connect the rod and

tubes. As the goal of those sensors was to test the tripod algorithm and investigate possible problems for the hexapod, the sensors would not be used in an environment in which the temperature changed significantly. Hence the design was acceptable for this purpose. However these difficulties ruled such a design out of consideration for use in LZ.

Appendix F

Engineering Drawings

Here follow the engineering drawings fig. F.1 to fig. F.14 for all the parts of the position sensor, the design of which was discussed in Chapter 4. Following these are engineering drawings for some parts of the hexapod, including a general overview, details of the mounting to the ICV dome and parts for connecting the hexapod to the PMT truss.



PARTS LIST

ITEM	QTY	PART NUMBER	DESCRIPTION	MATERIAL	MASS
1	1	tube		Copper (OHFC)	238.118 g
2	2	CirlexBoard		Cirlex	10.090 g
3	2	rods		Stainless Steel	12.158 g
4	2	rodHolder		Copper (OHFC)	28.220 g
5	2	flatRod		Copper (OHFC)	19.790 g
6	1	spacer		Copper (OHFC)	6.023 g
7	2	cirlexHolder		Copper (OHFC)	44.008 g
8	2	multiHolder2		Copper (OHFC)	6.855 g
9	1	bigStopper		PEEK	5.240 g
10	2	rodToBall		Stainless Steel	23.122 g
11	1	bigStopper2		PEEK	5.213 g
12	2	plunger	Assembly, see separate sheet		
13	8	AS 1427 - M3 x 6	ISO metric machine screws	Copper	
14	4	AS 1421 - M8 x 10 Flat Point	ISO metric hexagon socket set screws	PEEK	
15	4	BS 4183 - M2 x 10	Slotted cheese head machine screws - Metric	PEEK	
16	4	AS 1427 - M2 x 5	ISO metric machine screws	PEEK	
17	8	AS 1427 - M3 x 5	ISO metric machine screws	PEEK	
18	6	AS 1427 - M3 x 8	ISO metric machine screws	PEEK	

DRAWN BY K E Boast 06/04/2017
TECHNICAL REFERENCE H. Kraus 28/04/17
CHECKED BY M. Tacon 29/04/17
APPROVED BY H. Kraus 01/05/17

TD-1247-1000-A

Size A3

Position Sensor
assembly1.iam

DIMENSIONS IN mm UNLESS STATED
Projection

REV A

Project: LZ dark matter experiment
UNIVERSITY OF OXFORD, DEPARTMENT OF PHYSICS, KEBLE ROAD, OXFORD, OX1 3RH, UNITED KINGDOM

DO NOT SCALE

SHEET 1 OF 3

Figure F.1: The full position sensor with a parts list detailing the components.

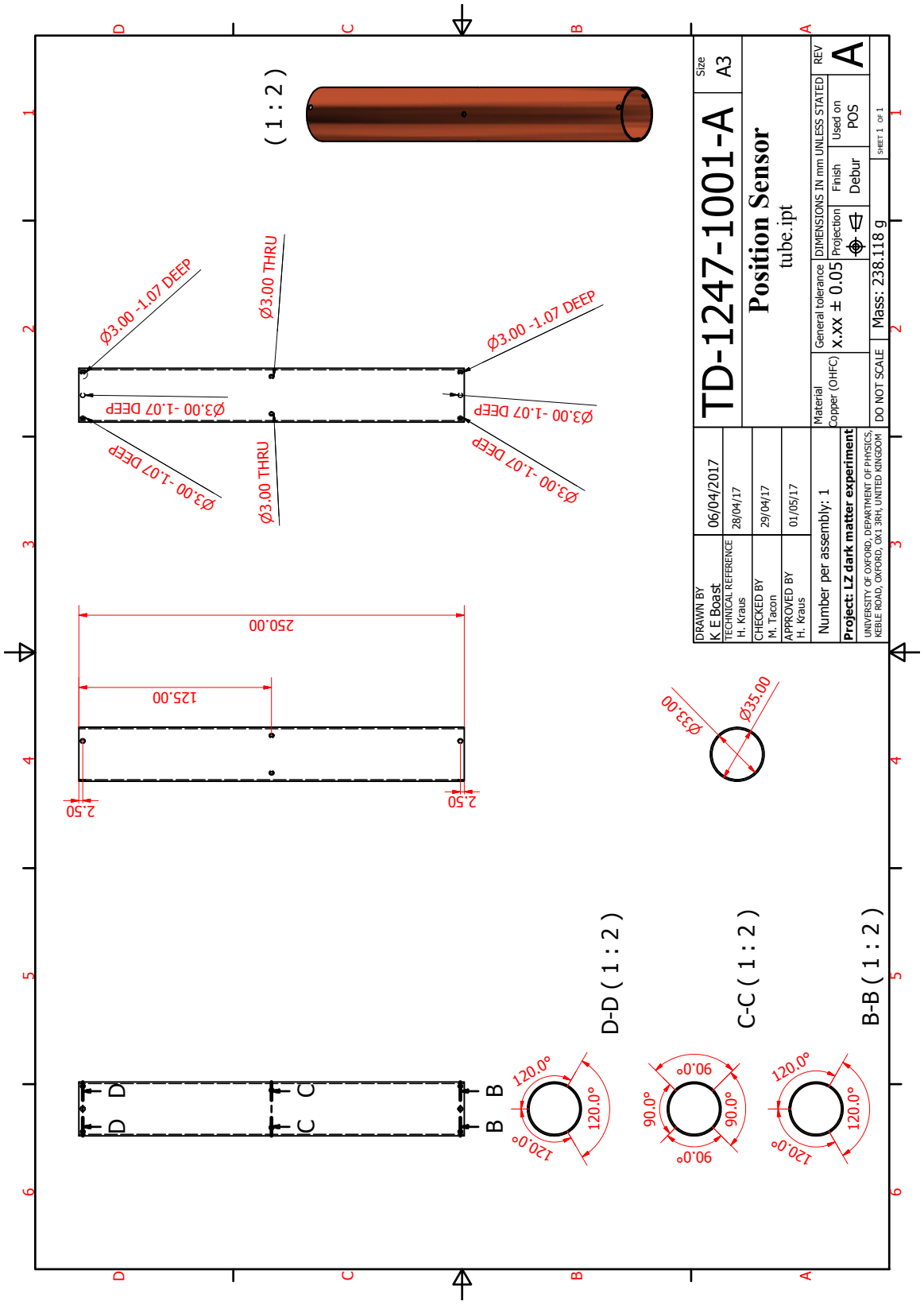


Figure F.2: The tube that shields the internals of the sensor and provides it with structure.

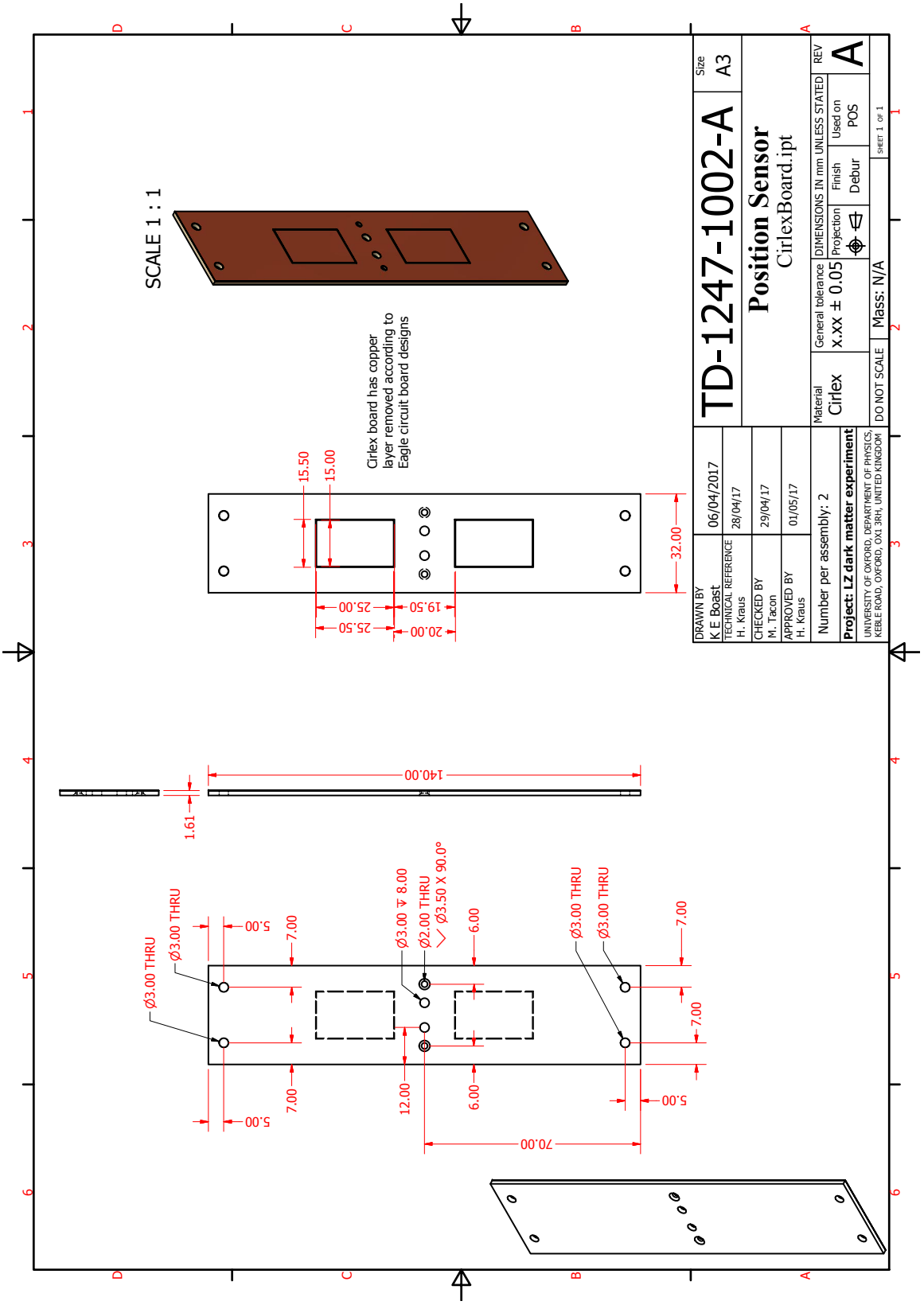


Figure F.3: The Cirlex plates that carry the sense and excitation electrodes.

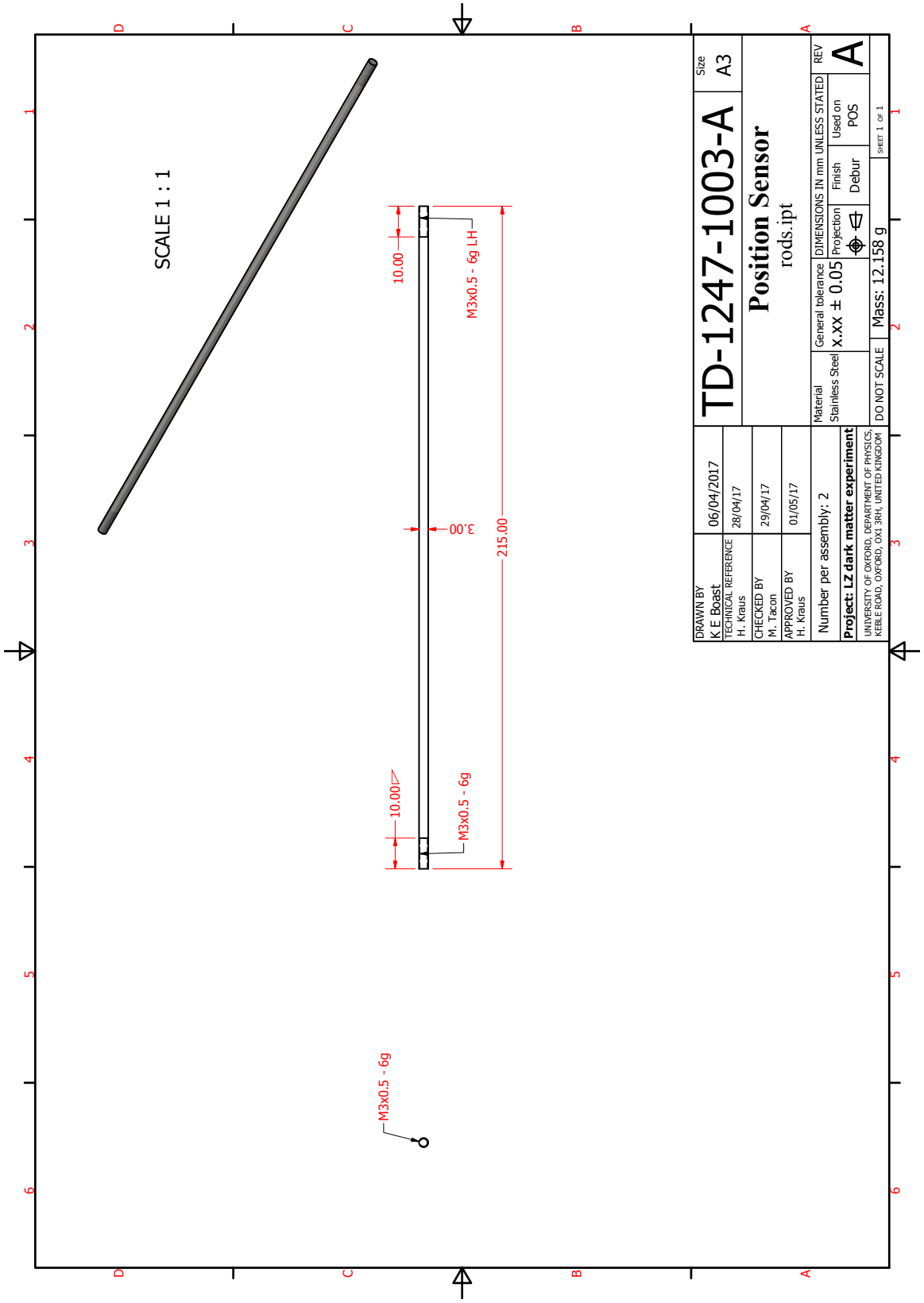


Figure F.4: The cylindrical rods on which the internals of the position sensor slide.

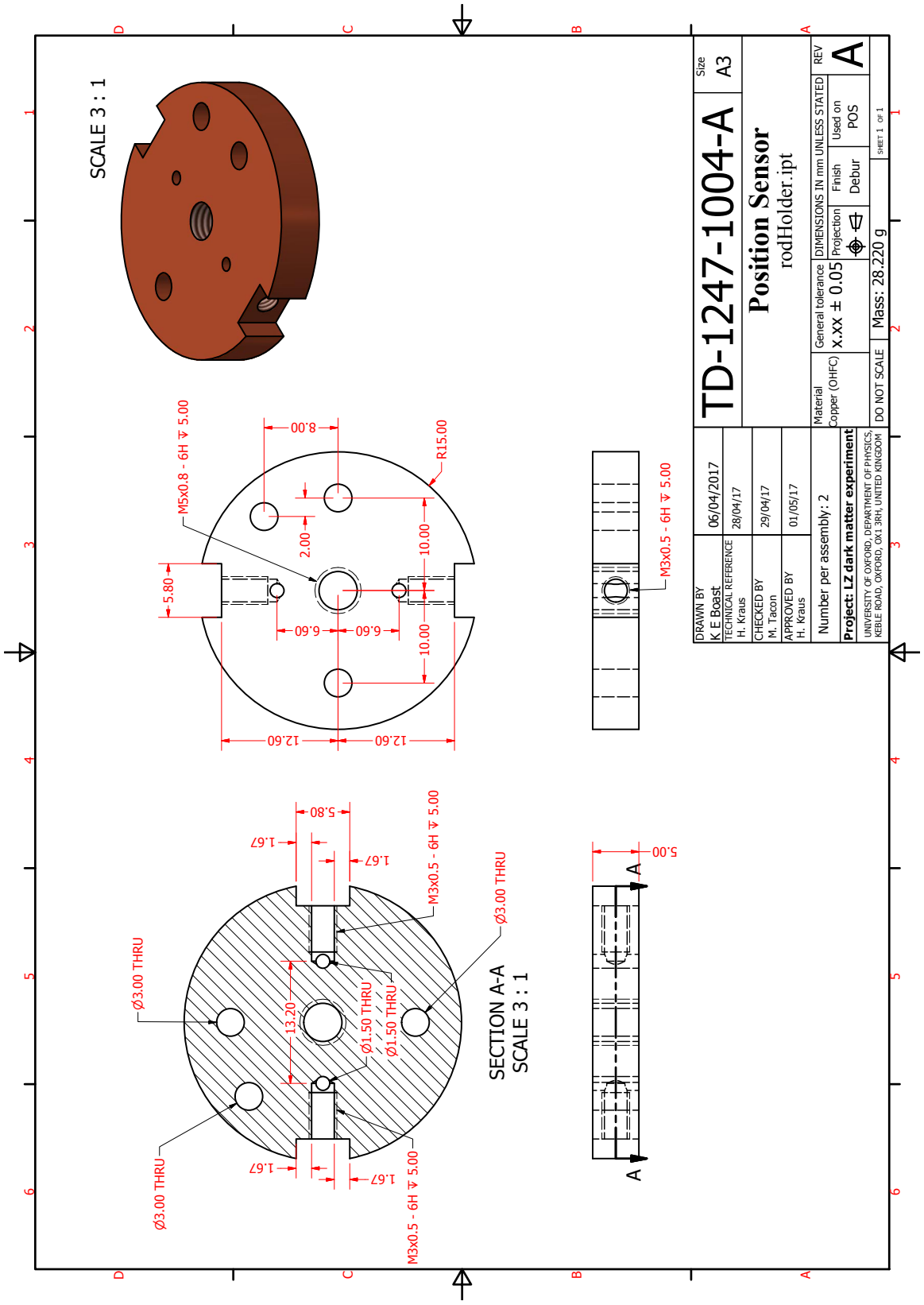


Figure F.5: The copper ends that hold the flat rods, which in turn support the moving metal blocks.

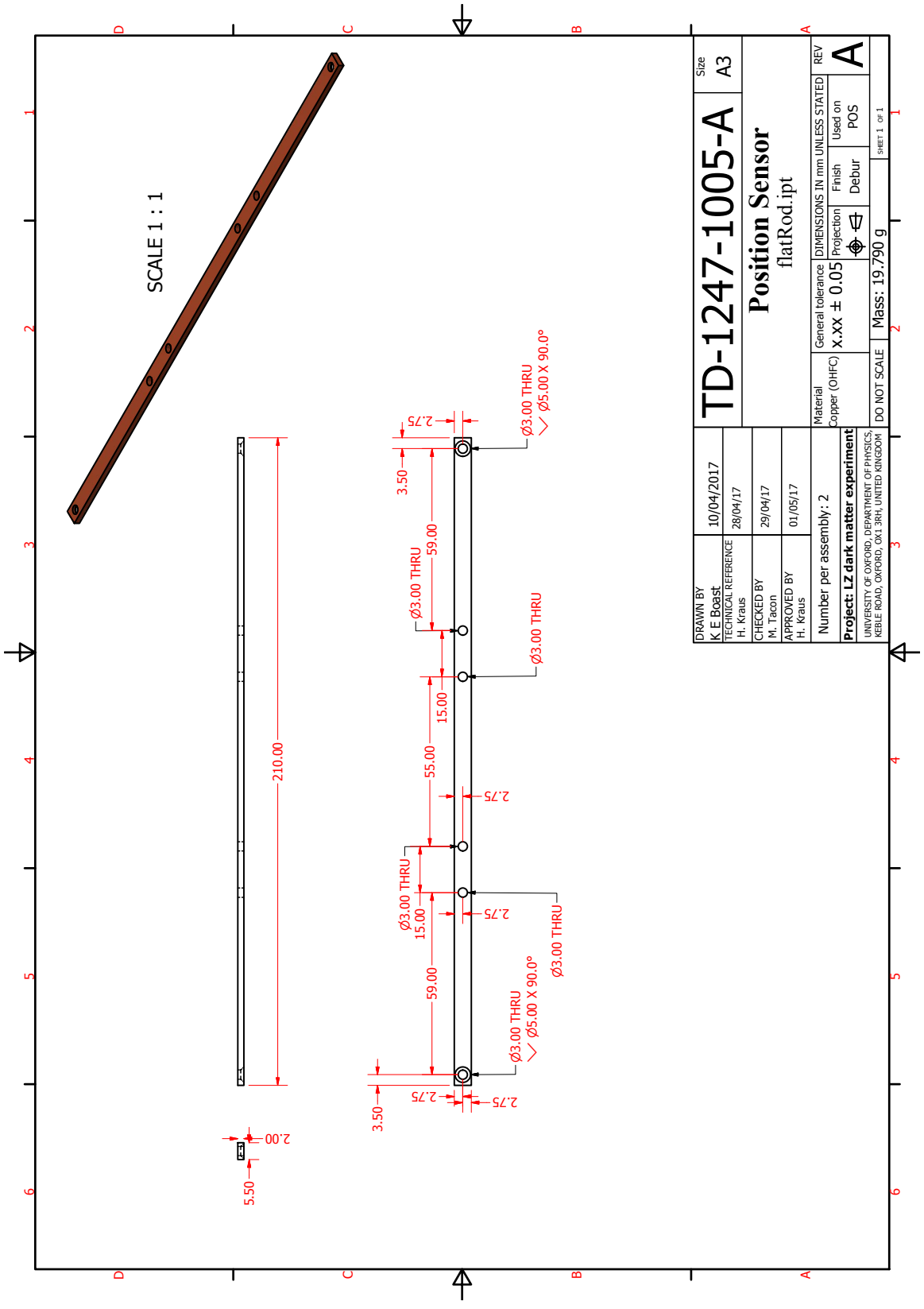


Figure F.6: The flat rods that support the moving metal blocks and connect them to the rest of the sensor.

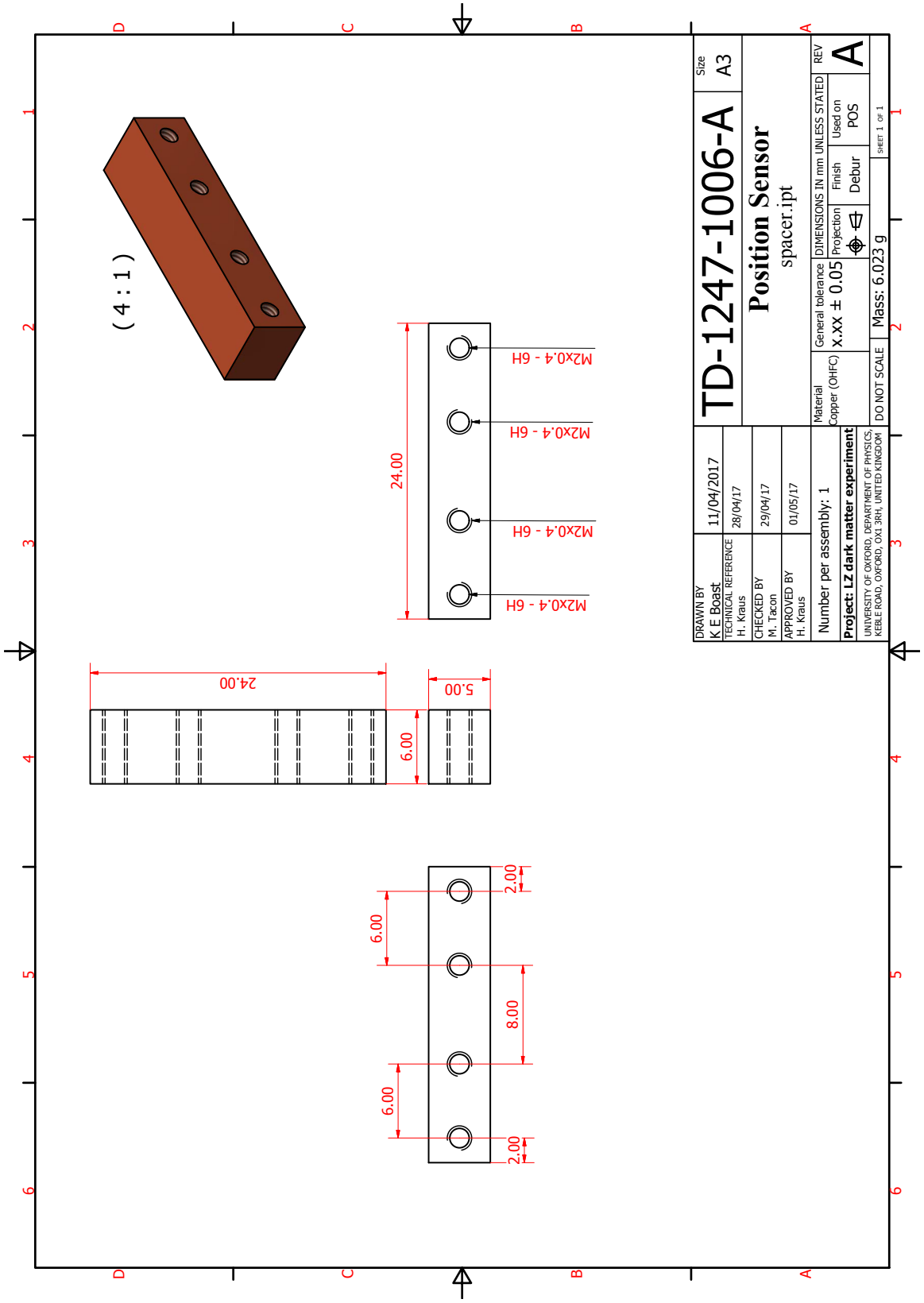


Figure F.7: The copper spacer that separates the Cirlex boards.

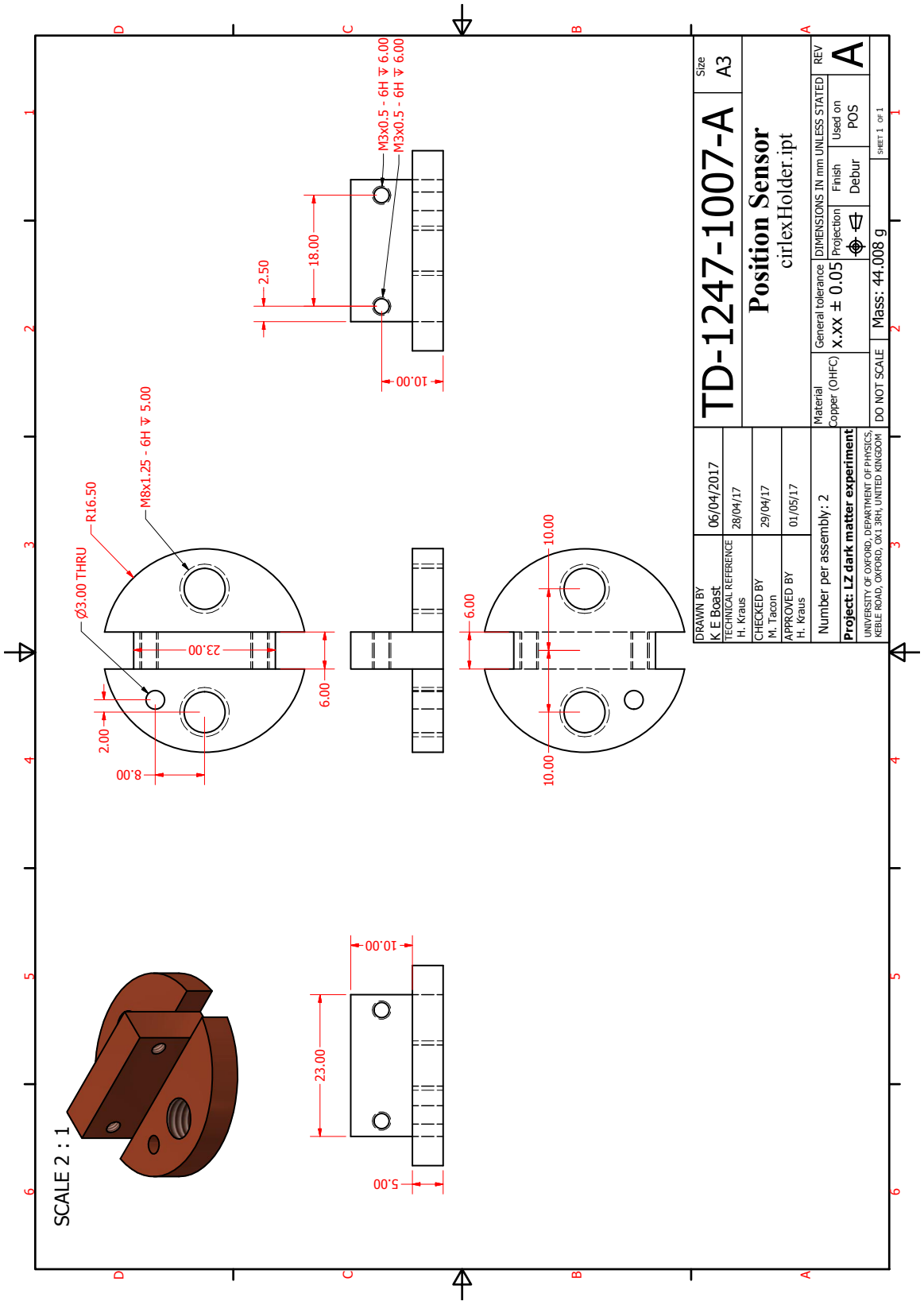


Figure F.8: The copper structures that support the ends of the Cirlex plates, and into which PEEK bushes are threaded. It is through these bushes that the cylindrical rods run.

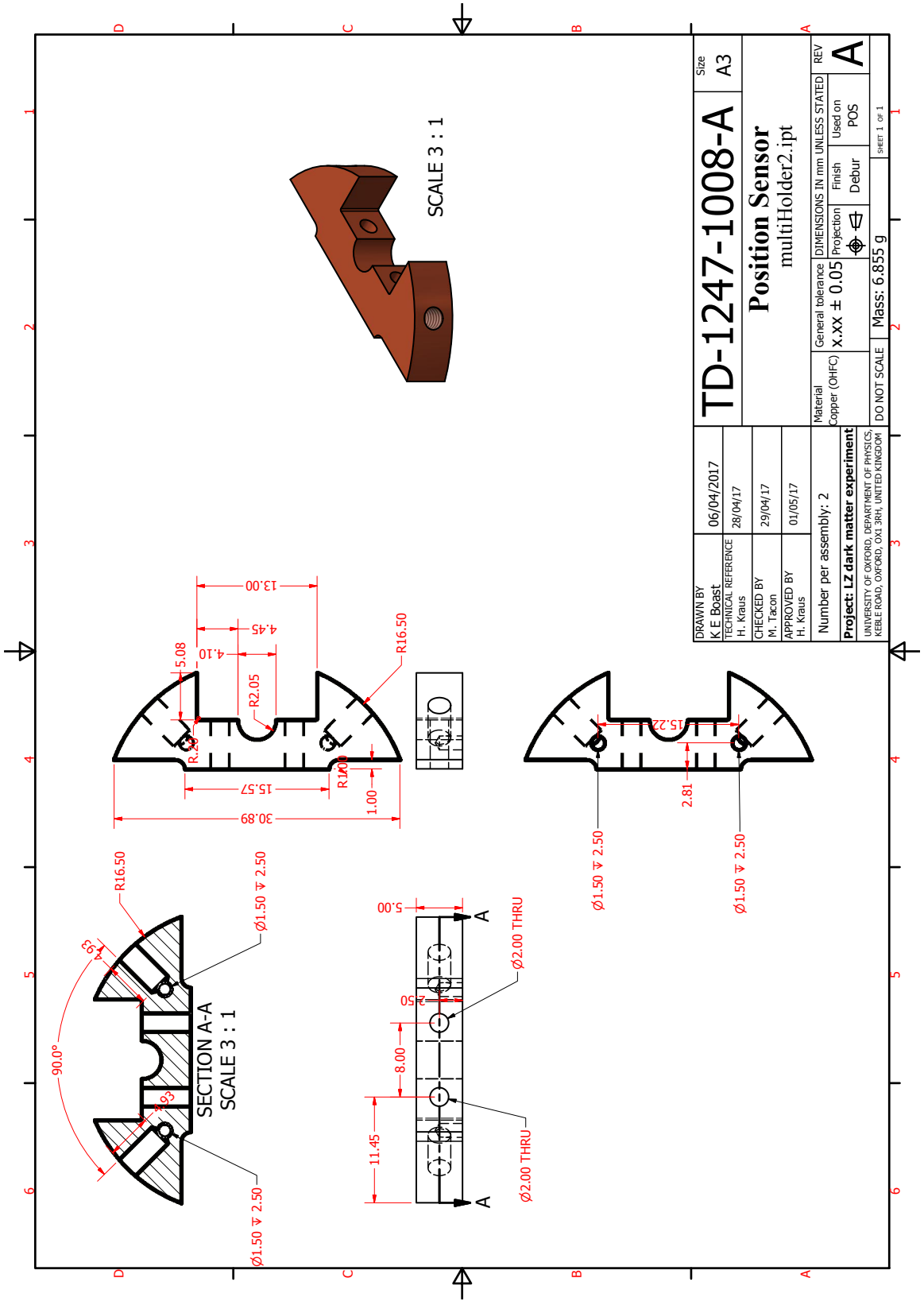


Figure F.9: The copper structures that connect the Cirlex plates to the tube.

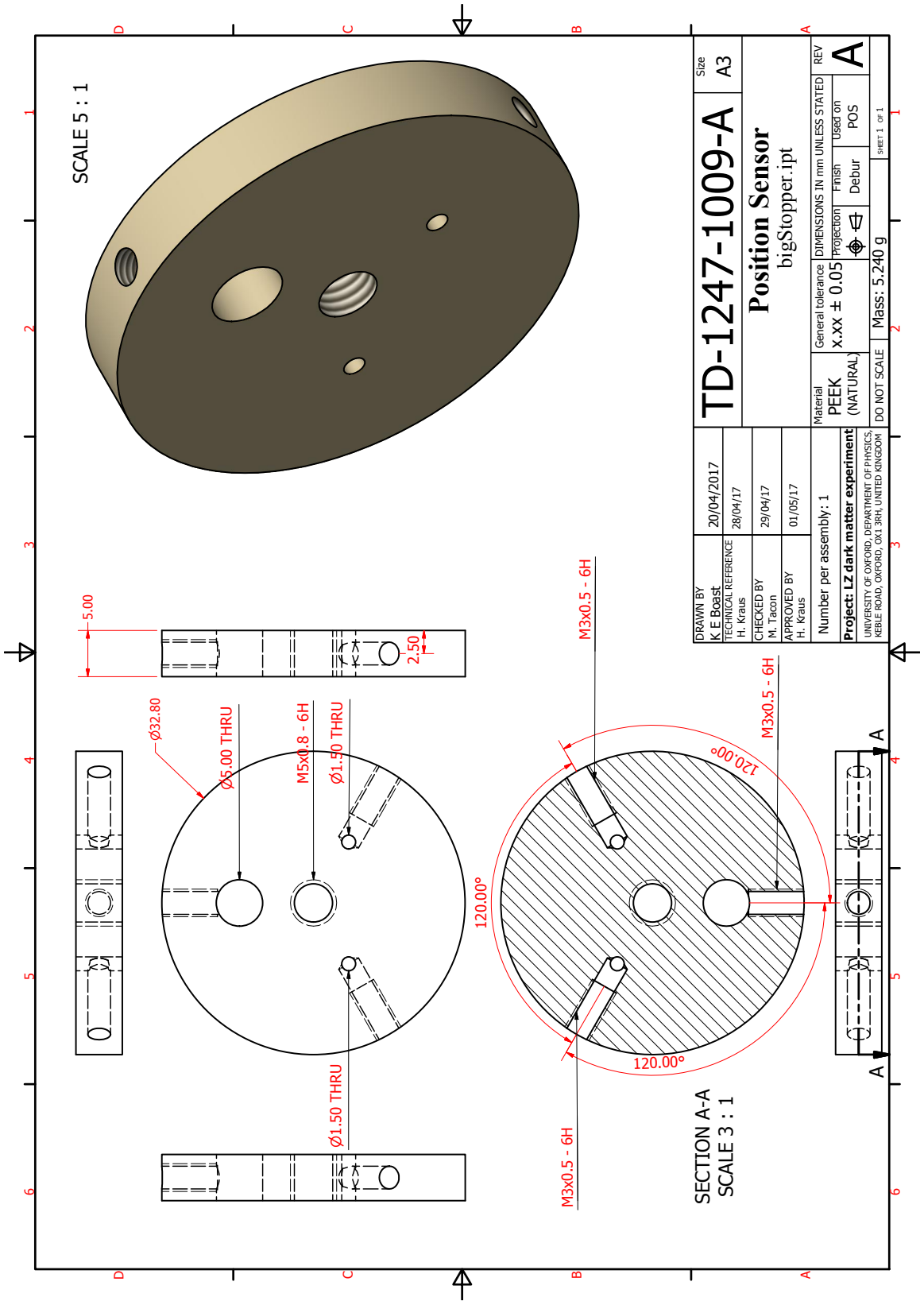


Figure F.10: The PEEK stopper that fits into the end of the copper tube. The rod to the ball-and-socket joint screws into this, connecting the ball-and-socket joint to the sensor body.

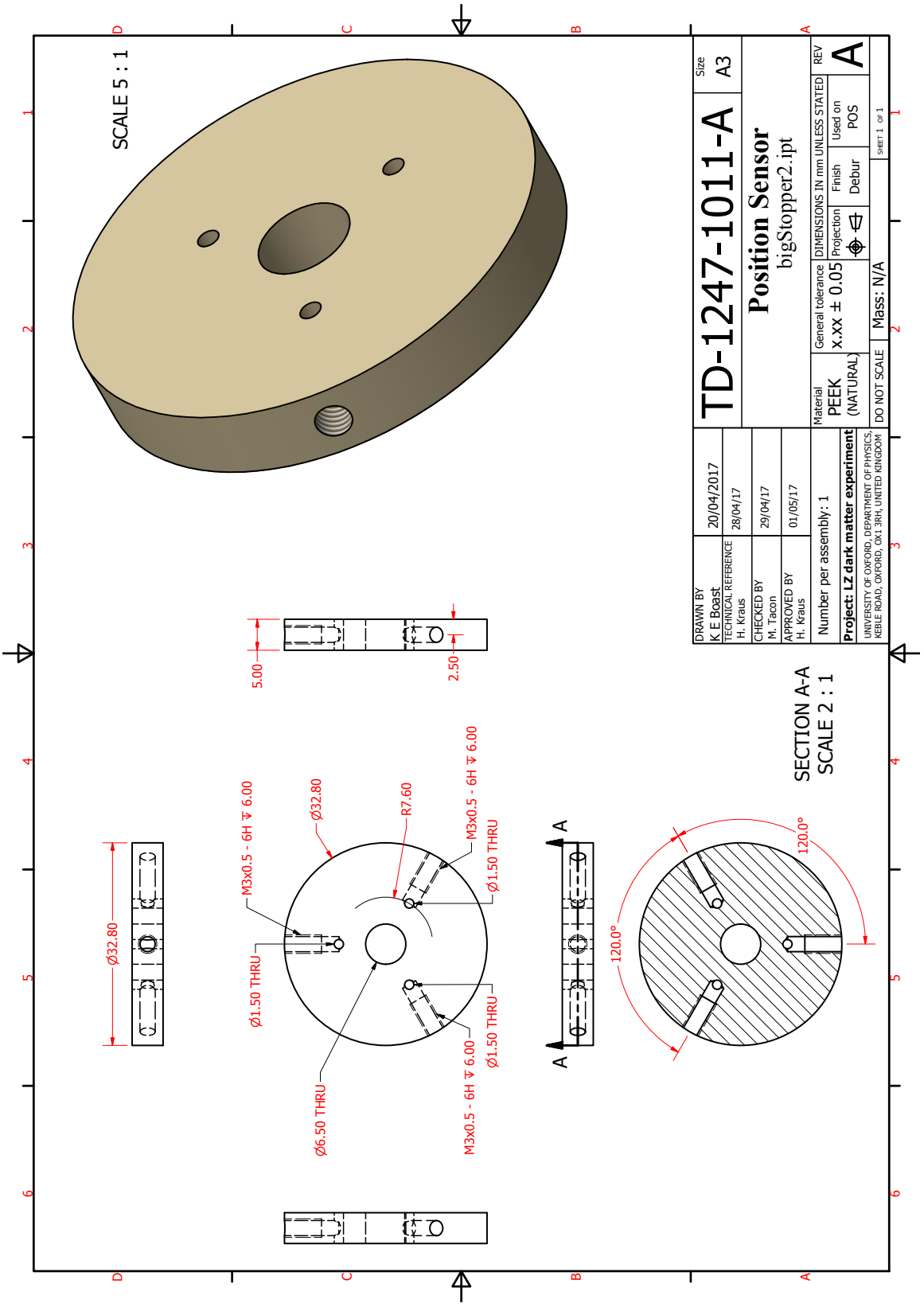


Figure F.11: The PEEK stopper for the other end of the copper tube. The rod to the ball-and-socket joint runs freely through the centre of this stopper.

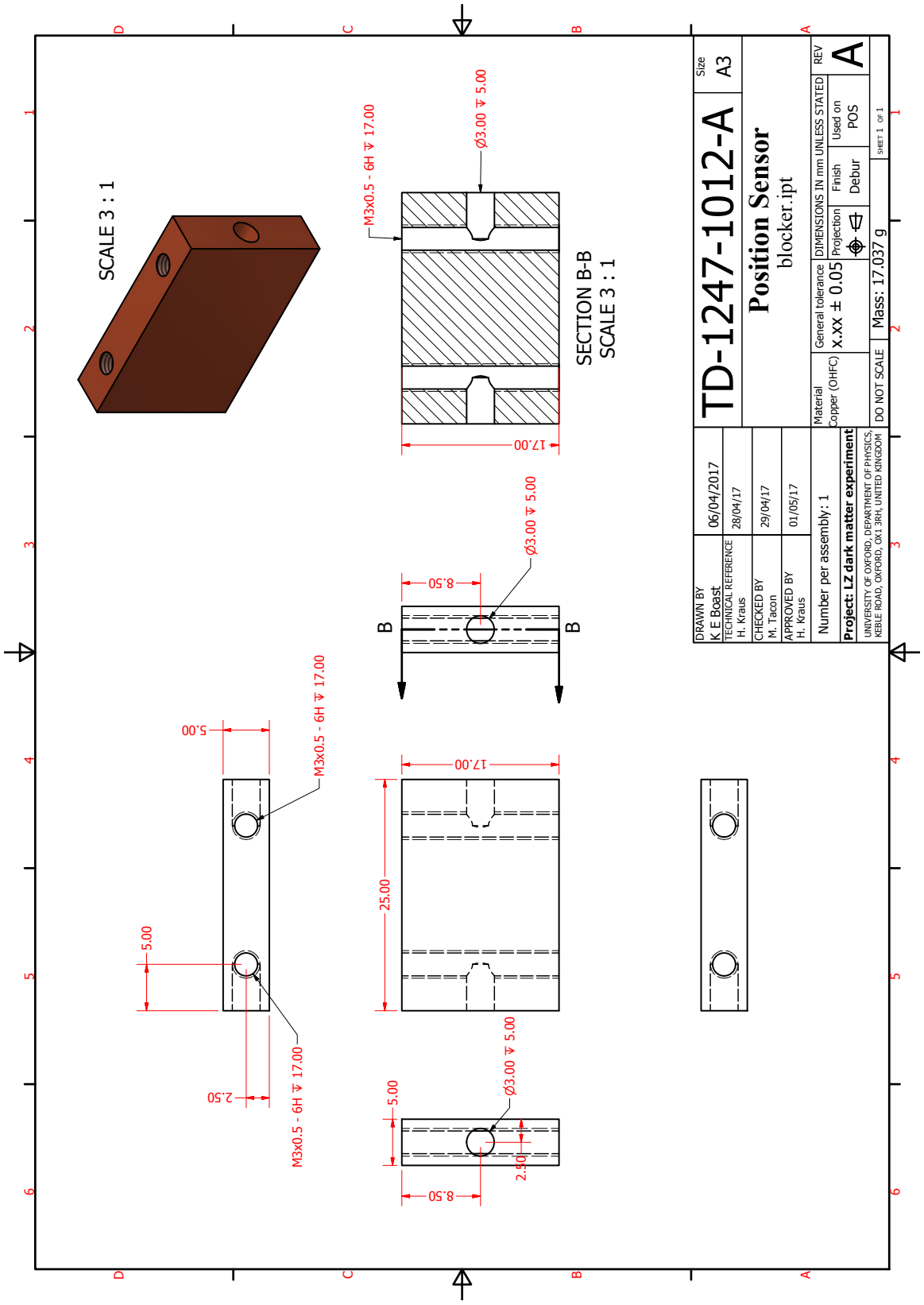


Figure F.12: The metal block that moves within the capacitor plates, changing the capacitance.

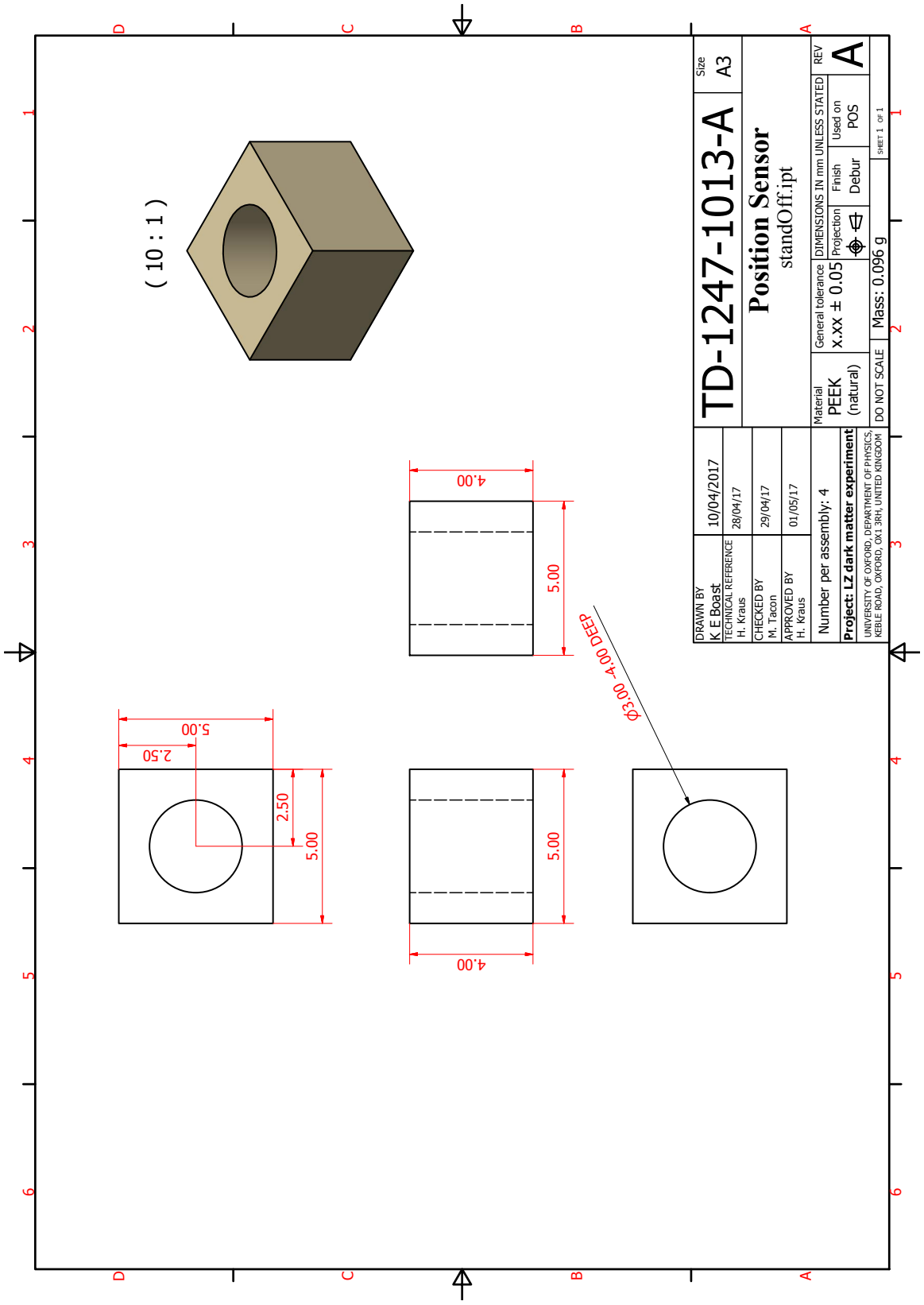


Figure F.13: The PEEK pieces that separate the moving metal blocks from the flat copper rods that support them. These ensure electrical isolation of the metal blocks. There are four per block.

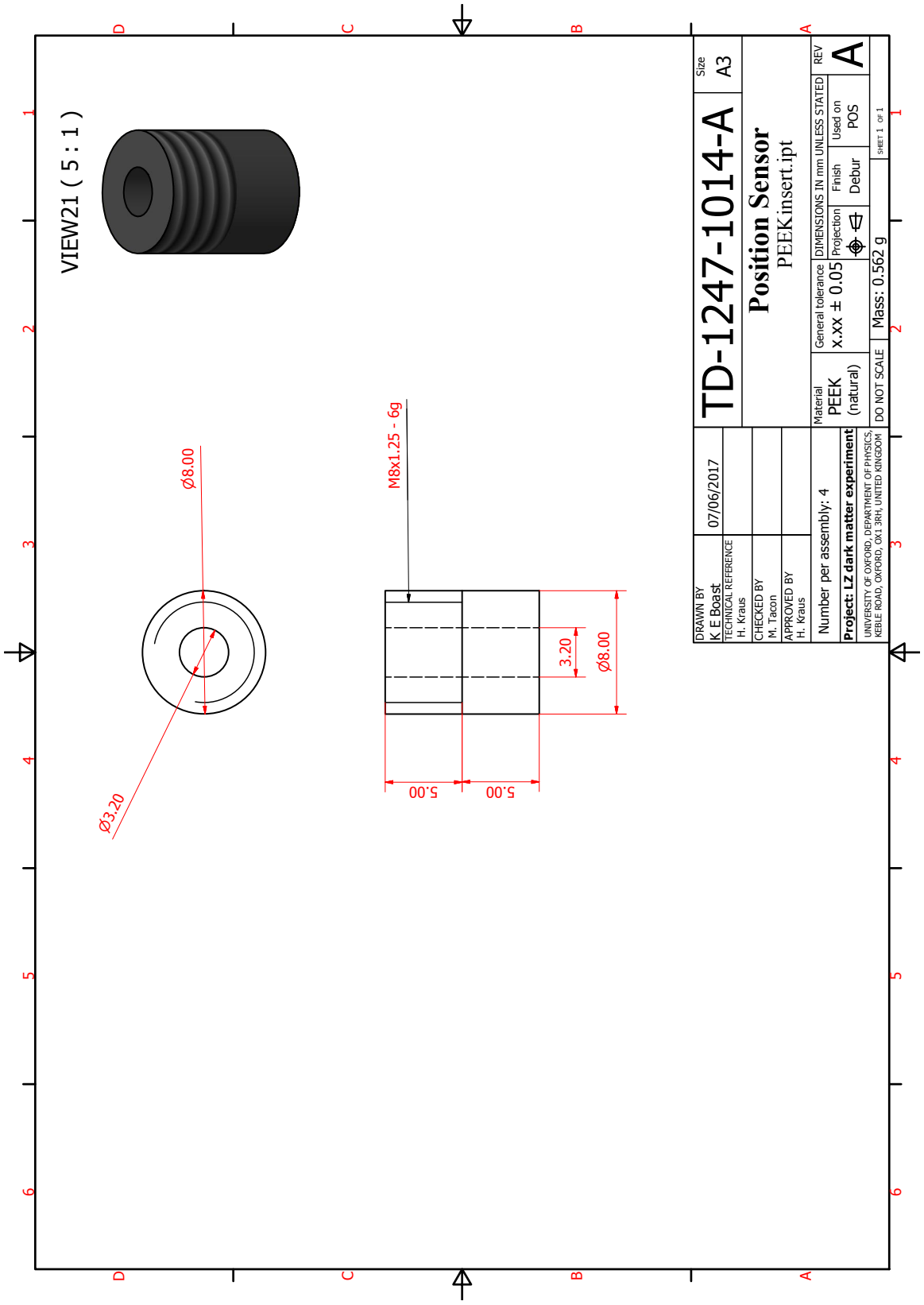


Figure F.14: The PEEK bushes that screw into the copper structure that holds the Cirlex plates. The cylindrical rods run smoothly through these.

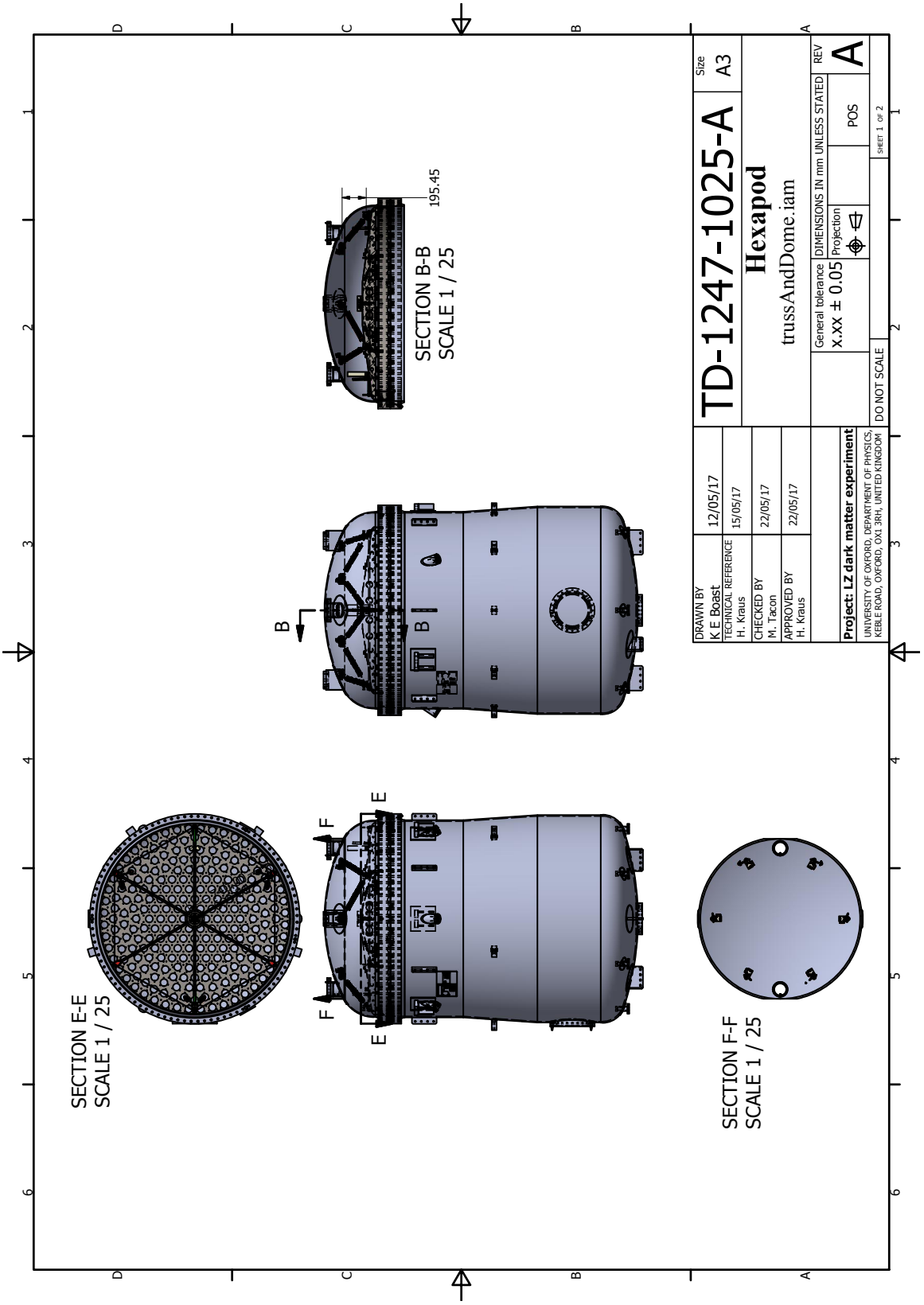


Figure F.15: An overview of the hexapod inside LZ.

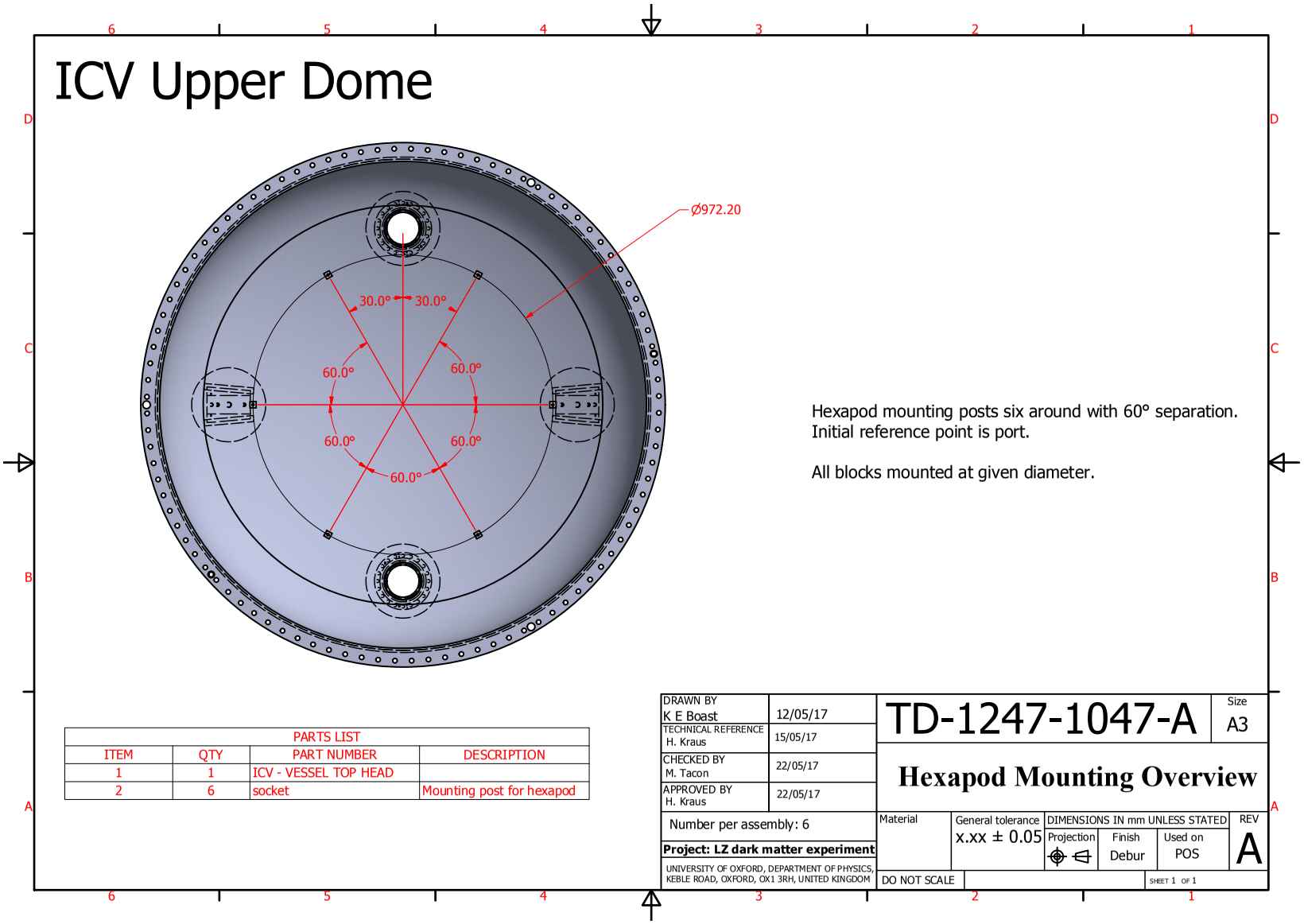


Figure F.16: The positions of the mounting points of the hexapod inside the ICV dome.

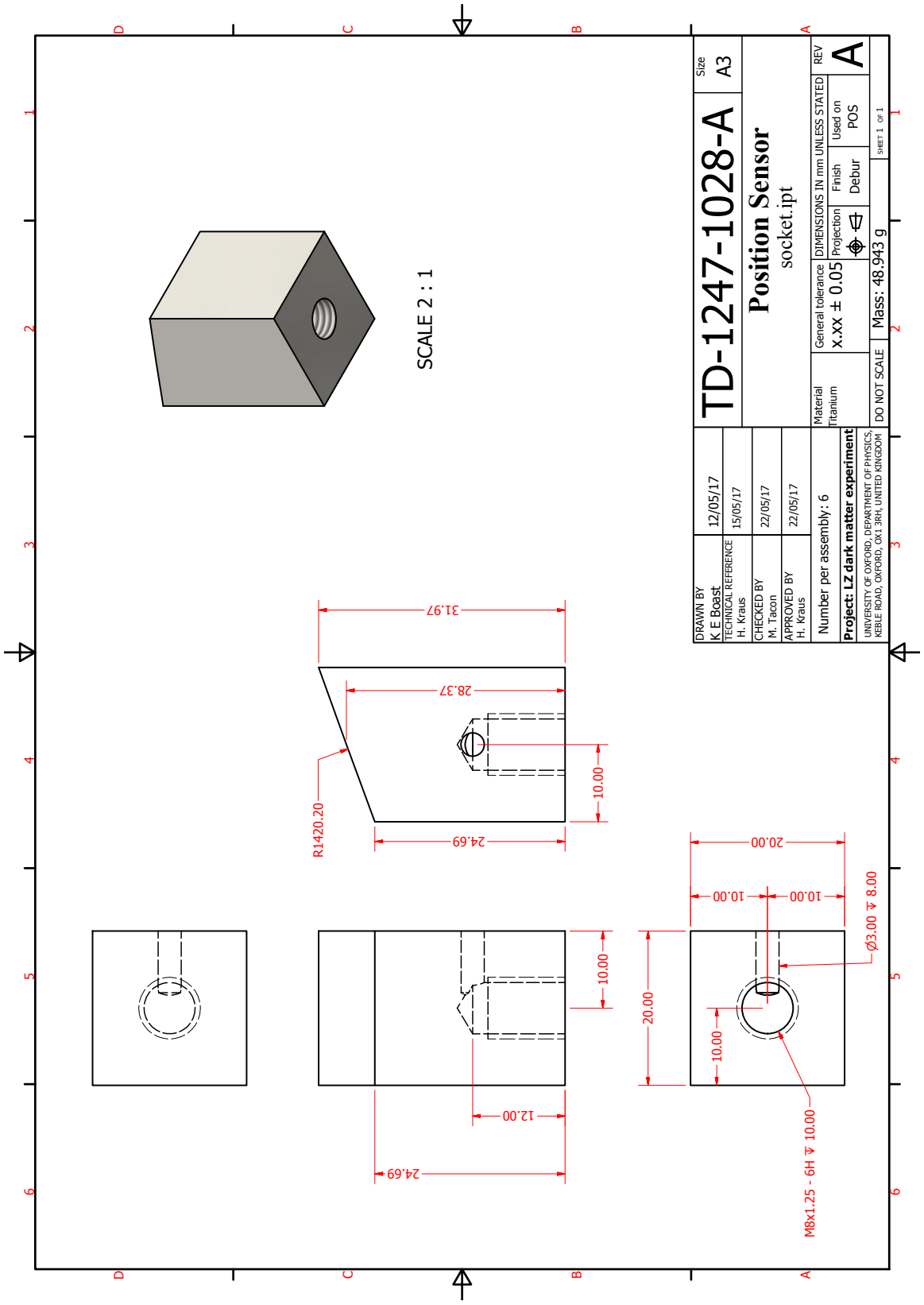


Figure F.17: The socket that will be welded to the inside of the cryostat dome, from which a connector to the ball and socket joint will hang.

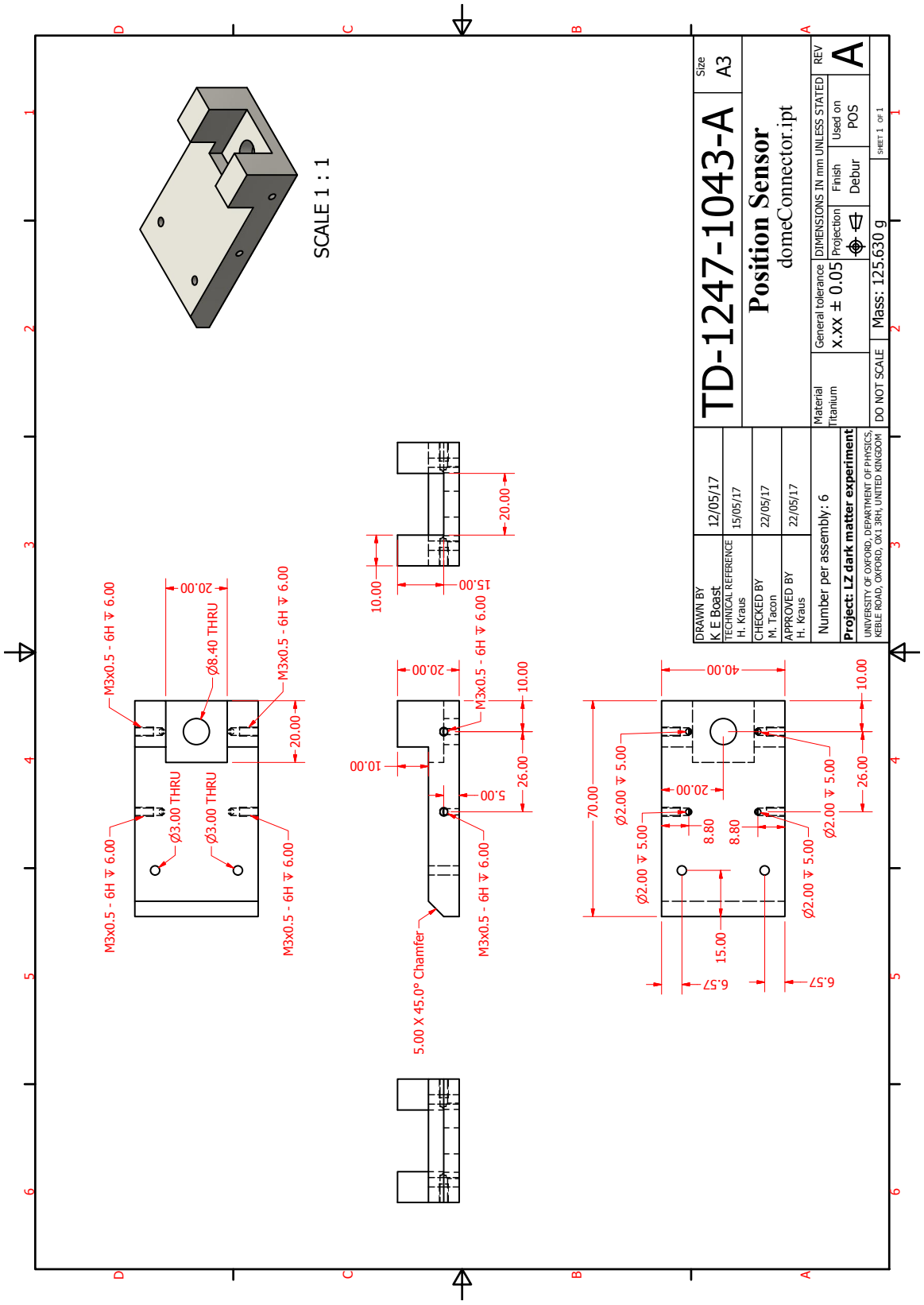


Figure F.18: The connector that screws onto the socket welded into the dome of the ICV. The ball-and-socket joint bolts onto the bottom of it.

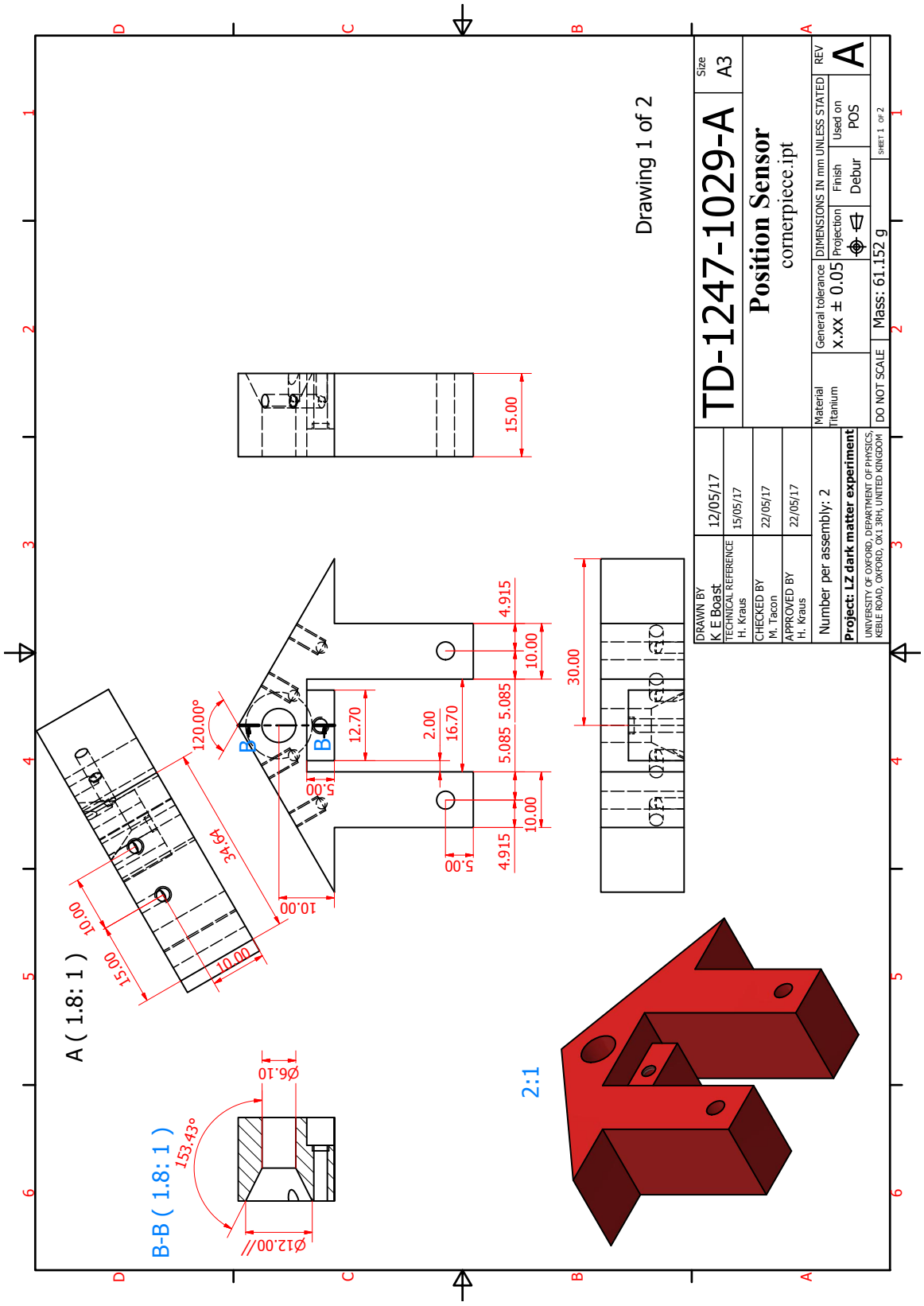


Figure F.19: The titanium corner piece that sits onto the PMT truss and connects two of the sides of the hexapod together.

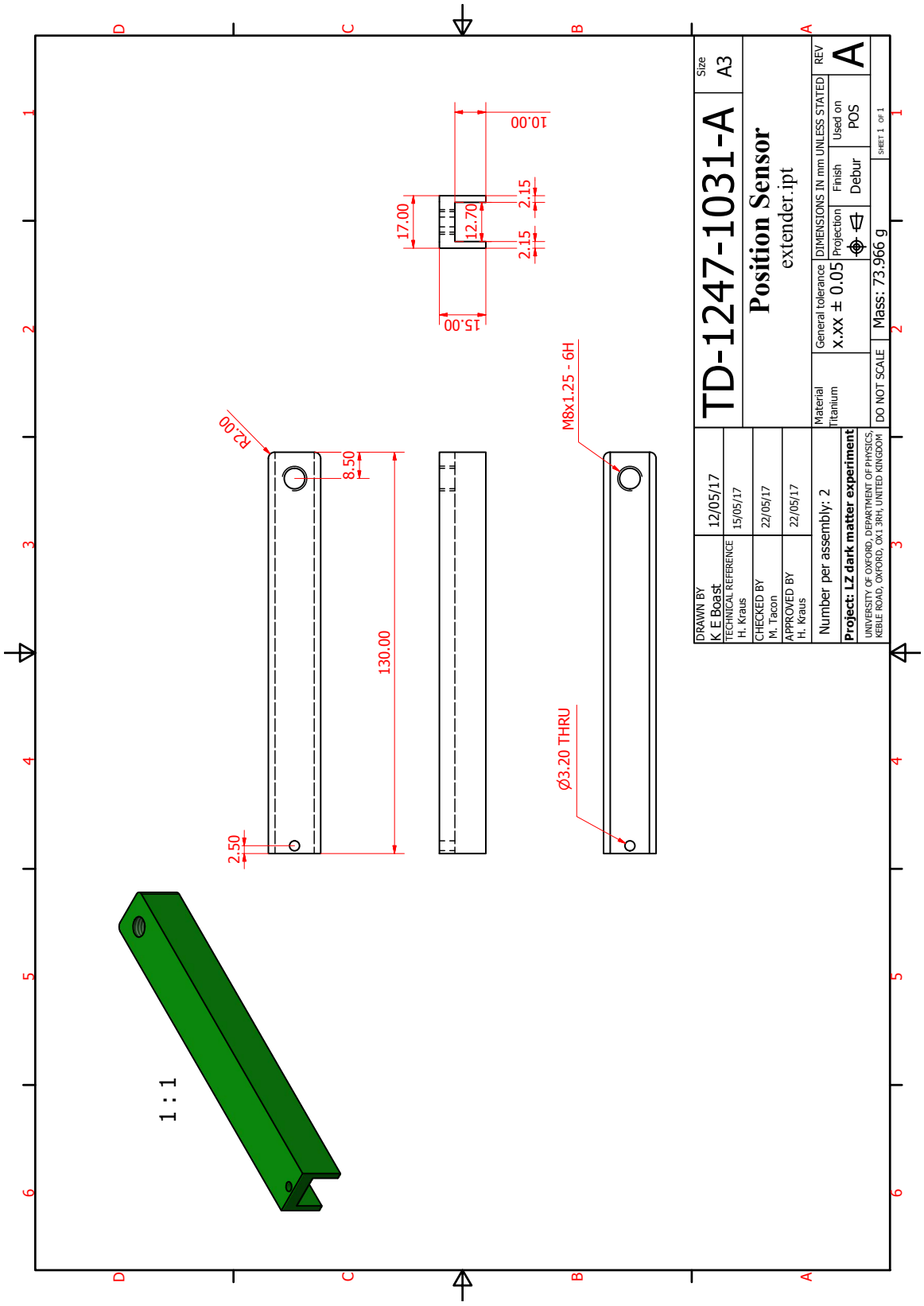


Figure F.20: The titanium piece that extends from a corner piece along the PMT truss and provides a point for the screw to screw into, connecting the PMT truss and hexapod. One end of the extender sits directly under the port in the cryostat dome.

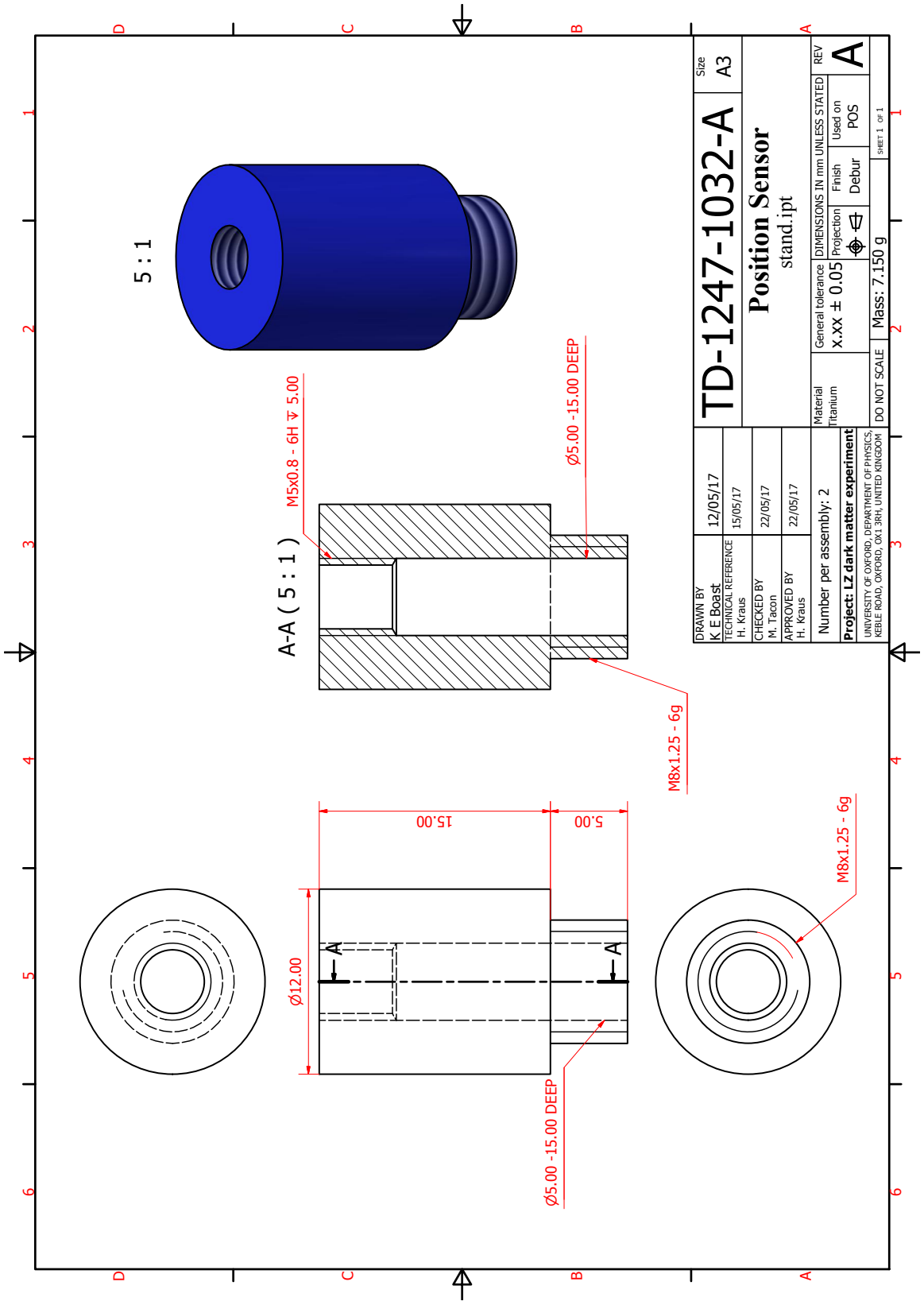


Figure F.21: The stand in which the captive screw sits, ready to connect the PMT truss and hexapod.

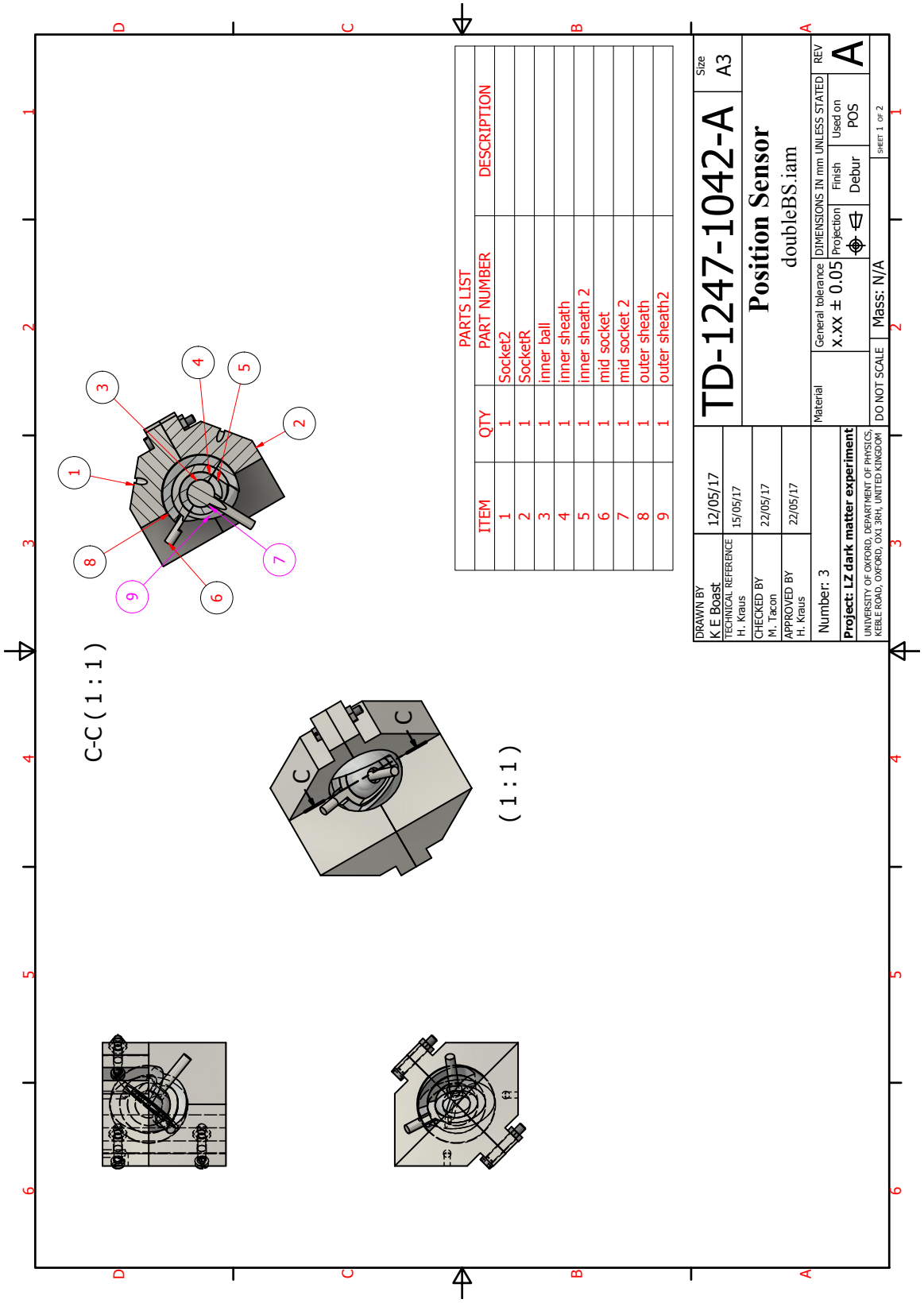


Figure F.22: The design for the double ball-and-socket joint.

Bibliography

[1] K. G. Begeman, A. H. Broeils, and R. H. Sanders, "Extended rotation curves of spiral galaxies: dark haloes and modified dynamics," *Monthly Notices of the Royal Astronomical Society*, vol. 249, pp. 523–537, 1991.

[2] K. Freese, "Status of Dark Matter in the Universe," in *The Fourteenth Marcel Grossmann Meeting*, pp. 325–355, 2017, https://www.worldscientific.com/doi/pdf/10.1142/9789813226609_0018.

[3] E. Aprile, J. Aalbers, and F. Agostini et al., "First Dark Matter Search Results from the XENON1T Experiment," *Phys. Rev. Lett.*, vol. 119, no. 18, p. 181301, 2017, 1705.06655.

[4] P. A. Amaudruz, M. Baldwin, and M. Batygov et al., "First results from the DEAP-3600 dark matter search with argon at SNOLAB," pp. 1–9, 2017, 1707.08042.

[5] G. Angloher, A. Bento, and C. Bucci et al., "Results on light dark matter particles with a low-threshold CRESST-II detector," *European Physical Journal C*, vol. 76, no. 1, pp. 1–8, 2016, 1509.01515.

[6] D. S. Akerib, S. Alsum, and H. M. Araújo et al., "Results from a Search for Dark Matter in the Complete LUX Exposure," *Physical Review Letters*, vol. 118, no. 2, pp. 1–8, 2017, 1608.07648.

[7] The DarkSide Collaboration, P. Agnes, and L. Agostino et al., "Results from the first use of low radioactivity argon in a dark matter search," *Physical Review D*, vol. 93, no. 8, p. 081101, 2015, 1510.00702.

[8] A. Tan, M. Xiao, and X. Cui et al., "Dark Matter Results from First 98.7 Days of Data from the PandaX-II Experiment," *Physical Review Letters*, vol. 117, no. 12, pp. 1–7, 2016, 1607.07400.

[9] B. W. Lee and S. Weinberg, "Cosmological Lower Bound on Heavy-Neutrino Masses," *Phys. Rev. Lett.*, vol. 39, no. 4, pp. 165–168, 1977.

[10] B. J. Mount, S. Hans, and R. Rosero et al., "LUX-ZEPLIN (LZ) Technical Design Report," p. 4, 2017, 1703.09144.

[11] R. Bernabei, P. Belli, and V. Landoni et al., "New limits on WIMP search with large-mass low-radioactivity NaI(Tl) set-up at Gran Sasso," *Physics Letters B*, vol. 389, pp. 757–766, dec 1996.

[12] R. Bernabei, P. Belli, and A. Di Marco et al., "DAMA/LIBRA results and perspectives," *EPJ Web of Conferences*, vol. 136, p. 05001, mar 2017, 1612.01387.

[13] A. Manzur, A. Curioni, L. Kastens, D. N. McKinsey, K. Ni, and T. Wongjirad, "Scintillation efficiency and ionization yield of liquid xenon for monoenergetic nuclear recoils down to 4 keV," *Physical Review C - Nuclear Physics*, vol. 81, no. 2, pp. 1–10, 2010, 0909.1063.

[14] D. S. Akerib, C. W. Akerlof, and S. K. Alsum et al., "Projected WIMP sensitivity of the LUX-ZEPLIN (LZ) dark matter experiment," *Physical Review D, American Physical Society*, pp. 1–16, Forthcoming 2018, 1802.06039.

[15] Analog Devices, "ADA4817-1/ADA4817-2 Data Sheet," tech. rep., Norwood, MA, 2016.

[16] Texas Instruments, "LMH6624/LMH6626 Single / Dual Ultra Low Noise Wideband Operational Amplifier," 2013.

[17] Texas Instruments, "LM7321x Single and LM7322x Dual Rail-to-Rail Input and Output 15-V , High-Output Current and Unlimited Capacitive Load Operational Amplifier," 2015.

[18] Analog Devices, "AD8065/AD8066 Data Sheet," tech. rep., Norwood, MA, 2010.

[19] K. D. Timmerhaus and R. Reed, *Cryogenic Engineering: Fifty Years of Progress*. Springer-Verlag New York, 2007.

[20] D. Stewart, "A platform with six degrees of freedom," *Proc. Institution of Mechanical Engineers (UK)*, vol. 180, no. Pt 1, No 15, 1965.

[21] P. M. Koch, M. Kesteven, and H. Nishioka et al., "The AMiBA Hexapod Telescope Mount," *The Astrophysical Journal*, vol. 694, no. 2, p. 1670, 2009, https://doi.org/10.1088/0004-637X/694/2/1670.

[22] B. L. Young, "A survey of dark matter and related topics in cosmology," *Frontiers of Physics*, vol. 12, no. 2, pp. 1–219, 2017.

[23] W. Thomson (First Baron Kelvin), "Baltimore lectures on molecular dynamics and the wave theory of light," (London), C. J. Clay and sons, 1904.

[24] H. Poincare, "The Milky Way and the Theory of Gases," *Popular Astronomy*, vol. 14, pp. 475–488, 1906.

[25] J. C. Kapteyn, "First Attempt at a Theory of the Arrangement and Motion of the Sidereal System," *The Astrophysical Journal*, vol. 55, no. 230, p. 302, 1922, arXiv:1303.5062.

[26] R. Clausius, "XVI. On a mechanical theorem applicable to heat," *The London, Edinburgh, and Dublin Philosophical Magazine and Journal of Science*, vol. 40, no. 265, pp. 122–127, 1870.

[27] S. J. Blundell and K. M. Blundell, *Concepts in Thermal Physics*. Oxford University Press, oct 2009.

[28] F. Zwicky, "On the Masses of Nebulae and of Clusters of Nebulae," *The Astrophysical Journal*, vol. 86, p. 217, 1937, 1937ApJ....86..217Z.

[29] G. Bertone and Hooper, "How dark matter became a particle," *CERN Courier*, vol. 47, no. 4, pp. 27–33, 2017.

[30] F. Zwicky, "Die Rotverschiebung von extragalaktischen Nebeln," *Helvetica Physica Acta*, vol. 6, pp. 110–127, 1933, arXiv:1011.1669v3.

[31] V. C. Rubin and W. K. Ford, "Rotation of the Andromeda nebula from a spectroscopic survey of emission regions," *The Astrophysical Journal*, vol. 159, no. February, 1970.

[32] A. Einstein, "Lens-Like Action of a Star by the Deviation of Light in the Gravitational Field," vol. 84, no. 2188, pp. 506–507, 1936.

[33] J.-P. Kneib, R. S. Ellis, I. Smail, W. J. Couch, and R. M. Sharples, "Hubble Space Telescope observations of the lensing cluster Abell 2218," *The Astrophysical Journal*, vol. 471, pp. 643–656, 1996.

[34] B. Paczynski, "Gravitational microlensing by the galactic halo," *The Astrophysical Journal*, vol. 304, pp. 1–5, 1986.

[35] D. Clowe, M. Bradac, and A. H. Gonzalez et al., "A direct empirical proof of the existence of dark matter," *The Astrophysical Journal*, vol. 648, pp. 109–113, 2006, 0608407.

[36] H. Böhringer, "ROSAT observations of galaxy clusters and cosmological implications," *Advances in Space Research*, vol. 13, no. 12, pp. 181–190, 1993.

[37] A. A. Penzias and R. W. Wilson, "A measurement of excess antenna temperature at 4080 Mc/s," *The Astrophysical Journal*, vol. 142, pp. 419–421, 1965.

[38] G. Duda, K. Garrett, and G. Duda, "Dark Matter: A Primer," *Advances in Astronomy*, vol. 2011, pp. 1–27, 2010, 1006.2483.

[39] Planck Collaboration, "Astrophysics Special feature Planck 2015 results," *Astronomy & Astrophysics*, vol. 13, pp. 1–39, 2016, 1502.01589.

[40] D. J. Fixsen, "The temperature of the cosmic microwave background," *Astrophysical Journal*, vol. 707, no. 2, pp. 916–920, 2009, 0911.1955.

[41] P. J. E. Peebles, "Large-scale background temperature and mass fluctuations due to scale-invariant primeval perturbations," *The Astrophysical Journal*, vol. 263, pp. L1–L5, 1982.

[42] D. Scott, G. F. Smoot, and Particle Data Group, "27 . Cosmic Microwave Background," *Chin. Phys. C*, vol. 38, no. 090001, pp. 1–24, 2014.

[43] U. Seljak and M. Zaldarriaga, "A Line-of-Sight Integration Approach to Cosmic Microwave Background Anisotropies," *The Astrophysical Journal*, vol. 469, pp. 437–444, 1996.

[44] M. Milgrom, "A modification of the Newtonian dynamics as a possible alternative to the hidden mass hypothesis," *The Astrophysical Journal*, vol. 270, pp. 365–370, 1983.

[45] G. Bertone and D. Hooper, "A History of Dark Matter," pp. 1–88, 2016, 1605.04909.

[46] S. Boran, S. Desai, E. Kahya, and R. Woodard, "GW170817 Falsifies Dark Matter Emulators," pp. 1–5, 2017, 1710.06168.

[47] LIGO Scientific Collaboration, Virgo Collaboration, Fermi Gamma-ray Burst Monitor, and INTEGRAL, "Gravitational Waves and Gamma-rays from a Binary Neutron Star Merger: GW170817 and GRB 170817A," *The Astrophysical Journal Letters*, vol. 848, no. 13, pp. 1–27, 2017, 1710.05834.

[48] S. White, C. S. Frenk, and M. Davis, "Clustering in a neutrino-dominated universe," *The Astrophysical Journal*, vol. 274, pp. L1–L5, 1983.

[49] M. Fukugita, C. J. Hogan, and P. J. E. Peebles, "The Cosmic Baryon Budget," *The Astrophysical Journal*, vol. 503, no. 2, pp. 518–530, 1998, 9712020.

[50] A. Milsztajn, T. Lasserre, and EROS collaboration, "Not enough stellar Mass Machos in the Galactic Halo," *Nuclear Physics B (Proc. Suppl.)*, vol. 91, pp. 413–419, 2001, 0002253.

[51] P. Tisserand, L. L. Guillou, and C. Afonso et al., "Limits on the Macho Content of the Galactic Halo from the EROS-2 Survey of the Magellanic Clouds," *Astronomy & Astrophysics*, vol. 469, pp. 387–404, 2007, 0607207.

[52] G. Bertone, *Particle Dark Matter*. Cambridge University Press, 2010.

[53] S. Dodelson and L. Widrow, "Sterile neutrinos as dark matter," *Physical Review Letters*, vol. 72, no. 1, pp. 17–20, 1994, 9303287.

[54] R. D. Peccei and H. R. Quinn, "CP conservation in the presence of pseudoparticles," *Physical Review Letters*, vol. 38, no. 25, pp. 1440–1443, 1977.

[55] R. D. Peccei, "QCD, Strong CP and Axions," no. 2, pp. 1–14, 1996, 9606475.

[56] J. M. Pendlebury, S. Afach, and N. J. Ayres et al., "Revised experimental upper limit on the electric dipole moment of the neutron," *Physical Review D - Particles, Fields, Gravitation and Cosmology*, vol. 92, no. 9, pp. 1–22, 2015, 1509.04411.

[57] J. Preskill, M. B. Wise, and F. Wilczek, "Cosmology of the invisible axion," *Physics Letters, Section B: Nuclear, Elementary Particle and High-Energy Physics*, vol. 120, no. 1-3, pp. 127–132, 1983.

[58] B. J. Mount, S. Hans, and R. Rosero et al., "LUX-ZEPLIN (LZ) Technical Design Report," 2017, 1703.09144.

[59] J. D. Lewin and P. F. Smith, "Review of mathematics, numerical factors, and corrections for dark matter experiments based on elastic nuclear recoil," *Astroparticle Physics*, vol. 6, no. 1, pp. 87–112, 1996.

[60] D. S. Akerib, X. Bai, and S. Bedikian et al, "The Large Underground Xenon (LUX) experiment," *Nuclear Instruments and Methods in Physics Research, Section A: Accelerators, Spectrometers, Detectors and Associated Equipment*, vol. 704, pp. 111–126, 2013, 1211.3788.

[61] C. F. P. da Silva, "Dark Matter Searches with LUX," 2017, 1710.03572.

[62] PandaX-II Collaboration, A. Tan, and X. Xiao et al., "Dark matter search results from the commissioning run of PandaX-II," *Physical Review D*, vol. 93, p. 122009, jun 2016, 1602.06563.

[63] M. Galloway, "Dark Matter Search at the Multi-Ton Scale with XENONnT," in *11th Identification of Dark Matter Conference*, 2016.

[64] E. Aprile, J. Aalbers, and F. Agostini et al., "Physics reach of the XENON1T dark matter experiment.," *Journal of Cosmology and Astroparticle Physics*, vol. 2016, no. 4, 2016, 1708.07051.

[65] V. Chepel and H. Araújo, "Liquid noble gas detectors for low energy particle physics," 2012, 1207.2292.

[66] C. E. Aalseth, F. Acerbi, and P. Agnes et al., "DarkSide-20k: A 20 Tonne Two-Phase LAr TPC for Direct Dark Matter Detection at LNGS," 2017, 1707.08145.

[67] P. Giampa, "In-situ Surface Contamination Removal and Cool-down Process of the DEAP-3600 Experiment," no. February, 2017, 1706.04854.

[68] R. Agnese, A. J. Anderson, and T. Aramaki et al., "Projected sensitivity of the SuperCDMS SNOLAB experiment," *Physical Review D*, vol. 95, no. 8, pp. 1–17, 2017, 1610.00006.

[69] R. Bernabei, "First model-independent results by DAMA / LIBRA phase2 [slides]," in *LNGS Scientific Committee Meeting, 2627 March 2018*, 2018.

[70] K. W. Kim, G. Adhikari, and P. Adhikari et al., "Pulse Shape Discrimination of Nuclear Recoil and Electron Recoil Events With a NaI(Tl) Crystal for Dark Matter Search," *IEEE Transactions on Nuclear Science*, vol. 63, no. 2, pp. 534–538, 2016.

[71] F. Froborg, "SABRE: WIMP modulation detection in the northern and southern hemisphere," *Journal of Physics: Conference Series*, vol. 718, no. 4, pp. 2–6, 2016, 1601.05307.

[72] B. J. Mount, S. Hans, and R. Rosero et al., "LUX-ZEPLIN (LZ) Technical Design Report," pp. 79–85, 2017, 1703.09144.

[73] B. J. Mount, S. Hans, and R. Rosero et al., "LUX-ZEPLIN (LZ) Technical Design Report," pp. 156–169, 2017, 1703.09144.

[74] B. J. Mount, S. Hans, and R. Rosero et al., "LUX-ZEPLIN (LZ) Technical Design Report," p. 13, 2017, 1703.09144.

[75] E. H. Miller, J. Busenitz, T. K. Edberg, and C. Ghag et al., "Constraining Radon Backgrounds in LZ," 2017, 1708.08533.

[76] E. Aprile, J. Aalbers, and F. Agostini et al., "Intrinsic backgrounds from Rn and Kr in the XENON100 experiment," *The European Physical Journal C*, vol. 78, p. 132, feb 2018, arXiv:1708.03617v2.

[77] B. J. Mount, S. Hans, and R. Rosero et al., "LUX-ZEPLIN (LZ) Technical Design Report," p. 204, 2017, 1703.09144.

[78] M. Leung, "Surface contamination from radon progeny," *AIP Conference Proceedings*, vol. 785, no. 2005, pp. 184–190, 2005.

[79] L. K. Baxter, "Capacitive Sensors: Design and Applications," in *Capacitive Sensors: Design and Applications*, ch. 4, pp. 48–60, Institute of Electrical and Electronics Engineers, Inc., 1997.

[80] C. C. Lim, D. H. Bowman, and R. A. Aziz, "Velocity of sound isotherms in liquid krypton and xenon," *Canadian Journal of Chemistry*, vol. 46, no. 22, pp. 3477–3482, 1968.

[81] Fralock, "Data Sheet for Cirlex." http://www.fralock.com/wp-content/uploads/2018/03/CIRLEX-DATA-SHEET-Technical.pdf accessed 25/05/18.

[82] B. Dasgupta and T. S. Mruthyunjaya, "Stewart platform manipulator: A review," *Mechanism and Machine Theory*, vol. 35, no. 1, pp. 15–40, 2000.

[83] A. Cauchy, "Deuxieme memoire sur les polygones et les polyedres," *Journal de l'Ecole Polytechnique*, pp. 87–98, 1813.

[84] DESI Collaboration, A. Aghamousa, and J. Aguilar et al., "The DESI Experiment Part II: Instrument Design," tech. rep., 2016, 1611.00037.

[85] J.-P. Merlet, "Parallel manipulators: state of the art and perspectives," *Advanced Robotics*, vol. 8, no. 6, pp. 589–596, 1993.

[86] J. Merlet, "Parallel manipulators: state of the art and perspectives," *Journal of the Robotics Society of Japan*, vol. 10, no. 6, pp. 751–756, 1992.

[87] W. Feng, W. Shimin, Z. Ying, and L. Qizheng, "Forward Displacement Analysis of a General 6-3 Stewart Platform Using Conformal Geometric Algebra," *Mathematical Problems in Engineering*, vol. 2017, 2016.

[88] M. Griffis and J. Duffy, "A Forward Displacement Analysis of a Class of Stewart Platforms," *Journal of robotic systems*, vol. 6, no. 6, pp. 703–720, 1989.

[89] J.-P. Merlet, "Direct kinematics of parallel manipulators," *IEEE Transactions on Robotics and Automation*, vol. 9, no. 6, pp. 842–846, 1993.

[90] P. R. McAree and R. W. Daniel, "A fast, robust solution to the Stewart platform forward kinematics," *Journal of Robotic Systems*, vol. 13, no. 7, pp. 407–427, 1996.

[91] A. Mura, "Six d.o.f. displacement measuring device based on a modified Stewart platform," *Mechatronics*, vol. 21, no. 8, pp. 1309–1316, 2011.

[92] E. Aprile, J. Aalbers, and F. Agostini et al., "Dark Matter Search Results from a One Tonne-Year Exposure of XENON1T," pp. 1–8, 2018, 1805.12562.

[93] P. Marion, F. Comin, G. Rostaing, M. Nicola, L. Eybert, and European Synchrotron Radiation Facility, "Hexapods at the ESRF: mechanical aspects, results obtained," in *Proceedings of Mechanical Engineering Design of Synchrotron Radiation Equipment and Instrumentation*, p. 42, 2004.